

Poznan University of Technology

Faculty of Materials Engineering and Technical Physics

DOCTORAL DISSERTATION

**Enhancement of structural stability and
operational reliability of perovskite solar cells**

Shyantana Dasgupta

Supervisor:

Prof. Alina Dudkowiak

Auxiliary Supervisor:

Konrad Wojciechowski Ph.D.

Poznan, 2023



The work presented in this Ph.D. thesis was conducted as an Implementation Doctorate Programme at Saule Research Institute.

List of contents

Abstracts	1
Acknowledgements	11
List of Abbreviations	12
List of Figures	15
CHAPTER 1. Motivation	17
CHAPTER 2. THEORETICAL PART A	25
2.1. Brief introduction to semiconductors	26
2.2. Recombination mechanisms in semiconductors	26
2.2.1. Radiative recombination	27
2.2.2. Auger recombination	27
2.2.3. Shockley-Read-Hall (SRH) recombination	28
2.2.4. Surface recombination	28
2.2.5. Thermal recombination	28
2.3. Trapping in semiconductors	29
2.4. Grain boundaries in semiconductors	31
2.5. Fundamentals of solar cell operation	32
2.6. Mechanisms for atmospheric absorption of sunlight	34
2.6.1. Ultraviolet (UV) range	34
2.6.2. Near UV range	35
2.6.3. Infrared (IR) range	35
2.6.4. Visible (Vis) range	35
2.7. The air mass (AM)	35
2.8. The extraterrestrial (AM0) solar spectrum	37
2.9. Intensity or photon flux	38
2.10. The global standard spectrum (AM1.5g)	39
CHAPTER 3. THEORETICAL PART B	41
3.1. Brief introduction to perovskite based semiconductors	41
3.2. Origin of perovskite solar cells	42

3.3. Perovskite properties, types, and the tolerance factor	43
3.3.1. Cubic Perovskites	44
3.3.2. Double Perovskites	44
3.3.3. 2D Layered Perovskites	44
3.4. Electronic properties of perovskite based semiconductors	45
3.5. Role of the halide ion	46
3.6. Role of the cation	48
3.7. Perovskite processing techniques	49
3.7.1. Evaporation	49
3.7.2. Chemical processing techniques	49
3.8. Perovskite device operation	54
3.9. Trapping mechanism in perovskite solar cells	56
3.10. Perovskite solar cell measurement parameters	58
CHAPTER 4. PREFACE TO THE EXPERIMENTAL PART	60
4.1. Influence of colloids and impurities on perovskite crystal growth ..	61
4.2. Study of the decomposition of aged perovskite solar cells using NIR spectroscopy	61
4.3. Perylene diimide based dyes as efficient electron transport layers for perovskite solar cells	63
4.4. Exploring the formation of a lower dimension perovskite structure at the solar cell interfaces for high efficiency and stability	66
4.5. A robust encapsulation route for plastic based flexible perovskite solar cells to withstand highly accelerated aging tests	68
CHAPTER 5	71
5.1. Conclusions	71
5.2. Use of perovskites in current industrial applications	72
REFERENCES	75
MANUSCRIPTS AND CERTIFICATIONS	86

Abstrakt

Rozdział 1 przedstawionej pracy doktorskiej opisuje efekty nasilających się zmian klimatycznych, wywołanych przez człowieka jak i naturalnych, oraz postępujące wyczerpywanie się tradycyjnych źródeł energii, co spowodowało poszukiwanie nowych ich źródeł takich jak biomasa, energia geotermalna, wiatr, a w szczególności energia słoneczna. Nowe źródła energii scharakteryzowano pod względem wydajności. Ponadto podano ogólne przepisy dotyczące ochrony środowiska. Wiele uwagi poświęcono wykorzystaniu energii słonecznej.

Rozdział 2 podaje teoretyczne podstawy dotyczące tematu badań prezentowanej pracy doktorskiej. Podano podstawowe informacje na temat poziomów energetycznych metali, półprzewodników i izolatorów. Pokrótce omówiono powstawanie ziaren podczas krystalizacji cienkowarstwowej oraz wpływ granic ziaren na transport ładunku w cienkich warstwach perowskitu. W tym rozdziale wyjaśniono także mechanizmy transportu i wychwytywania ładunku w cienkich warstwach. W tym rozdziale pokrótce opisano także mechanizmy rekombinacji w różnych rodzajach półprzewodników. Następnie szczegółowo wyjaśniono podstawy działania ogniw słonecznych opartych na złączu p-n, w którym wyjaśniono powstawanie ekscytonów lub pary elektron-dziura pod wpływem absorpcji światła. Zdefiniowano istotne parametry pomiarów dla ogniw słonecznych, takie jak gęstość prądu zwarcia (J_{sc}), napięcie obwodu otwartego (V_{oc}), współczynnik wypełnienia (FF) i wydajność konwersji mocy (PCE). Mechanizmy procesów wytwarzania ładunku w cienkowarstwowym ogniwie słonecznym po absorpcji energii świetlnej zostały omówione w dalszej części tego rozdziału wraz z krótkim opisem różnych obszarów widma elektromagnetycznego słońca, z których ogniwo słoneczne może pozyskiwać energię, tj. Zakres ultrafioletu (UV), zakres bliskiego UV, zakres podczerwieni (IR) i zakres widzialny (Vis). Przedstawiono definicję współczynnika masy powietrza (AM) i jego znaczenie w celu wyjaśnienia sposobu w jaki energia światła słonecznego jest rozpraszana dla różnych długości fal, co pozwala zrozumieć funkcjonowanie różnych ogniw słonecznych przy różnych długościach fal.

Rozdział 3 przedstawia rozwój technologii perowskitowych ogniw słonecznych w sektorze energetycznym i potencjał jej komercjalizacji, biorąc pod uwagę niski koszt, stabilność,

możliwość przeskalowania i zastosowania zielonej energii. Pokróctce wyjaśniono ewolucję perowskitowych ogniw słonecznych począwszy od ich starszej generacji barwnikowych ogniw słonecznych (DSSC). Pokróctce wyjaśniono struktury krystaliczne perowskitów, ich rodzaje ze względu na strukturę sieciową oraz współczynnik tolerancji Goldschmidta opisujący stabilność struktury perowskitu. Następnie szczegółowo wyjaśniono strukturę elektronową perowskitów, aby wyjaśnić jej przewagę nad technologiami GaAs i Si. Opisano funkcję każdego składnika struktury krystalicznej perowskitu ABX_3 , gdzie A jest kationem organicznym, B jest jonem metalu dwuwartościowego, a X jest jonem halogenkowym. Następnie omówiono różne techniki wytwarzania warstw perowskitu wraz z technikami wytwarzania chemicznego oraz szczegółowo omówiono model przesycenia La Mera podczas zarodkowania i wzrostu cienkiej warstwy. Omówiono różne antyrozpuszczalniki stosowane do wygaszania w technice wkrapiania antyrozpuszczalnika (ADT) w celu uzyskania gładszych i jednolitych warstw perowskitu oraz ich mechanizm zmniejszania rozpuszczalności rozpuszczalnika pierwotnego. W skrócony sposób wyjaśniono różne rodzaje antyrozpuszczalników oraz czas i tempo ich stosowania. Szczegółowo wyjaśniono mechanizm transportu ładunku wraz z mechanizmami wychwytywania w granicach ziaren perowskitowych ogniw słonecznych, a na koniec omówiono pomiary perowskitowych ogniw słonecznych dla standardowych protokołów w celu uzyskania parametrów pomiarowych (J_{sc} , V_{oc} , FF i PCE) wraz z periodycznym śledzeniem maksymalnego punktu mocy (MPPT), które zmniejsza efekty pre-bias, takie jak migracja jonów, która może prowadzić do niedokładności pomiarów urządzenia.

Rozdział 4 rozpoczyna się od wyjaśnienia wpływu koloidów na wzrost warstw perowskitu. Do śledzenia rozpuszczania koloidów w czasie, spowodowanego dodatkiem kwasów halogenowodorowych, wykorzystano analizę dynamicznego rozpraszania światła. Miejsca zarodkowania, jakie wydają się zapewniać te koloidy dla krystalizacji perowskitu, mają znaczący wpływ na kształt kryształu, jego jakość i możliwości optoelektroniczne, które zaobserwowano w tej pracy. Bardzo ważnym punktem badań było przeprowadzenie syntezy jodku metyloamoni (CH_3NH_3I , MAI) w unikalny sposób, który pozwala uzyskać ultra czysty materiał przy zastosowaniu taniego i prostego procesu. Ta metoda wytwarzania MAI zapewnia lepszą kontrolę nad koloidalnym roztworem prekursora perowskitu. Perowskitowe ogniwa słoneczne charakteryzujące się PCE powyżej 15% zostały wyprodukowane na podłożach na bazie szkła (2,0

x 1,5 cm²), ten protokół syntezy zastosowano również do innych jodków alkiloamoniowych. Do rozprawy doktorskiej dołączono kopię pracy zatytułowaną „*New Synthetic Route of Ultrapure Alkylammonium Iodides for Perovskite Thin Films of Superior Optoelectronic Properties*” (DOI: 10.1002/ente.202000478) prezentującą tę część badań wykonanych w ramach pracy doktorskiej.

W drugiej części rozdziału 4 zastosowano spektroskopię odbicia w bliskiej podczerwieni do elastycznych perowskitowych ogniw słonecznych na bazie politereftalanu etylenu/tlenku cynku (PET/IZO) (0,18 x 0,13 cm²) w celu zbadania kontrolowanego w czasie starzenia ogniw słonecznych. Zastosowano dwuwymiarową spektroskopię korelacyjną (2DCOS) dla zmiennej w czasie reflektancji w podczerwieni, aby wyjaśnić jednoczesne zmiany natężeń spektralnych, które były związane z chemicznymi i optycznymi zaburzeniami interakcji molekularnych różnych związków chemicznych podczas starzenia wytworzonych warstw perowskitu. Podano wyjaśnienie mechanizmu degradacji perowskitu. Najbardziej widoczne zmiany we współczynniku odbicia zaobserwowano w przypadku starzejących się ogniw słonecznych bez srebrnej elektrody, co sugeruje, że ogniwa bez bariery ochronnej mogą być bardziej podatne na zewnętrzne czynniki degradacji, takie jak stres związany ze światłem i termiczny. Do rozprawy doktorskiej dołączono kopię pracy „*Analysis of Perovskite Solar Cell Degradation over Time using NIR Spectroscopy – a Novel Approach*” (DOI: 10.3390/en15155397) poświęconą tej części badań wykonanych w ramach pracy doktorskiej.

Trzecia część rozdziału 4 skupia się na nowej molekułe perylenodiimidu (PDI), o której wiadomo, że wykazuje wysoką absorpcję molową i wysoką absorpcję w widmie widzialnym. PDI została funkcjonalizowana czterema różnymi grupami podstawników w pozycjach „bay”. Otrzymane materiały mogą w przyszłości zastąpić tradycyjne materiały do transportu elektronów na bazie fulerenów i prowadzić do lepszej wydajności poprzez minimalizację strat transportowych w perowskitowych ogniwach słonecznych. Grupy funkcyjne przyłączone do molekuly PDI wpływają na wyrównanie poziomów energetycznych pomiędzy molekułami PDI a perowskitem, prowadząc w ten sposób do lepszej ekstrakcji ładunku na granicy faz. Dzięki tej nowej molekułe PDI uzyskano PCE wynoszący 16,8% w elastycznych ogniwach perowskitowych z potrójnym kationem, o wymiarach 0,18 x 0,13 cm². Ta wartość była bliska PCE równemu 17,3% dla urządzenia na bazie estru metyloвого kwasu [6,6]-fenylo-C₆₁ masłowego (PCBM). W załączeniu

jest kopia pracy „*Solution-processable perylene diimide-based electron transport materials as non-fullerene alternatives for inverted perovskite solar cells*” (DOI: 10.1039/d2ta01321e) prezentująca szczegółowo tę część badań przeprowadzonych w ramach pracy doktorskiej.

W czwartej części rozdziału 4 badano efekty zmiany „buried interface” (ukrytej granicy faz) między materiałem transportującym dziury (HTM) a warstwą perowskitu przy użyciu dużych kationów organicznych (BOC), w celu zwiększenia kontaktu elektrycznego i jakości warstwy perowskitu. Badano również wpływ fluorowania kationu organicznego na skuteczność tej metody modyfikacji. Zilustrowano tworzenie faz perowskitu 2D na ukrytej granicy faz, badając odsłonięte dolne warstwy perowskitu i wskazując na integrację masywnych kationów w jego sieć. W przypadku zmodyfikowanych warstw liczne techniki spektroskopowe i pomiary elektryczne ujawniły lepszą ekstrakcję dziur i zmniejszone straty w wyniku rekombinacji niepromienistej. W różnych przeprowadzonych testach stabilności (test termiczny w temperaturze 85 °C, test działania w punkcie mocy maksymalnej, test wygrzewania w obwodzie otwartym) urządzenia ze stykiem po stronie p zmodyfikowanym BOC wykazują znacznie lepszą niezawodność długoterminową i wykazują lepszą wydajność fotowoltaiczną (blisko 19% dla najlepszego urządzenia wielkopowierzchniowego na elastycznym podłożu o wymiarach 0,18 x 0,13 cm²). Ponadto potwierdzono te wyniki, zwracając uwagę na wzmocnioną integralność strukturalną warstw perowskitu w następstwie zmiany granicy faz, co objawia się wolniejszym uwalnianiem jodu podczas ciągłego naświetlania. Potwierdzono to dodatkowo modelowaniem obliczeniowym zmodyfikowanych i niezmiennych oddziaływań HTM/perowskit. Dołączono kopię pracy „*Modification of a Buried Interface with Bulky Organic Cations for Highly Stable Flexible Perovskite Solar Cells*” (DOI: 10.1021/acsaem.2c02780) poświęconą tej części badań przeprowadzonych w ramach pracy doktorskiej.

W ostatniej części rozdziału 4 przedstawiono zaproponowaną technikę laminowania zapewniającą silną hermetyzację ogniw. Przedstawiono odpowiednie materiały klejące, folie barierowe i uszczelniacze krawędzi. Uniwersalność tej techniki wykazano poprzez zastosowanie opracowanej procedury do trzech różnych konfiguracji perowskitowych ogniw słonecznych (p-i-n z węglem, p-i-n ze srebrem i n-i z węglem) wytworzonych z dużą powierzchnią aktywną (1 cm²). Wysokowydajne, elastyczne ogniwa słoneczne (0,18 x 0,13 cm²) zachowały ponad 85% swojej

początkowej wydajności po serii testów przyspieszonego starzenia opartych na normach branżowych (IEC 61215 i IEC 61646), które obejmowały 1400 godzin w warunkach wysokiej wilgotności i wysokiej temperatury, 50 cykli termicznych i 10 cykli zamrażania w warunkach wysokiej wilgotności. Otrzymane wyniki były znaczącym przełomem w badaniach nad stabilnością perowskitowych ogniw słonecznych, ponieważ przedstawiono przekonującą ocenę długoterminowej niezawodności elastycznej fotowoltaiki perowskitowej w rzeczywistych warunkach zewnętrznych. Dołączono kopię pracy „*Encapsulation protocol for flexible perovskite solar cells enabling stability in accelerated aging tests*” (DOI: 10.1002/eem2.12434) opisującą tę część badań przeprowadzonych w ramach pracy doktorskiej.

W Rozdziale 5 podano podstawowe wyniki uzyskane w ramach tego projektu doktorskiego oraz ich konsekwencje w dziedzinie badań nad perowskitowymi modułami słonecznymi. Rozprawę zakończono wieloma propozycjami przyszłych prac w dziedzinie perowskitowych ogniw słonecznych oraz przedstawiono dodatkowe potencjalne udoskonalenie wyników.

Abstract

Chapter 1 of the presented doctoral dissertation describes the effects of growing climatic changes, caused by man and nature, and the depletion of traditional energy resources, which have stimulated the search for new sources of energy, including biomass, geothermal energy, wind, and in particular solar energy. The new sources of energy have been characterised by their efficiency. Moreover, the general regulations for natural environment protection have been mentioned. Much attention has been drawn to the specific advantages of using solar energy.

Chapter 2 gives the theoretical background of the subject of research undertaken in the doctoral dissertation. First, the energy levels of metals, semiconductors and insulators are explained. The formation of grains in the process of thin-layer crystallization and the effect of the grain boundaries on the charge transfer in perovskite thin layers are discussed. The mechanisms of charge transport and charge capturing in thin films are described together with the mechanisms of recombination in semiconductors of different types. The principles of work of solar cells based on p-n junction are explained along with the generation of excitons or electron-hole pair under the effect of absorbed light. The parameters describing the solar cells are defined, including short-circuit current density (J_{sc}), open-circuit voltage (V_{oc}), fill factor (FF) and power conversion efficiency (PCE). Further on the mechanisms involved in the process of charge generation in the thin-film solar cell are described. Also, the effects of solar light absorption from different spectral ranges are included, including those of absorption in ultraviolet (UV), near UV, infrared (IR) and visual (Vis). Moreover, the notion of air mass (AM) coefficient is introduced and its importance in explaining the sunlight energy dispersion at different wavelengths after it has passed through the atmosphere, which helps in understanding the functioning of different solar cells at different wavelengths.

Chapter 3 presents the progress made in the technology of perovskite solar cells in the aspect of their application in solar energy production and the potential of its commercialisation in view of its low cost, stability, rescaling ability, and green energy use. The evolution of perovskite solar cells, starting from an old generation of dye synthesized solar cells (DSSC) is briefly described. The crystalline structure of perovskites, its types differing in the lattice structure and the

Goldschmidt tolerance factor, used to describe the perovskite structure stability are defined. The electronic structure of perovskites has been given more attention to point out the advantages of perovskite technology over those of GaAs and Si. The function of each component of the crystalline structure of ABX_3 perovskite, where A is an organic cation, B is a divalent metal ion, and X is a halogen ion, is explained. Different techniques of perovskite thin layer production are presented, including the wet bench based techniques such as spin coating, while La Mer's supersaturation model of nucleation and thin film growth has been given particular attention. Different anti-solvents used for quenching in the anti-solvent dropping technique (ADT) for smoother and uniform perovskite films and their mechanism in reducing the solubility of the primary solvent have been discussed. Different types of anti-solvents and their application time and rates have been explained. The charge transport mechanism along with trapping mechanisms in grain boundaries of perovskite solar cells have been explained in detail and finally, the perovskite solar cell measurement for standard protocols to obtain measurement parameters (J_{sc} , V_{oc} , FF, and PCE) have been discussed along with the periodic maximum power point tracking (MPPT) which reduces pre biasing effects like ion migration which could lead to inaccuracy in device measurements.

Chapter 4 first starts with an explanation of the impact of colloids on the growth of perovskite films. Dynamic light scattering analysis was used to trace the dissolution of colloids initiated by the addition of hydrohalic acid, in time. The nucleation sites that these colloids offer for perovskite crystallization have a significant influence on the crystal's shape, quality, and its optoelectronic capabilities, observed in this study. An important issue was the synthesis of methylammonium iodide (CH_3NH_3I , MAI) that yields ultrapure material in a low-cost and straightforward process. This method of preparing MAI gives it better control over the colloidal perovskite precursor solution. Perovskite solar cells characterized with PCE of above 15% were fabricated on glass based substrates ($2.0 \times 1.5\text{cm}^2$), and the synthetic protocol applied was also followed for other alkylammonium iodides. A copy of the paper entitled '*New Synthetic Route of Ultrapure Alkylammonium Iodides for Perovskite Thin Films of Superior Optoelectronic Properties*' (DOI: 10.1002/ente.202000478) describing this new procedure is attached.

In the second part of Chapter 4, a near IR based reflectance spectroscopy was applied to flexible polyethylene terephthalate/indium zinc oxide (PET/IZO) based perovskite solar cells (0.18x 0.13 cm²) to study the time controlled aging of the solar cells. A two dimensional correlation spectroscopy (2DCOS) of time varying NIR reflectance was applied to explain the concurrent variations in spectral intensities which were related to chemical and optical perturbations of the molecular interactions of different chemical species in the process of ageing of fabricated perovskite films. This chapter offers an explanation of the perovskite degradation mechanism over time. The most prominent changes in reflectance were observed for aged solar cells without a silver electrode, which suggested that the cells without a protective barrier could be more susceptible to extrinsic factors of degradation like sunlight and thermal stress. A copy of the paper entitled '*Analysis of Perovskite Solar Cell Degradation over Time using NIR Spectroscopy – a Novel Approach*' (DOI: 10.3390/en15155397) devoted to this part of the doctoral dissertation is enclosed.

The third section of Chapter 4 is focused on a novel molecule of perylene diimide (PDI), known to display high molar absorptance and high absorption in the visible range. In this study, the PDI molecules were functionalized with four different substituent groups in the bay positions. The materials obtained could replace in future the traditional fullerene-based electron transport materials and lead to better efficiencies by minimizing transport losses in perovskite solar cells. The functional groups attached to the PDI molecule led to the alignment of energy levels between the PDI molecules and the perovskite, thus leading to better charge extraction at this interface. Thanks to this new PDI molecule, it was possible to achieve a PCE of 16.8%, using flexible substrate based perovskite solar cells with a triple cation, of the size 0.18 x 0.13 cm², which was close to the PCE of 17.3 % obtained for the cells based on methyl ester of [6,6]-phenyl-C₆₁ butyric acid (PCBM). A copy of the paper entitled '*Solution-processable perylene diimide-based electron transport materials as non-fullerene alternatives for inverted perovskite solar cells*' (DOI: 10.1039/d2ta01321e), reporting the above part of the doctoral dissertation, is enclosed.

The main issue of the fourth section of Chapter 4 is an investigation of the change in the buried interface between the hole transport (HTM) and perovskite layer, as a consequence of using bulky organic cations (BOC) to increase the electronic contact and perovskite thin layer quality. The

effect of fluorination of the organic cation on the results of this modification method was also considered. The formation of 2D perovskite phases at the buried interface was analysed by examining the lift-off perovskite samples, indicating the integration of massive cations into the perovskite lattice. At the modified interfaces, numerous spectroscopic and electrical characterization techniques revealed enhanced hole extraction and reduced non-radiative recombination losses. In various stability tests (thermal test at 85 °C, operational test at maximum power point, light soaking test at open-circuit), the devices with the BOC-modified p-side contact exhibited significantly improved long-term reliability and showed improved photovoltaic performance (approaching 19% for the champion large-area device on the flexible substrate of dimensions 0.18 x 0.13 cm²). Additionally, these findings were confirmed by pointing out the perovskite films strengthened structural integrity following interface alteration, which is demonstrated by slower iodine release during continuous light soaking. This is further supported by computational modelling of the modified and unaltered HTM/perovskite interactions. A copy of the paper '*Modification of a Buried Interface with Bulky Organic Cations for Highly Stable Flexible Perovskite Solar Cells*' (DOI: 10.1021/acsaem.2c02780) describing in detail this part of the doctoral dissertation, is enclosed.

The final section of Chapter 4 presents the proposed lamination technique that ensures strong hermitization of the cells. Also, the right adhesive materials, barrier foils and edge sealants are described. The universality of this technique is proved by the effects of its application to three different perovskite solar cell configurations (p-i-n with carbon, p-i-n with silver, and n-I with carbon) with large active areas (1 cm²). The high-performance flexible solar cell devices (0.18 x 0.13 cm²) retained more than 85% of their initial performance following a series of accelerated aging tests based on industry standards (IEC 61215 and IEC 61646), which included 1400 hours of moist heat, 50 thermal cycles, and 10 humidity freeze cycles. This result was a significant breakthrough in perovskite solar cell stability research, since it provided a convincing evaluation of feasibility evaluation for the long-term use of flexible perovskite photovoltaics in open air conditions, exposed to the elements. A copy of the paper on '*Encapsulation protocol for flexible perovskite solar cells enabling stability in accelerated aging tests*' (DOI: 10.1002/eem2.12434) reporting this part of the study performed within the doctoral dissertation is enclosed.

Finally, in Chapter 5, the primary results obtained in this Ph.D. study are described in detail together with their interpretation and predicted consequences in the research field of perovskite solar modules. The dissertation concludes with many proposals for future work in the field of perovskite solar cells and additional prospective advancements of the results have been provided.

Acknowledgements

Words cannot express my gratitude to my mentor and auxiliary supervisor Dr. Konrad Wojciechowski for his valuable guidance, patient hearing, and feedback along with Professor Dr. Alina Dudkowiak for her support and meticulous organization of this doctoral study. This thesis could not have been undertaken and completed without the financial aid of the Foundation of Polish Science (First TEAM/2017-3/30). Heartfelt thanks also go to the defense committee who have generously provided their knowledge and expertise towards the completion of this doctoral thesis.

This thesis also recognizes the gratitude of Dr. Olga Malinkiewicz, the CTO of Saule Technologies for granting an extension for this Ph.D. dissertation and inculcating a sense of punctuality and responsibility in me.

Heartfelt warmth and appreciation also go to my project peers, namely Dr. Rosinda Fuentes Pineda, Dr. Taimoor Ahmad and Dr. Vivek Babu who have taught me and helped me solve any barriers I faced during my Ph.D. laboratory work. I also express my gratitude to Dr. Wojciech Mróz of the Consiglio Nazionale delle Ricerche (CNR) who helped me to edit a few vital sections of this work.

A token of appreciation to my mother Mita Dasgupta, stepfather Col. Sangram Mahapatra, father Saibal Dasgupta, my grandmother Tripti Dasgupta who supported me financially and emotionally throughout this work. Sincere thanks also go to my close friend Aleksandra Leszczyszyn (Kitty) and graphic designer and friend Karolina Turczyn who helped me with editing the designs of pictures in this thesis. Finally, a round of thanks to my late science tutor, Mr. Moloy Pal, who helped me inculcate a love of science and mathematics during my childhood. My gratitude also extends to the scientific editorial boards, who have helped me publish my work in their respective journals, namely: Energy Technology (Wiley), Energies (MDPI), Journal of Materials Chemistry A (Royal Society of Chemistry), Applied Energy Materials (American Chemical Society), Energy and Environmental Materials (Wiley).

List of abbreviations

ADT	Anti-solvent dropping technique
PET/IZO	Polyethylene terephthalate/indium zinc oxide
PCBM	[6,6]-phenyl C ₆₁ butyric acid methyl ester
COP	Conference of Parties
PM	Particulate Matter
PV	Photovoltaic
RES	Renewable sources of energy
TWh	Terawatt-hour
CIGS	Cadmium Indium Gallium Selenide
CPV	Concentration photovoltaic
IL	Interfacial layers
CB	Conduction band
VB	Valence band
E _f	Fermi level
eV	Electron volt
SRH	Shockley Read Hall
EHP	Electron-hole pair
I-V	Current Voltage
MPP	Maximum Power Point
V _{oc}	Open circuit voltage
I _{sc}	Short circuit current
J _{sc}	Short circuit current density
FF	Fill Factor
PCE	Power Conversion Efficiency
AM	Air Mass
UV	Ultraviolet

(N)IR	(Near) Infrared
Vis	Visible
E_{ph}	Photon energy
PSC	Perovskite Solar Cell
OIHP	Organic-inorganic hybrid perovskite
CdTe	Cadmium Telluride
CIGS	Copper indium gallium diselenide
GaAs	Gallium arsenide
DSSC	Dye synthesized solar cell
HTM	Hole transport material
OPV	Organic photovoltaic
RP	Ruddleson-Popper
DJ	Dion-Jacobson
MAI	Methylammonium iodide
MAPI	Methylammonium lead iodide
DFT	Density functional theory
MA	Methylammonium
FA	Formamidium
HTL	Hole transport layer
IEC	International electrotechnical commission
FPEAI	Fluorinated phenyl-ethyl ammonium iodide
PEAI	Phenyl-ethyl ammonium iodide
CC	Critical Concentration
CS	Saturation concentration
ASE	Anti-solvent engineering
SSE	Solvent-solvent extraction
GGPM	Gas flow induced gas pumping
r_c	Critical radius

ΔG_c	Gibbs free energy
PL	Photoluminescence
S	Surface recombination velocity
D	Diffusion coefficient
LED	Light-emitting diode
GB	Grain boundary
HI	Hydro Iodic Acid
FTIR	Fourier Transform infrared spectroscopy
2DCOS	Two-dimensional correlation spectroscopy
THz	Terahertz
NMR	Nuclear Magnetic Resonance
PDI	Perylene diimide
PVSCs	Perovskite solar cell structures
PTAA	Polytryaryl amine
DMF	Dimethyl formaldehyde
BOC	Bulky organic cations
CTE	Coefficient of thermal expansion
CAGR	Compound Annual Growth Rate
R&D	Research and Development
BIPVs	Building integrated photovoltaics
VIPVs	Vehicle integrated photovoltaics
CAPEX	Cost Expenditure
OPEX	Operational Expenditure

List of figures

<i>Figure 1a. Graph displaying power generation from different renewable sources of energy in 2020.</i> ^[1]	21
<i>Figure 1b. Histograms displaying the net solar capacity of the world between 2018-2020.</i> ^[2] ...	22
<i>Figure 2a. Schematic of the band energy diagram of metal, semiconductor and insulator</i>	26
<i>Figure 2. Schematics of energy diagrams of a semiconductor displaying b) radiative recombination c) Auger recombination d) Shockley-Read-Hall (SRH) recombination e) surface recombination</i> ^[3] <i>f) thermal recombination</i> ^[4]	29
<i>Figure 2g. Schematic of the band energy diagram of a semiconductor with shallow and deep trapping energy levels</i> ^[5]	30
<i>Figure 2. Graphical plot of h) Current density versus voltage J-V measurement of a solar cell i) standardized solar irradiation.</i> ^[6]	34
<i>Figure 2j. Schematic showing the air mass dependence on the sun's elevation angle with the earth's surface</i> ^[7]	36
<i>Figure 2k. Air mass versus the zenith at different elevation angles.</i> ^[8]	37
<i>Figure 2l. Graphical representation of the variation of solar irradiance versus photon wavelength for AM0 spectra</i> ^[7]	38
<i>Figure 2. Graphical representation of m) Photon flux of AM0 spectrum vs photon wavelength; n) Photon flux of AM0 spectrum vs photon energy</i> ^[7]	39
<i>Figure 3. Schematics of perovskite structures a) cubic perovskites b) double perovskites c) layered perovskites</i> ^[9]	45
<i>Figure 3. Schematic of energy band diagrams of different generation solar cells d) 1st Generation e) 2nd Generation f) Halide Perovskites</i> ^[10] <i>and g) The photon energy-dependent absorption coefficients of the most common semiconductor materials used in solar cell applications.</i> ^[11]	46
<i>Figure 3h. The variation in the absorption coefficient of MAPb(IxBr1-x)3 systems as a function of composition.</i> ^[12]	47
<i>Figure 3. Perovskite film processing techniques i) co-evaporation</i> ^[13] <i>j) spin coating with anti-solvent dripping technique</i> ^[14] <i>k) La Mer's diagram for supersaturation</i> ^[15]	52

<i>Figure 3. l) Schematic of perovskite film formation by different types of antisolvent during spin coating technique</i>	
<i>m) Schematic of a different pipette tip widths resulting in different antisolvent application velocities^[16]</i>	54
<i>Figure 3n. Schematic of carrier transport and trapping in a perovskite solar cell^[17]</i>	56
<i>Figure 3. Schematic of perovskite grain formation by o) a single large grain forming the entire volume of the crystal</i>	
<i>p) several small grains stacked to form the entire crystal^[18]</i>	57
<i>Figure 4a. Schematic of the 2D correlation spectroscopy (2DCOS)^[19]</i>	63
<i>Figure 4b. Representative diagram of a PDI molecule^[20]</i>	65

CHAPTER 1.

Climatic changes, conventional and non-conventional sources of energy

The scientific world has faced many challenges in the search for solutions for improving the current climatic situation. In order for a deeper understanding of this diverse phenomenon and the synergy between human needs and nature, it is vital to address a few definitions. The climate is a well-studied term as the average state of the ocean and the atmosphere scaled from several to a million years, presented in the form of a statistical description with the help of statistical measures as the average or variance related to meteorological parameters. Climate change is a result of actions from natural (incoming solar radiation) or man-made activities (the greenhouse effect and global warming). They could also be a result of internal climatic fluctuations. During the beginning of the 21st century, the term ‘Global climatic change’ has been used to describe the context of global warming which is a rise in the temperature of the earth’s surface due to the increase in the concentration of greenhouse gases in the atmosphere along with other accompanying phenomenon like changes in precipitation conditions and extreme weather conditions.^[21] Global warming is formed in the following manner: the earth is heated by the Sun which then radiates the heat back to space as an infrared form of radiation. Several greenhouse gases such as carbon monoxide, methane, etc. interact with this outgoing radiation, thus leading to a rise in the temperature of the Earth’s surface. If it weren’t for the carbon dioxide in the earth’s atmosphere most of its surface would be frozen. However, the amount of carbon dioxide required to keep the earth warm enough for life support is much less compared to other gases.^[22] For 10,000 years the carbon dioxide levels in the earth’s atmosphere have been fairly stable, but since new forms of energy generation from oil, natural gas and coal were learned by humans, the amount of carbon dioxide in the atmosphere exceeded these of conventional sources of energy. Since the industrial revolution started, the carbon dioxide levels in the Earth’s atmosphere increased by 30% and as a consequence the average global temperature increased by 2.2 degrees Fahrenheit.^[23] Burning fossil fuels not only increases the earth’s temperature but also causes acidification of water thus endangering marine life.^[24] These deplorable conditions of the Earth have accelerated with visible effects everywhere:

the melting of ice sheets and glaciers and rising sea levels. The disappearance of Arctic Sea ice along with droughts and fires are a cause of concern.^[25] To counter these environmental problems caused by human activity – The Paris Agreement was drafted.^[26] It is a legal bound international treaty based on climatic changes. Adopted by a stunning number of 196 parties at COP 21 in Paris on the 12th of December 2016 and put into action on November 4th, 2021, many different countries including leaders of the world’s largest economies, took part in the meeting. The main goal of this summit was to limit global warming to a value below 2°C and keep it at 1.5°C. This agreement was meant to control climate changes and save humanity from the extreme climatic changes. Usage of non-conventional sources of energy is one method to reduce carbon dioxide emissions to the levels as denoted in the Paris Agreement. Therefore a tremendous opportunities for investments in renewable sources of energy like solar energy, wind energy, geothermal, biofuel and hydroelectricity have appeared.^[26] In his book “How to Avoid a Climate Disaster – The solutions We Have and the Breakthroughs We Need” Bill Gates has described the deplorable effects of global warming. The extinction of flora and fauna along with natural disasters, floods, draughts, and other unprecedented weather fluctuations are a few of the results of rising temperatures. This could result in billions of human populations suffering from hunger and disease.^[27] Gates didn’t just write empty scripts but has clearly emphasized on the effects of climatic change on the human and animal population. He clearly states in his book that renewable sources of energy are not just a panacea for the needs of mankind but an important factor in reducing the carbon dioxide emissions. For the survival of mankind everyone can start contributing for the planet’s safety by installing ecological solar panels to help reduce harmful carbon dioxide emissions.^[22] The installation of photovoltaic (PV) panels is environmentally safe as there are no greenhouse emissions or other harmful dust particles (e.g.: PM10), which are generated during fossil fuel combustion. Additionally, PV modules are 96% recycled. This would mean that almost all the materials used for fabrication of solar panels are recycled contributing to various branches of economy, including new solar panels. These panels utilize solar energy i.e., solar radiation which generates heat, in turn causing photophysical processes generating electricity. The amount of sunlight striking the earth in 90 minutes is enough to satisfy the entire world’s energy consumption for a whole year. When properly harnessed, solar energy can meet all future energy needs. Solar installations not only effectively reduce carbon dioxide emissions but also oxides of sulphur, nitrogen, carbon, and dust particles, leaving a significantly reduced carbon footprint. Photovoltaics

ensure environmental safety by reducing emission of greenhouse gases and other air pollutants. Solar energy usage has a positive direct impact on our ecosystem as it replaces or significantly reduces the usage of other conventional forms of energy like coal, natural gas or crude oil which deplete the quality of our environment. In a nutshell: the development of solar based energy systems is vital for sustainable development^[28] with its prognosis being optimistic. The modern world that we know strives on different sources of energy to satisfy the man's overwhelming thirst for technology. Our use and knowledge of different sources of energy have grown tremendously over the past few years. For the purpose of protecting life and nature on our planet, as well for economic conditions, we must switch from fossil fuels to renewable sources of energy. These sources of energy are also coined as non-conventional energy sources such as the sun (solar energy), wind (wind energy), rivers (hydro power) and hot springs (geothermal energy), tides and biomass (biofuels). There are abundant reasons to support the development of renewable sources of energy (RES). In a few countries it is vital to search for alternative sources of energy (apart from reduction of pollutant emissions and the release of greenhouse gases) due to growing concerns about the safety of nuclear energy production. The annual increase in these renewable sources of energy technology has been made easy due to technical installations to harness these RES to satisfy humanity's energy needs.^[29] Undoubtedly, all non-conventional sources of energy are clean and beneficial sources of energy, but solar energy is the most vital of all.

An important argument for the superiority over wind energy is its low cost. Wind turbines require more maintenance than photovoltaic solar panels.^[30] Moreover, wind farms are usually located in remote locations with little or no access to the real consumers. The wind energy distribution companies have imposed high fees over the years rendering their proposal unprofitable in recent times. Furthermore wind energy is unpredictable as wind velocities often increase and decrease which renders it less efficient than solar energy^[25]; the noise pollution from its turbines is another issue. Compared to solar energy, the costs of setting up new hydropower plants are much higher compared to setting up of solar fields/panels. Moreover, the construction of dams influences or created changes in the ecosystem in the surroundings.^[31] Hydropower plants change the natural course of rivers creating new lakes thus mitigating the natural flow of water. This impacts fisheries as it changes the courses of fish migration by changing their natural habitats. In addition, the hydropower plant functioning is influenced by seasonal fluctuations in the water supply.

Photovoltaic panels, on the other hand, do not alter the environmental conditions and also save installation space as it can be integrated to building roofs and other home-based systems.

Another source of RES is biomass. However, logistical issues and the overall energy consumption challenge its advantages since a tremendous amount of energy is needed for harvest and transportation of crops to the powerplant. The air pollution caused by burning of biomass is lower compared to traditional fossil fuels. But still causes the formation of volatile organic compounds like carbon monoxide and nitrogen oxide. Wood is the main source of biomass and an uncontrolled consumption of this source of energy can lead to deforestation which can further lead to several natural/man-made disasters like soil erosion, landslides, etc.^[32] Solar technologies do not consume land space that could be utilized for crop farming, building infrastructure, etc. thus rendering solar based sources of energy more efficient than biomass.

Geothermal energy powerplants can be built in few selective locations only.^[33] Geothermal powerplants need reservoirs above 100°C which are often found near the boundaries of tectonic plates or hotspots. Furthermore, it is worth highlighting that these geothermal facilities have high initial costs of construction which doesn't render it a cheap source of renewable energy source. Construction of geothermal power plants often involves deep drilling of the ground to free hot waters trapped in rock formations, which further leads to instabilities of underground structures often leading to earthquakes.^[34]

Another commonly known renewable source of energy is tidal energy. Similar to wind, hydropower, and geothermal energy plants, tidal powerplants require high maintenance and initial cost.^[35] The potential sites for installation of tidal powerplants require specific conditions. The powerplants generating tidal energy must be built on shorelines where the difference between the high tide and low tide is large enough for turbine functioning. This reason itself makes this technology not accessible abundantly. An elaborate statistical diagram displaying the power usage of renewable sources of energy is displayed in **Figure 1a**.

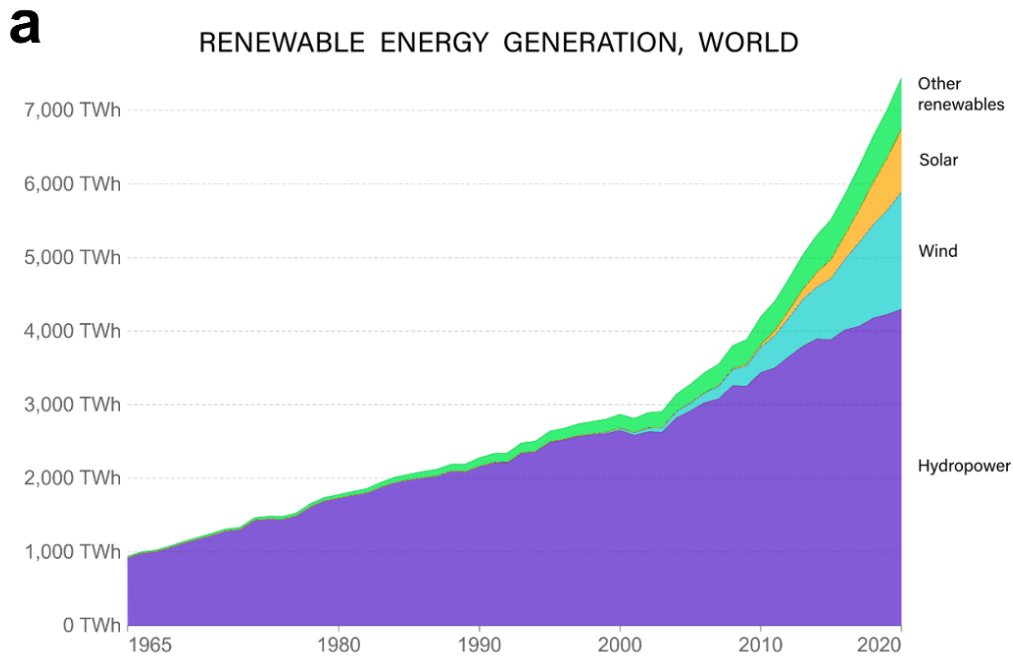


Figure 1a. Graph displaying power generation from different renewable sources of energy in 2020.^[1]

Solar energy is the most abundant form of renewable, environmentally clean, and cheapest form of energy. Installation of solar panels not only makes us save on electricity bills, but also makes the option of receiving payments for excess energy available to us. Solar energy is used for a variety of different purposes from generating electricity to heat. Thus, the utilization of solar energy is a great way to fight climatic changes and make our homes and lifestyle more environmentally friendly. Photovoltaics is becoming more and more popular as well as the lowest energy source to generate electricity in many countries of the world. Solar energy showed the second largest increase in absolute production of energy compared to all other sources of renewable energies in 2020. In total a record of 133 GW of photovoltaics were installed worldwide in 2020.^[36] **Figure 1b** displays the net solar energy utilization of the world from 2018-2020. According to data from the International Energy Agency, China has the largest solar capacity in the world, with 253 GW of installed solar capacity by the end of 2020 as recorded. The European Union on the other hand has a record of 151 GW. Furthermore, photovoltaic installations can smoothly function for over 100 years or longer and thus after its initial cost of setting up, the operating costs of solar powerplants are extremely low compared to existing sources of energy.^[37]

The first silicon solar cell which paved the way for other solar technologies was built by Bell laboratories in 1954. It was a giant milestone at the awakening of a new era which led to the realization of one of the most cherished dreams for mankind: harnessing the limitless energy of the sun for the sustainable growth of civilization.^[38] Photovoltaic sources of energy convert the radiation energy of sunlight into electrical energy using solar cell and store it in batteries. Various materials and technologies have been explored to fabricate efficient solar batteries/panels. The light striking a solar cell can be reflected, absorbed, or passed directly. A photovoltaic solar cell consists of several semiconducting materials sandwiched between two metal electrodes. Materials like semiconductors with appropriate bandgaps can absorb a certain spectrum of the sunlight and convert it into electrical energy. This electrical energy is used to supply the electricity network. The most commonly used PV technologies are silicon, perovskite, organic, quantum dot and chalcogenide, cadmium indium gallium selenide (CIGS) and concentration photovoltaic (CPV) technologies.^[39]

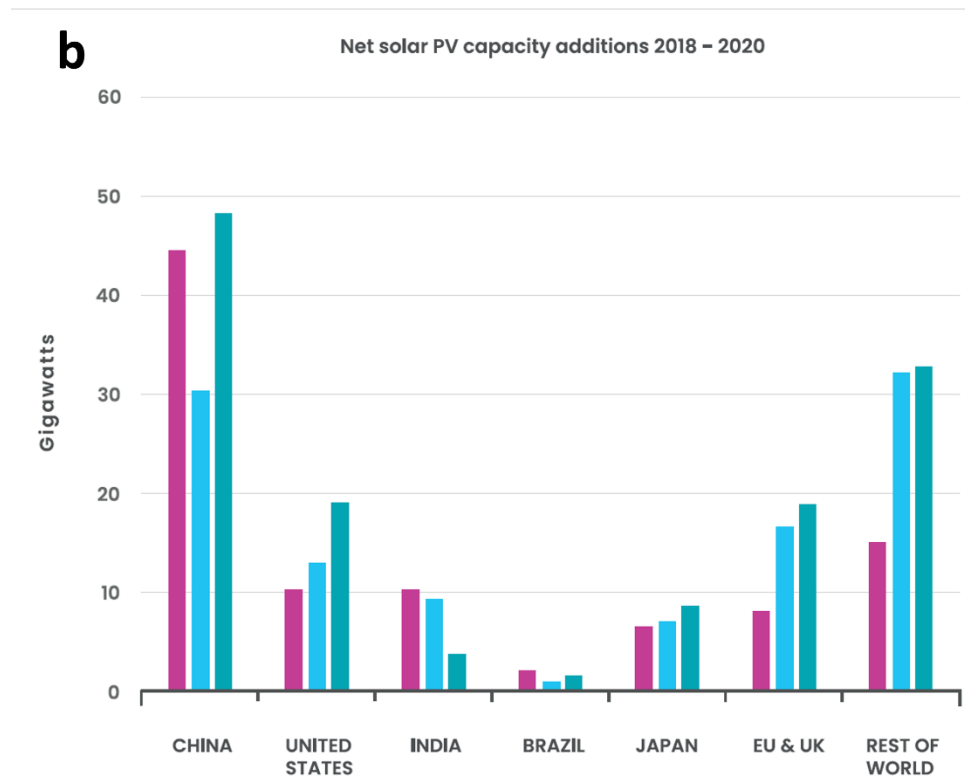


Figure 1b. Histograms displaying the net solar capacity of the world between 2018-2020.^[2]

The research to improve the photovoltaic technologies to create more efficient solar panels is a hotbed for scientists in the solar energy sector. In recent years, photovoltaic devices based on perovskite materials have become one of the most promising topics of research in the field of energy conversion. Organic inorganic lead halide perovskites have emerged as a propitious class of materials for solar-based applications reaching efficiencies from 3.8% in 2009 up to 25.5% in 2021.^[40–44] Perovskite solar cells are distinguished by the advantages of an appropriate band structure for harvesting sunlight, low exciton binding energies and long carrier diffusion lengths.^[45] However, it degrades under moist conditions reducing the shelf life of the devices.^[46] Many different strategies have been implied to overcome the instability factors and many of these approaches have proven to be multitasking, i.e., a single strategy or the addition of a single material can augment many factors. Among the latest trends additive based engineering like the utilization of Lewis acid/base molecules^[47], interface layers (IL)^[48], surface modifiers^[47] or formation of 2D/3D interfaces^[49] have shown to augment the stability and enhance the efficiency of perovskite solar cells. Utilization of colloidal free precursors for perovskite solutions have also been proved to fabricate defect free perovskite absorber layers by controlled growth of perovskite films during spin coating by controlling crystallization kinetics.^{[50][51]} Utilization of novel electron transport materials for efficient electron transport like perylene based molecules can also improve perovskite solar cell efficiencies.^[52] These techniques have greatly shown to aid stability against moisture and heat. Another method incorporated by researchers to make perovskite technology available for industrial purposes is the development of different encapsulation strategies. Thermal resistance, elastic modulus and chemical reactivity of different encapsulation/barrier materials can affect the stability of perovskite solar cells.^[53] The ultimate goal of perovskite solar technology is the production of solar cell modules that can produce electricity for real life events. A lot of strategies are still to be explored to enhance the efficiency and stability of perovskite solar cells making the growth and application of perovskite technologies in the near future optimistic.

This Ph.D. dissertation will be based on a cycle of scientific papers reporting scientific work on studying the degradation mechanisms in perovskite solar cells and enhancing their efficiency and stability along with a deep understanding of carrier transport mechanisms in them with the help of different steady state and transient based spectroscopy techniques.

Keywords: Global warming, particulate matter (PM), conventional sources of energy, non-conventional sources of energy

CHAPTER 2.

2.1 Brief introduction to semiconductors

Atomic orbitals divide into a large number of closely spaced levels when they are brought together in a solid material with a periodic structure, creating a band-like continuity of energy states.^[54] The main components of solar cells are semiconductor materials, and their band structure is divided into two areas with a variety of electronic states. There is no energy state in the energetic gap that separates these two locations. The bandgap of a material is the term used to describe this space.

In a semiconductor, electrons are mostly found in the bottom band, known as the valence band (VB), where they have very little freedom of movement since there are a lot of states occupying that space. An electronic transition to the upper band, or conduction band (CB), is feasible when energy equal to or greater than the bandgap is applied to the system. Since fewer electronic states are filled in the CB, electrons can freely travel between a large number of vacant states.

The Fermi level (E_f), also known as the electrochemical potential of the electrons, or the electronic state where the probability of finding an electron is 50%, is located within the conduction band in metallic materials, as opposed to semiconductors where it lies closer to the conduction or valence band depending on the nature of doping i.e. n or p type.^[55] In metals, the band structure frequently creates an electronic state continuum with no discernible bandgap. As a result, electrons have a high degree of freedom of motion and may be quickly stimulated between different states. Due to the increase in density of mobile carriers, these materials often have high conductivity values and are good heat and charge conductors. Insulators are substances that generally exhibit energy gaps over 4 eV and have very poor conductivities. **Figure 2a** displays a schematic diagram of the energy states for each of the three categories of materials. The Fermi level for each substance is shown by the dotted line.

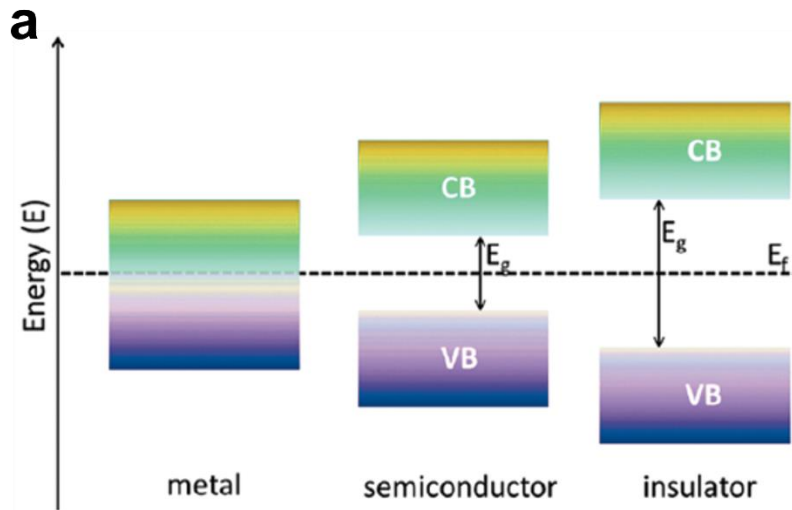


Figure 2a. Schematic of the band energy diagram of a metal, semiconductor, and insulator.

Doping is the process of adding electrons or holes to a semiconductor to tune its electronic properties i.e., having extra free carriers (electrons or holes in the conduction or valence band respectively). The Fermi level is raised by adding electrons (n-type doping), bringing it closer to the conduction band. On the other hand, p-type doping causes the Fermi level to move toward the valence band. To raise the carrier concentration, doping is frequently employed in semiconductors to change their optoelectronic characteristics and enhance their conductivities. Impurity atoms are inserted into the crystal lattice by chemical doping. These atoms have the capacity to add extra electrons or holes to the valence band or conduction band of the semiconductor, as appropriate. The most common semiconducting substance, silicon (Si), serves as a classic example of chemical doping. Silicon contains four valence electrons and is a group IV element. A modest concentration of group III element atoms, such as boron, gallium, or indium, is added to this substance in order to p-dope it. These elements increase the hole density or make the material electron deficient since they only have three valence electrons. On the other hand, group V elements, like phosphorus, are added to Si in order to n-dope it. These five-valence elements boost the electron density of Si, essentially n-doping it, when added to the material.

2.2 Recombination mechanisms in semiconductors

In semiconductors, the bandgap separates the conduction and valence band as reported earlier in this thesis. When an electron possesses more energy than the band gap energy, it moves to the conduction band and enters a metastable state leaving a vacancy or a hole behind in the valence band. It would again move to the valence band to lose its energy to attain equilibrium and rejoin the hole left behind. The electron and hole recombine with this process. In semiconductors, this is referred to as electron-hole pair recombination or just plain recombination. Recombination removes the unbound electrons and holes in semiconductors, establishing equilibrium and steady state.

Many recombination pathways might contribute to the charge transport properties of semiconductors. They could be free carrier bulk recombination mechanisms like Auger recombination (at high carrier concentrations), quasi-monomolecular deep trap aided non-radiative recombination (Shockley Read Hall recombination or SRH), radiative recombination and thermal recombination. Additionally, it is typical in the literature to take into account the non-radiative carrier recombination processes on layers' surfaces independently.

2.2.1 Radiative recombination

An electron-hole pair (EHP) recombines with the emission of a photon in a radiative recombination event as shown in **Figure 2b**. A hole in the valence band and the electron from the conduction band recombine leading to this process. Radiative recombination, which involves the optical processes of spontaneous emission, absorption or gain, and stimulated emission, is the radiative transfer of the electron from the conduction band to the valence band. Direct-bandgap semiconductor lasers are prone to this type of recombination.

2.2.2 Auger recombination

An exciton or an electron-hole pair (EHP) recombination and energy transfer from the recombined EHP to a free carrier, which is subsequently stimulated to high energy inside the band, are the two steps that make up an Auger recombination process as shown in **Figure 2c**. Impact ionization refers to the inverse Auger effect in which an EHP is generated. In this instance, a high-energy free carrier collides with the lattice and gives an electron in the valence band some of its extra

kinetic energy, moving it into the conduction band. As a result, an EHP is created following the incident.^[56]

2.2.3 Shockley-Read-Hall (SRH) recombination

Electrons recombine with holes through defect energy levels (trap states) in the bandgap in a two-step process known as trap assisted recombination as shown in **Figure 2d**. An electron is trapped by the energy state in a forbidden area created by the defects in the semiconductor crystal lattice. Electron-hole recombination occurs when a hole reaches the same energy level before the electron is re-emitted into the conduction band. Shockley-Read-Hall (SRH) recombination is another name for this form of recombination. Injection lasers utilize this kind of recombination process.

2.2.4 Surface recombination

Another kind of a SRH recombination is surface recombination which is also a form of non-radiative trap assisted recombination. The surface is a significant disruption of the crystal lattice. Dangling bonds are created on the surfaces of semiconductor crystal lattices and are exposed to the environment shown in **Figure 2e**. Such exposed surfaces develop isolated sources of faults after absorbing contaminants from the surrounding environment. The likelihood of non-radiative recombination is increased by the large concentration of flaws on surfaces. Injection lasers with cleaved facets have been developed to improve surface recombination in semiconductors.^[57]

2.2.5 Thermal recombination

The lattice vibrations are necessary for a carrier to travel from one site to another if it is localized because of flaws, disorder, or self-localization, such as in the case of polarons. The mobility of hopping transport increases with rising temperature. Such hopping transport occurs when electrons and holes recombine due to phonon induced lattice vibrations or thermal recombination as shown in **Figure 2f**.

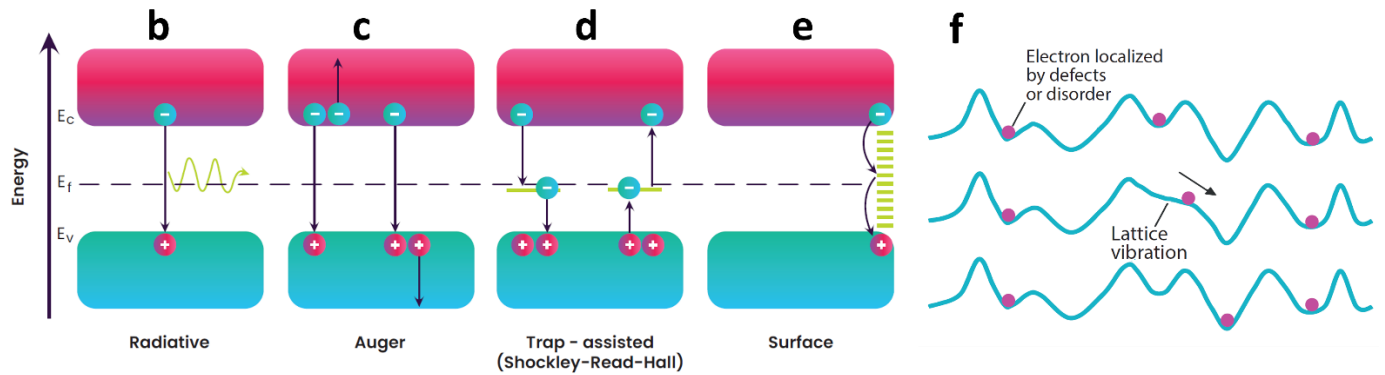


Figure 2. Schematics of energy diagrams of a semiconductor displaying b) radiative recombination c) Auger recombination d) Shockley-Read-Hall (SRH) recombination e) surface recombination^[3] f) thermal recombination.^[4]

2.3 Trapping in semiconductors

Through the recombination process, energy is released in the form of secondary electrons (Auger recombination), photons (radiative recombination), phonons (non-radiative recombination), etc. A carrier that has been captured on a localized state can follow two physical processes: it can be released in the associated band (the conduction band for electrons and the valence band for holes), or it can recombine with a carrier of the opposite sign if it is later captured on the same localized state. Recombination in a localized state is the annihilation of the pair caused by the capture of a second carrier with the opposite sign in the same localized state. The capture center is referred to as a trap if the caught carrier is set free in the band. This capture process is referred to as trapping and its release process is termed as detrapping.

The traps may be categorized using a variety of factors. There are two different types of traps associated with charge carriers: traps for electrons and traps for holes. There are also two different types of traps associated with the location: bulk traps and surface/interface traps. For trapping centres, contaminants, point defects, surface states, dangling bonds, and localized tensions can all be used. The trapping levels can also be found in the conduction band or the valence band, albeit they are often found in the band gap. The traps present in the volume of the crystals, such as point defects, extended defects like grain boundaries, impurities, and local tensions, dominate the trapping phenomenon in bulk semiconductors. At the same time, the traps at the surface or interfaces control these processes in nanocrystals. Due to the extremely high surface-to-volume

ratio (on the order of 10^6 cm^{-1}), the latter is the case. The number of atoms at the surface or contact is therefore in the same order of magnitude as the overall number of atoms. These atoms have the potential to serve as a trap or a site of recombination, making the surface and interface of a nanosystem crucial to the non-equilibrium processes. Adsorbed atoms or molecules, dangling bonds, or internal tensions caused by twining or stacking faults of grain boundaries account for the majority of surface/interface traps.

Shur and Hack created the Multiple Trapping and Release (MTR) model to explain the mobility in hydrogenated amorphous silicon.^[58] Later, it was expanded to include organic semiconductors by Horowitz et al.^[59,60] Although most of the carriers that are introduced into the semiconductor are stuck in states that are concentrated in the forbidden gap, the model implies that charge transport happens in extended states. If the energy level of these traps is close to the band gap's center, they can be deep; if they are close to the conduction or valence band, they can be shallow.

Figure 2g serves as an illustration of this.

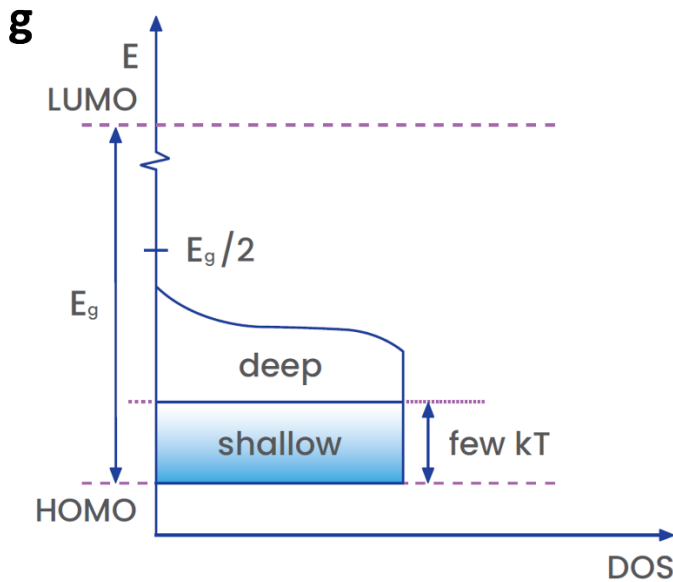


Figure 2g. Schematic of the band energy diagram of an organic semiconductor with shallow and deep trapping energy levels.^[5]

According to the model, the carrier mobility is dependent on temperature, the energy level of the traps, the carrier density, and therefore, the voltage supplied to a device.^[5] **Equation 2.1** displays the drift mobility for one trap level with energy E_{tr} .

$$\mu_D = \mu_0 \alpha \exp(-E_{tr}/kT) \tag{2.1}$$

where μ_D is drift mobility, μ_0 is the mobility within the grain boundary, α is the effective overlap parameter, E_{tr} is the energy of the trap state, kT is the thermal energy.

The size of the semiconductor grains must be taken into consideration. The polycrystalline semiconductor is defined as having borders with a high trap density separating trap-free grains. The distribution of the traps can be thought of as uniform if their size is less than the Debye length. Charges pass across the grain borders, nevertheless, if the grains are substantially bigger than the Debye length. This happens via thermionic emission at high temperatures, and it is discovered that the mobility is temperature dependent. At low temperatures, the charges may tunnel through the grain boundaries, making the mobility temperature independent. Thermally triggered tunneling controls charge transfer at intermediate temperatures.

2.4 Grain boundaries in semiconductors

It is commonly known that solution-processed perovskite films have boundaries between their grains. For the charge carriers, these grain boundaries serve as trap centers. Due to lower activation energies at the grain boundaries, ions prefer to pass through them rather than the bulk of grains.^[61,62] Reduced ion transport channels and non-radiative recombination result from reduction of grain boundaries, which enhance power conversion efficiency and lower hysteresis.^[63]

A brief understanding of how grain boundaries assist in trapping of charge carriers in perovskite based polycrystalline materials is stated in the next chapter.

Horowitz first addressed the semiconductor's granular nature.^[60] His research makes the assumption that the grain borders, where the conductivity is significantly lower than in the crystal grain, are what restrict mobility. Inorganic polycrystalline materials, whose mobility is shown to increase with the size of the grains, have already been examined for this behavior.^[64] Since the borders and grains are linked in series, the mobility is best described as in **Equation 2.2**

$$\frac{1}{\mu} = \frac{1}{\mu_b} + \frac{1}{\mu_g} \quad 2.2$$

where μ_g is the mobility in the grain, whose size is expected to be significantly bigger than the border region, and μ_b is the mobility at the boundary. A Schottky barrier that is back-to-back is created between the grains. The current will be described differently depending on the temperature

since tunnel transport may predominate at lower temperatures while thermionic emission predominates at higher temperatures.

2.5 Fundamentals of solar cell operation

A solar cell is defined as a device that absorbs light (typically, a semiconductor) that is linked to an external circuit while maintaining electrical asymmetry to allow for the extraction of carriers produced by photoexcitation. It functions like a diode in the dark, only allowing electricity to flow in one way. When a semiconductor is illuminated, photons with energies above its bandgap are absorbed, causing the electron to move from the valence band to the conduction band. The exciton is an electron-hole pair formed when a hole is made in the valence band and the excited electron is held by the electrostatic force. The dielectric constant of the semiconductor determines the intensity of the electron-hole attraction, or binding energy, which differs between different materials. The exciton can dissociate, and electrons and holes can be removed due to built-in asymmetry (difference in electron affinity of neighboring layers). This asymmetry can be achieved by specifically doping one material into p-type (electron-deficient) and n-type (electron-surplus), resulting in a p-n homojunction, or by sandwiching an inherent semiconductor between n-type and p-type materials (heterojunction). When p-type and n-type materials are combined, the difference in electron concentration forces carriers to migrate in order to restore the balance. Carriers first diffuse towards the contact and recombine, generating a depletion area. When electrons (and holes) migrate, they leave the core ions (negative in p-type materials and positive in n-type materials) behind, resulting in an electric field in the junction. The greater the doping density, the more electric field is generated, resulting in a greater built-in potential V_{bi} . The magnitude of V_{bi} is equal to the difference between two semiconductors' Fermi levels. When illuminated, the density of carriers increases, disrupting thermal equilibrium and splitting a Fermi level into two quasi-Fermi levels.^[65]

The current-voltage (I-V) characteristics of a solar cell in **Figure 2h** describes its operation. The current created when two terminals are linked is known as the short circuit current (I_{sc}), and it occurs at the intersection of the I-V curve and the Y-axis. When the circuit is open and the current flow is zero, the voltage is known as the open-circuit voltage (V_{oc}), and it is an I-V intersection with the X-axis. According to the Ohm's law ($V = IR$), during typical operation on a load with

resistance R , the voltage can fluctuate between zero and V_{OC} and the current can vary between zero and I_{SC} . Because current levels are directly proportional to the active area of the illuminated device, current density J_{SC} is frequently used and is expressed in mA/cm^2 .

The spectrum of the incoming light and the bandgap of the absorber both affect how much current is produced. The electron can only be promoted to the conduction band and made accessible for extraction by light with energy equal or greater than the bandgap. Therefore, in order to convert light into current, the material's bandgap needs to be appropriate for a certain light spectrum.

The energy difference between the extracted electron and hole's quasi-Fermi levels, and therefore the absorber's bandgap, determines the voltage of a solar cell. It is always lowered in actual circumstances by non-radiative recombination mechanisms. The defects in the lattice and on the grain boundaries of a polycrystalline absorber are a prominent source of this recombination, therefore the film's quality is critical for maximizing the device's performance.

The solar cell's power is the product of voltage and current and the Maximum Power Point (MPP) refers to the point on the curve when it achieves its highest value. This value is always lower than the theoretical maximum that a functional solar cell might attain with maximum voltage (V_{OC}) and current (J_{SC}). The percentage variation from the theoretical maximum is known as the Fill Factor (FF). The most essential measure characterizing the performance of a solar cell is power conversion efficiency (PCE), which is a ratio of the device's power density to the incident light power density.^[65]

The power conversion efficiency is proportional to the number of photons absorbed and the spectrum of input light flux. To standardize the measurements of solar cells, a constant solar spectrum reference is constructed that represents the solar spectrum at ground level for mid-latitude locations at a sun zenith angle of 48° . It was determined for an annual average at mid-latitudes and is known as an Air Mass 1.5 spectrum (AM 1.5). Similarly, the standard irradiance is considered to be $100 \text{ mW}/\text{cm}^2$ on average. **Figure 2i** depicts the standardized solar irradiation. It is vital to remember that each solar cell uses a certain portion of the spectrum based on its bandgap. Combining two separate materials with shifting absorption onsets to create a tandem cell is an intriguing method for extending the spectrum of absorption. A higher amount of light may be absorbed in this manner, resulting in a higher current generation. The extraterrestrial spectrum, atmospheric influences, and the AM 0 and AM 1.5 spectrum will be discussed in the next section of this chapter.

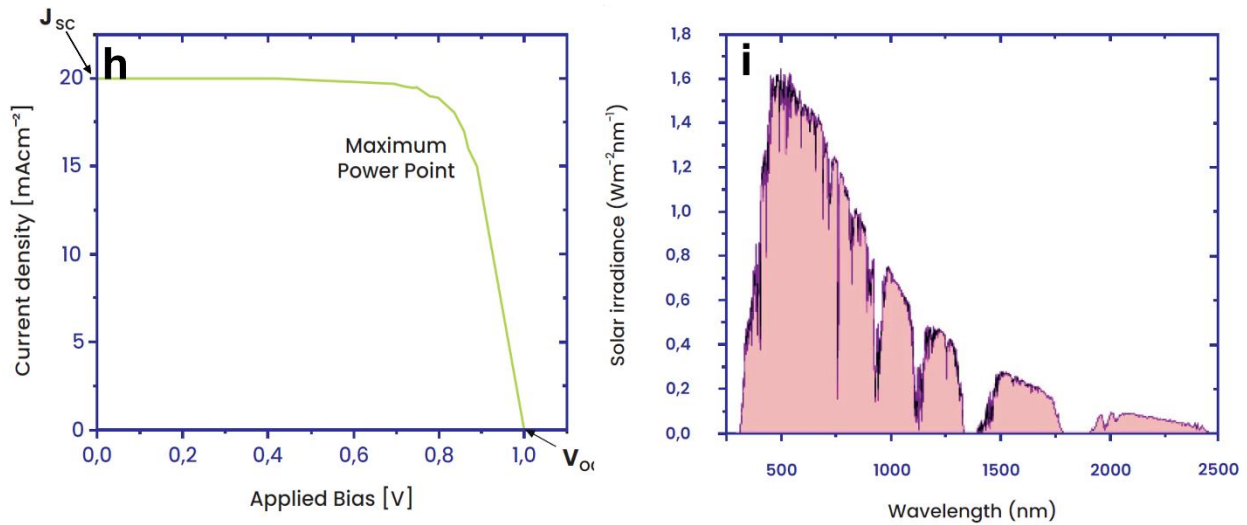


Figure 2. Graphical plot of a h) Current density versus voltage J_{SC} - V_{OC} measurement of a solar cell i) standardized solar irradiation.^[6]

2.6 Mechanisms for atmospheric absorption of sunlight

The two major mechanisms involved which cause absorption in a gas molecule are:

- The electron gets excited to a high atomic/molecular shell (shell transitions). In atoms and simple molecules, the atomic shells possess distinct energies, narrow absorption lines are mostly caused by shell transitions.
- The photon can cause parts of molecules to vibrate or rotate in different manner (rotational-vibrational transitions). The more complex the molecular structure is, the more ways it can rotate and vibrate with hardly distinct energies (in comparison to electronic transitions), thus the formation of broad absorption bands.^[66] The different regions of absorption in the electromagnetic spectrum of sunlight are:

2.6.1 Ultraviolet (UV) range

At very short wavelengths photons bear a large amount of energy E_{ph} . They get absorbed by shell-transitions in simple molecules and thus the energy levels are strongly bound (i.e., their atomic shells are energetically far apart from each other). Molecules like hydrogen, oxygen, and nitrogen are quite abundant and thus the atmosphere stays opaque below 300 nm.

2.6.2 Near UV range

In this range the heavier and less bound molecules come into play. The molecule which absorbs most of the sunlight is the ozone layer (O_3). Because of its complicated structure, a broad range of shell transitions are possible in ozone's molecular structure.^[67] Thus, this molecule plays an important role in the broad wavelength range of 230-290 nm. Thus, ozone plays a significant role in the amount of UV light reaching the earth's surface.

2.6.3 Infrared (IR) range

At long wavelengths the photons have a small E_{ph} , and they are unable to excite the electrons to higher shells. However, they can cause changes to rotations and vibrational states within the asymmetric molecules like water and carbon dioxide leading to broad absorption bands. Thus, the atmosphere is completely opaque beyond the near-IR (NIR) end in the visible spectrum even down to radio frequencies.

2.6.4 Visible (Vis) range

At wavelength range of 380-780 nm, the photons have neither too high E_{ph} to cause vibrational/rotational transitions nor possess enough energy to excite electrons to the higher electronic states. A small amount of light thus gets absorbed in this region allowing for an atmospheric window in the visible range.

2.7 The air mass (AM)

Both absorption and scattering processes depend mostly on the length determining the path of sunlight through the atmosphere and the angle of elevation of the sun above the horizon. When the sun is closer to the horizon, the light passes through more air particles within the earth's atmosphere. When the sun shines at an angle of 90° above the earth's horizon- from the zenith- the light goes by definition of optical AM1 or air mass 1. When the sun makes an angle z with the earth's zenith (or forms an angle h with the horizon) the airmass is set to be higher: and by first approximation, assuming the earth is flat, we obtain AM from the **Equation 2.3**. In **Figure 2j**, the schematic of the elevation angle of the sun with the earth's horizon and the zenith is shown.

$$AM = \frac{1}{\cos z} = \frac{1}{\sin h}$$

2.3

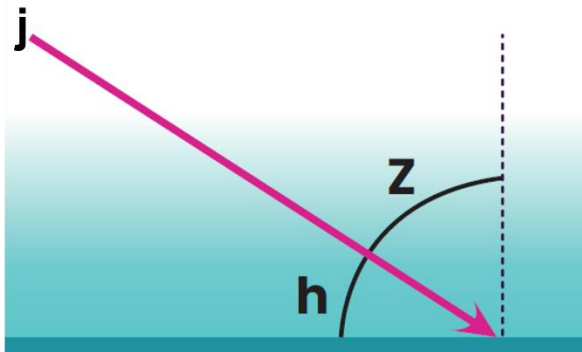


Figure 2j. Schematic showing the air mass dependence on the sun's elevation angle with the earth's surface.^[7]

This **Equation 2.3** holds valid at $h > 10^\circ$, thus applicable for most photovoltaic applications. At lower angles, however it matters the earth's round shape and that the light path from the sun is refracted within the atmosphere's vertical density profile. The presence of gases like water vapour also affects this phenomenon near the earth's surface while gases like ozone affect this phenomenon at high altitudes. **Figure 2k** shows the air mass versus the Earth's zenith at different elevation angles.

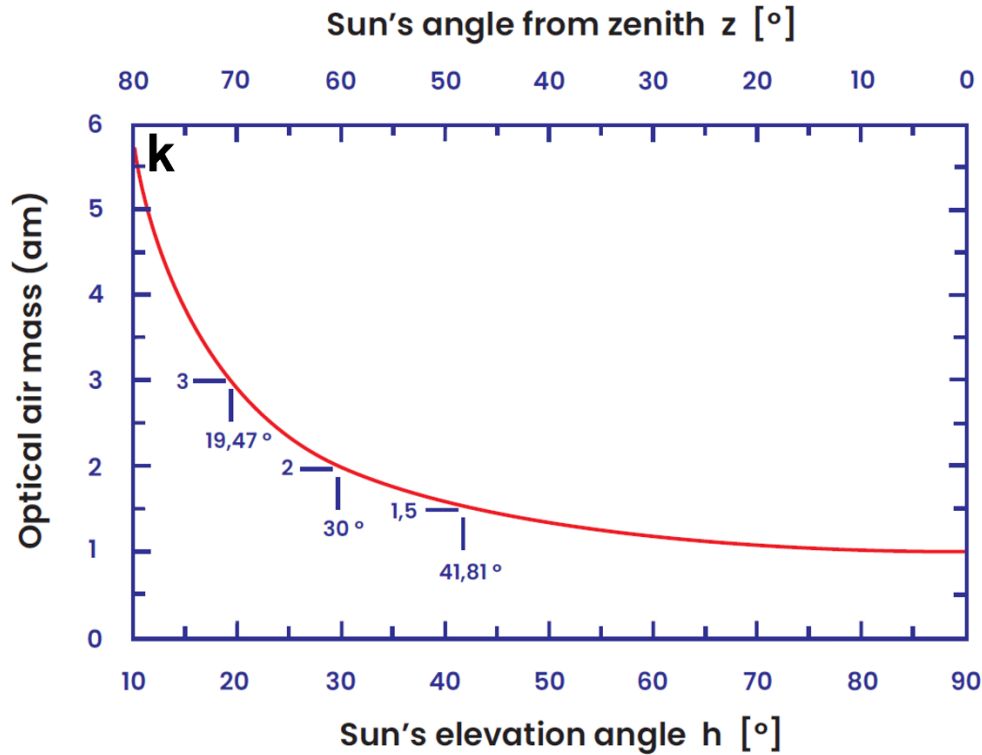


Figure 2k. Air mass versus the zenith at different elevation angles.^[8]

2.8 The Extraterrestrial (AM0) solar spectrum

The energy of sunlight is distributed across wavelengths or the equivalent photon energy. This could help in understanding why particular kinds of solar cells have good performances at shorter wavelengths than longer wavelengths and vice versa. Thus, the total radiation energy alone is an insufficient measure for solar cell characterization. The energy from the Sun's spectrum is called spectral irradiance. **Figure 2l** displays the spectral irradiance of the sun over the photon wavelength.^[68] This was measured above the top regions of the earth's atmosphere (navy blue outline). Different colors of the visible spectrum are also indicated. This spectrum shown in **Figure 2l** is called the AM0 spectrum which stands for air mass zero, which depicts that the spectrum was measured with no air between the sun and the receiving body.

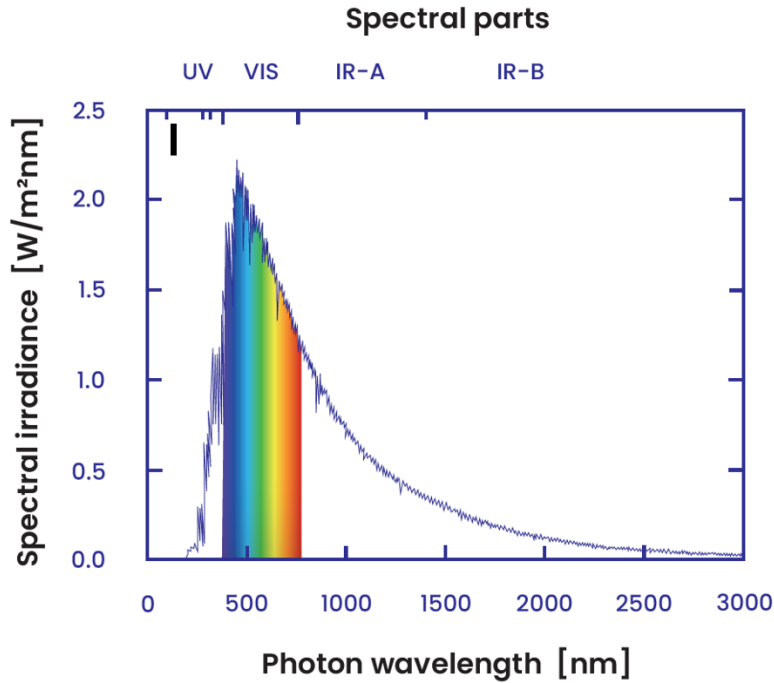


Figure 2l. Graphical representation of the variation of solar spectral irradiance versus photon wavelength for AM0 spectra.^[7]

2.9 Intensity or photon flux

The amount of solar radiation can be quantified in two different ways a) light intensity b) photon flux. In photovoltaics, we normally use either.

- Light intensity: It is also called the irradiance, which is the energy per area per time usually in $[\text{W}/\text{m}^2]$ or $[\text{mW}/\text{cm}^2]$
- Photon flux: It is the number of photons per area per time in $[\text{cm}^{-2}\text{s}^{-1}]$. It is much more convenient to quantify photon flux N_{ph} in equivalent units of the electric current, $J_{ph} = q \cdot N_{ph}$ $[\text{mA}/\text{cm}^2]$, because J_{ph} is equal to the current that the solar cell could generate if it converted every photon into a free electron-hole pair.

Figure 2m and **Figure 2n** display the AM0 spectra plotted as photon flux as a function of photon wavelength and photon energy respectively.

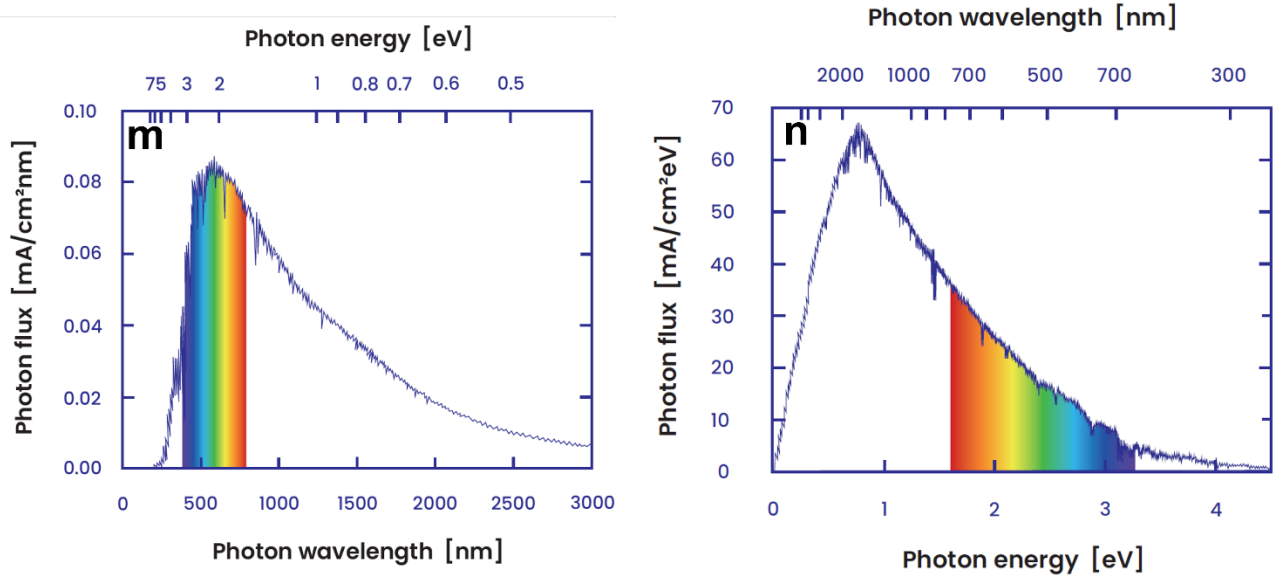


Figure 2. Graphical representation of m) spectral photon flux of AM0 spectrum vs photon wavelength; n) spectral photon flux of AM0 spectrum vs photon energy.^[7]

From **Figure 2l** and **Figure 2m** we observe that the IR spectrum contains a larger number of photons as compared to other spectral regions. More than half of the photons in the solar spectrum lie in the IR. This is because the photons bear lower energy in the IR than the blue region. This is quantified according to the **Equation 2.4**

$$E = \hbar\omega = hc/\lambda \quad 2.4$$

where E is the photon energy [eV], ν is the photon frequency [s^{-1}], ω is the photon angular frequency $2\pi\nu$ [s^{-1}], λ is the wavelength, c is the speed of light (3×10^8 m/s), h is Planck's constant ($4.13566733 \times 10^{-15}$ eVs), and “ \hbar ” is the abbreviation for $h/2\pi$.

Thus, it is observed that per given radiation energy, there are more photons in the IR spectrum than there are in the blue part of the spectrum. The presence of more photons in the IR range of the solar spectrum has an important impact on different photovoltaics. For example, an improvement of the IR absorption of a silicon based solar cell greatly enhances its photogenerated current as silicon-based cells absorb IR photons weakly.

2.10 The global standard spectrum (AM1.5g)

Due to the variations in the terrestrial spectrum, a reference spectrum will display some arbitrariness. To consider the standard spectrum^{[69] [70]} which could represent as many PV applications as possible, the standard spectrum is not derived from a particular measured spectrum, but is calculated from the reference AM0 spectrum under representative conditions of the atmosphere^[71]. These conditions have been established from an analysis of a previous reported work in the United States^[72] and are given as follows:

- The air mass is 1.5 with the sun at about 41° above the earth's horizon.
- The solar cell is at a tilt of 37° from the horizon (i.e., the sun shines at a given angle of 11.2° from the normal vector of the cell.
- The cell lacks an optical concentration system, i.e., the cell faces the hemisphere including the ground surrounding it (light sandy soil); a spectrum including the blue sky and the surrounding ground called the global spectrum, thus called AM 1.5g.
- The measurement site is at sea level under standard pressure (1013.25 millibars).
- The atmospheric conditions follow a U.S. standard atmosphere, which represents for geographical mid latitudes; but
- A higher carbon dioxide level is taken into account.
- The haziness-which is typical in the United States on a clear day is tuned (to a turbid value of 0.084 at 500 nm) so
- The total irradiance is at 100 mW/cm².

This AM 1.5g global standard spectrum is a good representation of the illuminative conditions as observed on a tilted PV flat plate array on a cloudless day around noon in the geographical mid latitude locations and is neither too blue nor yellow.

Keywords: Semiconductors, atomic orbitals, energy states, bandgap, Fermi level, degree of freedom, doping, grain boundaries, tunnel transport, trapping, polycrystalline, Debye length, exciton, thermionic emission, recombination, Shockley Read Hall (SRH) recombination, electron-hole pair (EHP), depletion area, junction, quasi fermi level splitting, absorber, light flux, air mass (AM), solar constant (S), irradiance, photons, wavelength, infrared (IR) spectrum, density of states (*D*), occupational probability (*f*), vacuum, absorption.

CHAPTER 3.

3.1 Brief introduction to perovskite based semiconductors

Metal halide perovskites have developed as a new class of materials for extremely efficient solar cells in the last decade, with a power conversion efficiency of 25.7%.^{[73][74]} Long carrier diffusion lengths, high carrier mobilities, low exciton binding energies, high absorption coefficients, and band gap tunability via precursor component interchanges are all intrinsic benefits of perovskite photoactive materials that contribute to high power conversion efficiencies.^{[54][55]} Another significant advantage of these materials is the ability to manufacture thin films at low temperatures using solution-based processing. It offers low-cost production on flexible polymeric substrates using high-throughput roll-to-roll manufacturing.^[75] Perovskite solar cell (PSC) technology is expected to account for 29% of the worldwide PV industry by 2030.

Apart from high PCE values, research groups around the world are now stabilizing at nearly 20%, which is good enough value for perovskites to enter the commercial market. Since the efficiency goal is being fulfilled, the scientific community is now striving to achieve four other objectives for commercializing PSCs with competitive silicon technology.

- Cost
- Stability
- Upscaling
- Environmental impact

Given the tremendous progress in the past decade with numerous research teams worldwide striving to achieve a similar goal, it's only a matter of time before commercial perovskites solar devices become a reality. This Ph.D. dissertation is aimed at developing a promising perovskite solar cell device architecture focusing on novel and impurity free routes of perovskite layer fabrication, understanding perovskite degradation mechanisms, efficient interfacial engineering for good carrier extraction, novel charge transport materials for better efficiencies, and development of robust encapsulation strategies for paving the way of PSCs to the industrial level.

3.2 Origin of perovskite solar cells

Organic-inorganic hybrid perovskites (OIHPs) are the most studied class of light-harvesting perovskite materials due to their unique properties of high absorption coefficient, long carrier diffusion lengths, effective bandgap tuning, and high tolerance to electronic and structural defects.^[43,45,76-91] Since the year of 2009 there have been tremendous developments in improving the power conversion efficiency (PCE) of perovskite solar cell devices, which has now reached a value of 26%.^{[40-44][92]} Solar technologies utilizing light harvesting semiconducting materials such as cadmium-telluride (CdTe), copper indium gallium diselenide (CIGS), gallium arsenide (GaAs,) and copper zinc tin selenide are mostly covalent bonded between their atoms in the crystal lattice, whereas the perovskite lattice comprises of mostly ionic interactions although some covalency exists due to lower electronegativity of the heavier halides.^[93] The first perovskite/Dye synthesized solar cell (DSSC) came into the laboratory by a Japanese research group led by Professor Miyasaka who introduced methyl ammonium lead iodide ($\text{CH}_3\text{NH}_3\text{PbI}_2$) as a dye sensitizer on a mesostructured titanium dioxide (TiO_2), achieving a PCE of 3.8%, which was a stepping stone for the perovskite research industry.^[94] Another research group led by Professor Nam-Gyu Park reported the PCE of 6.5% soon after.^[95] However, for the DSSC community, the traditional iodine based liquid electrolyte used in the architectures was led to the dissolution of the photo absorber material, which further led to the rapid degradation of the solar cells. A few years later another research group led by Professor Kanatzidis reported a dramatic improvement in the PCE of DSSC by replacing the liquid-based electrolyte with CsSnI_3 as the hole transport material (HTM).^[96] This was the first perovskite based solid-state DSSC.^[96] This solar cell reached a PCE of over 10% which was a significant improvement for the DSSC community. Another major breakthrough was by a research group in Oxford, when the liquid electrolyte was replaced by spiro-OMeTAD as HTM which eliminated the rapid degradation in the DSSC solar cells as reported by Miyasaka earlier.^[43,83] The Oxford group reported an additional groundbreaking discovery by replacing the mesoporous TiO_2 film with an insulating Al_2O_3 scaffold, which further improved performance results. This was a proof that perovskites were capable of ambipolar charge transport over longer distances (which exceeded the material's absorption lengths). Thus, the presence of a mesoporous TiO_2 film for charge extraction was not essential.^[45] These findings paved the way for the development and realization of perovskite-based thin film architectures. These scientific findings

also diverted the research progress to perovskite solar cells from DSSC and organic photovoltaics (OPVs). The following sections will contain elaborate and straightforward explanations of the structure of perovskites, their processing techniques and also review the challenges of these materials for commercialization.

3.3 Perovskite properties, types, and the tolerance factor

Methylammonium lead iodide (MAPI) based perovskite structures (MAPbI_3) have remained one of the most intensely researched photoactive perovskite structures, and thus have remained a standard example of a perovskite crystal structure being a model compound.^[55,97] Similar to most of perovskite structures used for photoenergy conversion, there were three major components: the monovalent cation, a divalent metallic cation and halogenic based anion (I^-). The structure was first defined by Victor Goldschmidt in the year 1926.^[98] These photoactive perovskite structures have also been known to show piezoelectric and ferroelectric properties and superconductivity at high temperatures owing to their crystal structure. In order to construct a perovskite crystal, the constituting ions must fulfil certain requirements regarding their charge and sizes. These parameters form the Goldschmidt Tolerance Factor as shown in **Equation 3.1**.^[99]

$$t = \frac{r_A + r_X}{\sqrt{2}(r_B + r_X)} \quad 3.1$$

Where t is the tolerance factor, r_A is the cationic radius, r_B is the divalent ion radius and r_X is the radius of the halogen anion. In the ideal case the structure mostly depicts a cubic symmetry which corresponds to a tolerance factor of 1. To satisfy this condition, the A site must be larger than the B site. Rhombohedral, orthorhombic, and tetragonal structures are also formed depending on the ionic sizes constituting them. These crystalline phases of perovskite crystal structures make a strong impact on the optoelectronic properties of perovskites especially that of photoactive lead halide based perovskites. As these crystalline phases are temperature dependent, the same perovskite crystal can exist with different symmetries depending on thermal factors.^[100] The different types of synthetic perovskite structures currently being used for optoelectronic research are classified as follows^[101]:

3.3.1 Cubic (3D) perovskites

Their general formula is defined by ABX_3 where A and B are cations as shown in **Figure 3a**. They are normally defined in terms of the BX_6 octahedra sharing all corners infinitely in all three dimensions making an ordered and symmetric structure. The A site cations occupy each hole created by the BX_6 octahedra making the A site cation a 12-fold O_2 coordination and the B site cation a 6-fold oxygen coordination. In the example shown below of $MAPbI_3$, the MA atoms sit at the 12 coordinate A site, while the Pb atoms occupy the 6 coordinate B sites.

3.3.2 Double perovskites (3D)

These perovskites are named as its unit cell is double that of a perovskite crystal. It preserved the same architecture of the 12 coordinate A sites and 6 coordinated B sites, but with two atoms occupying this site. An example of this structure as shown in **Figure 3b** is Sr_2FeMoO_6 . Here the Fe and Mo atoms display an ordered 3D chessboard fashion.

3.3.3 2D (Layered perovskites)

When the A site cation becomes substantially larger than the space between the octahedra, it will violate the Goldschmidt Tolerance factor forming crystals consisting of thin slabs surrounded by large organic spacer molecules as shown in **Figure 3c**. These materials are generally called as layered perovskites and belong to the Ruddleson-Popper (RP)^[102] or the Dion-Jacobson (DJ) phase.^[103] The general formula which describes RP2D is $(A)_2A'_{n-1}MX_{3n+1}$, where A represents the large monovalent organic cation (ending with the amine group of NH_3), acting as organic spacer between the inorganic octahedral slabs.^[104] In case of the DJ phase, the organic spacer is ended by amine groups on both sides and their formula is given by $(A)A'_{n-1}MX_{3n+1}$.

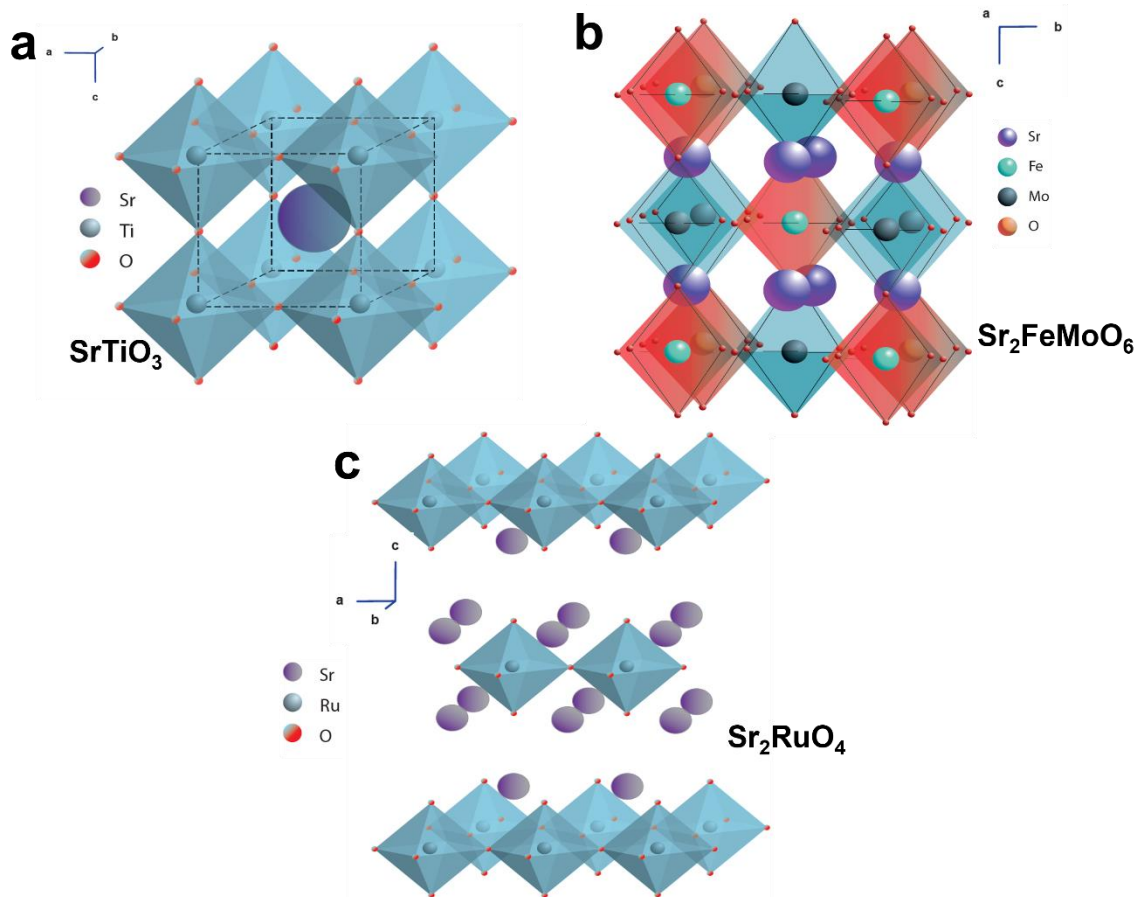


Figure 3. Schematics of perovskite structures a) cubic perovskites b) double perovskites c) layered perovskites.^[9]

3.4 Electronic properties of perovskite based semiconductors

Thin film technology based gallium arsenide (GaAs) solar cells is one of the highest existing state-of-the-art efficiency for photovoltaics.^[105] Could metal halide based perovskites compete against such technologies? From density functional theory (DFT) simulation studies it has been observed that in case of a methylammonium lead iodide (MAPI) based perovskite structure, the $[\text{PbI}_6]^{4-}$ octahedral framework dominated the energetic levels close to the band edge.^[10] The A site cations mainly control the tolerance factor and structural stability of the perovskite crystal structure, thus contributing mostly to the physical properties of the crystal structure.^[10] However the nitrogen atom in the MAPI structure has been reported to have certain influence on its electronic

properties.^[106] However, the valence band minimum (VBM) consists of strong Pb *s* orbitals and I *p* orbital antibonding character, and the conduction band consists of Pb *p* orbitals as shown in **Figure 3f**, showing superior optoelectronic properties compared to the indirect bandgap based Si technology, depicted in **Figure 3d**.^[107] In GaAs, the VBM is mostly constituted of a *p* orbital and the conduction band minimum (CBM), constitutes of a *s* orbital as shown in **Figure 3e**.^[10] The conduction band of perovskites have a greater advantage over GaAs, Si and other thin film technologies in absorbing a large amount of radiation in the visible spectrum due to the presence of *p* orbitals as shown in **Figure 3g**.

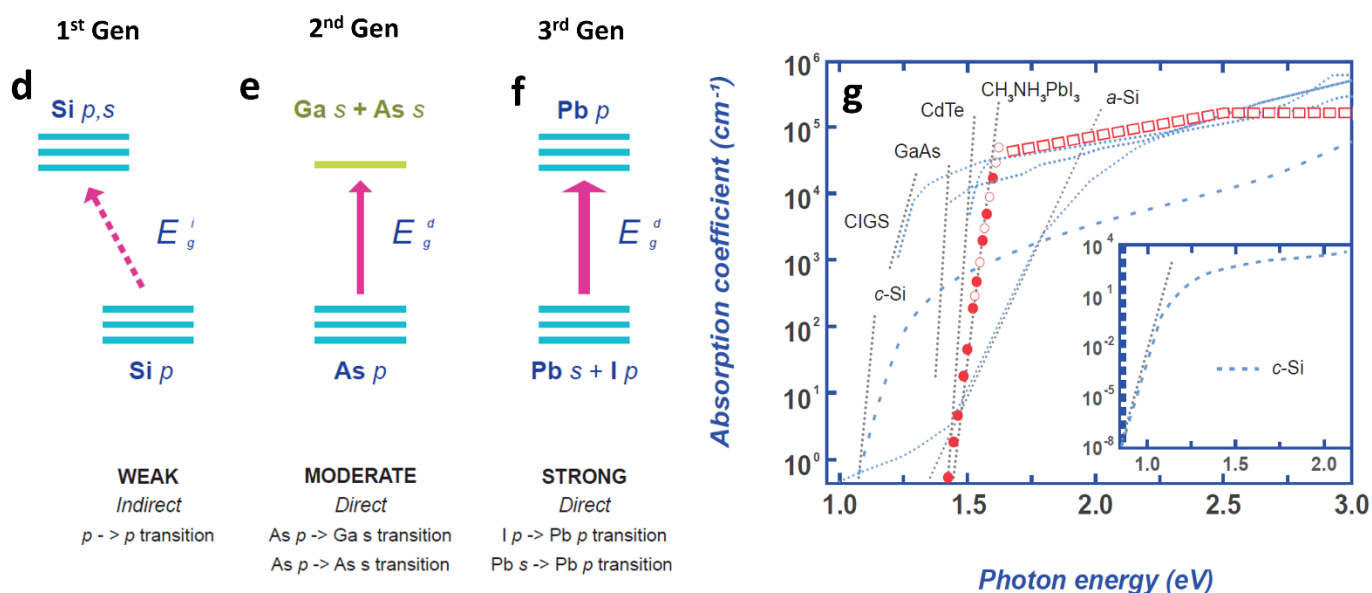


Figure 3. Schematic of energy band diagrams of different generation solar cells d) 1st Generation e) 2nd Generation f) Halide Perovskites and g) The photon energy-dependent absorption coefficients of the most common semiconductor materials used in solar cell applications. Adapted and reproduced with permission from *Copyright 2015 Royal Society of Chemistry*^[10] and *2014 American Chemical Society*^[11]

3.5 Role of the halide ion

Direct bandgap semiconductors have beneficial effects in applications for photovoltaic materials. Due to different sizes of halide ions fitting the lattice, the size of unit cell can be varied in a broad

range, which in turn results in a varied bandgap values like 1.5 eV for pure iodides. This property of metal halide perovskites allow flexibility in tuning their bandgap for a broader absorption of solar radiation for different optoelectronic purposes.^[108] This is due to the contribution of the lead iodide octahedra which has a strong influence on the perovskite's optoelectronic properties. A replacement of the halide ion can alter the unit cell size and thus alter the bandgap. It was studied that if the requirements of phase stability can be modified, the onset of absorption could be met with ease.^{[109][110]} Noh et al. studied that with the replacement of iodine by bromine atom in MAPbI_3 to MAPbBr_3 , there is a contraction of the unit cell structure, increasing the band gap of the perovskite material, which are in line with the Vegard's law.^{[111][112]} The change in the absorption coefficient of $\text{MAPb}(\text{I}_x\text{Br}_{1-x})_3$ systems as function of its composition is shown in **Figure 3h**.

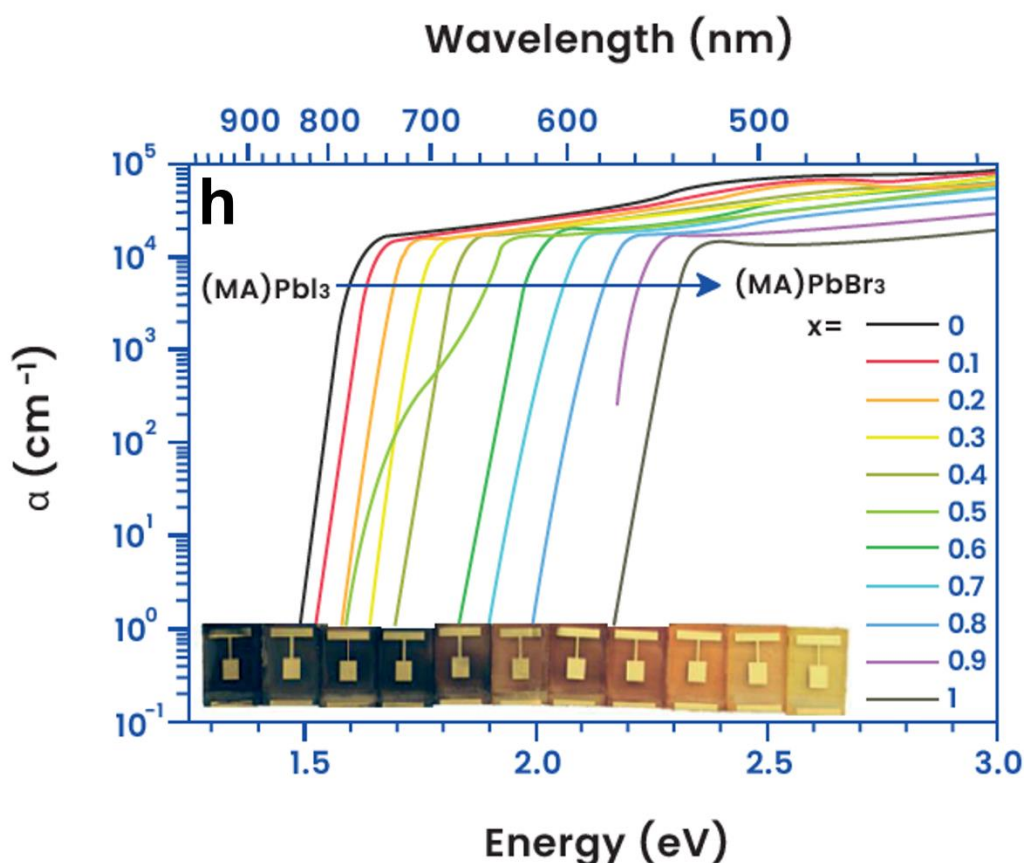


Figure 3h. The variation in the absorption coefficient of $\text{MAPb}(\text{I}_x\text{Br}_{1-x})_3$ systems as a function of the composition. Adapted and reproduced with permission from *Copyright 2015 Royal Society of Chemistry*^[12]

With the halides ion's reduction in sizes, the band gap increases in these materials, making this class of materials as an interesting applicant for both single and multi-junction photovoltaics, and also as light emitting diodes. Besides, the versatility in bandgap this halide ion tunability also enabled fabrication of perovskite solar cells in a wide range of colors. However, the tuning of halide anions can lead to halide-based segregation which could lead to depleted absorption properties of perovskites by affecting the phase stability and can be further managed by implementing larger cations in the A site like cesium, which will be mentioned further in this thesis.^[113]

3.6 Role of the cation

The role of cations in influencing the electronic properties of the perovskite structure is still being studied. However, they affect the perovskites' solubility during the fabrication process. The smaller sized monovalent cations are easily soluble in strong polar solvents, and their halide counterparts assist in the complexation of lead-based ions.^[114] The cations help in defining the geometry of the lattice, which helps scientists to engineer perovskites in order to achieve certain selective properties. When methylammonium (MA) cations were exchanged by formamidium (FA) cations, a redshift in the absorption onset was observed.^[115] The bandgap of the perovskite semiconductor was also tunable by replacing MA with FA cation, leading to an improved short-circuit current. The thermal and light based stability of the perovskite structure above 1000 hours in a controlled atmosphere was also achieved by a double cationic structure incorporating cesium and FA cations replacing the MA cation based perovskite which degraded above 100°C.^[116] These cells with proper encapsulation strategies fulfilled IEC-61215:2016 heat damp, thermal recycling, and humidity freeze tests.^[117] This work shall be discussed in detail in one of the manuscripts published in chapter 4 of this thesis. Apart from MA and FA cations, passivants such as Rb⁺ and K⁺ can be also incorporated in halide perovskite for enhanced efficiencies.^[118-120] Addition of organic cations with longer chain amines can result in formation of 2D structures, Ruddleson-Popper (RP) or the Dion-Jacobson (DJ) phase.^[121] By tuning the stoichiometry of such perovskites, the bandgap, stability and conductivity of these materials can be changed. In p-i-n structured perovskites, such modification of the hole transport layer (HTL) by fluorinated bulky organic

cations like fluorinated phenyl-ethyl ammonium iodide (FPEAI) and phenyl-ethyl ammonium iodide (PEAI) can lead to a formation of 2D/3D perovskites which has been known to improve HTL/perovskite interface leading to greater stabilities and higher efficiencies.^{[121][81]} A detailed work on such 2D/3D interface passivation for attaining high stabilities under light and heat induced stress will be mentioned in chapter 4 of this doctoral thesis.

3.7 Perovskite processing techniques

This section of the chapter will discuss more on the laboratory-based fabrication of perovskite thin film layers. The deposition of perovskite thin films grown from solution processing routes is followed by a crystallization phase which greatly impacts the performances of the solar cell. Being a facile process, it can occur spontaneously in the presence of a precursor.^[81] However, to achieve desired properties in the material requires a deep understanding of the system and a wide range of contributing factors which leads to its evolution. Different methods of perovskite deposition methods will be described here.

3.7.1 Evaporation

This deposition technique involves both one and two step techniques. This method is carried out by placing the different precursors into separate crucibles in a sealed chamber and then heating them up to their sublimation temperature at high vacuum conditions as shown in **Figure 3i**. The vapor of precursor materials then condenses and reacts with the substrates which are fixed at a given distance from their sources leading to the formation of compact perovskite films at low temperature conditions. A major advantage of this technique is that of its intrinsic additivity - that a wide combination of materials can be incorporated into the stack, without the requirement of an orthogonal solvent as required in a solution-based process which will be discussed in detail below. Perovskite films grown by this technique are generally uniform and smooth which provides a reliable approach to perovskite thin film processing.^[13] On the other hand, this process relies on high vacuum conditions and high maintenance cost, rendering it cumbersome.

3.7.2 Chemical processing techniques

From all of the perovskite fabrication approaches, this technique is a low cost and low temperature based method for perovskite processing.^[45] These approaches can include a two-step fabrication technique^[122,123], solvent variation^[14,108] and processing temperature of perovskite precursors^[124], formation of solvent-coordinated intermediates^[125], additive addition to perovskite precursors^{[126][108]}, perovskite film post treatment techniques.^[127,128] A detailed schematic in **Figure 3j** displays the spin coating steps which is a wet bench based technique used to fabricate perovskite solar cells for the experimental part of the thesis. A deep understanding of all the mechanism is still being widely researched. To be able to control perovskite film nucleation and growth on a wide range of substrates is a key factor to achieve highly compact and crystalline films of larger grain sizes.^[129] The process of nucleation is a stochastic process i.e., two similar systems will undergo nucleation at different time intervals. Growth of crystalline perovskite films on a substrate is a heterogeneous nucleation growth process as nucleation occurs via a substrate. This again depends on a large number of factors such as composition, concentration and precursor solution solvent^[130,131] and its temperature of deposition^[132], chemical structure of the substrates^[133], etc. To understand this nucleation and grain growth process for producing high quality crystalline films, the La Mer's model as shown in **Figure 3k** is adopted to study underlying mechanisms of spin coating and other wet chemical processing techniques for perovskites.^[134] According to this model, the perovskite solution upon drying reaches the critical concentration (CC), where many nuclei begin to form and grow. As long as the solution concentration is above CC, many new nuclei form and grow along with old nuclei. Now when the rate of evaporation of the solvent is slower than the solute consumption the processes of nucleation ceases but the nuclei continue to grow in size until the solution reaches a concentration called the saturation concentration (CS). The nuclei generation and growth further resume again once the perovskite concentration is reaching CC. This cycle repeats itself once all the time till all solvent molecules have been evaporated. This repetition of nucleation and growth cycles can lead to the crystals of perovskite aggregating in a three-dimensional fashion thus leading to a rougher film growth. Given the perovskite precursor solvent is evaporated very fast or exchanged by an antisolvent, the nucleation will occur once and thus lead to smoother films.

Anti-solvent engineering (ASE) or solvent-solvent extraction (SSE) is a very commonly used technique used to generate smooth, dense, and uniform films for the one step spin coating process through rapid solvent exchange processes.^[135,136] Gas blowing fabrication, gas pumping and gas

flow induced gas pumping (GGPM) are some reported methods of fabrication high quality smooth perovskite films.^[137–139] A few of these techniques like ASE and gas blowing have been utilized in the experimental part of this Ph.D. thesis to fabricate highly crystalline and smooth films for high power conversion efficiencies. Although these techniques help in the uniform growth of films, the rapid quenching by gas blowing and ASE techniques can reduce the solubility of perovskite precursors rapidly and can lead to uncontrollable grain sizes and density. Thus, a much deeper research and understanding is needed. According to the classical theory of nucleation, one can control the growth and behavior of nuclei in the precursor solution during perovskite film fabrication.^{[140][141]} The Gibbs free energy (ΔG_c) after nucleation occurrence and the critical radius (r_c) determine if the nucleus will be dissolved or formed during the nucleation process. The r_c depends on the temperature, surface energy and the degree of supersaturation with temperature as the most important factor. To attain nucleus growth, constituent molecules of a perovskite solution should overcome the ΔG_c which like the r_c depends strongly on the temperature as seen in **Equation 3.2** and **3.3**.

$$r_c \propto (\Delta T)^{-1} \quad 3.2$$

$$\Delta G_c \propto (\Delta T)^{-2} \quad 3.3$$

The ΔT is the difference of solid-liquid equilibrium temperature and the surrounding temperature. As the temperature increases, both the r_c and ΔG_c increase, and thus fewer nuclei are formed. The formation of these nuclei into large nuclei and further to larger crystals are given by **Equation 3.4**.

$$n = n_0 \exp^{-L/G\tau} \quad 3.4$$

where, n represents the number of crystals in the system, n_0 is the number of nuclei, L is the crystal size of the film, G is the growth rate of the films and τ is the residence time of the process.

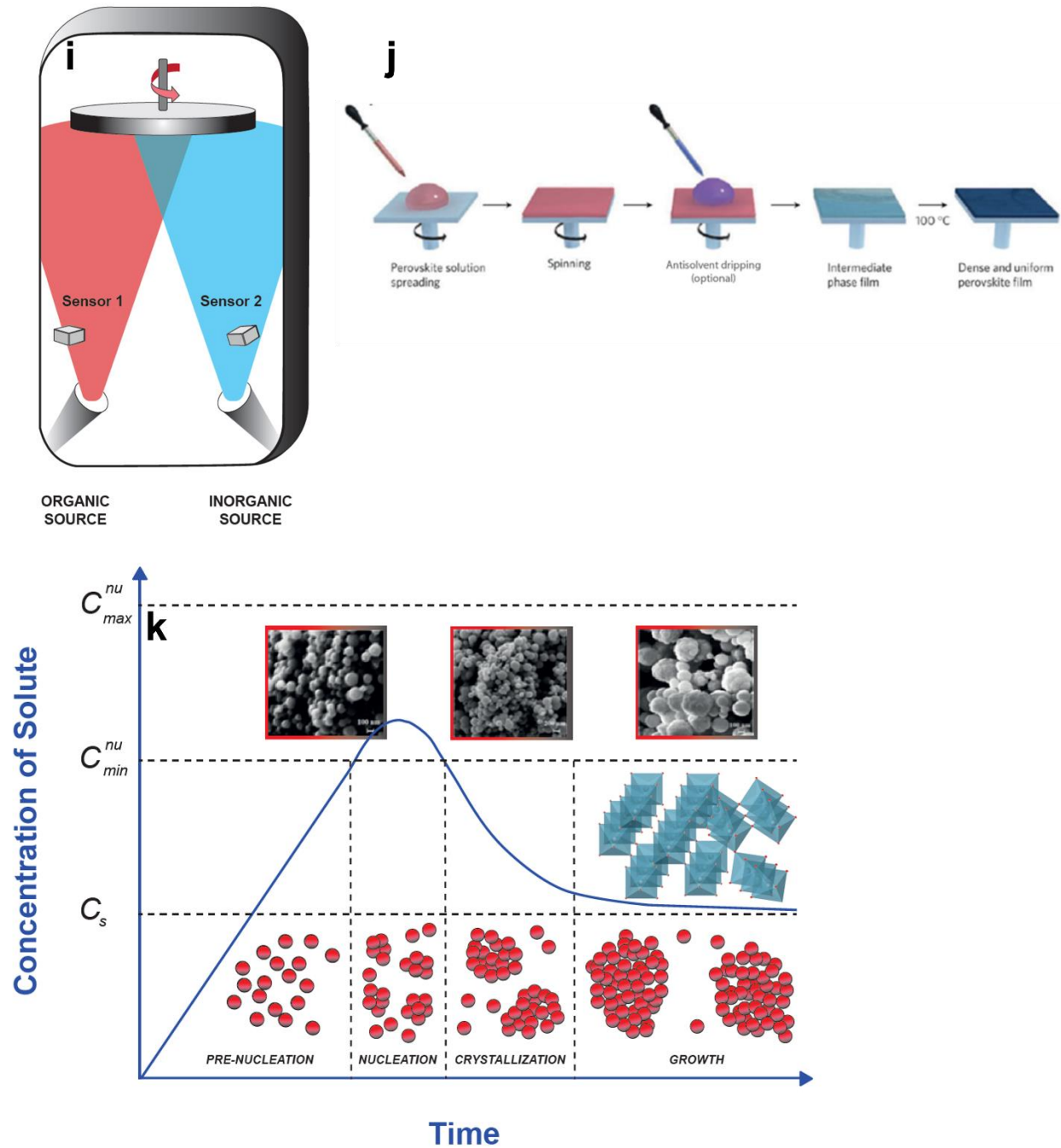


Figure 3. Perovskite film processing techniques i) co-evaporation j) spin coating with anti-solvent dripping technique k) La Mer's diagram for supersaturation. Adapted and reproduced with permission from *Copyright 2013-2014 Nature publishing, 2018 ACS Nano*^[13–15]

Apart from the aforementioned factors a few other factors strongly contribute to the crystallization kinetics which need to be kept in mind like physiochemical nature of the antisolvent, extrusion

speed of the antisolvent and application times of the antisolvent. High performance solar cells have been fabricated with antisolvents with different physiochemical properties: like polar solvents like ethyl acetate and non-polar solvents like toluene, leading to high quality perovskite films.^[14,142] Boiling point variations in anti-solvent did also not affect the performance of perovskite films. For example both diethyl ether (low boiling point) and chlorobenzene (high boiling point) help to fabricate high performance perovskite films.^[143,144] Majority of solvents do not work as anti-solvent as they are not miscible with the precursor solvent or do not dissolve the organic iodides, thus leading to poor solar cell devices.^[145] Recently Taylor et.al reported that anti-solvents fell into three categories^[16]: ones favouring short application times (type 1), one being unaffected by the application time (type 2) and ones favouring long application times (type 3) as shown in the schematic of **Figure 3l**.

Type 1 anti-solvents were: ethanol, butanol and iso propyl alcohol.

Type 2 anti-solvents were: ethyl acetate, chlorobenzene, butyl acetate and anisole.

Type 3 anti-solvents were: diethyl ether, xylene, toluene and mesitylene.

Finally, the extrusion speed of the anti-solvent from the pipette tip also plays an important role in the formation of smooth perovskite films. As shown in **Figure 3m**, the anti-solvent in a 1000 μL pipette tip was at a closer distance to the substrate than the 250 μL for a fixed volume. Thus, the travel time of the anti-solvent in the broader pipette is faster than that of the narrower pipette. However too slow or too fast extrusion times can lead to washing away of solvent too late or too early respectively thus leading to non-uniform nucleation and poorer perovskite films. A uniform extrusion rate of the anti-solvent helps achieving uniform nucleation throughout the sample and thus lead to high performance solar cells.

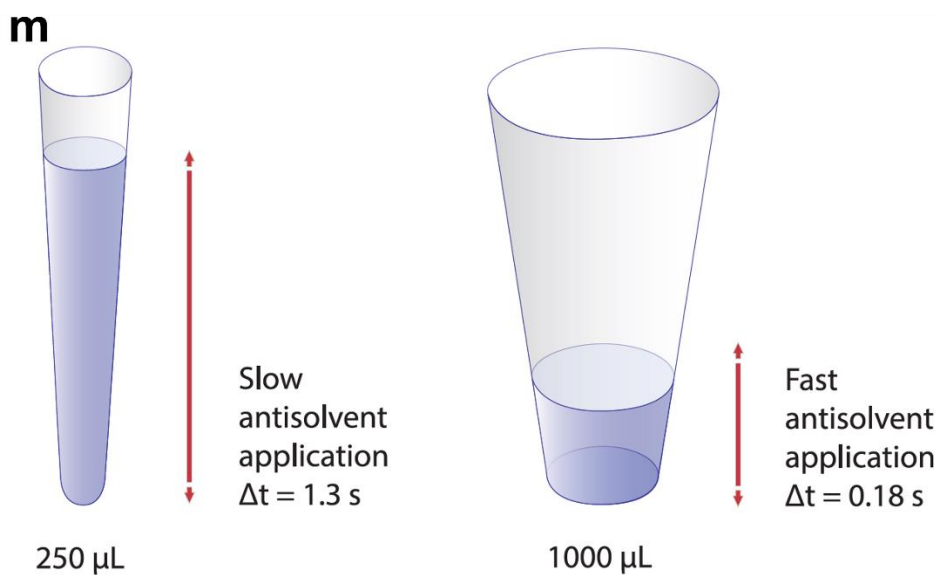
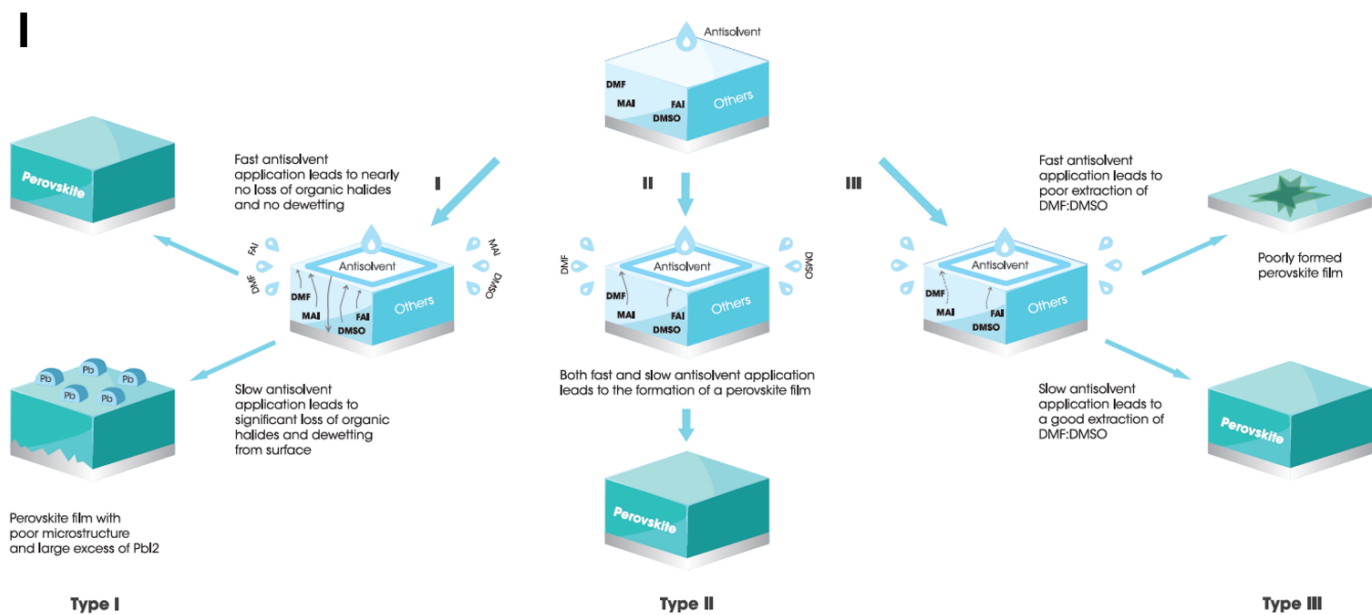


Figure 3. l) Schematic of perovskite film formation by different types of antisolvent during spin coating technique m) Schematic of a different pipette tip widths resulting in different antisolvent application velocities. Adapted and reproduced with permission from *Copyright 2021 Nature publishing*^[16]

3.8 Perovskite device operation

When an incoming photon hits the photo absorber layer which is the perovskite material in the solar cell, it is absorbed by the layer depending on its energy and the bandgap of the perovskite material. If the absorption process is successful, it generates free carriers within the perovskite material. The electrons generated with a negative charge will leave a positively charged hole behind. This electron and hole bound together strongly by a coulombic force leads to the formation of an exciton. In order to produce current, these excitons need to be dissociated and to be transported to their respective contact electrodes. Perovskites are known to possess a high enough dielectric constant which is further increased upon illumination.^[146] The exciton binding energies at higher dielectric constant values are lowered. The generation of such free carriers has also been supported by the absence of excitonic peaks in the absorption spectra of halide based perovskite structures. However, one can observe such excitonic peaks in lower dimension perovskite. Only at lower temperatures around 100K an exciton peak in such halide perovskite structures were observed.^[100] Once the free carriers have been generated, they travel through the perovskite bulk material to reach their respective electrodes.^[147] This could happen with the help of two mechanisms: drift, where the carriers are transported in the presence of an internal electric field or diffusion, where the transport of carriers depend on the concentration gradient of carriers. A highly efficient contact will extract carriers faster than the diffusion rate in the bulk of the perovskite material generating a diffusion gradient in the perovskite absorber material. If the carrier extraction is slower than the diffusion in the bulk, then charges developed at the vicinity of the electrode will retard the carrier extraction further. If the recombination of carriers exceeds the extraction of carriers, there will a reduction of extracted carriers which is absorbed leading to a lower power output.^[107] Thus, the importance of knowing the diffusion lengths in a given halide perovskite structure is important as it determines the maximum layer thickness which could be efficient for transport in the perovskite material. Diffusion lengths exceeding one micron have been observed for halide based perovskites.^[45] **Figure 3n** shows a detailed schematic of a perovskite device operation.

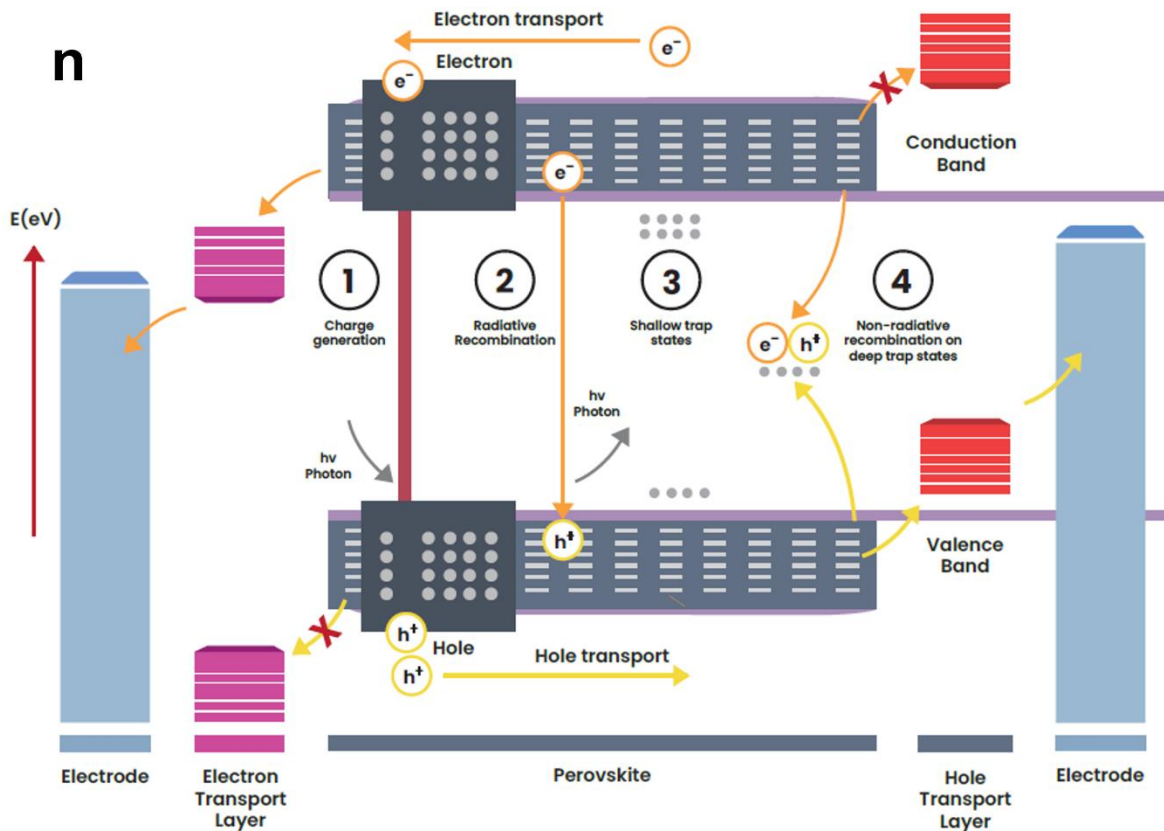


Figure 3n. Schematic of carrier transport and trapping in a perovskite solar cell. Adapted and reproduced with permission from *Copyright Springer Series in Optical Sciences*^[17]

3.9 Trapping mechanism in perovskite solar cells

The perovskite layers, which are often made by spin coating precursor solutions (solution-deposited layers) or by vacuum deposition of sublimated precursors (vacuum-deposited layers), are made up of grains that are closely spaced apart from one another. In theory, there are two different ways that the layers may look with individual grains filling the whole thickness of the layer as shown in **Figure 3o** or with many grains piled on top of one another to create the layer thickness as shown in **Figure 3p**. Recent research has demonstrated that the borders between the grains inside the layer do not contribute to the creation of the photoluminescence (PL) decay kinetics by quenching the photoluminescence. Perovskite PL quenching (carrier non-radiative

recombination) often only occurs at grain boundaries that create the layer's external surfaces (both front and rear surfaces). There is enough evidence that the layer surfaces play a key part in the creation of the PL kinetics, as shown by the considerable (ten-fold and more) extension of the PL lifespan in a perovskite layer as a result of chemical passivations of their front surface.^[148,149] Therefore, non-radiative recombination at the layer surfaces is the most effective mechanism causing carrier recombination in perovskite layers, according to evidence from the literature. The most logical way to analyze the PL kinetics in this situation, from the perspective of obtaining the most physical information, is to fit them using a one-dimensional diffusion equation. It enables the simultaneous measurement of the surface recombination velocity (S) and the carrier ambivalent diffusion coefficient (D).^[150]

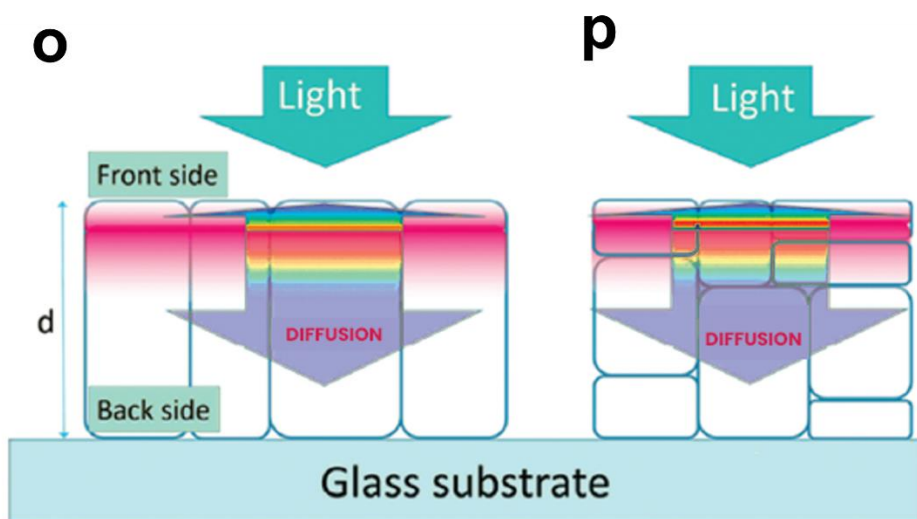


Figure 3. Schematic of perovskite grain formation by o) a single large grain forming the entire volume of the crystal p) several small grains stacked to form the entire crystal. Adapted and reproduced with permission from *Copyright 2015 Elsevier B.V.*^[18]

It should be emphasized that the diffusion equation normally only applies to homogenous materials. It is clear that polycrystalline perovskite layers are not homogenous since they have grain boundaries in addition to bulk material, which is roughly equivalent in various grains. The situation is actually quite favorable from the perspective of interpreting the luminescence kinetics because, following photoexcitation, the diffusion only moves the charges through the layer thickness in the vertical direction because only in this direction does the initial photoinduced concentration gradient exist (the gradient is indicated by the red color shown in **Figure 3p**).

Therefore, from the perspective of diffusion throughout the layer thickness, the morphology seen in **Figure 3o** may be regarded as homogenous. Most modern perovskite films are thought to be continuous and monocrystalline in the vertical direction, according to the literature as shown in **Figure 3p**.^[151,152] Although tiny grain sizes are desirable in the films used in the production of light-emitting diodes (LEDs), the architectures depicted in **Figure 3p** are also conceivable. Perovskite layers in these structures are made up of grains that stack on top of one another. This non-homogeneous material is necessary because it requires carriers to cross several internal barriers in order to reach the layer surfaces, which can significantly slow down diffusion.^[153] Another observation relates to the idea of taking the bimolecular recombination of carriers in the bulk film into account. From our personal experience, it makes sense to minimize this mechanism's effect on the kinetics since it complicates the diffusion equation and reduces the precision with which D and S values may be calculated. Reducing the photoexcited carrier concentration below a certain level, around 10^{17} cm^{-3} , will prevent bimolecular recombination.^[154]

3.10 Perovskite solar cell measurement parameters

Current density-voltage (J-V) measurements are generally used to characterize solar cells. This standardized technique consists of illuminating the solar cell with the AM 1.5G spectrum with the intensity of 100 mW/cm^2 and recording the I-V values with an applied voltage. Generally, three parameters are extracted from the J-V measurements: the open circuit voltage (V_{OC}), the short circuit current density (J_{SC}) and the fill factor (FF). These parameters together determine the power conversion efficiency (PCE) of the device. The voltage is scanned in two directions - the forward and the reverse direction i.e., the forward and reverse scans respectively. The forward scan is from the J_{SC} to the V_{OC} and the reverse scan is from the V_{OC} to the J_{SC} . The J-V curves of perovskite solar cell always display a loop, called hysteresis.^[155] Hysteresis exists in a solar cell regardless of the method of deposition and the charge transport layers used. This effect depends mostly on the biasing of the solar cell and also the speed at which the measurement sweep has been carried out.^{[156][157]} Many studies have shown a multitude of causes for hysteresis like ferroelectricity, carrier trapping, interface effects and ion migration of which the ionic movement has been known to be the most prominent cause of hysteresis.^[155,158] When an electric field is present, the mobile ions accumulate at the vicinity of the electrodes building a space charge region in the vicinity of

the charge collection layers which could hinder carrier transport, recombination and extraction. Beside affecting the internal electric field within the device, ionic species also interact with heat and electromagnetic radiation.^[159] To overcome the problem of presence of such mobile ionic species, and to determine the actual performance of the solar cell, slow sweeps of J-V measurement and the maximum power point (MPP) tracking is recommended by the perovskite community as standard measurement protocols.^[85,160]

Keywords: Organic inorganic hybrid perovskites (OIHPs), perovskite solar cell (PSC), power conversion efficiency (PCE), band gap, crystal lattice, covalent bonded, ambipolar, Goldschmidt Tolerance Factor, rhombohedral, orthorhombic, tetragonal, Ruddleson-Popper (RP), Dion-Jacobson (DJ) phase, photon energy, semiconductors, LaMer's model, anti-solvent engineering (ASE), solvent-solvent extraction (SSE), gas flow induced gas pumping (GGPM), critical radius (r_c), Gibbs free energy (ΔG_c), anti-solvents, exciton binding energy, diffusion length, hysteresis, electric field, electromagnetic radiation, maximum power point tracking (MPP).

CHAPTER 4.

4.1 Influence of colloids and impurities on perovskite crystal growth

Different additives incorporated to perovskite precursor solution can drastically impact the morphology, nucleation rate, grain size, and crystallinity of the perovskite films fabricated from it. Studies have been carried out to improve the perovskite film quality, stability, optoelectronic properties, and overall photovoltaic performance by inserting additives, such as polymers^[161], water^[162], small molecules^[163,164], metal ions^[165], and acid-based additives.^[110,166] It has been reported by McMeekin et al. that the morphology of mixed cation-based metal halide perovskites can be controlled by tuning the colloidal density in the perovskite precursor.^[140] These soft coordination frameworks of lead polyhalide networks, such as $[\text{PbX}_3]^-$, $[\text{PbX}_4]^{2-}$, and $[\text{PbX}_6]^{4-}$ act as centers for nucleation during perovskite film formation.^[114] From the classical nucleation theory, it is known that there are two kinds of nucleation - homogeneous and heterogeneous.^[167] Since perovskite film growth is on a foreign substrate (glass or plastics), and occurs via nuclei, this would be a heterogeneous nucleation route. Tuning the morphologies of perovskite layers by implementing p- and n-type layers has been reported by Bi et al.^[133] Assuming that perovskite is a simple example of a heterogeneous nucleation system where a solid spherical nucleus is immersed in a liquid close to the solid surface. Then, the heterogeneous free energy barrier is equal to the homogeneous free energy barrier multiplied by a factor of the interfacial tensions Γ , and since this factor is less than unity, heterogeneous nucleation has a lower energy barrier than its counterpart^[168,169], as shown in **Equation 4.1**

$$G_{\text{Heterogeneous}} = G_{\text{Homogeneous}} \frac{(2 + \cos \theta)}{4} (1 - \cos \theta)^2 \quad 4.1$$

where θ represents the angle of contact between the crystalline deposit and the surface of the solid or the interface wetting angle. Thus, by controlling the amount of lead polyhalide based colloidal network in the perovskite solution, the interfacial tensions between the solid surface and the solution can be modulated giving the room for tuning the heterogeneous nucleation sites. It has been observed that a controlled amount of colloidal particles is needed for a pinhole free perovskite

film growth, as in the presence of colloidal particles perovskite grains impinge upon one another, leading to a densely grown perovskite layer.^[170]

The stabilizer - hypophosphorous acid (H_3PO_2), commonly present in commercial solutions of hydroiodic acid (HI), acts as a reducing agent additive, preventing iodide oxidation. The presence of this additive impacts the purity of the methylammonium iodide (MAI), which is typically synthesized using HI. MAI on the other hand is a key component of the methylammonium lead iodide (MAPI) perovskite thin film formation.^[171] This stabilizer has been known to incorporate methylammonium hypophosphite (MAH_2PO_2) impurities in the synthesized MAI precursor powder, as it reacts with methylamine (MA) in the aqueous solution. These salt impurities affect colloidal network in the precursor solution, slowing down the crystallization of the MAPI perovskite layer by the formation of the intermediate phase - lead hypophosphite (PbH_2PO_2).^[172] However, removing unwanted MAH_2PO_2 impurities is technically very difficult, and also would lead to coarse perovskite grains. Thus, a controlled addition of MAH_2PO_2 additive could help tuning the number of colloidal impurities, and thus lead to better perovskite crystal growth. The following manuscript entitled '*New Synthetic Route of Ultrapure Alkylammonium Iodides for Perovskite Thin Films of Superior Optoelectronic Properties*' (DOI: 10.1002/ente.202000478) is attached as a partial fulfilment of my Ph.D. thesis and shows a novel synthetic route of methylammonium iodide ($\text{CH}_3\text{NH}_3\text{I}$, MAI), producing ultra-pure MAI with a less expensive and simple reaction route. This route helped control a colloidal network in the precursor solution by precise addition of specific impurities, which in turn helped achieving a more controlled growth of perovskite thin films with largely improved morphologies and properties. This synthetic route can also be applied to other alkylammonium iodides for laboratory and commercial uses.

4.2 Study of decomposition of aged perovskite solar cells using NIR spectroscopy

The use of infrared spectroscopy (IR) in the study of perovskite degradation has already been widely explored. Williams et al. demonstrated by combining thermal analysis and Fourier Transform infrared spectroscopy (FTIR) that MAI ($\text{CH}_3\text{NH}_3\text{I}$) does not produce gaseous products until 240°C .^[173] Another recent technique involving IR-based study for the degradation of perovskites was carried out by Pegu et al., where a polarized modulated IR excitation was used to

study the surface dipole orientation of fluorinated phenylethylammonium iodide (FPEAI) and phenylethylammonium iodide (PEAI) molecular groups on the perovskite surface.^[174] However, the use of IR spectroscopy to study intermolecular interactions has been conducted at the end of the twentieth century by Isao Noda who invented the two-dimensional correlation spectroscopy (2DCOS) to study the dipole interactions within atactic polystyrene.^[175] The generalized 2DCOS has been developed into a very potent analytical tool in many disciplines of spectroscopic investigations, particularly in conducting polymer studies, since the concept of 2DCOS was enlarged to the many spectroscopic applications in Noda's work in 1993.

The generalized 2DCOS can reveal information in spectral fluctuations, including thermal, electrical, optical, magnetic, and chemical perturbations,^[175,176] IR,^[177,178] Raman,^[179,180] terahertz (THz),^[181] X-ray,^[182] UV-vis,^[183,184] NMR,^[185,186] fluorescence,^[187,188] and even chromatography. The use of generalized 2D correlation spectra has several advantages over traditional spectroscopy, including the ability to examine inter- or intramolecular interactions, and establish the sequence in which sub-molecular events occur.

The synchronous 2D correlation spectrum depicts the concurrent or coincidental variations in spectral intensities at ν_1 and ν_2 . The auto-correlation functions of spectral intensity variations, often known as auto peaks, are represented by positive correlation peaks on the diagonal synchronous 2D correlation spectrum. Cross peaks in the synchronous 2D correlation spectrum, which are found in the off-diagonal positions show contemporaneous or simultaneous changes in spectral intensities seen at two separate spectral variables. Positive cross-peaks show that corresponding spectral variables' intensities rise or fall together. The negative cross-peaks, on the other hand, show that one of the spectral intensities rises while the other falls.^[19] These processes help in detecting the sub-molecular alignment, as well as the strength of intermolecular interactions and dipolar arrangements at the surface. A schematic of the 2DCOS IR spectroscopy layout is shown in **Figure 4a**.

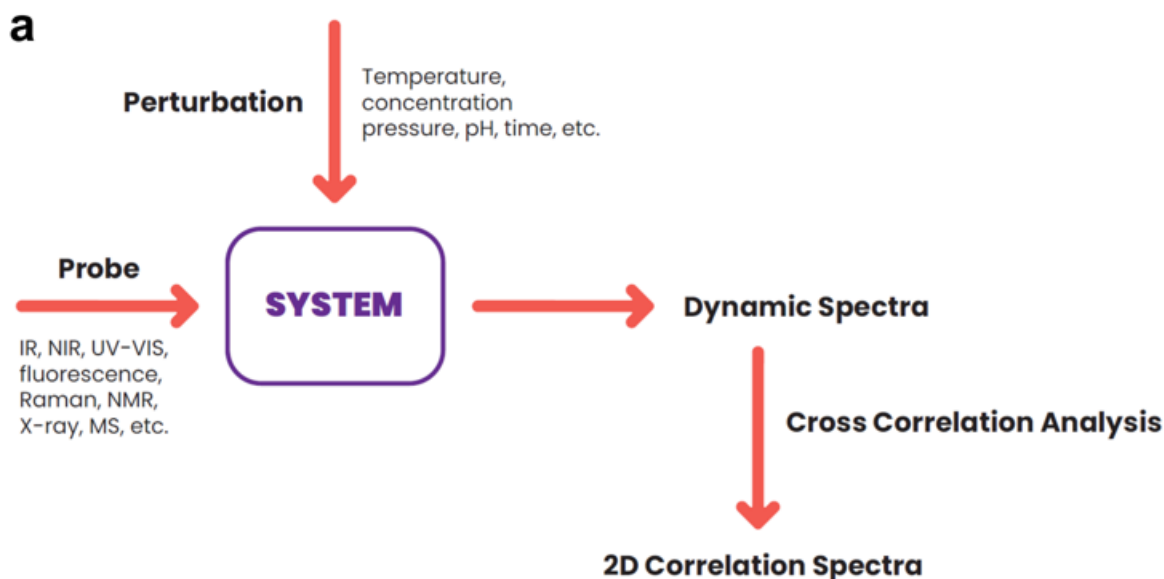


Figure 4a. Schematic of the 2D correlation spectroscopy (2DCOS). Adapted and reproduced with permission from *Copyright 2015 Frontiers in Chemistry*^[19]

The following manuscript, entitled ‘*Analysis of Perovskite Solar Cell Degradation over Time using NIR Spectroscopy – a Novel Approach*’ (DOI: 10.3390/en15155397), is an attachment in this thesis for the partial fulfilment of this Ph.D. study. Here, the potential for observing the aging of perovskite structures over time, using optical reflectance in the NIR range (900-1700 nm) has been explored. Changes in the optical reflectance spectra of the original perovskite solar cell structures during the first month following PSC production have been recorded. Two-dimensional correlation spectroscopy (2D-COS) approach statistical analysis and the ratio of distinguishing peaks in reflection spectra have been investigated. This technique enables accurate timed detection of important thermal aging sites. Furthermore, in the future, this technique combined with FTIR could help us further detect the functional groups during perovskite film degradation.

4.3 Perylene diimide based dyes as efficient electron transport layers for perovskite solar cells

Perylene dye-based molecules (perylene-3,4,9,10-tetracyclic acid diimides) and their derivatives have been known to be promising electron transport materials in organic and hybrid solar cells due to their high electron mobilities and high molar extinction coefficient values. Their rigid network

and the presence of aromatic rings in their molecular structure help in the better transport of electrons in perovskite solar cell structures. The synthesis of organic molecules such as perylene-based small molecules are feasible to synthesize in the laboratory.

In organic and hybrid photovoltaics, the conversion of light energy to electric energy depends on the photo-induced charge transport process of the electron acceptor and the hole acceptor with different electron affinity and different ionization potentials. Although a large number of electron acceptor materials have been widely investigated for photovoltaic applications, organic materials are still being studied for efficient photovoltaic applications.^[135,189] Thus, the use of perylene diimide based dyes is one of the widely explored molecules replacing the traditional fullerene-based derivatives.^[190] However, researchers have to keep in mind a few factors before integrating such molecules for solar cell applications. These include easy processing conditions, good stability and solubility, high charge mobilities and charge injection, and collection properties at the interfaces.^[20] In perylene diimide (PDI)-based dyes such properties can be tuned by careful chemical engineering and via supramolecular assemblies in their solid state.^[20,190]

However, there are certain challenges to be kept in mind while engineering and designing such class of molecules in the laboratory, such as: lower symmetries and high polarizability when compared to fullerene-based molecular moieties. Furthermore, the charge transport mobilities and electron affinities of PDI-based dyes are lower than that of traditional fullerene-based dyes. This is the biggest obstacle for utilizing PDIs as electron transport layers in perovskite solar cell applications. The PDI-based dyes, however, have a higher molar absorption coefficient and higher absorbance in the visible range than fullerenes, thus contributing to a better light harvesting in solar cells.^[191] Perylene-3,4,9,10-perylene tetracarboxylic acid diimides (PDIs), as shown in **Figure 4b**, can be easily modified for optimized electronic and optical properties by introduction of alkyl or aryl structures at the bay core positions^[192,193] or its N-positions.^[194]

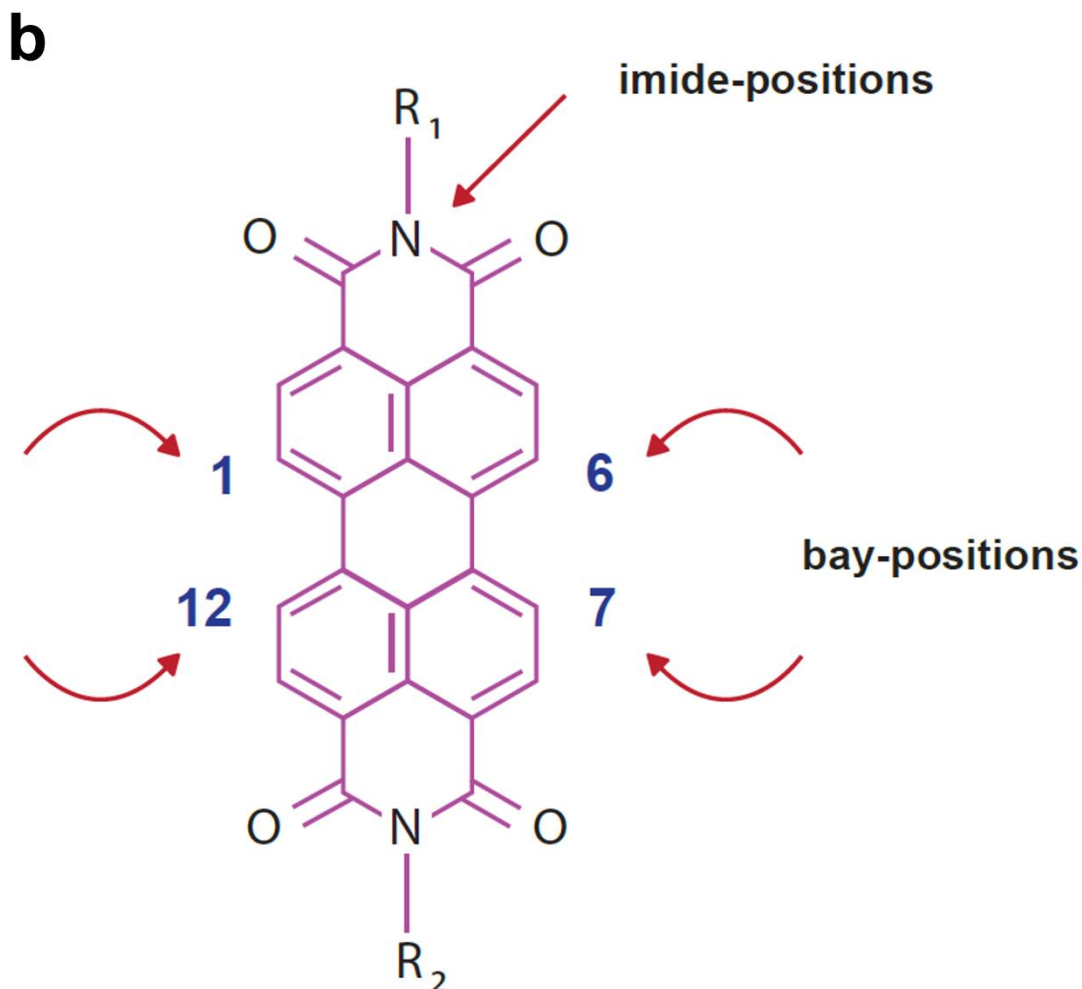


Figure 4b. Representative diagram of a PDI molecule. Adapted and reproduced with permission from *Copyright 2013 Elsevier Ltd*^[20]

PDI molecules on top of having desirable chemical, thermal and photochemical stabilities, also exhibit large optical absorption in the visible and near IR range where they emit light with high quantum yields, and show excellent charge transport properties.^[195] The following manuscript entitled ‘*Solution-processable perylene diimide-based electron transport materials as non-fullerene alternatives for inverted perovskite solar cells*’ (DOI: 10.1039/d2ta01321e) is attached as a partial fulfilment of this Ph.D. thesis and is based on the synthesis of three highly soluble perylene diimide electron acceptor molecules based on the core contortion approach,^[196] making

them solution-processable, while also avoiding the use of long isolating alkyl-based chains. These PDI-based molecules with four substituent groups in their bay positions have not been widely investigated by researchers earlier.^[197] Their synthesis had been carried out by the initial reaction of benzylamines in the position of imides by further attachment of different functional group at their respective bay positions. The optoelectronic properties of these PDI molecules were studied in an inverted perovskite device architecture, achieving desirable solar cell properties, and thus assessing them to be potential alternatives for traditional fullerene-based dyes as electron transport materials.

4.4 Exploring the formation of a lower dimension perovskite structure at the solar cell interfaces for high efficiency and stability

Incorporation of bulky organic cations (BOC) between the hole transport layer and perovskite layer can lead to significant reduction of non-radiative energy losses at both perovskite interfaces, top and bottom, at the same time. Moreover, BOC molecules prevent phase segregation on the perovskite surface, resulting in uniform surface characteristics. As a result, p-i-n structured perovskite solar cells (PSCs) achieved a champion efficiency of over 23.7%, which is among the best efficiencies ever recorded for the p-i-n type PSCs.^[48,81] The presence of such polar bulky organic salts atop the hydrophobic poly(triaryl amine) (PTAA) layer increases the surface energy of that layer, which improves the perovskite precursor solution's wettability. This was observed by Degani et al., where the perovskite deposition process on dimethyl formaldehyde (DMF)-washed PTAA was compared with the PEAI/DMF-washed PTAA samples. The latter case clearly showed better wettability of perovskite precursor solution. The perovskite layer's microstructure and the presence of nanovoids at the perovskite/HTL interface are both improved by the improved wetting.^[81]

Passivation of the interfacial defects with BOC molecules minimizes surface recombination and augments J-V performance.^[198-200] The unsaturated chemical bond at the perovskite surface can be immediately passivated by the chemical interactions between the 2D spacers and the perovskite layer. Because of the up-shifted energy levels at the anode contact, the development of 2D/3D heterojunction can also facilitate hole transfer while blocking electron flow.^[201,202]

Furthermore, to reduce the impact of dispersion forces, the use of conformal and homogeneous hydrophobic layers has been investigated by researchers to be carefully deposited on top of bulk perovskite layers. Such fluorinated chemicals with carbon-fluorine (C-F) bonds and low polarizability contribute to the material's stability and prevent moisture ingress within the perovskite lattice.^[203,204] Fluorinated substances have been reported to assist the interaction of electronegative fluorine atoms and the surface of perovskites thus creating hydrogen/halogen-bonding interactions.^[205] It has been recently postulated that the use of highly electronegative BOC molecules like FPEAI, governs the stronger van der Waals contacts, serving as a barrier to moisture decomposition by enhancing orientation and performance.^[174]

'Modification of a Buried Interface with Bulky Organic Cations for Highly Stable Flexible Perovskite Solar Cells' (DOI: 10.1021/acsaem.2c02780) is a scientific published work attached with this Ph.D. thesis as a partial fulfilment of the desired study. Here, an effective method for enhancing the stability and efficiency of flexible perovskite solar cells has been reported. The buried interface between a hole-transporting layer and a perovskite-absorbing film has been modified using bulky organic ammonium molecules. These BOC-modified perovskite solar cells significantly outperform the original, unaltered system. Applying the 4-fluorophenethylammonium iodide (FPEAI) for this modification resulted in obtaining the 18.66% efficiency for the large-area (1 cm²) flexible solar cell. Better hole extraction and less nonradiative recombination loss at the buried interface were shown to be the cause of the performance enhancement. The presence of low-dimensional perovskite phases close to the hole-transporting material by the use of these BOC passivation has also been reported. As a result, the thermal and light-soaking stability of manufactured devices is greatly improved. With the optimal passivation treatment with the FPEAI, no loss in 1000 hours of aging at 85°C along with no loss in 1000 hours of light soaking at open circuit was obtained, and less than 10% drop in 1000 hours of operation at maximum power point was also recorded. Such BOC passivation also led to the structural stability of the perovskite lattice which was ensued by studying the amount of iodine vapor release during the light soaking stability tests.

4.5 A robust encapsulation route for plastic based flexible perovskite solar cells to withstand highly accelerated aging tests

Although high efficiencies for the flexible solar cells have been reported, the main challenge lies in the commercializing of this technology due to its limited stability. When perovskite solar cells (PSCs) are exposed to ambient air conditions, their performance starts to suffer greatly. Making PSCs that have long enough operating lifetimes for their intended end-user applications is therefore still a cumbersome task. A crucial technique needed for the use and commercialization of perovskite solar cells is thin-film encapsulation. For the necessary increase in reliability and longer device lifetime, it is essential to avoid the intrusion of moisture and oxygen. To prevent a significant decrease in device performance, more research is required to better understand how encapsulation affects the stability of flexible perovskite solar cells.

Lead iodide can form when volatile organic species evolve as a result of being catalyzed by heat or moisture.^[206–208] Thermal and moisture stability can be improved by replacing methylammonium (MA) with less volatile cations and utilizing a barrier materials. PSCs are also prone to delamination due to their low fracture energy^[209] and the presence of many layers with different thermal expansion coefficients (CTE).^[210]

To compete with other commercial technologies, PSC encapsulation must provide resilience against temperature and humidity extremes at a low cost. Work utilizing single-layer hydrophobic thin films has been reported earlier.^[211,212] Also thin multi-layers utilizing different organic electronic technologies used as encapsulation layers for solar cells have been reported.^[213] A robust barrier must prevent moisture from entering at high temperatures, sustain temperature changes without delamination, and promote steady and effective operation. Apart from barrier films which are needed to prevent the interaction of extrinsic species like moisture and air, the incorporation of an edge sealant is also necessary for a complete and protective encapsulation stack. An edge sealant's primary role is to prevent moisture from entering. An encapsulant binds the package in a compact manner and guarantees that the edge seal stays compressed even after prolonged field exposure by filling in any extra volume in the package. It must have high volume resistivity, minimal moisture absorption, no reactive chemical species, high transmission, and high UV resistance.^[53]

In general, perovskite photovoltaic modules installed for outdoor applications must be able to endure a mix of moisture ingress and temperature extremes, even though much of the stability work on PSCs is reported at 85°C.^[116] Hence, IEC61215:2016^[214] damp heat, thermal cycling, and humidity freeze are some common accelerated tests mandated for commercial modules that must pass these tests with less than 5% relative efficiency loss. The humidity freeze test places the toughest impact on the encapsulation quality, since it combines thermal cycling and damp heat. For instance, moisture that has gotten into the encapsulation will harden during freezing and cause the encapsulant to delaminate. Perovskites' degradation can be also induced by temperature fluctuations^[215] Thus, a weakly encapsulated PSC stack or any intrinsic perovskite material instability will be revealed by the humidity freeze test. According to Shi et al^[117], an effective encapsulation scheme is one that provides a pressure tight environment for the PSC. As a result, any decomposition reaction, as given by **Equation 4.2**, quickly reaches equilibrium before the PSC sustains considerable damage. In a pressure-tight environment, when the concentration of products rises, Q rises and ΔG tends to shift toward 0, which shows the reaction has reached equilibrium. The variation in temperature may even cause an unexpected reaction or a positive ΔG which depicts an unspontaneous reaction. Even when the decomposition reaction is partially reversible, as with MA or FA/MA combined, sealing the PSC in a pressure-tight environment substantially suppresses it.

$$\Delta G = \Delta G^{\circ} + RT \ln Q \quad 4.2$$

Where Q is the proportion of the product concentration to the reactant concentration, and ΔG and ΔG° are the free energy changes that occur during the decomposition reaction, and while the reactants and products are in their standard states, respectively.

Also encapsulation stacks which are less sensitive to UV radiation have better stability.^[216] The scientific manuscript entitled '*Encapsulation protocol for flexible perovskite solar cells enabling stability in accelerated aging tests*' (DOI: 10.1002/eem2.12434) has been attached as a partial fulfilment of this Ph.D. thesis in which an effective device hermitization is achieved by developing a lamination process that includes adhesive materials, barrier foils, and edge sealants. The universality of this method is demonstrated in the three different flexible perovskite solar cell configurations (p-i-n with carbon, p-i-n with silver, and n-i with carbon), with large active areas (1 cm²). After undergoing a series of accelerated aging tests, based on industry standards (compatible with the IEC 61215 and IEC 61646), which included 1400 hours of moist heat, 50

thermal cycles, and 10 cycles of the humidity freeze test, the best devices maintained more than 85% of their initial performance.

Keywords: Additives, interface wetting angle, colloidal, stabilizer, infrared (IR) spectroscopy, polarized, 2D correlation spectroscopy (2DCOS), NMR, chromatography, cross-peaks, PDI, supramolecules, molar extinction coefficient, bulky organic cations (BOC), surface energy, hydrophobic, lift-off, polarizability, optoelectronic, encapsulant, IEC, delamination, degradation, free energy, hermitization.

CHAPTER 5.

5.1 Conclusions

The Ph.D. research work described in this thesis first explored the effect of controlled incorporation of additives in the precursor solution for methylammonium lead iodide (MAPI)-based perovskite solar cells, where a novel synthetic route of methylammonium iodide was reported, which lead to smoother and pinhole-free perovskite films. Following the improved perovskite formation, an understanding of the perovskite degradation during thermal aging of the photovoltaic devices was studied with the help of NIR-based 2D cross-correlation spectroscopy (2DCOS). In this method, different solar cells, with and without metal back-contact electrodes, were tested, and it was revealed that perovskite layers exposed to ambient air without any protective layer degraded faster than perovskite layers with a metal coating, thus paving a way for understanding the need of a protective barrier layer for perovskite long-term stability. The research work focused then on the synthesis of a functionalized perylene diimide (PDI) molecule, which was applied as a highly effective electron transport material in perovskite solar cells. By changing the functional groups in this molecule, the energetics between the triple cation perovskite and the PDI molecule were optimized leading to high efficiencies, comparable to those of the conventional fullerene-based electron transport layers. The thesis then explains the formation of low dimensional perovskite structures at the buried interface by incorporating bulky organic cations (BOC) between the hole transport layer and the perovskite absorber layer in a p-i-n solar cell structure. This modification significantly improved carrier extraction and also led to the passivation of defects at that interface. Finally, this thesis highlighted the significance of a proper encapsulation strategy to bring the perovskite technology close to an industrial feasibility. In this part of the research work, adhesive materials, barrier foils, and edge sealants were explored to encapsulate flexible perovskite solar cell devices, leading to robust device hermitization. Following a series of accelerated aging tests based on industry standards (IEC 61215 and IEC 61646), including 1400 hours of moist heat, 50 thermal cycles, and 10 humidity freeze cycles, these encapsulated solar cells preserved more than 85% of their initial performance.

5.2 Use of perovskites in current industrial applications

The worldwide perovskite solar cell market has a bright future, with prospects in aerospace and defence, industrial, commercial, residential, and utility applications. The worldwide perovskite solar cell market is predicted to reach \$2.02 billion by 2028, rapidly growing at a CAGR value of 40.0% between 2023 and 2028. Growing demand for low-cost and lightweight solar cells, supporting government regulations, growing environmental concerns about carbon emission reduction, and increased domestic solar power penetration are the primary drivers for this industry.^[217]

The current state of perovskite solar cells is promising but faces several challenges. Perovskite solar cells have a stark potential to be both cheap and efficient, but their stability is a setback. Several businesses, however, including Saule Technologies, Oxford PV, and Microquanta Semiconductor, claim to have made substantial work in resolving the stability issue and are nearing commercialization. Furthermore, the low cost and relative ease of synthesizing perovskite materials make them an appealing commercialization alternative. The capacity to make thin-film solar cells that are light and flexible, as well as the possibility for high efficiencies, contribute to their commercial feasibility. To increase their stability and performance, the aforementioned companies are researching on various technologies such as ink-jet printing, combination of perovskite-silicon cells, and glass-encased cells. While some experts are suspicious, these firms have passed cell functional testing and are confident in the stability of their fabricated solar cells. The long-term survivability of perovskite solar cells versus regular silicon cells remains unknown. However, experts believe that perovskite technology has the potential to make solar electricity more affordable and accessible. Continued R&D efforts are aimed at enhancing the stability, scalability, and commercialization of perovskite solar cells.

As the research continues, the preliminary findings are still encouraging. Oxford PV, for example, used a tandem strategy to obtain a high conversion efficiency with its perovskite-silicon solar cell. The perovskite material is layered on top of a regular silicon solar cell in this method. Oxford PV was able to develop a 28% conversion efficiency on a 1cm² cell that was certified by the United

States National Renewable Energy Laboratory as well as researchers in KAUST have achieved a certified efficiency of 33%.

Perovskite solar cells offer a number of characteristics that make them suited for a variety of commercialization applications. Some of these applications are as follows:

- Building-integrated photovoltaics (BIPV): Perovskite solar cells may be incorporated into building elements such as windows, facades, and roofs to generate power while retaining the structure's aesthetic appeal.^[218]
- Portable electronics: Because perovskite solar cells are lightweight and flexible, they are perfect for powering portable electronic devices such as smartphones, tablets, light emitting diodes (LED) and wearables.
- Off-grid applications: Perovskite solar cells can be used to power isolated places, rural populations, and poor countries that are devoid of dependable electricity.^[219]
- Electric cars: Perovskite solar cells can be utilized for VIPVs (Vehicle Integrated Photovoltaics) as they may be placed into the body of electric vehicles to supply additional power and enhance driving range.^[220]
- Consumer electronics: Perovskite solar cells can power a variety of consumer gadgets, such as smartwatches, fitness trackers, and wireless charging devices.
- Space applications: Because of its high efficiency and small weight, perovskite solar cells are well suited for space applications where weight and efficiency are crucial.^[221]
- Lower cost for technological applications: This advantage states the use of liquid-based materials and processes to fabricate perovskite solar cells. This method has a number of advantages, including cheaper capital expenditure (CAPEX) and operating expenditure (OPEX) expenses. Perovskite solar cell components can be dissolved in a solvent and deposited onto a substrate using processes such as spin-coating, inkjet printing, or spray coating. These solution-based technologies are simple and easy to scale up for mass production, resulting in cheaper costs and environmentally friendly techniques when compared to more sophisticated and expensive fabrication procedures.^[222] Furthermore, solution-based processing permits the use of low-temperature deposition processes. This means that the perovskite layer may be placed on a wide substrate range, including flexible and lightweight materials, without requiring high-temperature processing processes and.

This versatility in substrate selection leads to the development of novel applications in fields such as building-integrated photovoltaics and portable electronics as talked earlier in this section.

These are only a few instances of perovskite solar cell commercialization opportunities. As technology advances and improves, it is projected to find even more uses in a variety of sectors. Due to a variety of issues, commercial viability of perovskite solar cells (PSCs) remains a difficulty. One of the most significant impediments is the expense of PSCs in comparison to traditional fossil fuels. According to a US Energy Information Administration estimate, the Levelized Cost of Electricity (LCOE) for PV is around three times that of coal. To secure the public's attention, the LCOE of PSCs must be reduced to that of silicon PV or petroleum. PSC prices have been reduced with the use of solution deposition processes, which minimize manufacturing costs. Furthermore, the US Department of Energy's Sunshot Initiative set a goal for the LCOE of PV to be under 6 US cents kWh⁻¹ in order to increase its competitiveness compared to other energy sources.^[223]

In terms of scalability, PSCs must be manufactured on a big scale in order to supply the rising need for renewable energy. The development of manufacturing facilities and testing processes is critical to the commercialization of PSCs. Furthermore, the scalability of PSCs is intimately tied to their manufacturability, which entails developing efficient and cost-effective production procedures.

Sustainability is yet another crucial factor for the commercialization of PSCs. This involves lowering PSCs' environmental effect, such as reducing lead toxicity and using sustainable materials and production techniques. To address the issue of lead toxicity in PSCs, efforts have been undertaken to produce lead-free and double perovskite materials.^{[224][225]}

Finally, storage is a critical factor in the commercialization of PSCs. Intermittency is a problem for PV technology, and methods like linking PV systems to the grid or employing self-rechargeable batteries have been proposed to overcome it. The development of cost-effective and efficient technologies for energy storage is critical for PSC deployment.^[226]

REFERENCES

- [1] BP, *BP Energy Outlook 2021*, 70, 72.
- [2] IEA, *IEA, Net Solar PV Capacity Additions 2018-2020*, IEA, Paris
<https://www.iea.org/data-and-statistics/charts/net-solar-pv-capacity-additions-2018-2020>, IEA. Licence: CC BY 4.0, **2020**.
- [3] M. Plakhotnyuk, Nanostructured Heterojunction Crystalline Silicon Solar Cells with Transition Metal Oxide Carrier Selective Contacts, Technical University of Denmark, **2018**.
- [4] E. Meijer, *Charge Transport in Disordered Organic Field-Effect Transistors Eduard Meijer*, **2003**.
- [5] S. Locci, *Thesis 2009*, 29–65.
- [6] NREL, *Reference Air Mass 1.5 Spectra.*, **2003**.
- [7] P. Altermatt, “‘The Solar Spectrum’, The Altermatt Lectures, PV Lighthouse,” can be found under https://pvlighthouse.com.au/cms/lectures/altermatt/solar_spectrum, **2011**.
- [8] www.pvlighthouse.com.au, *The Air Mass (AM)*, **2016**.
- [9] R. J. C. G. Cava Lab:, “Perovskite Structure and Derivatives,” **n.d.**
- [10] S.-H. W. Wan-Jian Yin, Ji-Hui Yang, Joongoo Kang, Yanfa Yan, *J. Mater. Chem. A* **2015**, 8926–8942, 1–23.
- [11] F. Haug, J. Yum, C. Ballif, **2014**.
- [12] E. T. Hoke, D. J. Slotcavage, E. R. Dohner, A. R. Bowring, H. I. Karunadasa, M. D. McGehee, *Chem. Sci.* **2015**, 6, 613–617.
- [13] M. Liu, M. B. Johnston, H. J. Snaith, *Nature* **2013**, 501, 395–398.
- [14] N. J. Jeon, J. H. Noh, Y. C. Kim, W. S. Yang, S. Ryu, S. Il Seok, *Nat. Mater.* **2014**, 13, 897–903.
- [15] C. H. Chiang, C. G. Wu, *ACS Nano* **2018**, DOI 10.1021/acsnano.8b05731.
- [16] A. D. Taylor, Q. Sun, K. P. Goetz, Q. An, T. Schramm, Y. Hofstetter, M. Litterst, F. Paulus, Y. Vaynzof, *Nat. Commun.* **2021**, 12, 1–11.
- [17] V. Petrova-koch, *High-Efficient Low Cost Photovoltaics (Saule Chapter)*, **2009**.
- [18] V. S. Chirvony, K. S. Sekerbayev, H. Pashaei Adl, I. Suárez, Y. T. Taurbayev, A. F. Gualdrón-Reyes, I. Mora-Seró, J. P. Martínez-Pastor, *J. Lumin.* **2020**, 221, 117092.
- [19] Y. Park, I. Noda, Y. M. Jung, **2015**, 3, 1–16.
- [20] E. Kozma, M. Catellani, *Dye. Pigment.* **2013**, 98, 160–179.
- [21] The Intergovernmental Panel on Climate Change 2018 Special Report Glossary: J.B Mathews, **2018**.

- [22] A. Voigt, J. Marotzke, *Clim. Dyn.* **2010**, 35, 887–905.
- [23] The Discovery of Global Warming.” American Institute of Physics, **2018**.
- [24] NOAA fisheries, *Natl. Ocean. Atmos. Adm.* **n.d.**
- [25] Julia Rosen, *The Science of Climate Change Explained: Facts, Evidence and Proof*, **2021**.
- [26] United nations, “The Paris Agreement,” can be found under <https://unfccc.int/process-and-meetings/the-paris-agreement/the-paris-agreement>, **2016**.
- [27] Bill Gates, *How to Avoid a Climate Disaster: The Solutions We Have and the Breakthroughs We Need*, Nature Public Health Emergency Collection, **2021**.
- [28] R. Emas, **2015**.
- [29] O. Nitsch, J. and Krewitt, W. and Langniss, *Encycl. Energy* **2004**, 5, 202.
- [30] Wind Energy Advantages & Disadvantages: The Pros & Cons Of Wind Power From Turbines-Graham Sawrey, **2023**.
- [31] David NEWLAND, *Hydroelectric Power 101*, **2018**.
- [32] Rinkesh, *Various Pros and Cons of Biomass Energy*, **2016**.
- [33] energysage, “Geothermal energy pros and cons,” can be found under <https://www.energysage.com/about-clean-energy/geothermal/pros-cons-geothermal-energy/>, **2021**.
- [34] energysage, “Geothermal energy pros and cons,” **n.d.**
- [35] Catherine Lane, “Tidal energy pros and cons,” can be found under solarreviews.com/blog/tidal-energy-pros-and-cons, **2021**.
- [36] Heymi Bahar, B. Piotr, “Solar PV,” can be found under <https://www.iea.org/reports/solar-pv>, **2020**.
- [37] A. Turgeon, E. Morse, *Natl. Geogr. Soc.* **2012**.
- [38] N. J. Murray Hill, *New York Times* **1954**, 1.
- [39] ENERGY.GOV, “Solar Photovoltaic Cell Basics,” can be found under <https://www.energy.gov/eere/solar/solar-photovoltaic-cell-basics>, **2016**.
- [40] US National Renewable Energy Laboratory, *Nrel* **2019**, 1.
- [41] A. Kojima, K. Teshima, Y. Shirai, T. Miyasaka, *J. Am. Chem. Soc.* **2009**, 131, 6050–6051.
- [42] M. M. Lee, J. Teuscher, T. Miyasaka, T. N. Murakami, H. J. Snaith, *Science (80-.)*. **2012**, 338, 643–647.
- [43] H.-S. Kim, C.-R. Lee, J.-H. Im, K.-B. Lee, T. Moehl, A. Marchioro, S.-J. Moon, R. Humphry-Baker, J.-H. Yum, J. E. Moser, et al., *Sci. Rep.* **2012**, 2, 591.
- [44] M. A. Green, E. D. Dunlop, J. Hohl-Ebinger, M. Yoshita, N. Kopidakis, X. Hao, *Prog. Photovoltaics Res. Appl.* **2021**, 29, 657–667.

- [45] S. D. Stranks, G. E. Eperon, G. Grancini, C. Menelaou, M. J. P. Alcocer, T. Leijtens, L. M. Herz, A. Petrozza, H. J. Snaith, *Science* (80-.). **2013**, *342*, 341–344.
- [46] T. Zhou, H. Lai, T. Liu, D. Lu, X. Wan, X. Zhang, Y. Liu, Y. Chen, *Adv. Mater.* **2019**, *31*, 1–9.
- [47] J. F. Liao, W. Q. Wu, J. X. Zhong, Y. Jiang, L. Wang, D. Bin Kuang, *J. Mater. Chem. A* **2019**, *7*, 9025–9033.
- [48] S. Wu, J. Zhang, Z. Li, D. Liu, M. Qin, S. H. Cheung, X. Lu, D. Lei, S. K. So, Z. Zhu, et al., *Joule* **2020**, *4*, 1248–1262.
- [49] A. A. Sutanto, N. Drigo, V. I. E. Queloz, I. Garcia-Benito, A. R. Kirmani, L. J. Richter, P. A. Schouwink, K. T. Cho, S. Paek, M. K. Nazeeruddin, et al., *J. Mater. Chem. A* **2020**, *8*, 2343–2348.
- [50] D. P. McMeekin, Z. Wang, W. Rehman, F. Pulvirenti, J. B. Patel, N. K. Noel, M. B. Johnston, S. R. Marder, L. M. Herz, H. J. Snaith, *Adv. Mater.* **2017**, *29*, DOI 10.1002/adma.201607039.
- [51] S. Dasgupta, K. Misztal, R. Fuentes Pineda, W. Mróz, Ł. Pawlaczyk, J. Serafińczuk, A. J. Barker, T. Ahmad, A. P. Herman, S. Sahayaraj, et al., *Energy Technol.* **2020**, *8*, 1–12.
- [52] G. S. Perez, S. Dasgupta, Z. Wiktor, **2022**, 11046–11053.
- [53] R. Cheacharoen, C. C. Boyd, G. F. Burkhard, T. Leijtens, J. A. Raiford, K. A. Bush, S. F. Bent, M. D. McGehee, *Sustain. Energy Fuels* **2018**, *2*, 2398–2406.
- [54] M. A. Green, A. Ho-Baillie, H. J. Snaith, *Nat. Photonics* **2014**, *8*, 506–514.
- [55] S. D. Stranks, H. J. Snaith, *Nat. Nanotechnol.* **2015**, *10*, 391–402.
- [56] K. F. Brennan, *The Physics of Semiconductors With Applications to Optoelectronic Devices*, Cambridge University Press, Georgia, U.S.A, **1999**.
- [57] cadence multiphysics system Analysis, “The Types of Recombination in Semiconductors,” **2016**.
- [58] M. Shur, M. Hack, *J. Appl. Phys.* **1984**, *55*, 3831–3842.
- [59] G. Horowitz, R. Hajlaoui, P. Delannoy, *J. Phys. III* **1995**, *5*, 355–371.
- [60] G. Horowitz, M. E. Hajlaoui, R. Hajlaoui, *J. Appl. Phys.* **2000**, *87*, 4456–4463.
- [61] J. Xing, Q. Wang, Q. Dong, Y. Yuan, Y. Fang, J. Huang, *Phys. Chem. Chem. Phys.* **2016**, *18*, 30484–30490.
- [62] B. Roose, A. Ummadisingu, J. P. Correa-Baena, M. Saliba, A. Hagfeldt, M. Graetzel, U. Steiner, A. Abate, *Nano Energy* **2017**, *39*, 24–29.
- [63] D. Y. Son, S. G. Kim, J. Y. Seo, S. H. Lee, H. Shin, D. Lee, N. G. Park, *J. Am. Chem. Soc.* **2018**, *140*, 1358–1364.
- [64] J. W. Orton, M. J. Powell, *Reports Prog. Phys.* **1980**, *43*, 1263–1307.

- [65] J. A. Nelson, *The Physics Of Solar Cells*, Imperial College Press, 2003, **2003**.
- [66] V. Kothekar, *Protocol* **2012**, 1–28.
- [67] Y. Li, S.-R. Lee, C.-Y. Wu, *Aerosol Air Qual. Res.* **2006**, 6, 418–429.
- [68] C. A. Gueymard, *Sol. Energy* **2004**, 76, 423–453.
- [69] ISO_25178-2:2012, *International Standard International Standard*, **2003**.
- [70] ASTM, *Astm* **2013**, 03, 1–21.
- [71] C. A. Gueymard, D. Myers, K. Emery, *Sol. Energy* **2002**, 73, 443–467.
- [72] M. Sengupta, A. Habte, Y. Xie, A. Lopez, C. A. Gueymard, M. Sengupta, A. Habte, Y. Xie, A. Lopez, C. A. Gueymard, **2018**.
- [73] H. Min, D. Y. Lee, J. Kim, G. Kim, K. S. Lee, J. Kim, M. J. Paik, Y. K. Kim, K. S. Kim, M. G. Kim, et al., *Nature* **2021**, 598, 444–450.
- [74] National Renewable Energy Laboratory, **2021**, <https://www.nrel.gov/pv/cell-efficiency.html>.
- [75] T. Y. Yang, Y. Y. Kim, J. Seo, *APL Mater.* **2021**, 9, DOI 10.1063/5.0064073.
- [76] B. Science, **2011**, 0–20.
- [77] W. Yang, D. Zhong, M. Shi, S. Qu, H. Chen, *iScience* **2019**, 22, 534–543.
- [78] S. Sien, Y. Ming, S. Gautam, T. Chien, *Science (80-.)*. **2013**, 342, 344–347.
- [79] O. Oni, K. Sujit, S. Kasemsuwan, T. Sakpuaram, D. U. Pfeiffer, *Vet. Rec.* **2007**, 160, 368–371.
- [80] J. Jing, K. Liu, J. Jiang, T. Xu, S. Wang, J. Ma, Z. Zhang, W. Zhang, T. Liu, *Photonics Res.* **2022**, 10, 126.
- [81] M. Degani, Q. An, M. Albaladejo-Siguan, Y. J. Hofstetter, C. Cho, F. Paulus, G. Grancini, Y. Vaynzof, *Sci. Adv.* **2021**, 7, 1–10.
- [82] D. Shi, V. Adinolfi, R. Comin, M. Yuan, E. Alarousu, A. Buin, Y. Chen, S. Hoogland, A. Rothenberger, K. Katsiev, et al., **2015**, 347, 6221.
- [83] B. Podolsky, N. Rosen, J. F. Clauser, A. M. Steinberg, R. Y. Chiao, A. Vaziri, G. Weihs, A. Zeilinger, R. S. Bennink, S. J. Bentley, et al., **2012**, 338, 643–648.
- [84] L. Schmidt-Mende, V. Dyakonov, S. Olthof, F. Ünlü, K. M. T. Lê, S. Mathur, A. D. Karabanov, D. C. Lupascu, L. M. Herz, A. Hinderhofer, et al., *APL Mater.* **2021**, 9, DOI 10.1063/5.0047616.
- [85] S. Gharibzadeh, B. Abdollahi Nejand, M. Jakoby, T. Abzieher, D. Hauschild, S. Moghadamzadeh, J. A. Schwenzler, P. Brenner, R. Schmager, A. A. Haghighirad, et al., *Adv. Energy Mater.* **2019**, 9, 1–10.
- [86] V. D’Innocenzo, G. Grancini, M. J. P. Alcocer, A. R. S. Kandada, S. D. Stranks, M. M.

- Lee, G. Lanzani, H. J. Snaith, A. Petrozza, *Nat. Commun.* **2014**, *5*, 1–6.
- [87] S. Bai, P. Da, C. Li, Z. Wang, Z. Yuan, F. Fu, M. Kawecki, X. Liu, N. Sakai, J. T. W. Wang, et al., *Nature* **2019**, *571*, 245–250.
- [88] H. Min, M. Kim, S.-U. Lee, H. Kim, G. Kim, K. Choi, J. H. Lee, S. Il Seok, *Science (80-)*. **2020**, *370*, 749–753.
- [89] J. Burschka, N. Pellet, S. J. Moon, R. Humphry-Baker, P. Gao, M. K. Nazeeruddin, M. Grätzel, *Nature* **2013**, *499*, 316–319.
- [90] S. Chen, X. Xiao, B. Chen, L. L. Kelly, J. Zhao, Y. Lin, M. F. Toney, J. Huang, *Sci. Adv.* **2021**, *7*, 26–29.
- [91] Y. Li, *Sci. China Chem.* **2015**, *58*, 830.
- [92] Z. Guo, A. K. Jena, G. M. Kim, T. Miyasaka, *Energy Environ. Sci.* **2022**, *15*, 3171–3222.
- [93] Q. Chen, N. De Marco, Y. Yang, T. Bin Song, C. C. Chen, H. Zhao, Z. Hong, H. Zhou, Y. Yang, *Nano Today* **2015**, *10*, 355–396.
- [94] M. T. K. A, T. K, S. Y, *J. Am. Chem. Soc.* **2009**, *131*, 6050–1.
- [95] J. H. Im, C. R. Lee, J. W. Lee, S. W. Park, N. G. Park, *Nanoscale* **2011**, *3*, 4088–4093.
- [96] I. Chung, B. Lee, J. He, R. P. H. Chang, M. G. Kanatzidis, *Nature* **2012**, *485*, 486–489.
- [97] N. G. Park, M. Grätzel, T. Miyasaka, K. Zhu, K. Emery, *Nat. Energy* **2016**, *1*, DOI 10.1038/nenergy.2016.152.
- [98] A. S. Lin, P. Parashar, C. C. Yang, W. M. Huang, Y. W. Huang, D. R. Jian, M. H. Kao, S. W. Chen, C. H. Shen, J. M. Shieh, et al., *IEEE Photonics J.* **2017**, *9*, DOI 10.1109/JPHOT.2017.2750487.
- [99] W. Travis, E. N. K. Glover, H. Bronstein, D. O. Scanlon, R. G. Palgrave, *Chem. Sci.* **2016**, *7*, 4548–4556.
- [100] K. Wu, A. Bera, C. Ma, Y. Du, Y. Yang, L. Li, T. Wu, *Phys. Chem. Chem. Phys.* **2014**, *16*, 22476–22481.
- [101] Robert. J. Cava, “Perovskite Structure and Derivatives,” **2017**.
- [102] C. C. Stoumpos, D. H. Cao, D. J. Clark, J. Young, J. M. Rondinelli, J. I. Jang, J. T. Hupp, M. G. Kanatzidis, *Chem. Mater.* **2016**, *28*, 2852–2867.
- [103] L. Mao, W. Ke, L. Pedesseau, Y. Wu, C. Katan, J. Even, M. R. Wasielewski, C. C. Stoumpos, M. G. Kanatzidis, *J. Am. Chem. Soc.* **2018**, *140*, 3775–3783.
- [104] Y. Chen, Y. Sun, J. Peng, J. Tang, K. Zheng, Z. Liang, *Adv. Mater.* **2018**, *30*, 1–15.
- [105] D. A. R. Barkhouse, O. Gunawan, T. Gokmen, T. K. Todorov, D. B. Mitzi, *Prog. Photovoltaics Res. Appl.* **2015**, *20*, 6–11.
- [106] M. Kot, K. Wojciechowski, H. Snaith, D. Schmeißer, *Chem. - A Eur. J.* **2018**, *24*, 3539–3544.

- [107] W. Tress, *Adv. Energy Mater.* **2017**, 7, DOI 10.1002/aenm.201602358.
- [108] F. Paquin, J. Rivnay, A. Salleo, N. Stingelin, C. Silva, *J. Mater. Chem. C* **2015**, 3, 10715–10722.
- [109] S. A. Kulkarni, T. Baikie, P. P. Boix, N. Yantara, N. Mathews, S. Mhaisalkar, *J. Mater. Chem. A* **2014**, 2, 9221–9225.
- [110] G. E. Eperon, S. D. Stranks, C. Menelaou, M. B. Johnston, L. M. Herz, H. J. Snaith, *Energy Environ. Sci.* **2014**, 7, 982–988.
- [111] J. H. Noh, S. H. Im, J. H. Heo, T. N. Mandal, S. Il Seok, *Nano Lett.* **2013**, 13, 1764–1769.
- [112] C. P. Kempter, *Phys. Status Solidi* **1966**, 18, K117–K118.
- [113] D. J. Slotcavage, H. I. Karunadasa, M. D. McGehee, *ACS Energy Lett.* **2016**, 1, 1199–1205.
- [114] K. Yan, M. Long, T. Zhang, Z. Wei, H. Chen, S. Yang, J. Xu, *J. Am. Chem. Soc.* **2015**, 137, 4460–4468.
- [115] T. M. Koh, K. Fu, Y. Fang, S. Chen, T. C. Sum, N. Mathews, S. G. Mhaisalkar, P. P. Boix, T. Baikie, *J. Phys. Chem. C* **2014**, 118, 16458–16462.
- [116] J. A. Schwenzler, T. Hellmann, B. A. Nejdand, H. Hu, T. Abzieher, F. Schackmar, I. M. Hossain, P. Fassl, T. Mayer, W. Jaegermann, et al., *ACS Appl. Mater. Interfaces* **2021**, 13, 15292–15304.
- [117] L. Bertoluzzi, J. B. Patel, K. A. Bush, C. C. Boyd, R. A. Kerner, B. C. O'Regan, M. D. McGehee, E. Booker, J. B. Boutin, C. Roux, et al., *Science (80-.)*. **2021**, 11, 1–13.
- [118] M. G. Michael Saliba, Taisuke Matsui, Konrad Domanski, Ji-Youn Seo, Amita Ummadisingu, Shaik M. Zakeeruddin, Juan-Pablo Correa-Baena, Wolfgang R. Tress, Antonio Abate, Anders Hagfeldt, *Science (80-.)*. **2016**, 354, 206–210.
- [119] P. Gratia, I. Zimmermann, P. Schouwink, J. H. Yum, J. N. Audinot, K. Sivula, T. Wirtz, M. K. Nazeeruddin, *ACS Energy Lett.* **2017**, 2, 2686–2693.
- [120] M. Abdi-Jalebi, Z. Andaji-Garmaroudi, S. Cacovich, C. Stavrakas, B. Philippe, J. M. Richter, M. Alsari, E. P. Booker, E. M. Hutter, A. J. Pearson, et al., *Nature* **2018**, 555, 497–501.
- [121] J. Li, L. Zuo, H. Wu, B. Niu, S. Shan, G. Wu, H. Chen, *Adv. Funct. Mater.* **2021**, 31, 1–10.
- [122] Q. Jiang, Z. Chu, P. Wang, X. Yang, H. Liu, Y. Wang, Z. Yin, J. Wu, X. Zhang, J. You, *Adv. Mater.* **2017**, 29, 1–7.
- [123] K. Hongstith, S. Wongrerkdee, A. Ngamjarurojana, S. Choopun, *Thin Solid Films* **2019**, 684, 9–14.
- [124] Y. K. Ren, X. H. Ding, Y. H. Wu, J. Zhu, T. Hayat, A. Alsaedi, Y. F. Xu, Z. Q. Li, S. F. Yang, S. Y. Dai, *J. Mater. Chem. A* **2017**, 5, 20327–20333.

- [125] W. Li, J. Fan, J. Li, Y. Mai, L. Wang, *J. Am. Chem. Soc.* **2015**, *137*, 10399–10405.
- [126] B. Yang, O. Dyck, J. Poplawsky, J. Keum, A. Poretzky, S. Das, I. Ivanov, C. Rouleau, G. Duscher, D. Geohegan, et al., *J. Am. Chem. Soc.* **2015**, *137*, 9210–9213.
- [127] M. Yang, T. Zhang, P. Schulz, Z. Li, G. Li, D. H. Kim, N. Guo, J. J. Berry, K. Zhu, Y. Zhao, *Nat. Commun.* **2016**, *7*, 2–10.
- [128] W. Zhu, T. Yu, F. Li, C. Bao, H. Gao, Y. Yi, J. Yang, G. Fu, X. Zhou, Z. Zou, *Nanoscale* **2015**, *7*, 5427–5434.
- [129] Z. Yang, C. C. Chueh, F. Zuo, J. H. Kim, P. W. Liang, A. K. Y. Jen, *Adv. Energy Mater.* **2015**, *5*, 1–6.
- [130] J. C. Hamill, J. Schwartz, Y. L. Loo, *ACS Energy Lett.* **2018**, *3*, 92–97.
- [131] Y. Zhou, O. S. Game, S. Pang, N. P. Padture, *J. Phys. Chem. Lett.* **2015**, *6*, 4827–4839.
- [132] W. Nie, H. Tsai, R. Asadpour, A. J. Neukirch, G. Gupta, J. J. Crochet, M. Chhowalla, S. Treiak, M. A. Alam, H. Wang, **2015**, *347*, 522–526.
- [133] C. Bi, Q. Wang, Y. Shao, Y. Yuan, Z. Xiao, J. Huang, *Nat. Commun.* **2015**, *6*, 1–7.
- [134] L. Chao, T. Niu, W. Gao, C. Ran, L. Song, Y. Chen, W. Huang, *Adv. Mater.* **2021**, *33*, 1–23.
- [135] T. Ahmad, B. Wilk, E. Radicchi, R. Fuentes Pineda, P. Spinelli, J. Herterich, L. A. Castriotta, S. Dasgupta, E. Mosconi, F. De Angelis, et al., *Adv. Funct. Mater.* **2020**, *30*, 1–11.
- [136] M. Yang, Y. Zhou, Y. Zeng, C. S. Jiang, N. P. Padture, K. Zhu, *Adv. Mater.* **2015**, *27*, 6363–6370.
- [137] B. Ding, L. Gao, L. Liang, Q. Chu, X. Song, Y. Li, G. Yang, B. Fan, M. Wang, C. Li, et al., *ACS Appl. Mater. Interfaces* **2016**, *8*, 20067–20073.
- [138] T. Gotanda, S. Mori, A. Matsui, H. Oooka, *Chem. Lett.* **2016**, *45*, 822–824.
- [139] B. Ding, Y. Li, S. Y. Huang, Q. Q. Chu, C. X. Li, C. J. Li, G. J. Yang, *J. Mater. Chem. A* **2017**, *5*, 6840–6848.
- [140] D. P. McMeekin, Z. Wang, W. Rehman, F. Pulvirenti, J. B. Patel, N. K. Noel, M. B. Johnston, S. R. Marder, L. M. Herz, H. J. Snaith, *Adv. Mater.* **2017**, *29*, 1607039.
- [141] J. W. Mullin, *Crystallization*, Elsevier B.V. And Science Press, United States of America, **2009**.
- [142] J. Liu, N. Li, J. Jia, J. Dong, Z. Qiu, S. Iqbal, B. Cao, *Sol. Energy* **2019**, *181*, 285–292.
- [143] L. Yang, Y. Gao, Y. Wu, X. Xue, F. Wang, Y. Sui, Y. Sun, M. Wei, X. Liu, H. Liu, *ACS Appl. Mater. Interfaces* **2019**, *11*, 792–801.
- [144] M. Xiao, L. Zhao, M. Geng, Y. Li, B. Dong, Z. Xu, L. Wan, W. Li, S. Wang, *Nanoscale* **2018**, *10*, 12141–12148.

- [145] J. G. Manion, A. H. Proppe, G. E. J. Hicks, E. H. Sargent, D. S. Seferos, *ACS Appl. Mater. Interfaces* **2020**, *12*, 26026–26032.
- [146] E. J. Juarez-Perez, R. S. Sanchez, L. Badia, G. Garcia-Belmonte, Y. S. Kang, I. Mora-Sero, J. Bisquert, *J. Phys. Chem. Lett.* **2014**, *5*, 2390–2394.
- [147] U. Wurfel, A. Cuevas, P. Wurfel, *IEEE J. Photovoltaics* **2015**, *5*, 461–469.
- [148] D. W. DeQuilettes, S. Jariwala, S. Burke, M. E. Ziffer, J. T. W. Wang, H. J. Snaith, D. S. Ginger, *ACS Nano* **2017**, *11*, 11488–11496.
- [149] I. L. Braly, D. W. Dequilettes, L. M. Pazos-Outón, S. Burke, M. E. Ziffer, D. S. Ginger, H. W. Hillhouse, *Nat. Photonics* **2018**, *12*, 355–361.
- [150] Y. Yang, M. Yang, D. . Moore, Y. Yan, E. . Miller, K. Zhu, M. . Beard, *Nat. Energy* **2017**, 1–7.
- [151] N. Giesbrecht, J. Schlipf, L. Oesinghaus, A. Binek, T. Bein, P. Müller-Buschbaum, P. Docampo, *ACS Energy Lett.* **2016**, *1*, 150–154.
- [152] N. Giesbrecht, J. Schlipf, I. Grill, P. Rieder, V. Dyakonov, T. Bein, A. Hartschuh, P. Müller-Buschbaum, P. Docampo, *J. Mater. Chem. A* **2018**, *6*, 4822–4828.
- [153] R. Ciesielski, F. Schäfer, N. F. Hartmann, N. Giesbrecht, T. Bein, P. Docampo, A. Hartschuh, *ACS Appl. Mater. Interfaces* **2018**, *10*, 7974–7981.
- [154] K. Tvingstedt, K. Vandewal, F. Zhang, O. Inganäs, *J. Phys. Chem. C* **2010**, *114*, 21824–21832.
- [155] V. W. Bergmann, Y. Guo, H. Tanaka, I. M. Hermes, D. Li, A. Klasen, S. A. Bretschneider, E. Nakamura, R. Berger, S. A. L. Weber, *ACS Appl. Mater. Interfaces* **2016**, *8*, 19402–19409.
- [156] E. A. Duijnste, J. M. Ball, V. M. Le Corre, L. J. A. Koster, H. J. Snaith, J. Lim, *ACS Energy Lett.* **2020**, 376–384.
- [157] W. Tress, *J. Phys. Chem. Lett.* **2017**, *8*, 3106–3114.
- [158] J. Haruyama, K. Sodeyama, L. Han, Y. Tateyama, *J. Am. Chem. Soc.* **2015**, *137*, 10048–10051.
- [159] E. L. Unger, E. T. Hoke, C. D. Bailie, W. H. Nguyen, A. R. Bowring, T. Heumüller, M. G. Christoforo, M. D. McGehee, *Energy Environ. Sci.* **2014**, *7*, 3690–3698.
- [160] M. V. Khenkin, K. M. Anoop, E. A. Katz, I. Visoly-Fisher, *Energy Environ. Sci.* **2019**, *12*, 550–558.
- [161] C. Y. Chang, C. Y. Chu, Y. C. Huang, C. W. Huang, S. Y. Chang, C. A. Chen, C. Y. Chao, W. F. Su, *ACS Appl. Mater. Interfaces* **2015**, *7*, 4955–4961.
- [162] X. Gong, M. Li, X. B. Shi, H. Ma, Z. K. Wang, L. S. Liao, *Adv. Funct. Mater.* **2015**, *25*, 6671–6678.
- [163] C. C. Chen, S. H. Bae, W. H. Chang, Z. Hong, G. Li, Q. Chen, H. Zhou, Y. Yang, *Mater.*

- Horizons* **2015**, 2, 203–211.
- [164] J. Xu, A. Buin, A. H. Ip, W. Li, O. Voznyy, R. Comin, M. Yuan, S. Jeon, Z. Ning, J. J. McDowell, et al., *Nat. Commun.* **2015**, 6, 1–8.
- [165] J. T. W. Wang, Z. Wang, S. Pathak, W. Zhang, D. W. Dequillettes, F. Wisnivesky-Rocca-Rivarola, J. Huang, P. K. Nayak, J. B. Patel, H. A. Mohd Yusof, et al., *Energy Environ. Sci.* **2016**, 9, 2892–2901.
- [166] P. K. Nayak, D. T. Moore, B. Wenger, S. Nayak, A. A. Haghghirad, A. Fineberg, N. K. Noel, O. G. Reid, G. Rumbles, P. Kukura, et al., *Nat. Commun.* **2016**, 7, 1–8.
- [167] J.W . Mullin, *Cyrstallization*, Elsevier, 2001, U.S.A, **2001**.
- [168] W. H. Newhouse, A. F. Hagner, G. W. DeVore, *Science (80-.)*. **1949**, 109, 168.
- [169] N. T. K. Thanh, N. Maclean, S. Mahiddine, *Chem. Rev.* **2014**, 114, 7610–7630.
- [170] S. Christiansen, M. Albrecht, H. P. Strunk, D. P. McMeekin, Z. Wang, W. Rehman, F. Pulvirenti, J. B. Patel, N. K. Noel, M. B. Johnston, et al., *Adv. Mater.* **2017**, 29, 1607039.
- [171] I. Levchuk, Y. Hou, M. Gruber, M. Brandl, P. Herre, X. Tang, F. Hoegl, M. Batentschuk, A. Osvet, R. Hock, et al., *Adv. Mater. Interfaces* **2016**, 3, 1600593.
- [172] Z. Xiao, D. Wang, Q. Dong, Q. Wang, W. Wei, J. Dai, X. C. Zeng, J. Huang, *Energy Environ. Sci.* **2016**, 9, 867–872.
- [173] A. Manuscript, **2014**, DOI 10.1039/C4TA04725G.
- [174] M. Pegu, S. Kazim, T. Bu, D. M. Bassani, S. Ahmad, **2021**, DOI 10.1021/acsami.1c13166.
- [175] I. Noda, **1990**, 44.
- [176] C. O. S. Analysis, **2009**, 10582–10590.
- [177] H. J. Kim, S. Bin Kim, J. K. Kim, K. A. Lavery, T. P. Russell, **2006**, 408–412.
- [178] H. J. Kim, S. Bin Kim, J. K. Kim, **2006**, 23123–23129.
- [179] L. Ma, Z. Ahmed, S. A. Asher, **2011**, 4251–4258.
- [180] S. Radice, M. Tommasini, C. Castiglioni, *J. Mol. Struct.* **2010**, 974, 73–79.
- [181] H. Hoshina, S. Ishii, Y. Morisawa, H. Sato, I. Noda, **2012**, 011907, 17–20.
- [182] L. Guo, N. Spegazzini, H. Sato, T. Hashimoto, H. Masunaga, S. Sasaki, M. Takata, Y. Ozaki, **2011**.
- [183] X. Zhong, Y. Liu, X. Tang, Q. Wu, **2012**, DOI 10.1007/s00396-012-2688-9.
- [184] S. Hong, Y. M. Jung, S. Bin Kim, S. Park, **2005**, 3844–3850.
- [185] X. Li, Q. Shen, D. Zhang, X. Mei, W. Ran, Y. Xu, G. Yu, **2013**, 8, DOI 10.1371/journal.pone.0065949.

- [186] T. Oh, J. Nam, Y. Mee, **2009**, *51*, 15–21.
- [187] M. Zhang, Y. Dang, T. Liu, H. Li, Y. Wu, Q. Li, K. Wang, B. Zou, **2013**.
- [188] J. Hur, K. Jung, Y. Mee, *Water Res.* **2011**, *45*, 2965–2974.
- [189] Y. Jiang, S. Liu, S. Priya, *Nano Lett.* **2019**, *19*, 3313–3320.
- [190] F. Würthner, C. R. Saha-Möller, B. Fimmel, S. Ogi, P. Leowanawat, D. Schmidt, *Chem. Rev.* **2016**, *116*, 962–1052.
- [191] P. Cheng, X. Zhao, X. Zhan, *Accounts Mater. Res.* **2022**, *3*, 309–318.
- [192] Z. Chen, U. Baumeister, C. Tschierske, F. Würthner, *Chem. - A Eur. J.* **2007**, *13*, 450–465.
- [193] F. Würthner, V. Stepanenko, Z. Chen, C. R. Saha-Möller, N. Kocher, D. Stalke, *J. Org. Chem.* **2004**, *69*, 7933–7939.
- [194] H. Langhals, *Cyclic Carboxylic Imide Structures as Structure Elements of High Stability. Novel Developments in Perylene Dye Chemistry*, Elsevier B.V. And Science Press, **1995**.
- [195] C. Huang, S. Barlow, S. R. Marder, *J. Org. Chem.* **2011**, *76*, 2386–2407.
- [196] B. M. Weckhuysen, R. Ramachandra Rao, J. Pelgrims, R. A. Schoonheydt, P. Bodart, G. Debras, O. Collart, P. Van Der Voort, E. F. Vansant, *Chem. - A Eur. J.* **2000**, *6*, 2960–2970.
- [197] H. Langhals, *Helv. Chim. Acta* **2005**, *88*, 1309–1343.
- [198] Y. Chen, C. Xu, B. Xu, Z. Mao, J. Li, Z. Yang, N. R. Peethani, C. Liu, G. Shi, F. L. Gu, et al., **2019**, DOI 10.1039/c9qm00312f.
- [199] **2019**, *9*, 2019.
- [200] A. Manuscript, **2020**, DOI 10.1039/C9TA12597C.
- [201] X. Zhang, G. Wu, W. Fu, M. Qin, W. Yang, J. Yan, Z. Zhang, X. Lu, H. Chen, **2018**, *1702498*, 1–9.
- [202] Y. Jang, S. Lee, K. M. Yeom, K. Jeong, K. Choi, M. Choi, J. H. Noh, *Nat. Energy* **2021**, *6*, DOI 10.1038/s41560-020-00749-7.
- [203] I. García-benito, C. Quarti, V. I. E. Queloz, Y. J. Hofstetter, D. Becker-koch, P. Caprioglio, D. Neher, S. Orlandi, M. Cavazzini, G. Pozzi, et al., **2020**, *7*, 1–11.
- [204] Q. Zhou, L. Liang, J. Hu, B. Cao, L. Yang, T. Wu, X. Li, **2019**, *1802595*, 1–11.
- [205] S. Sadhu, K. Aqueche, T. Buffeteau, J. M. Vincent, L. Hirsch, D. M. Bassani, *Mater. Horizons* **2019**, *6*, 192–197.
- [206] T. Leijtens, K. Bush, R. Cheacharoen, R. Beal, A. Bowring, M. D. McGehee, *J. Mater. Chem. A* **2017**, *5*, 11483–11500.
- [207] J. Yang, B. D. Siempelkamp, D. Liu, T. L. Kelly, *ACS Nano* **2015**, *9*, 1955–1963.

- [208] B. Conings, J. Drijkoningen, N. Gauquelin, A. Babayigit, J. D’Haen, L. D’Olieslaeger, A. Ethirajan, J. Verbeeck, J. Manca, E. Mosconi, et al., *Adv. Energy Mater.* **2015**, *5*, 1–8.
- [209] N. Rolston, B. L. Watson, C. D. Bailie, D. Michael, J. Bastos, R. Gehlhaar, J. Kim, D. Vak, A. Tej, G. Gupta, et al., *Extrem. Mech. Lett.* **2016**, DOI 10.1016/j.eml.2016.06.006.
- [210] R. Cheacharoen, N. Rolston, D. Harwood, *Energy Environ. Sci.* **2017**, DOI 10.1039/C7EE02564E.
- [211] K. O. Brinkmann, J. Zhao, N. Pourdavoud, T. Becker, T. Hu, S. Olthof, K. Meerholz, L. Hoffmann, T. Gahlmann, R. Heiderhoff, et al., **2017**, 1–9.
- [212] F. Bella, G. Griffini, G. Saracco, M. Grätzel, A. Hagfeldt, S. Turri, C. Gerbaldi, **2016**, 354.
- [213] B. Park, N. Kedem, M. Kulbak, D. Y. Lee, W. S. Yang, N. J. Jeon, J. Seo, G. Kim, K. J. Kim, T. J. Shin, et al., *Nat. Commun.* **2018**, 1–8.
- [214] I. E. Commission, *Terrestrial Photovoltaic (PV) Modules - Design Qualification and Type Approval - Part 1-1: Special Requirements for Testing of Crystalline Silicon Photovoltaic (PV) Modules*, IEC 61215-1-1:2021 RLV, **2021**.
- [215] C. H. Nh, S. R. Raga, L. K. Ono, P. Y. Qi, S. Yabing, **2016**, DOI 10.1039/c6ee02016j.
- [216] M. V. Khenkin, E. A. Katz, A. Abate, G. Bardizza, J. J. Berry, C. Brabec, F. Brunetti, V. Bulović, Q. Burlingame, A. Di Carlo, et al., *Nat. Energy* **2020**, *5*, 35–49.
- [217] Lucintel, *Perovskite Solar Cell Market: Trends, Opportunities and Competitive Analysis [2023-2028]*, **2023**.
- [218] A. Extance, *RSC Adv.* **2019**.
- [219] B. Roose, E. M. Tennyson, G. Meheretu, A. Kassaw, S. A. Tilahun, L. Allen, S. D. Stranks, *Energy Environ. Sci.* **2022**, *15*, 3571–3582.
- [220] E. Bellini, *Enecoat, Toyota Develop Perovskite Solar Cells for Vehicle-Integrated Applications*, **2023**.
- [221] Y. Tu, J. Wu, G. Xu, X. Yang, R. Cai, Q. Gong, R. Zhu, W. Huang, *Adv. Mater.* **2021**, *33*, 1–22.
- [222] M. T. Hoang, F. Ünlü, W. Martens, J. Bell, S. Mathur, H. Wang, *Green Chem.* **2021**, *23*, 5302–5336.
- [223] M. De Bastiani, V. Larini, R. Montecucco, G. Grancini, *Energy Environ. Sci.* **2022**, *16*, 421–429.
- [224] G. Schileo, G. Grancini, *J. Mater. Chem. C* **2021**, *9*, 67–76.
- [225] M. G. Basavarajappa, S. Chakraborty, *ACS Mater. Au* **2022**, *2*, 655–664.
- [226] J. K. Ling, P. K. K. Kizhakkedath, T. M. Watson, I. Mora-Seró, L. Schmidt-Mende, T. M. Brown, R. Jose, *Sol. RRL* **2021**, *5*, 1–48.

MANUSCRIPTS AND CERTIFICATIONS

Influence of colloids and impurities on perovskite crystal growth

S. Dasgupta, K. Misztal, R. Fuentes Pineda, W. Mróz, Ł. Pawlaczyk, J. Serafinczuk, A. J. Barker, T. Ahmad, A. P. Herman, S. Sahayaraj, R. Kudrawiec, A. Petrozza, A. Dudkowiak, K. Wojciechowski - “**New Synthetic Route of Ultrapure Alkylammonium Iodides for Perovskite Thin Films of Superior Optoelectronic Properties**” - *Energy Technology* 8(10), 2020, 2000478-1-2000478-12 - DOI: 10.1002/ente.202000478

Study of decomposition of aged perovskite solar cells using NIR spectroscopy

M. Gašiorowski, **S. Dasgupta**, L. Bychto, T. Ahmad, P. Szymak, K. Wojciechowski, A. Patryn - “**Analysis of Perovskite Solar Cell Degradation over Time using NIR Spectroscopy - a Novel Approach**” - *Energies* 15(15), 2022, 5397-1-5397-11 - DOI: 10.3390/en15155397

Perylene diimide based dyes as efficient electron transport layers for perovskite solar cells

G. Soto-Perez, **S. Dasgupta**, W. Żuraw, R. Fuentes Pineda, K. Wojciechowski, L. K. Jagadamma, I. Samuel, N. Robertson - “**Solution-processable perylene diimide-based electron transport materials as non-fullerene alternatives for inverted perovskite solar cells**” - *Journal of Materials Chemistry A*, 10, 2022, 11046-11053 - DOI: 10.1039/d2ta01321e

Exploring the formation of a lower dimension perovskite structure at the solar cell interfaces for high efficiency and stability

S. Dasgupta, W. Żuraw, T. Ahmad, L. A. Castriotta, E. Radicchi, W. Mróz, M. Ścigaj, Ł. Pawlaczyk, M. Tamulewicz-Szwajkowska, M. Trzcíński, J. Serafińczuk, E. Mosconi, A. Di Carlo, F. De Angelis, A. Dudkowiak, K. Wojciechowski - **“Modification of a buried interface with bulky organic cations for highly stable flexible perovskite solar cells”** - *ACS Applied Energy Materials* 5(12), 2022, 15114-15124 - DOI: 10.1021/acsaem.2c02780

A robust encapsulation route for plastic based flexible perovskite solar cells to withstand highly accelerated aging tests

T. Ahmad †, S. Dasgupta †, S. Almosni, A. Dudkowiak, K. Wojciechowski - **“Encapsulation protocol for flexible perovskite solar cells enabling stability in accelerated aging tests”** - *Energy and Environmental Materials* 6(5), 2023, 12434-1-12434-8 - DOI: 10.1002/eem2.12434

(† Authors contributed equally)

New Synthetic Route of Ultrapure Alkylammonium Iodides for Perovskite Thin Films of Superior Optoelectronic Properties

*Shyantana Dasgupta, Kasjan Misztal, Rosinda Fuentes Pineda, Wojciech Mróz, Łukasz Pawlaczyk, Jarosław Serafińczuk, Alex J. Barker, Taimoor Ahmad, Artur P. Herman, Sylvester Sahayaraj, Robert Kudrawiec, Annamaria Petrozza, Alina Dudkowiak, and Konrad Wojciechowski**

In the past decade, metal halide perovskites grew from a mere scientific sensation to a tangible photovoltaic technology, being on the brink of commercial entrance. Certified efficiency value reported for these devices exceeded 25%. However, there still remains a large scope for further advancement, particularly in better understanding of the formation process of polycrystalline thin films of these materials. Insight into the interplay between colloidal precursor solution and nucleation of perovskite crystallites is highly desirable to obtain well-controlled crystallization process, essential for reproducible manufacturing at large scale. Herein, a novel synthetic route of methylammonium iodide ($\text{CH}_3\text{NH}_3\text{I}$, MAI) is reported, which produces ultrapure material with a cheap and simple method. MAI prepared this way obtains better control over the perovskite precursor colloidal solution. Furthermore, MAPbI_3 perovskite layers processed from solutions are formulated with different MAI powders, and these films are applied into a simple planar heterojunction solar cell stack. Through photovoltaic performance characterization and multiple spectroscopic measurements, superior optoelectronic properties of samples made with an optimized solution are demonstrated. The influence of a precursor solution and its colloidal distribution on the final film properties is reported. The reported synthetic protocol is also applicable to other alkylammonium iodides.

1. Introduction

Metal halide perovskites emerged over the past decade as a promising class of materials for solar energy conversion. Photovoltaic devices based on these semiconducting thin films demonstrated rapid improvement in reported power conversion efficiencies (PCEs), evolving from just 3.8% in 2009 to 25.4% in 2019, with the first solid-state solar cell based on MAPbI_3 perovskite reported in 2012.^[1–4] The efficiencies of laboratory-scale devices exceeded the record values of commercial second-generation photovoltaics (PV) technologies as perovskite PV is rapidly moving toward the commercialization phase. Such progress was obtained thanks to remarkably favorable optoelectronic characteristics of perovskite thin films which was fueled by the explosion of scientific interest and huge worldwide research efforts.^[5,6] The key aspect of perovskite solar cell operation is the quality of photoactive layer, hence the control and understanding of the crystallization process is of paramount importance.

S. Dasgupta, Dr. K. Misztal, Dr. S. Sahayaraj, Dr. K. Wojciechowski
Saule Research Institute
Dunska 11, Wrocław 54-427, Poland
E-mail: konrad.wojciechowski@sauletech.com

S. Dasgupta, Prof. A. Dudkowiak
Faculty of Materials Engineering and Technical Physics
Poznan University of Technology
Piotrowo 3, Poznan 60-965, Poland

Dr. K. Misztal, Dr. R. Fuentes Pineda, T. Ahmad, Dr. K. Wojciechowski
Saule Technologies
Dunska 11, Wrocław 54-427, Poland

 The ORCID identification number(s) for the author(s) of this article can be found under <https://doi.org/10.1002/ente.202000478>.

DOI: 10.1002/ente.202000478

Dr. W. Mróz, Dr. A. J. Barker, Prof. A. Petrozza
Centre for Nano Science and Technology (CNST@PoliMi)
Istituto Italiano di Tecnologia (IIT)
Via Pascoli, 70/3, Milano 20133, Italy

Ł. Pawlaczyk, Dr. J. Serafińczuk
Department of Nanometrology
Wrocław University of Science and Technology
Janiszewskiego 11/17, Wrocław 50-372, Poland

Dr. J. Serafińczuk
Łukasiewicz Research Network – PORT Polish Center for Technology
Development
Stabłowicka 147, Wrocław 54-066, Poland

Dr. A. P. Herman, Prof. R. Kudrawiec
Department of Semiconductor Materials Engineering
Wrocław University of Science and Technology
Wyb. Wyspiańskiego 27, Wrocław 50-370, Poland

High crystallinity, high absorptivity, and low defect density allowing exceptional charge carrier transport properties (very long carrier diffusion lengths) can be obtained at low temperatures (low crystallization activation energy barrier) with facile solution-based processing.^[7,8] However, these characteristics are highly sensitive to the processing conditions and formulation chemistry. Significant research efforts have been devoted to perovskite film formation to enable uniform and dense surface morphology, large grain size, perovskite crystal-phase purity and crystallinity, which are important for reproducible photovoltaic performance and long-term device stability.^[5,9]

Precursor solution chemistry and its complex coordination interactions have a strong influence on nucleation and crystallization processes of perovskite layer, and in turn film morphology, its optoelectronic properties and device performance.^[10] In depth understanding of these fundamental complexities remains not fully resolved. Yan et al. were the first to report that most of the perovskite precursor solutions are colloidal dispersions in the mother solutions.^[11] It was revealed that these colloids are made of an iodo-plumbate coordination network formed between organic and inorganic components. The coordination degree can be adjusted by the ratio of particular components present in the solution. The size and concentration of the colloids can impact the crystal quality and morphology of the perovskite thin film. McMeekin et al. showed the influence of these lead polyhalide networks present in the solution on the crystal nucleation and growth kinetics of the perovskite layer.^[12] It was suggested that these colloids can offer preferential sites for heterogeneous nucleation which in turn affects the rate of crystallization and final film properties.

It was also reported that the chemical purity of perovskite precursor components can affect the morphology of the perovskite polycrystalline layer.^[10] The purity aspect is particularly relevant for the methylammonium iodide (or other alkylammonium iodides), where hydroiodic acid (HI) is typically used for the synthesis of these materials. HI contains 1.5–2% of a stabilizer, hypophosphorous acid (H_3PO_2 , HPA), which was shown to produce side products during the alkylammonium iodide formation. Xiao et al. hypothesized the formation of methyl ammonium hypophosphorous acid (MAH_2PO_2) as a byproduct of the reaction between methylamine (MA, CH_3NH_2) and H_3PO_2 during the MAI synthesis.^[13] This in turn could lead to the formation of insoluble $\text{Pb}(\text{H}_2\text{PO}_2)_2$ nanoparticles during the perovskite precursor solution preparation. It was suggested that these nanoparticles could act as nucleation centers during perovskite thin-film crystallization and support large domain formation. Another report identified methylammonium hypophosphite (MAH_2PO_2) and methylammonium phosphite (MAH_2PO_3) as impurities formed by HPA reaction with methylamine during MAI synthesis.^[14] It was postulated that these salts act as an effective anion source for PbHPO_3 nanoparticles formation, which in turn serve as nucleation centers for perovskite crystal domain growth. The chemistry triggered by H_3PO_2 can be extendable to other alkylammonium iodides where hydroiodic acid with stabilizer is used for their synthesis. Similarly, other additives and impurities (acids, amines, organic halides, and water additive) can affect the colloidal chemistry occurring in the perovskite precursor solution, which in turn would have an impact on the nucleation process and perovskite thin-film morphology.^[10,15,16] As an alternative to one-step,

solution-based processing, multiple variations of a two-step fabrication route of metal halide perovskite films were reported.^[17,18] Particularly, gas-induced growth method, where lead iodide films are exposed to alkylamine vapor, constitutes a deposition strategy which eliminates the problem of poorly controlled purity of alkylammonium salts.^[19,20] The entire fabrication process is much more complex, though, and therefore more challenging for scaling-up.

Herein, we present a novel synthetic route for the fabrication of methylammonium iodide, based on in situ reduction of iodine. Avoidance of the use of hydroiodic acid as a reagent allows us to produce very pure alkylammonium iodide, free of phosphorous-based impurities. We demonstrate that MAI synthesized with this method allows us to get better control of the perovskite precursor ink formulation, and in turn deposition of polycrystalline thin films of higher optoelectronic quality. Precise addition of the controlled amount of hypophosphite salts adjusts the coordination chemistry in the solution and improves the crystallization process. We demonstrate applicability of this route for the archetypical metal halide perovskite material, methylammonium lead triiodide, derived from the lead acetate route. Using a range of spectroscopic and electrical characterization methods we demonstrate superior optoelectronic properties of the perovskite layer fabricated from the newly developed formulation. In addition, we carry out X-ray diffraction analysis, which evidences superior crystallinity, smaller microstrain, and more preferred orientation of the perovskite grains in this layer. The reported strategy can be applied wider into other alkylammonium iodides, which also involve the use of stabilized hydroiodic acid.

2. Results and Discussion

We developed and optimized a novel synthetic route for the production of methylammonium iodide. In a conventional route, methylamine is mixed with hydroiodic acid at 0° , followed by an evaporation step to recover the product.^[21] The obtained white powder is typically washed with diethyl ether and recrystallized from ethanol. The commercial hydroiodic acid is often stabilized with HPA, forming phosphorous acid (H_3PO_3) upon longer storage. This leads to the formation of hypophosphites and phosphite impurities after their reaction with methylamine.^[13] These impurities can remain in the final product in uncontrolled amounts, even after the recrystallization process.^[14]

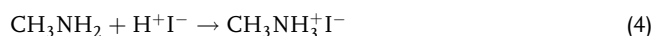
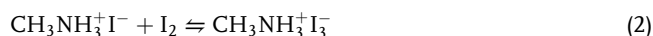
To avoid the use of hydroiodic acid and accompanying HPA stabilizer, we applied molecular iodine as a halide source, which is subsequently reduced in situ by controlled addition of a selected compound. We tested different reducing agents, among them formic acid and hydrazine, which were the most promising reagents in the screening test. However, under the reaction conditions, the formation of ammonium iodide was inevitable, and due to its similarity to methylammonium iodide, it was impossible to separate these two materials. The best results were obtained with formic acid, although we had to watch for the formation of methylammonium formate. Prolonged reaction times and adjusted stoichiometry of the reagents allowed us to avoid occurrence of this formate, but the major product had to be purified from the iodine (formic acid was added in substoichiometric

amount). Overall, with the optimized amount and application conditions of the formic acid reducing agent, we were able to form in situ an appropriate concentration of hydroiodic acid, which subsequently reacted with the methylamine to form methylammonium iodide. The synthesis of ammonium iodide from in situ-generated HI is described based on the literature reports.^[22] Therefore, we propose the following reactions to occur during the process:

Complete reaction:



Partial reactions:



We carried out elemental analysis of the methyl ammonium iodide synthesized by the described method and compared it with materials made in a conventional way (different number of recrystallization steps), and also MAI powder obtained from a commercial supplier. We show the results of these studies, done by inductively coupled plasma mass spectrometry (ICP-MS), in **Table 1**.

The MAI synthesized with the conventional route involving stabilized HI, displays significant amounts of phosphorus-based impurities, even after recrystallization. Furthermore, obtained results vary from batch to batch. We recorded phosphorus content ranging between 0.022% and 0.095% after two rounds of recrystallization. In another synthetic batch, we obtained 0.041% of phosphorous after three consecutive rounds of recrystallization. The largest amount of impurities was found in the commercial MAI, which was made with an undisclosed protocol. The MAI synthesized according to the procedure described earlier, which does not involve HI reagent, did not show any phosphorus

Table 1. Phosphorus content in different MAI powders determined using ICP-MS, along with the estimated cost of each MAI type.

Sample	wt% of P	Estimated cost per 1 kg of material
MAI with HI (1× recrystallized), "old MAI 1 × RC"	0.281	670 €
MAI with HI (2× recrystallized), "old MAI 2 × RC," sample 1	0.022	730 €
MAI with HI (2× recrystallized), "old MAI 2 × RC," sample 2	0.040	730 €
MAI with HI (2× recrystallized), "old MAI 2 × RC," sample 3	0.095	730 €
MAI with HI (3× recrystallized), "old MAI 3 × RC"	0.041	790 €
MAI without HI, "new MAI"	Below detection limit	490 €
Commercial MAI (supplier 1), "comm. MAI"	0.688	2300 € (purchase price)
Commercial MAI (supplier 2), "comm. MAI 2"	0.486	2500 € (purchase price)

in the elemental analysis. Different MAI powders were also examined with ¹H NMR analysis. The spectra are shown in Figure S1, Supporting Information. We identified the presence of phosphinic salts (peak in the region 6.60–6.65 ppm) for the commercial and old synthetic route MAIs. There is no evidence of signals originating from the phosphorus-based impurities in the MAI made according to the new methodology. In Table 1, we also provide an estimated cost of the production (or acquisition cost) of 1 kg of each MAI type. The new method is significantly more cost effective than the conventional route, mainly due to elemental iodine being much cheaper than stabilized hydroiodic acid. Furthermore, in the old method, multiple recrystallization steps are needed to lower the content of phosphorous-based impurities, which sizably increases the overall cost.

To demonstrate the wider applicability of the described synthetic route, we also applied it for making two other alkylammonium iodides. We synthesized formamidinium iodide (FAI), and *n*-octylammonium iodide (OAI), proving the universality of this method. We show ¹H NMR spectra of OAI and FAI in Figure S1, Supporting Information.

To see the effect of MAI purity and accompanying hypophosphite salts on the coordination chemistry in the solution, we prepared a simple methylammonium lead iodide perovskite precursor formulations in dimethylformamide (DMF). We formulated the solutions based on a sacrificial anion recipe, using lead acetate as a primary lead source and an excess of organic halide (MAI). This recipe, resulting in a very smooth MAPbI₃ perovskite layer was first reported by Zhang et al.^[23] In the follow-up work, they reported the enhancement of optoelectronic properties of perovskite layers processed from the same precursor composition, further optimized with the addition of hypophosphorus acid.^[24]

We prepared four solutions, each containing different type of MAI (the powders studied with the ICP-MS), and analyzed resulting colloidal solutions using dynamic light scattering (DLS) technique. The graphs shown in **Figure 1** are obtained in intensity mode. The precursor solution containing the MAI powder synthesized with the new method displayed the smallest average particle size. Conversely, the commercial MAI, which was found to have the largest phosphorus content from the elemental analysis, showed the highest volume of large colloids in the solution. We also noted that increasing the number of recrystallization rounds

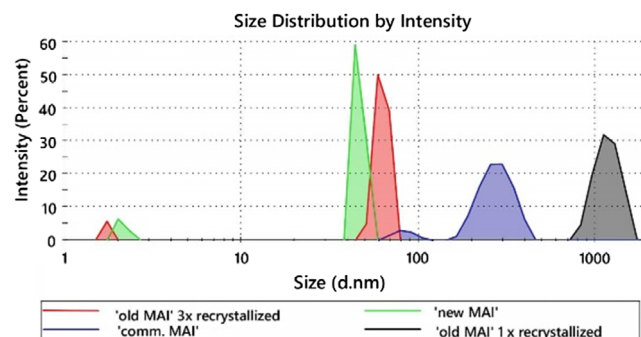


Figure 1. DLS graphs showing a distribution of particles in perovskite precursor solutions formulated with different MAI materials. The plot displays size distributions obtained with a volumetric analysis.

for the conventionally synthesized MAI (from one to three) lead to the significant reduction of large species in the solution.

We corroborated DLS results by analyzing the Tyndall effect in the same perovskite precursor solutions. When the light path coming from a laser pointer is visibly propagating in the solution, it indicates a significant photon scattering caused by the presence of large particles in the solution. The solution made with three-time recrystallized conventional MAI displays weak light propagation, similar to the solution containing MAI powder synthesized with the new method. Oppositely, the solutions formulated with the commercial MAI and standard MAI with a single recrystallization step show large scattering, indicating the presence of bigger colloids. The image of studied solutions and the observed Tyndall effect is shown in Figure S2, Supporting Information. We can link the amount of phosphorus-based impurities in the MAI powder to the size of colloidal species present in the perovskite precursor solution, which is consistent with the observations made by Levchuk et al.^[14] It was proposed in multiple reports that colloids present in the perovskite precursor solutions are based on lead polyhalide coordination networks.^[15,25] These species can substantially affect the nucleation and crystallization rates of perovskite layer. McMeekin et al. proposed that they could act as heterogeneous nucleation centers.^[12] Certain concentration and size of these species could be beneficial for perovskite formation dynamics. It is likely that the beneficial effect of these colloids depends on their character and can be specific for a given perovskite formation process.

It was also reported that phosphorus-based impurities identified in MAI powder might exist in the form of methylammonium hypophosphite salts.^[13,14] As shown earlier, these impurities affect the colloidal nature of the precursor solution. In the next step, we investigated the effect of hypophosphite salt on the perovskite layer formation and its properties by fabricating simple planar heterojunction perovskite solar cells using precursor solutions with different amount of impurities.

We formulated the solutions following a modified lead acetate recipe, and used the new MAI powder (free of phosphorus-based compounds) with varied amount of methylammonium hypophosphite (MAH_2PO_2) salt added separately to the precursor solution (concentration range of MAH_2PO_2 : 0–2 wt% with respect to MAI). We used a p-i-n device configuration of the following architecture: glass-indium tin oxide (ITO)/poly(3,4-ethylenedioxythiophene) polystyrene sulfonate (PEDOT:PSS)/ MAPbI_3 /[6,6]-phenyl- C_{61} -butyric acid methyl ester (PCBM)/bathocuproine (BCP)/Ag.

The morphology of perovskite layers processed from these solutions and characterized by scanning electron microscope (SEM) imaging is shown in Figure S3, Supporting Information. We can observe that with increasing amount of MAH_2PO_2 additive, the perovskite domains become bigger, but at higher contents, the layer's coverage can be affected. The sample with 0.3 wt% additive shows a regular and compact morphology, with reduced number of pinholes. We analyzed the crystallographic properties of these films with X-ray diffraction measurements. We show the diffractograms in Figure S4, Supporting Information. The intense peaks at 14.2° and 28.6° are assigned to (110) and (220) reflections of MAPbI_3 tetragonal structure ($I4/mcm$), respectively.^[26] The sample with 0.3 wt% MAH_2PO_2 displays significantly higher

intensity of the diffraction pattern. Considering the same thickness of the perovskite layer (≈ 230 nm, as derived from focused ion beam-SEM cross-sectional images, as shown in Figure S5, Supporting Information) in all the samples, and qualitatively very similar diffraction pattern (no significant differences in grain orientations), this could suggest higher crystallinity of the perovskite film in the sample with 0.3 wt% additive. The current density–voltage (JV) characteristics of the cells with different amounts of MAH_2PO_2 additive (champion devices) are shown in Figure S6a, Supporting Information. The pristine device (new MAI, no additive) yields a PCE value of 8.69%, with a short-circuit current density (J_{SC}) of 16.64 mA cm^{-2} , an open-circuit voltage (V_{OC}) of 0.89 V, and fill factor (FF) of 79.61%. Upon hypophosphite addition, the performance improves significantly, reaching the optimum level at 0.3 wt% additive (with respect to MAI). The most notable is V_{OC} increase, which reaches 0.98 V. Combined with the 18.66 mA cm^{-2} of J_{SC} and 82.13% of FF, it results in the PCE of 15.64%. In Figure S6b, Supporting Information, we are showing a steady-state maximum power output (commonly referred to as stabilized power output, SPO) of these devices, confirming the beneficial effect of the additive. The efficiency derived from the SPO measurement is very close to the value obtained from the JV characterization, which indicates that these cells did not have significant hysteretic effects. The statistics of photovoltaic performance parameters of the larger set of samples (more than 20 individual cells for each variation, four separate experimental batches) are shown in Figure S7, Supporting Information and Table 2. Larger amounts of MAH_2PO_2 additive result in a higher spread of photovoltaic parameters and lower performance. This could be a result of a deteriorated film's morphological uniformity.

The presence of phosphorus-based impurities has a significant impact on the formation process of perovskite thin films. It is also clear that it has a large impact on the photovoltaic performance of the resulting solar cells. The optimum concentration of MAH_2PO_2 additive for the photovoltaic performance was 0.3 wt%, and this amount was used for the remainder of the study.

In the next step, we compared the morphologies and crystallographic properties of MAPbI_3 perovskite films processed from precursor solutions with different MAI types (perovskite precursor recipe based on excess organic, molar ratio of MAI to $\text{Pb}(\text{OAc})_2$ and PbCl_2 equals 3:0.8:0.2), making the following variations: 1) Conventionally synthesized MAI with stabilized HI as a reagent, 3 times recrystallized, abbreviation: “old MAI”; 2) MAI synthesized with the new method, avoiding HI as a reagent, with optimized amount of MAH_2PO_2 additive (0.3 wt%) as shown earlier, abbreviation: “new MAI + add”; 3) MAI from a commercial supplier, abbreviation: “comm. MAI.” Figure 2a–c shows the top-view SEM images of the perovskite layers processed on top of glass ITO/PEDOT:PSS surface from the aforementioned solutions. We observe rather similar morphologies, with minor differences in film compactness, uniformity, and distribution of domain sizes. We point out slightly larger grains for the “new MAI + add” sample. We further characterized the films by atomic force microscopy (AFM). The images, together with the calculated root mean-squared roughness (RMS) are shown in Figure 2d–f. All the layers displayed comparable smoothness, with the “new MAI + add” sample, yielding the lowest RMS value of 10 nm.

Table 2. Photovoltaic parameters extracted from current–voltage characterizations of perovskite solar cells fabricated from precursor solutions containing different amounts of MAH₂PO₂ additive.

Sample	J_{SC} best (J_{SC} average \pm sd) [mA cm ⁻²]	V_{OC} best (V_{OC} average \pm sd) [V]	FF best (FF average \pm sd) [%]	PCE best (PCE average \pm sd) [%]	SPO best [%]
0% add.	16.64 (12.52 \pm 4.07)	0.89 (0.85 \pm 0.04)	79.61 (66.2 \pm 15.8)	8.69 (7.29 \pm 2.47)	8.69
0.1% add.	18.76 (15.49 \pm 4.54)	1.00 (0.77 \pm 0.32)	84.26 (70.13 \pm 12.22)	14.98 (8.61 \pm 4.20)	13.83
0.3% add.	18.66 (17.91 \pm 0.60)	0.98 (0.96 \pm 0.01)	82.13 (72.37 \pm 12.53)	15.64 (13.80 \pm 0.74)	14.22
0.6% add.	18.66 (15.59 \pm 4.23)	0.95 (0.77 \pm 0.32)	77.53 (59.54 \pm 13.88)	13.34 (8.86 \pm 3.59)	13.00
1% add.	18.62 (17.37 \pm 0.79)	1.00 (0.97 \pm 0.02)	81.86 (80.07 \pm 2.63)	14.39 (12.91 \pm 1.15)	14.15
2% add.	18.05 (14.14 \pm 5.02)	0.96 (0.77 \pm 0.31)	82.04 (70.37 \pm 18.13)	13.78 (10.53 \pm 3.61)	13.85

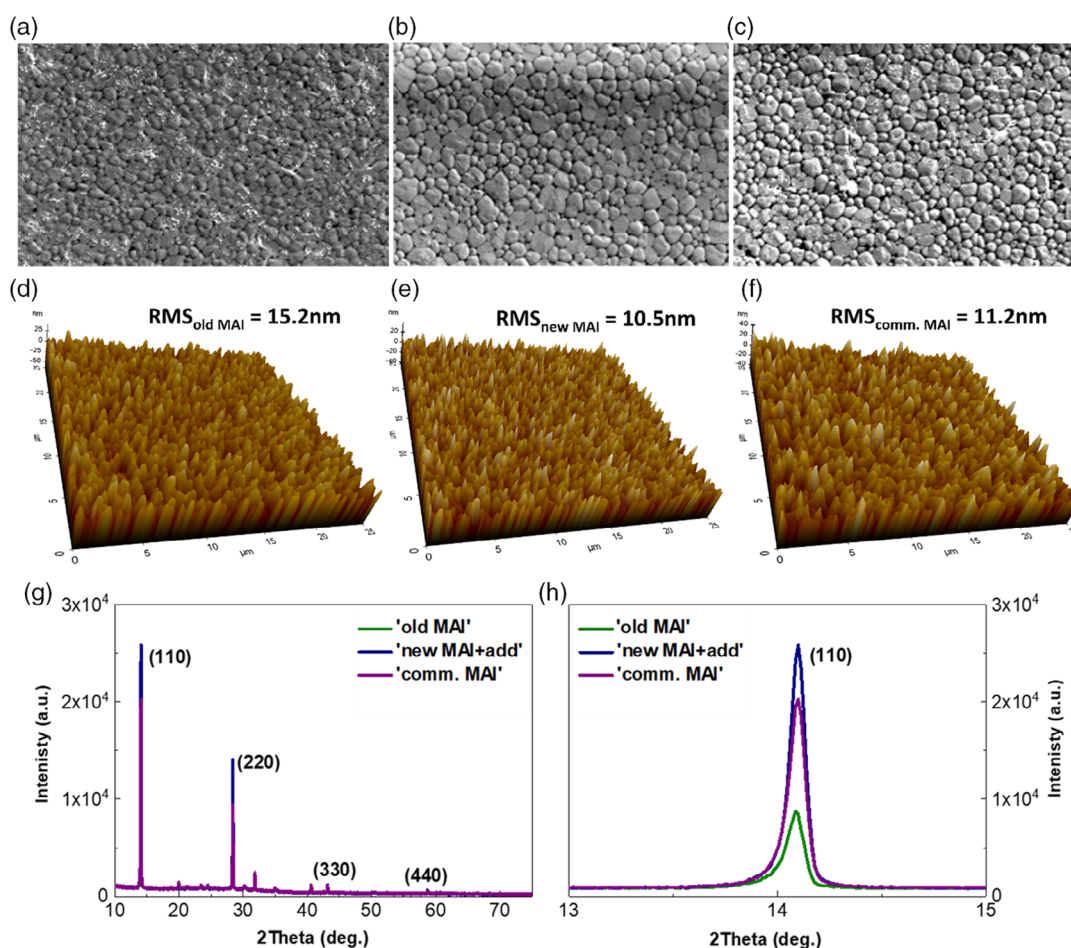


Figure 2. SEM top-view images displaying morphologies of MAPbI₃ perovskite layers, processed from different precursor solutions: a) “old MAI,” b) “new MAI + add.,” c) “comm. MAI”; AFM images of the same samples, d) “old MAI,” e) “new MAI + add.,” f) “comm. MAI”; g) X-ray diffractograms of the same films, and h) zoom-in at the (110) reflection peak of these diffractograms.

The X-ray diffractograms of these layers are shown in Figure 2d,e. All the perovskite samples, similar to the layers analyzed above, also display a typical tetragonal crystal structure (*I4/mcm*). The peaks at 14.2°, 28.6°, 43.5°, and 59.4° can be assigned to (110), (220), (330), and (440) reflections.^[26] The absence of a peak at 12.7°, which refers to the lead iodide reflection, confirms the complete perovskite transformation in all samples. We notice that the “new MAI + add” sample displays fewer additional peaks,

which could infer more oriented growth of perovskite crystallites in that layer. The intensity of the dominant (110) reflection is also the highest for the “new MAI + add” sample. Furthermore, we applied Williamson–Hall method to calculate the size of perovskite crystallites,^[12,27–29] and obtained microstrain values from this analysis.^[30] Detailed description of the method is provided in Supplementary Note 1, Supporting Information. **Table 3** shows the results obtained for each perovskite sample.

Table 3. Crystal sizes and microstrain values obtained from XRD measurements of MAPbI₃ perovskite films processed from different precursor solutions.

Sample	Crystallites size [nm]	Microstrain [%]
“old MAI”	98.3	0.87
“new MAI + add”	137.3	0.65
“comm. MAI”	113.6	0.77

We note reduced microstrain value for the “new MAI + add” sample, which is combined with the largest average crystallite size. Conversely, the “old MAI” perovskite layers display largest microstrain and smallest grain size. It was recently reported that increased microstrain in the perovskite polycrystalline films could induce larger concentration of defect sites, in turn leading to enhanced nonradiative recombination losses.^[31–33]

To translate the observed crystallographic differences between perovskite films processed with different MAIs to optoelectronic properties of these layers, we carried out a range of spectroscopic characterizations on those samples. We carried out steady-state (ss-PL) and time-resolved photoluminescence (TRPL) measurements, additionally we derived photoluminescence quantum yield (PLQY) for each photoactive layer. The samples composed of perovskite films processed on plain glass substrates were prepared with precursor solutions described earlier. We show the results in **Figure 3**.

The PL yield and lifetimes in perovskite layers at carrier densities corresponding to illumination intensities below standard 1

sun (100 mW cm²), are limited by trap sites and nonradiative processes.^[34,35] The PLQY describes the ratio of radiative recombination rate to all the decay rates, we can write it as^[36]

$$\text{PLQY} = \frac{k_{\text{rad}}}{(k_{\text{rad}} + k_{\text{nonrad}})} \quad (5)$$

where k_{rad} is radiative recombination rate and k_{nonrad} is nonradiative recombination rate.

All the studied samples displayed a commonly observed photobrightening effect for these materials, as incurred from the PLQY evolution over illumination time (Figure 3a).^[37,38] The increase in PLQY can be attributed to the trap states filling with continuous light soaking, and reduced trap-assisted nonradiative recombination rates. The highest PLQY showed the perovskite layer processed from the “new MAI + add” sample reaching over 6.6%, which compares with 1.1% and 2.3% obtained for the “old MAI” and “comm. MAI,” respectively. This implies reduced nonradiative recombination channels (bulk and surface recombination), potentially due to lower defect density in this newly developed perovskite formulation. The steady-state PL spectra show the same peak position for all perovskite films, centered at 775 nm, with “new MAI + add” sample yielding the highest intensity. TRPL measurements (laser power density: 15 mW cm^{−2}) corroborate these results, “new MAI + add” sample shows the longest lifetime, as shown in Figure 3c. The PL decays were fitted with a stretch exponential function,^[39] the stretch parameter, and obtained lifetimes are shown in Table S1, Supporting Information.

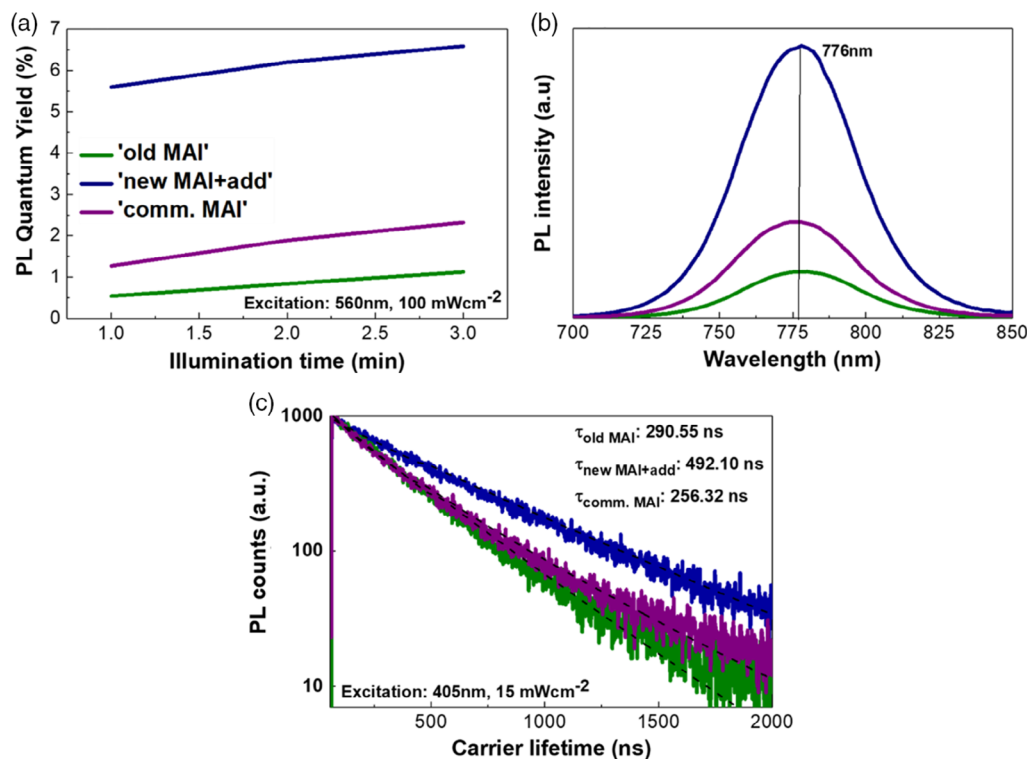


Figure 3. a) Time evolution of PLQY values of different perovskite layers, b) steady-state photoluminescence spectra of the same perovskite films, and c) TRPL decay curves of the studied samples.

Furthermore, we studied the lifetime of photoexcited free carriers in these perovskite films using time-resolved microwave conductivity (TRMC). In contrast to TRPL, TRMC probes not only the radiative recombination events, but all the annihilation processes. TRMC reveals the change in conductivity of a sample caused by photoexcitation. Free carriers were generated using a 532 nm laser (power: 36 mW cm⁻²). Detailed description of the technique can be found in literature.^[40–42] Decay curves for studied samples are shown in Figure S9, Supporting Information. Carrier lifetimes determined from the fitting (Table S1, Supporting Information) were quite similar for all the samples with slightly larger values (slower recombination) obtained for the “new MAI + add” sample. Interestingly, all the lifetimes were much shorter than the observed PL lifetimes. The TRPL and TRMC measurements were carried out with different light intensities, both being significantly smaller than 1 sun, where carrier dynamics are dominated by trapping processes, which can make direct comparison of these two techniques difficult.^[43]

Next, we applied the same set of MAPbI₃ films into solar cells and compared their photovoltaic performance. We used the p-i-n solar cell architecture, as described earlier (ITO/PEDOT:PSS/

MAPbI₃/PCBM/BCP/Ag). Figure 4a,b shows *JV* and SPO curves for the best performing solar cells with the optimized “new MAI” recipe (“new MAI + add”), “old MAI,” and “comm. MAI.” The solar cell performance parameters along with the SPO-derived efficiencies are shown in Table 4. Graphical representation of the statistics of photovoltaic parameters extracted from the dataset of 24 devices for each variation is shown in Figure S10, Supporting Information. The precursor solution applying the “new MAI” powder delivers devices surpassing the performance of cells made with the conventionally synthesized MAI. We obtained the PCE of 15.4% for the “new MAI + add,” which compares with 13.4% and 13.3% for the “old MAI” and “comm. MAI,” respectively. The improvements in *J*_{SC} and *V*_{OC} can be observed for the “new MAI + add” variation, consistent with enhanced crystallinity and reduced recombination losses in this perovskite film, as shown earlier. The steady-state maximum power outputs display moderate drop in efficiencies compared with *JV*-derived values for all studied cells, reaching 15.06% for the optimized “new MAI” recipe.

We also measured external quantum efficiency (EQE) for each cell variation. The spectra are shown in Figure 4c. Current

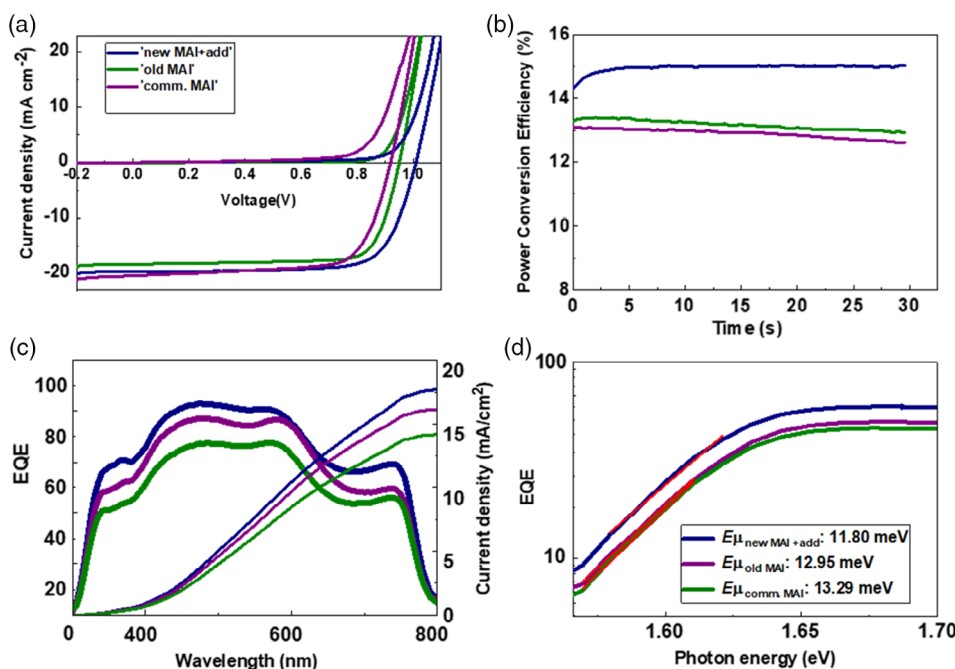


Figure 4. a) *JV* characteristics of the best perovskite solar cells processed from different precursor solutions (MAI variations), b) SPO measurements of the same devices, c) EQE spectra and integrated current density values of perovskite solar cells processed from the same precursor solution variations, d) semi-log plot of the EQE onset used for Urbach energy determination.

Table 4. Photovoltaic parameters extracted from the current–voltage characterization measurements of the perovskite solar cells fabricated with different precursor solutions.

Sample	<i>J</i> _{SC} best (<i>J</i> _{SC} average ± SD) [mA cm ⁻²]	<i>V</i> _{OC} best (<i>V</i> _{OC} average ± SD) [V]	FF best (FF average ± SD) [%]	PCE best (PCE average ± SD) [%]	SPO best [%]
“old MAI”	18.24 (17.93 ± 0.60)	0.94 (0.94 ± 0.01)	81.39 (63.94 ± 16.07)	13.44 (11.47 ± 2.47)	13.01
“new MAI + add”	19.92 (19.01 ± 1.11)	1.01 (0.97 ± 0.01)	78.92 (71.93 ± 7.62)	15.38 (14.03 ± 1.42)	15.06
“comm. MAI”	20.38 (18.55 ± 2.16)	0.91 (0.73 ± 0.34)	79.10 (69.93 ± 15.08)	13.29 (9.16 ± 5.13)	12.60

density–voltage curves corresponding to these cells are shown in Figure S11, Supporting Information. Integrated current densities are comparable with the J_{SC} values extracted from the JV curves (see Figure S11, Supporting Information), with the “old MAI,” “new MAI + add,” and “comm. MAI” displaying current densities of 14.1, 17.8, and 16.2 mA cm⁻², respectively. The highest EQE was recorded for the “new MAI + add” device. In addition, we fitted the EQE onset curves and calculated Urbach energy values (E_U) for each perovskite variation shown in Figure 4d. The Urbach energy describes the level of electronic disorder in the semiconducting material, where the lower values mean fewer absorption sub-bandgap states, thus the better optoelectronic quality of the material.^[44] We obtained 11.80 meV for the “new MAI + add” sample, which compares to 13.29 and 12.95 meV for the “old MAI” and “comm. MAI,” respectively.

To understand better the origin of losses in the studied solar cells as a function of MAI type, we carried out a range of additional characterization methods on the same samples. First, we measured electroluminescence (EL) of devices made with a varying MAI type (“old MAI,” “new MAI + add,” and “comm. MAI”). In this measurement, forward voltage bias is applied to the device terminals and emitted light is measured, so the solar cell is run in an light emitting diode mode of operation. EL can provide information about any changes to the radiative versus nonradiative recombination processes in the device. Here, the comparison of EL spectra of the three solar cell types reveals similarity of their shapes and resembles well the photoluminescence of MAPbI₃ (Figure 5a). However, registered maximal intensity of the EL emission was about three times smaller for the “old MAI” and “comm.

MAI” samples than the “new MAI + add,” a clear indication of higher quality of the perovskite film in the latter device. The transient EL intensities obtained for the applied 3 V bias are shown in Figure 5b. In agreement with the EL spectra, the registered intensity of the “old MAI” and “comm. MAI” cells are about 3 times smaller than the “new MAI + add” sample. More importantly, the behavior of the EL emission in time is different for all the three sample types, as shown in Figure 5b. The emission intensity of the “old MAI” device decreased fast during the first 8 s and stabilized afterward. In contrast, the emission in the “new MAI + add” device was more stable, with only small decrease in intensity over time. Considering the timescale of the observed changes being in the range of tens of seconds, it is reasonable to assume that the variations in EL intensity are caused by migration of some species inside the perovskite layer. The diffusion of ionic species in perovskites have been widely reported in literature.^[45–48] We note that the device samples used in this experiment were encapsulated, to protect them from moisture, the condition that was recognized as a source of fast and irreversible degradation in the presence of an electric field.^[49,50] In contrast, it has also been shown that during the decomposition of MAPbI₃, iodine ions migrate toward the anode, whereas iodine vacancies diffuse to the cathode. The accumulation of both species near the electrodes creates build-in electric field, reverse to the applied external electric field. This screening effect hampers the migration of both species inside the perovskite and suppresses decomposition of MAPbI₃, creating a negative feedback.^[49,51] Therefore, we exclude the deterioration of samples as the origin of observed EL variations in time. It should be stressed that the nature of migrating species is not easy

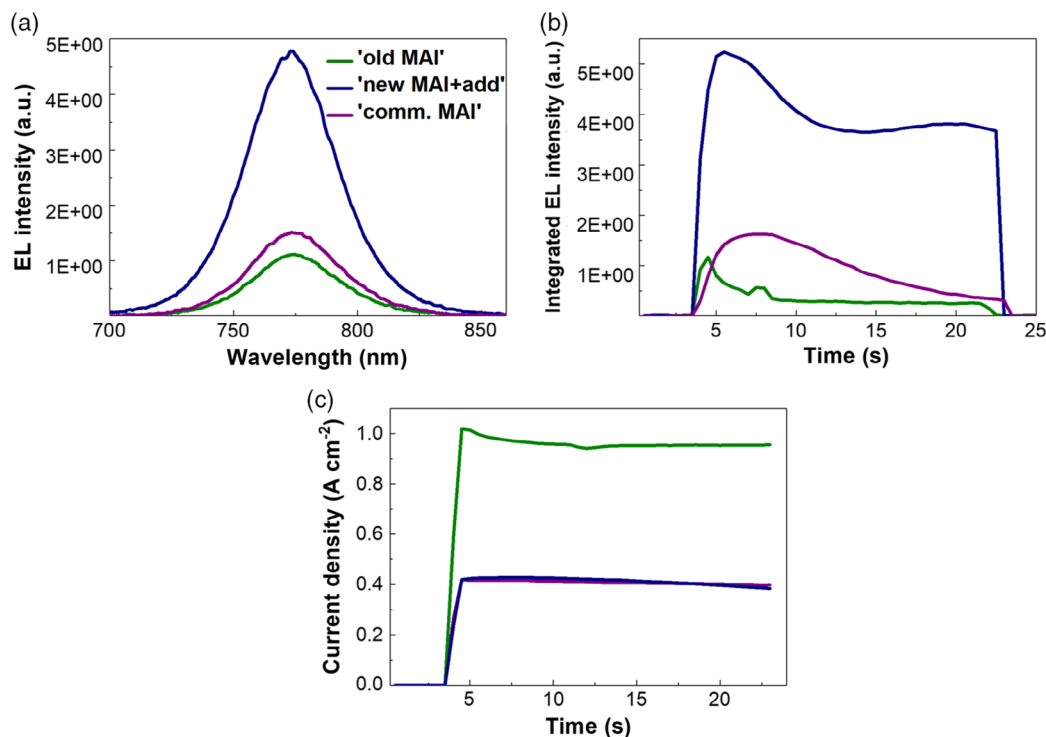


Figure 5. a) EL spectra recorded at 3 V bias of perovskite solar cells processed from different precursor solutions; b) integrated EL intensities as a function of time at a fixed voltage of 3 V for the same samples; c) current densities corresponding to transient EL from b) for the “old MAI,” “new MAI + add,” and “comm. MAI” device type.

to determine, as a variety of effects can be involved, like mobile charges, mobile ions, defects and their passivation, solid-state reactions (interaction with iodide-related defects and iodine vapor), and so on.^[51] Figure 5c shows current densities as a function of time for the three samples, which correspond to the integrated EL intensities from Figure 5b. We notice that current densities of the “new MAI + add” and “comm. MAI” are in the range of 0.38–0.425 A cm⁻², whereas one of the “old MAI” is much higher, and approaches 1 A cm⁻². All the three curves are quite stable during the entire measurement (applied 3 V forward bias), with a small decrease in the case of “old MAI” and “new MAI + add” samples. Confrontation of the current density time evolution (Figure 5c) with the integrated EL intensity evolution (Figure 5b) indicates that the ‘old MAI’ device is the least efficient emitter (for the highest registered current density the smallest EL intensity is obtained). As the current density values display similar magnitudes for the “new MAI + add” and “comm. MAI,” we conclude that the improved emission ability of the “new MAI + add” perovskite is responsible for the higher EL intensity, which is also corroborated by the PLQY measurements (Figure 3a).

Therefore, the optimized recipe with the newly synthesized MAI introduces less nonradiative channels into MAPbI₃ when compared with the formulation using conventional MAI synthetic route, and consequently the intensity and stability of emission is enhanced. To get more in-depth insight into the differences in trap-state density of MAPbI₃ perovskite layers processed from different precursor solutions, we conducted space-charge-limited current (SCLC) measurements. We fabricated hole-only devices of the following structure: glass ITO/PEDOT:PSS/MAPbI₃/poly(triaryl)amine (PTAA)/Au. We used the same MAI variations in the precursor solution as before, namely the “new MAI + add,” “old MAI,” and “comm. MAI.” Figure 6 shows *JV* curves obtained during the measurement (carried out in dark). We can distinguish three regions in the plots: ohmic region at low voltage bias, trap-filled limited region at intermediate voltage bias, and space-charge-limited region at high voltage bias.^[52] When the trap sites present in the photoactive layer get filled up with the injected carriers, the current

values rapidly increase (trap-filled region). The inflection point where the device operation mode changes to the trap-filled limit can be described by Equation (6)

$$V_{\text{TFL}} = \frac{eN_t L^2}{2\epsilon_0 \epsilon_r} \quad (6)$$

where e is elementary charge, ϵ_r is perovskite’s dielectric constant, ϵ_0 is vacuum permittivity, N_t is trap state density in the semiconductor’s layer, and L refers to perovskite film thickness.

Therefore, by defining the onset voltage point (V_{TFL}), we can estimate the trap-state density in the photoactive layer and compare between the layers processed from different precursor solutions. We extracted the trap state densities of 2.44×10^{16} , 3.34×10^{16} , and 5.89×10^{16} cm⁻³, for the “new MAI + add,” “comm MAI,” and “old MAI,” respectively. The literature values of defect densities in MAPbI₃ vary significantly depending on the measuring method, typically reported in the range 10^{16} – 10^{17} cm⁻³ when determined by optical techniques.^[53] We note that these defect density values should be rather used for a comparative analysis. It was recently reported that due to perovskites’ ionic nature, the precise position of the inflection point can largely depend on the experimental conditions (voltage scan rate, scan direction, temperature).^[54] The findings obtained from the SCLC measurements are consistent with all the previous characterization methods, confirming superior optoelectronic properties of MAPbI₃ layer processed from the newly developed formulation (ultrapure MAI with the controlled addition of impurities).

3. Conclusion

In summary, we have demonstrated a new synthetic route for making methylammonium iodide free of phosphorus-based impurities by avoiding the use of hydroiodic acid as a reagent. We used such MAI powder as a component for making MAPbI₃ perovskite thin films and applied these layers into a simple planar heterojunction solar cell architecture. The impurities have a significant impact on the nature of the perovskite precursor solution, which we studied with DLS technique. We developed a new perovskite precursor composition based on pure MAI and controlled amount of additives, which allows for fine-tuning the properties of the colloidal solution, and in turn obtain improved optoelectronic properties of the photoactive layer. With multiple optical and electrical characterization methods, we have demonstrated lower defect densities in such perovskite films and reduced nonradiative recombination rates in respective devices. This work highlights the importance of the interplay between the purity of perovskite precursor components, precise solution composition, and highly sensitive crystallization process of perovskite layers. Other alkylammonium iodides (e.g., formamidinium iodide) used for fabrication of various perovskite materials face similar problems, as their synthesis typically involves the use of stabilized hydroiodic acid. We expect that the reported synthetic route will motivate other groups to extend it to different alkylammonium iodides for developing well-controlled precursor solutions, leading to higher reproducibility and improved performance of solution-processed perovskite solar cells.

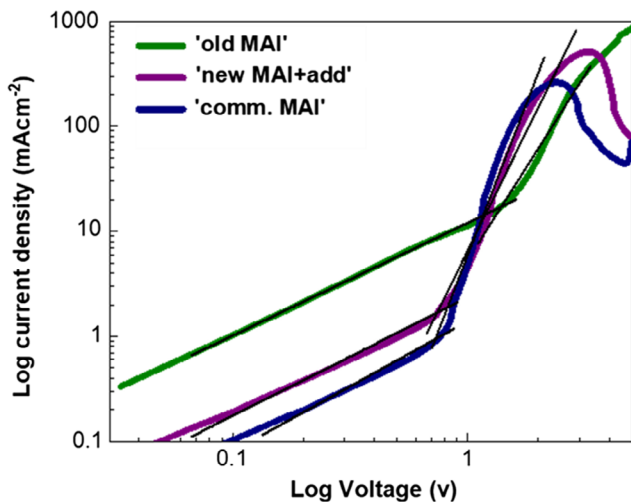


Figure 6. SCLC measurements of hole-only devices using perovskite layers processed from different precursor solutions.

4. Experimental Section

Experimental details about the used characterization methods (EQE, PL, EL, TRMC, DLS, SEM, XRD, and ICP-MS) are provided in Supporting Information.

Materials: Unless otherwise stated, all the materials were purchased from Sigma-Aldrich or Alfa Aesar and used as received. Methylammonium bromide (MABr) was synthesized internally according to the previously reported recipe.¹⁵ Methylammonium iodide (MAI) was synthesized internally (two different methods) and purchased from commercial supplier (Lumtec and Solenne). Methylammonium hypophosphite (MAH_2PO_2) was synthesized internally (as described in the text). Other materials used: poly(3,4-ethylenedioxythiophene) polystyrene sulfonate, PEDOT:PSS (AI4083, Heraeus), [6,6]-phenyl- C_{61} -butyric acid methyl ester, PCBM (Lumtec), [6,6]-phenyl- C_{61} -butyric styryl dendron ester, PCBSD (Nano-C), silver pellets (Kurt Lesker). Lead acetate trihydrate, $\text{Pb}(\text{OAc})_2 \cdot 3\text{H}_2\text{O}$ (Sigma-Aldrich) was dried before use to remove all the hydrated water.

Synthesis of Methylammonium Iodide (Route with HI Reagent), “old MAI”: Hydroiodic acid (57 wt% in water, stabilized with HPA, 80 mL, 0.58 mol) was poured through a dropping funnel into a methylamine solution (33 wt% in absolute ethanol, 107 mL, 0.87 mol) without any additional solvent within the period of 20 min in 500 mL round-bottomed flask. The reaction mixture was stirred at room temperature in a nitrogen atmosphere for 3 h. The solvent was removed by a rotary evaporation until white crystals started to appear. The product was collected and recrystallized in absolute EtOH (≈ 200 mL) and left overnight in a fridge. Precipitate was collected and dried 6 h under vacuum (2 mbar) at 60 °C until stable mass. Obtained product was denoted as 1 \times recrystallized. To obtain higher purity, recrystallized product was subjected to multiple recrystallization steps. This had significant effect on the overall reaction yield. About 89% was obtained for the MAI 1 \times recrystallized, and only 43% for the MAI 3 \times recrystallized.

Synthesis of Methylammonium Iodide (Route without HI Reagent), “new MAI”: In a 250 mL round-bottomed flask, immersed in a room temperature bath, 1 g of pure MAI (from previous batches of “new MAI,” the first time “old MAI” 3 \times recrystallized was used) was dissolved in an absolute EtOH, resulting in a clear solution. Then, molecular iodine (26.7 g, 105 mmol) was added, producing deep brown suspension, which got mostly solubilized after 5 min. Then, formic acid (4.0 mL, 100 mmol) was added at once. After that, slow addition of methylamine solution (33 wt% in absolute ethanol, 31 mL, 0.25 mol) was started through a dropping funnel. It was completed within 30 min, accompanied with the formation of fumes and rise of the inner temperature. The temperature was maintained below 80 °C by replenishing water bath. After fumes ceased to arise, the reaction was kept at 80 °C for 2 h. After that time, reaction mixture was dark brown (excess of iodine) and was evaporated to dryness. Then, it was recrystallized from absolute ethanol (≈ 50 mL), and upon cooling, additional 100 mL of diethyl ether was added. Precipitate was collected and dried for 6 h under vacuum (2 mbar) at 60 °C until stable mass yielding 27.6 g (87%) of white powder.

Synthesis of n-Octylammonium Iodide (Route without HI Reagent): In a round-bottomed flask, a portion of iodine (6.67 g, 26.25 mmol, 1 eq.) was dissolved at once in 40 mL of absolute ethanol, resulting in a deep brown, nontransparent solution, with a clear presence of iodine particles. After 5 min all the solids dissolved, making a brown solution. Then, formic acid (1.00 mL, 25 mmol, 0.97 eq.) was added to the mixture, no changes were observed. Subsequently, dropwise addition of octylamine was carried out (10.77 mL, 65 mmol, 2.6 eq.). Every added drop caused foaming and heating of the solution (reaction is exothermic). The bubbling was only observed after the octylamine addition, because the consumption of HI generated in situ greatly accelerates the rate of its formation. After the addition was completed, the reaction mixture was still brown. The solution was heated at 80 °C for 2 h. After that time, the color faded a little bit, but was still vivid due to the use of over-stoichiometric amount of iodine in respect formic acid. The excess of iodine is important to avoid the formation of octylammonium formate as a side product. The reaction mixture was evaporated on a rotary evaporator under reduced pressure (30 mbar, heating bath 50 °C), leaving a yellow-brown solid, which was subsequently

solubilized in a boiling absolute ethanol (≈ 1 mL/1 g of expected product). When the mixture cooled down to room temperature, diethyl ether was added to precipitate higher fraction of the product. The precipitate was filtered and thoroughly rinsed with diethyl ether until the white color powder was obtained. The solid was dried under vacuum (<0.2 mbar) for 5 h. The yield of the reaction was 9.75 g (76%).

Synthesis of Formamidineum Iodide (Route without HI Reagent): In a round-bottomed flask a portion of iodine (12.07 g, 26.25 mmol, 1 eq.) was dissolved at once in 60 mL of absolute ethanol, resulting in a deep brown, nontransparent solution, with a clear presence of iodine particles. After 5 min all the solids dissolved, making a brown solution. Then, formic acid (1.84 mL, 46.1 mmol, 0.97 eq.) was added to the mixture, all the amount at once, no changes were observed. Subsequently, formamidineum acetate (10.41 g, 100 mmol, 2.1 eq.) was added at once. The reaction mixture was heated to 50 °C and kept at this temperature for 12 h. After that time, the reaction mixture was evaporated on a rotary evaporator under reduced pressure (30 mbar, heating bath 50 °C), leaving a yellow-brown solid, which was subsequently solubilized in a boiling absolute ethanol (≈ 1 mL/1 g of expected product). When the mixture cooled down to room temperature, diethyl ether was added to precipitate higher fraction of the product. The precipitate was filtered and thoroughly rinsed with diethyl ether until the white color powder was obtained. The solid was dried under vacuum (<0.2 mbar) for 5 h. The yield of the reaction was 13.32 g (82%).

Synthesis of Methylammonium Hypophosphite (MAH_2PO_2): In a 100 mL round-bottomed flask, hypophosphorous acid (H_3PO_2 , 50% in H_2O , 5.45 mL, 50 mmol) was poured through a dropping funnel into a methylamine solution (33 wt% in absolute ethanol, 12.45 mL, 100 mmol) in 50 mL of H_2O , within the period of 5 min under inert atmosphere. After stirring for 90 min in an ice bath, the solvent was removed by a rotary evaporation at 100 °C. The obtained MAH_2PO_2 was a transparent viscous liquid ($m = 4.68$ g, $\gamma = 96\%$).

Device Fabrication: The perovskite precursor solution was prepared by dissolving methylammonium iodide (old MAI, new MAI, or commercial MAI) (304.15 mg), anhydrous $\text{Pb}(\text{OAc})_2$ (166.5 mg), and PbCl_2 (35.58 mg) in 1 mL of DMF. About 46 μL of dimethyl sulfoxide was added (1:1 molar ratio with respect to Pb). The molar ratio of the components, MAI: $\text{Pb}(\text{OAc})_2$: PbCl_2 was 3.0:0.8:0.2, with the total concentration of 35 wt%. The MAH_2PO_2 salt was added in varied amounts (0.1–2 wt% with respect to MAI). In the end, the following compounds were added to the precursor solution: MABr (1.5 mol% with respect to Pb), PCBSD (concentration: 0.5 mg mL^{-1}), ethyl 2-cyano acrylate, E2CA (concentration: 5 mg mL^{-1}). For the colloidal solution studies (DLS, Tyndall effect), simpler version of the above ink was prepared. Methylammonium iodide (old MAI, new MAI, or commercial MAI) (304.15 mg), anhydrous $\text{Pb}(\text{OAc})_2$ (166.5 mg), and PbCl_2 (35.58 mg) was dissolved in 1 mL of DMF.

ITO-patterned glass substrates (2.0×1.5 cm², Lumtec) were cleaned by sequential sonication in aqueous Hellmanex solution (Hellma analytics), DI water, acetone, and IPA for 10 min. The as-cleaned ITO substrates were then treated with O_2 plasma for 2 min. PEDOT:PSS solution with ammonium metatungstate hydrate (AMH) additive (5 vol% of AMH with respect to PEDOT:PSS solution) was spin coated at 7000 rpm and annealed for 35 min at 130 °C. Subsequently, the samples were transferred to the nitrogen-filled glovebox. The perovskite precursor solutions were coated at 3000 rpm for 30 s. In the past 2 s of the spin-coating process, the nitrogen gas blowing was applied to the sample. After the spin coating was finished, the samples were left for another 2.5 min at room temperature, and then placed on a hot plate at 95 °C for 15 min. The PCBM solution was prepared in chlorobenzene (20 mg mL^{-1}), with the following additives: (dimethyloctadecyl[3-(trimethoxysilyl)propyl]ammonium chloride [DMOAP], 0.7 wt% with respect to PCBM) and (poly(methyl methacrylate) [PMMA], 3 wt% with respect to PCBM). The PCBM solution was spin coated at 2000 rpm for 30 s, and then annealed at 60 °C for 10 min. Finally, 5 nm of BCP and 100 nm of Ag electrode were thermally evaporated on top of devices at $\approx 10^{-6}$ bar, through a shadow mask. For SCLC measurements, the samples were prepared in the same manner up to perovskite layer. PTAA (Ossila) solution (2 mg mL^{-1} in toluene) was spin coated at 5000 rpm for 30 s. The samples were finished with 95 nm of Au thermally evaporated on top at $\approx 10^{-6}$ bar, through a shadow mask.

Current–Voltage Measurements: JV characterization and SPO measurements were carried out using a Keithley 2461 source measure unit (SMU) under simulated AM1.5G irradiation (100 mW cm^{-2}) using an AAA-rated solar simulator (Abet Technologies, sun 2000) calibrated against an RR-208-KG5 silicon reference cell (Abet Technologies). The mismatch factor for the studied perovskite solar cells was calculated to be 0.968 using EQEs of the reference and test cells, lamp's spectrum, and AM1.5G, and this value was used to correct the intensity of the solar simulator lamp to provide one-sun illumination.^[56] Solar cells were masked to 0.06 cm^2 . JV measurements were carried out in two scan directions, from forward bias to short circuit and from short circuit to forward bias. The scanning rate was set to 500 mV s^{-1} . The SPO was measured at the maximum power point voltage for a duration of 30 s.

For the SCLC measurements, JV curves of hole-only devices were measured in dark, scanning from 0 to 5 V, at a scan rate of 10 mV s^{-1} .

Supporting Information

Supporting Information is available from the Wiley Online Library or from the author.

Acknowledgements

The authors acknowledge funding from the Foundation of Polish Science (First TEAM/2017-3/30). K.M. thanks the National Science Centre (Poland) for the NCN OPUS grant no. UMO-2016/23/B/ST5/02861. J.S. acknowledges support from the Statutory Grant of the Department of Nanometrology of WrUST. The authors acknowledge the research team at Saule Technologies for their support.

Conflict of Interest

The authors declare no conflict of interest.

Keywords

colloids, defects, methylammonium iodide, perovskites, solar cells

Received: May 26, 2020

Revised: August 13, 2020

Published online: September 9, 2020

- [1] US National Renewable Energy Laboratory, *Nrel* **2019**, 1.
- [2] A. Kojima, K. Teshima, Y. Shirai, T. Miyasaka, *J. Am. Chem. Soc.* **2009**, *131*, 6050.
- [3] M. M. Lee, J. Teuscher, T. Miyasaka, T. N. Murakami, H. J. Snaith, *Science* **2012**, *338*, 643.
- [4] H.-S. Kim, C.-R. Lee, J.-H. Im, K.-B. Lee, T. Moehl, A. Marchioro, S.-J. Moon, R. Humphry-Baker, J.-H. Yum, J. E. Moser, M. Grätzel, N.-G. Park, *Sci. Rep.* **2012**, *2*, 591.
- [5] M. Saliba, J.-P. Correa-Baena, M. Graetzel, A. Hagfeldt, A. Abate, *Angew. Chem., Int. Ed.* **2017**, *57*, 2554.
- [6] P. Roy, N. Kumar Sinha, S. Tiwari, A. Khare, *Sol. Energy* **2020**, *198*, 665.
- [7] S. D. Stranks, H. J. Snaith, *Nat. Nanotechnol.* **2015**, *10*, 391.
- [8] S. Akin, N. Arora, S. M. Zakeeruddin, M. Grätzel, R. H. Friend, M. I. Dar, *Adv. Energy Mater.* **2020**, *10*, 1903090.
- [9] D. Forgacs, K. Wojciechowski, O. Malinkiewicz, in *High-Efficient Low-Cost Photovoltaics* (Eds: V. Petrova-Koch, R. Hezel, A. Goetzberger), Springer, Cham **2020**, pp. 219–255.
- [10] M. Jung, S.-G. Ji, G. Kim, S. Il Seok, *Chem. Soc. Rev.* **2019**, *48*, 2011.
- [11] K. Yan, M. Long, T. Zhang, Z. Wei, H. Chen, S. Yang, J. Xu, *J. Am. Chem. Soc.* **2015**, *137*, 460.
- [12] D. P. McMeekin, Z. Wang, W. Rehman, F. Pulvirenti, J. B. Patel, N. K. Noel, M. B. Johnston, S. R. Marder, L. M. Herz, H. J. Snaith, *Adv. Mater.* **2017**, *29*, 1607039.
- [13] Z. Xiao, D. Wang, Q. Dong, Q. Wang, W. Wei, J. Dai, X. C. Zeng, J. Huang, *Energy Environ. Sci.* **2016**, *9*, 867.
- [14] I. Levchuk, Y. Hou, M. Gruber, M. Brandl, P. Herre, X. Tang, F. Hoegl, M. Batentschuk, A. Osvet, R. Hock, W. Peukert, R. R. Tykewinski, C. J. Brabec, *Adv. Mater. Interfaces* **2016**, *3*, 1600593.
- [15] B. Li, D. Binks, G. Cao, J. Tian, *Small* **2019**, *15*, 1902579.
- [16] F. Zhang, K. Zhu, *Adv. Energy Mater.* **2019**, *10*, 1902579.
- [17] N. G. Park, K. Zhu, *Nat. Rev. Mater.* **2020**, *5*, 333.
- [18] P. Roy, N. Kumar Sinha, S. Tiwari, A. Khare, *Sol. Energy* **2020**, *198*, 665.
- [19] S. R. Raga, L. K. Ono, Y. Qi, *J. Mater. Chem. A* **2016**, *4*, 2494.
- [20] S. Sasmal, S. K. Sharma, S. Chatterjee, A. J. Pal, S. P. Turaga, A. A. Bettiol, R. G. S. Pala, S. Sivakumar, S. Valiyaveetil, *ACS Appl. Mater. Interfaces* **2019**, *11*, 43708.
- [21] J.-H. Im, C.-R. Lee, J.-W. Lee, S.-W. Park, N.-G. Park, *Nanoscale* **2011**, *3*, 4088.
- [22] F. F. Bethel, *Process Mak. Halogen Salts* (Ed: J. A. Garrison), Huntington Beach, CA **1978**, p. 991.
- [23] W. Zhang, M. Saliba, D. T. Moore, S. K. Pathak, M. T. Hörantner, T. Stergiopoulos, S. D. Stranks, G. E. Eperon, J. A. Alexander-Webber, A. Abate, A. Sadhanala, S. Yao, Y. Chen, R. H. Friend, L. A. Estroff, U. Wiesner, H. J. Snaith, *Nat. Commun.* **2015**, *6*, 6142.
- [24] W. Zhang, S. Pathak, N. Sakai, T. Stergiopoulos, P. K. Nayak, N. K. Noel, A. A. Haghighirad, V. M. Burlakov, D. W. deQuilettes, A. Sadhanala, W. Li, L. Wang, D. S. Ginger, R. H. Friend, H. J. Snaith, *Nat. Commun.* **2015**, *6*, 10030.
- [25] K. Yan, M. Long, T. Zhang, Z. Wei, H. Chen, S. Yang, J. Xu, *J. Am. Chem. Soc.* **2015**, *137*, 4460.
- [26] T. Baikie, Y. Fang, J. M. Kadro, M. Schreyer, F. Wei, S. G. Mhaisalkar, M. Gratzel, T. J. White, *J. Mater. Chem. A* **2013**, *1*, 5628.
- [27] V. S. Vinila, R. Jacob, A. Mory, H. G. Nair, S. Issac, S. Rajan, A. S. Nair, D. J. Satheesh, J. Isac, *Cryst. Struct. Theory Appl.* **2014**, *3*, 57.
- [28] J. Serafińczuk, K. Moszak, Ł. Pawlaczyk, W. Olszewski, D. Pucicki, R. Kudrawiec, D. Hommel, *J. Alloys Compd.* **2020**, *825*, 153838.
- [29] S. Christiansen, M. Albrecht, H. P. Strunk, *Philos. Mag. A* **1998**, *77*, 1013.
- [30] Y. Zhao, J. Zhang, *J. Appl. Crystallogr.* **2008**, *41*, 1095.
- [31] T. W. Jones, A. Osheroov, M. Alsari, M. Sponseller, B. C. Duck, Y. K. Jung, C. Settens, F. Niroui, R. Brenes, C. V. Stan, Y. Li, M. Abdi-Jalebi, N. Tamura, J. E. MacDonald, M. Burghammer, R. H. Friend, V. Bulović, A. Walsh, G. J. Wilson, S. Lilliu, S. D. Stranks, *Energy Environ. Sci.* **2019**, *12*, 596.
- [32] T. Zhao, C. C. Chueh, Q. Chen, A. Rajagopal, A. K. Y. Jen, *ACS Energy Lett.* **2016**, *1*, 757.
- [33] E. Aydin, M. De Bastiani, S. De Wolf, *Adv. Mater.* **2019**, *31*, 1900428.
- [34] S. D. Stranks, V. M. Burlakov, T. Leijtens, J. M. Ball, A. Goriely, H. J. Snaith, *Phys. Rev. Appl.* **2014**, *2*, 034007.
- [35] M. B. Johnston, L. M. Herz, *Acc. Chem. Res.* **2016**, *49*, 146.
- [36] F. Deschler, M. Price, S. Pathak, L. E. Klintberg, D. D. Jarausch, R. Higler, S. Hüttner, T. Leijtens, S. D. Stranks, H. J. Snaith, M. Atature, R. T. Phillips, R. H. Friend, *J. Phys. Chem. Lett.* **2014**, *5*, 1421.
- [37] D. W. DeQuilettes, W. Zhang, V. M. Burlakov, D. J. Graham, T. Leijtens, A. Osheroov, H. J. Snaith, D. S. Ginger, S. D. Stranks, *Nat. Commun.* **2016**, *7*, 11683.
- [38] R. Brenes, D. Guo, A. Osheroov, N. K. Noel, C. Eames, E. M. Hutter, S. K. Pathak, F. Niroui, R. H. Friend, M. S. Islam, H. J. Snaith, V. Bulović, T. J. Savenije, S. D. Stranks, *Joule* **2017**, *1*, 155.

- [39] S. N. Habisreutinger, B. Wenger, H. J. Snaith, R. J. Nicholas, *ACS Energy Lett.* **2017**, 2, 622.
- [40] M. Kunst, G. Beck, *J. Appl. Phys.* **1986**, 60, 3558.
- [41] K. Wojciechowski, S. D. Stranks, A. Abate, G. Sadoughi, A. Sadhanala, N. Kopidakis, G. Rumbles, C. Li, R. H. Friend, A. K. Jen, H. J. Snaith, *ACS Nano* **2014**, 8, 12701.
- [42] T. J. Savenije, D. Guo, V. M. Caselli, E. M. Hutter, *Adv. Energy Mater.* **2020**, 10, 1903788.
- [43] V. S. Chirvony, K. S. Sekerbayev, H. Pashaei Adl, I. Suárez, Y. T. Taurbayev, A. F. Gualdrón-Reyes, I. Mora-Seró, J. P. Martínez-Pastor, *J. Lumin.* **2020**, 221, 117092.
- [44] J. T.-W. Wang, Z. Wang, S. K. Pathak, W. Zhang, D. DeQuilettes, F. Wisnivesky, J. Huang, P. Nayak, J. Patel, H. Yusof, Y. Vaynzof, R. Zhu, I. Ramirez, J. Zhang, C. Ducati, C. Grovenor, M. B. Johnston, D. S. Ginger, R. J. Nicholas, H. J. Snaith, *Energy Environ. Sci.* **2016**, 9, 2892.
- [45] G. Y. Kim, A. Senocrate, T. Yang, G. Gregori, M. Grätzel, J. Maier, *Nat. Mater.* **2018**, 17, 445.
- [46] A. Walsh, S. D. Stranks, *ACS Energy Lett.* **2018**, 3, 1983.
- [47] H. Khassaf, S. K. Yadavalli, O. Sharad, Y. Zhou, N. P. Padture, A. I. Kingon, *J. Phys. Chem. C* **2019**, 7, 4029.
- [48] W. Tress, *J. Phys. Chem. Lett.* **2017**, 8, 3106.
- [49] X. Deng, X. Wen, C. F. J. Lau, T. Young, J. Yun, M. A. Green, S. Huang, A. W. Y. Ho-Baillie, *J. Mater. Chem. C* **2016**, 4, 9060.
- [50] T. Leijtens, E. T. Hoke, G. Grancini, D. J. Slotcavage, G. E. Eperon, J. M. Ball, M. De Bastiani, A. R. Bowring, N. Martino, K. Wojciechowski, M. D. McGehee, H. J. Snaith, A. Petrozza, *Adv. Energy Mater.* **2015**, 5, 1500962.
- [51] C. Li, A. Guerrero, S. Huettner, J. Bisquert, *Nat. Commun.* **2018**, 9, 5113.
- [52] K. C. Hsiao, M. H. Jao, B. T. Li, T. H. Lin, S. H. C. Liao, M. C. Wu, W. F. Su, *ACS Appl. Energy Mater.* **2019**, 2, 4821.
- [53] J. M. Ball, A. Petrozza, *Nat. Energy* **2016**, 1, 16149.
- [54] E. A. Duijnste, J. M. Ball, V. M. Le Corre, L. J. A. Koster, H. J. Snaith, J. Lim, *ACS Energy Lett.* **2020**, 5, 376.
- [55] R. K. Singh, R. Kumar, A. Kumar, N. Jain, R. K. Singh, J. Singh, *J. Alloys Compd.* **2018**, 743, 728.
- [56] B. V. Shrotriya, G. Li, Y. Yao, T. Moriarty, K. Emery, Y. Yang, *Adv. Funct. Mater.* **2006**, 16, 2016.

Article

Analysis of Perovskite Solar Cell Degradation over Time Using NIR Spectroscopy—A Novel Approach

Marek Gašiorowski¹, Shyantana Dasgupta^{2,3}, Leszek Bychto¹ , Taimoor Ahmad^{4,5} , Piotr Szymak⁶ ,
Konrad Wojciechowski^{3,5}  and Aleksy Patryń^{1,*} 

¹ Faculty of Electronics and Computer Science, Koszalin University of Technology, 75-453 Koszalin, Poland; gasiorowski.marek@o2.pl (M.G.); leszek.bychto@tu.koszalin.pl (L.B.)

² Faculty of Materials Engineering and Technical Physics, Poznan University of Technology, Piotrowo 3, 60-965 Poznan, Poland; shyantan.dasgupta@saulerresearch.com

³ Saule Research Institute, Wrocław Technology Park, 54-130 Wrocław, Poland; konrad.wojciechowski@sauletech.com

⁴ Department of Physical Science and Engineering, King Abdullah University of Science and Technology, Thuwal 23955-6900, Saudi Arabia; taimoor.ahmad@kaust.edu.sa

⁵ Saule Technologies, Wrocław Technology Park, 54-130 Wrocław, Poland

⁶ Faculty of Mechanical and Electrical Engineering, Polish Naval Academy, 81-127 Gdynia, Poland; p.szymak@amw.gdynia.pl

* Correspondence: aleksy.patryn@tu.koszalin.pl

Abstract: In recent years, there has been a dynamic development of photovoltaic materials based on perovskite structures. Solar cells based on perovskite materials are characterised by a relatively high price/performance ratio. Achieving stability at elevated temperatures has remained one of the greatest challenges in the perovskite solar cell research community. However, significant progress in this field has been made by utilising different compositional engineering routes for the fabrication of perovskite semiconductors such as triple cation-based perovskite structures. In this work, a new approach for the rapid analysis of the changes occurring in time in perovskite structures was developed. We implemented a quick and inexpensive method of estimating the ageing of perovskite structures based on an express diagnosis of light reflection in the near-infrared region. The possibility of using optical reflectance in the NIR range (900–1700 nm) to observe the ageing of perovskite structures over time was investigated, and changes in optical reflectance spectra of original perovskite solar cell structures during one month after PSC production were monitored. The ratio of characteristic peaks in the reflection spectra was determined, and statistical analysis by the two-dimensional correlation spectroscopy (2D-COS) method was performed. This method allowed correctly detecting critical points in thermal ageing over time.

Keywords: perovskite solar cell degradation; NIR Spectroscopy; optical reflectance; express-measurement method; the two-dimensional correlation spectroscopy



Citation: Gašiorowski, M.; Dasgupta, S.; Bychto, L.; Ahmad, T.; Szymak, P.; Wojciechowski, K.; Patryń, A. Analysis of Perovskite Solar Cell Degradation over Time Using NIR Spectroscopy—A Novel Approach. *Energies* **2022**, *15*, 5397. <https://doi.org/10.3390/en15155397>

Academic Editors: Akansha Mehta and Rayees Ahmad Rather

Received: 24 June 2022

Accepted: 21 July 2022

Published: 26 July 2022

Publisher's Note: MDPI stays neutral with regard to jurisdictional claims in published maps and institutional affiliations.



Copyright: © 2022 by the authors. Licensee MDPI, Basel, Switzerland. This article is an open access article distributed under the terms and conditions of the Creative Commons Attribution (CC BY) license (<https://creativecommons.org/licenses/by/4.0/>).

1. Introduction

The development of photovoltaics is still generally costly. This also applies to the production of photovoltaic systems and the installation of such systems for the production of electricity. According to the latest report of the Fraunhofer Institute of Solar Energy Systems ISE [1] dated 24 February 2022, the total PV Market growth during one year, from the end of 2020 to the end of 2021, accounted for approximately 27% (from 144 GW to 183 GW), with the total installed capacity at the end of 2020 exceeding 700 GW, and the total global energy production (PV Power Generation) amounting to 855.7 TWh. Compared to other thin film technologies, organic–inorganic hybrid halide-based perovskites have received widespread attention from researchers due to the rapid improvement in their power conversion efficiencies (PCE), which rose from 3.8% in 2009 to 25.5% in 2021 [2–6].

In this general progress of PV development, simultaneously with the traditional technologies based on monocrystalline and multicrystalline silicon and other typical thin-film technologies such as CIGS and CdTe, other technologies have progressed, based on the use of materials that, according to the NREL terminology [2], are referred to as emerging materials and include perovskite-based photovoltaic materials and structures. The highest efficiency of perovskite solar cells achieved in the last seven years increased from 14% (EPFL) in 2014 to 26.1% (INST) [7] in 2022 and even to 29.6% (NZB) for tandem perovskite solar cells [8]. These values are comparable with those of the most efficient silicon-based cells [2]. The success associated with achieving very high-performance indicators for the best perovskite cells and the low cost of producing cells with average performance indicators comparable to those of commercial silicon or thin-film cells provide the basis for forecasting a significant share of perovskite cells and systems in photovoltaic systems in the near future. Despite being a highly promising class of semiconductors, perovskite materials suffer from various types of mechanical and thermal-based degradation, which has hindered their commercialisation. Elevated temperatures and hygroscopic conditions can lead to the evolution of organic volatile chemical species leading to the formation of lead-based iodides [9–12]. In addition, perovskite materials display low fracture energy, and perovskite-based solar cell architectures consist of multiple charge transport layers with highly mismatched coefficients of thermal expansion (CTE), making them easily prone to delamination [13–15]. However, thanks to new achievements of composition engineering, especially robust encapsulation strategies, perovskite solar cells are capable of achieving over 1000 h of stability under thermal, humidity and light-based stresses [14,16].

In connection with the above, the rapid and effective analysis of changes in the time domain in perovskite structures is essential for the entire technological spectrum of perovskite solar cells.

There are several effective methods for controlling the quality and performance of PV structures at different stages of their production, which are also used for the analysis of perovskite cells. These methods are also used in the analysis of the degradation of structures and links in the time domain. Among these methods, it is worth highlighting photo and electroluminescence methods [17–19], X-ray methods, especially X-ray diffraction (GIWAXD) and high-resolution X-ray photoelectron spectroscopy (HR-XPS) [18–20], and optical spectroscopic methods VS/NIR, in particular the FTIR method [18,19,21].

These methods, especially when applied in combination, are very effective and allow for a profound explanation not only of the parameters characterising changes in cell structures over time, but also of the physical mechanisms of this process.

It should be emphasised that, currently, the application of these methods requires a quite complex and expensive equipment. This limits the expressiveness and mobility of measurements of specific solar cell structures necessary for long-term cell analysis.

An attempt to propose such a quick and inexpensive method of estimating the ageing of perovskite structures with time was undertaken in this paper, based on the express diagnosis of the spectrum of light reflection in the near infrared (900–1700 nm) from perovskite solar cells, analogically to a method previously used [22,23]. The applied method uses miniature, very mobile equipment, allows us to conduct and record a six-fold measurement of the entire spectrum in a few seconds and is characterised by exceptional mobility and simplicity. Such approach, having an obvious limitation as to the depth of the analysis of the processes involved, opens a new path for the practical analysis of the temporal stability of perovskite solar cells.

2. Samples and the Method of Measurement

Materials: Unless otherwise stated, all the materials were purchased from Sigma-Aldrich Chemie GmbH (Taufkirchen, Germany) and used as received. Silver pellets were obtained from Kurt Lesker Company Ltd. (Dresden, Germany); PET substrates coated with IZO (sheet resistance of $15 \Omega \text{cm}^{-1}$) were obtained from Eastman Chemical B.V. (Rotterdam, The Netherlands), formamidinium iodide was obtained from Ajay North America (Powder

Springs, GA, USA), and poly-triarylamine (PTAA) from Ossila BV (Leiden, The Netherlands). Methylammonium bromide was synthesised in house using a reported method [24]. The chemical component [6,6]-phenyl-C61 butyric acid *n*-hexyl ester (PCB6) was obtained from Nano-C.

Planar heterojunction PSCs were fabricated with the following architecture: ITO/PTAA/Cs_{0.04}(MA_{0.17}FA_{0.83})_{0.96}Pb(I_{0.83}Br_{0.17})₃/PCB6/Ag. First, a PTAA solution (1.5 mg/mL in toluene) was spin-coated at ambient conditions at 5000 rpm for 30 s, followed by annealing at 100 °C for 10 min (\approx 20 nm thick). Subsequently, the samples were transferred into a nitrogen-filled glovebox for perovskite layer deposition. For perovskite precursor preparation, stock solutions of PbI₂ and PbBr₂ (1.5 M) in a dimethylformamide (DMF)/dimethyl sulfoxide (DMSO) mixture [4:1 *v/v*] were prepared. Then, for the FAPbI₃ and MAPbBr₃ solutions, FAI and MABr powders were weighed into separate vials, followed by the addition of PbI₂ (into FAI) and PbBr₂ (into MABr) solutions. Both lead solutions were added in excess to obtain an over-stoichiometric lead content (FAI/MABr:PbI₂/PbBr₂ equals 1.0:1.09). The final perovskite precursor solution was prepared by mixing the solutions of FAPbI₃ and MAPbBr₃ in a 5:1 *v/v* ratio. Then, 40 μ L of a CsI solution (1.5 M solution in DMSO) was added to 1 mL of the mixture. A perovskite layer (\approx 580 nm thick) was deposited on top of PTAA with a two-step spin-coating procedure, at 650 rpm for 2 s and 4500 rpm for 32 s. Anhydrous diethyl ether (150 μ L) was dispensed on the sample in the last 11 s of the spinning sequence. The sample was dried for two minutes, then annealed for ten minutes at 50 °C and then annealed for 60 min at 100 °C for the final crystallisation. For the electron transport material (PCB6), a PCB6 solution (20 mg/mL in chlorobenzene) was spin-coated at 4000 rpm for 30 s and annealed at 60 °C for 10 min. Finally, 5 nm of BCP buffer layer and 95 nm of Ag electrode were deposited on the top of the devices by thermal evaporation at \approx 10⁻⁶ mbar, through a shadow mask.

A schematic of the perovskite solar cell stack is shown in Figure 1, and a view of a cross section of a typical solar cell structure was investigated. The chosen parameters of the measured solar cell structures are listed in Table 1.

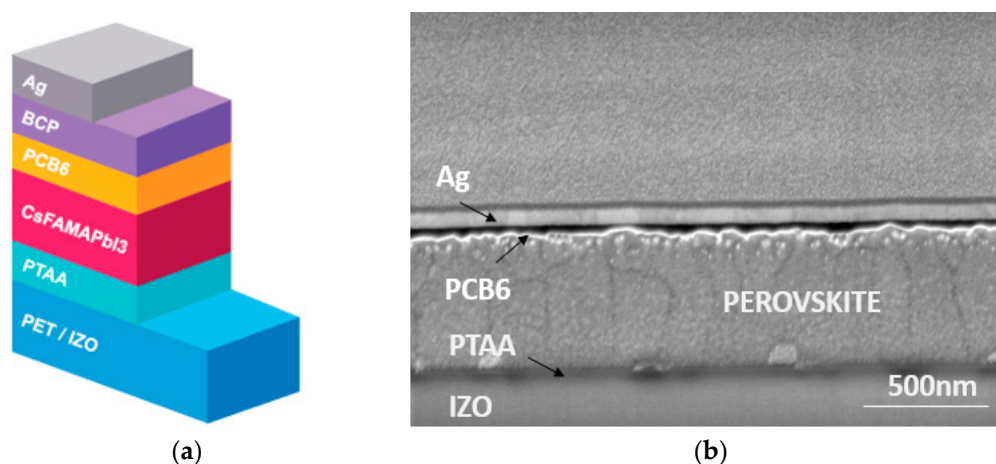


Figure 1. A cross section of the perovskite solar cell stack (a) and a SEM view of cross section (b).

Current–voltage measurements: J–V characterisation and stabilised power output measurements were performed using a Keithley 2461 source measure unit (SMU) under simulated AM1.5G irradiation (100 mW/cm²) using an Sun 3000 AAA-rated solar simulator (Abet Technologies Inc., Milford, CT, USA) calibrated against an RR-208-KG5 silicon reference cell (Abet Technologies Inc.). The mismatch factor for the studied perovskite solar cells was calculated to be 0.968 using external quantum efficiencies (EQEs) of the reference and test cells, lamp’s spectrum and AM1.5G, and this value was used to correct the intensity of the solar simulator lamp to provide one sun illumination [25]. Typically, the PCE efficiency was about 18% under AM1.5.

Table 1. Table describing the investigated samples.

Sample	Ag Electrode
S1	Yes
S2	Yes
S3	Yes
S4	Yes
S5	No
S6	No
S7	No
S8	No

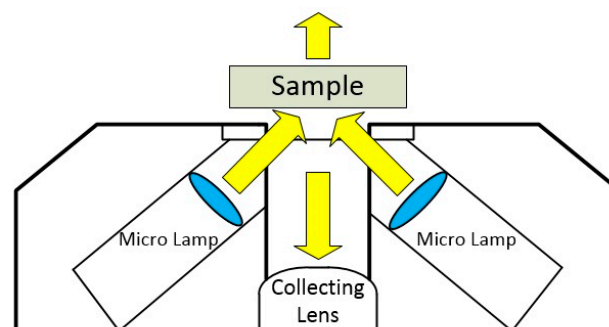
DLP NIRSCAN Measurements: The DLP NIRSCAN NANO device, a compact spectrometer from Texas Instruments, Dallas, TX, USA, operating in the wavelength band from 900 to 1700 nm, was used to record spectra. Its dimensions, 58 mm × 62 mm × 36 mm, and the absence of an external power source make it possible to perform mobile spectra measurements [26]. The device works in reflectance mode. Reflectance (R) is the ratio between the intensity of light reflected from the sample (I) and the intensity of reflected background light or of light reflected from a reference surface (I_r) [22]:

$$R = \frac{I}{I_r} \cdot 100\% \quad (1)$$

The main advantages of the device are its mobility and capability to perform measurements under various conditions.

The standard software, compatible with a PC running on a Windows operating system, enables registration, acquisition and data visualisation. It is possible to control the device using a mobile application via the Bluetooth standard. The spectrometer can register 228 measurement points in the wavelength band from 900 to 1700 nm within 2.63 s, repeating the measurement six times for every point, then calculating the mean for a given point. The result is presented in a dialog window of the software in the form of a chart or file in DAT or CSV format. The number of scans can be changed, which directly influences the time of measurement.

Figure 2 presents the principle of the device's operation and how it performs measurements. The sample situated near the spectrometer's window is illuminated by two light sources in the form of lightbulbs controlled by the device's controller.

**Figure 2.** Method of performing measurements in reflectance mode.

The reflectance spectrum of the lightbulbs from the reference surface is known and saved in the device's memory. Depending on the tested object, a specific part of the light is absorbed by the sample, a certain amount is scattered, and a part of the light is reflected off the object's surface into the slit of the device. Further on, the light goes to the optical system in the process, where it is split by a diffraction grating and directed by a lens to the DMD micro-mirror array, which directs the light in a particular sequence to the detector, where it is processed into an analogue signal [23].

3. Results and Discussion

Figures 3 and 4 show the results of the measurement of the reflectance spectrum of PSC structures (perovskite solar cells) made consistently every 24 h under identical conditions using the Express NIR San method from the foil side and the electrode side. The measurements started within about seven days from the production of the structures tested. From end of production to the commencement of the measurements, the samples were stored in hermetic packaging under a nitrogen atmosphere.

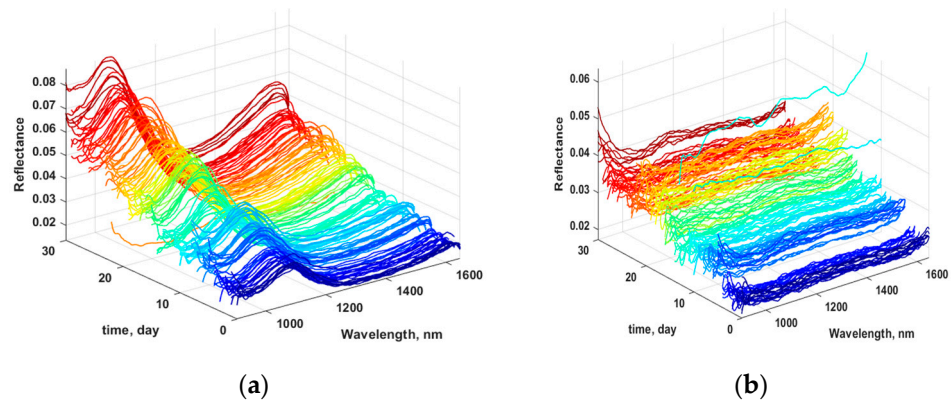


Figure 3. Development of the reflectance spectra of sample S1: (a) foil side excitation, (b) electrode side excitation. One color groups data measured during one day.

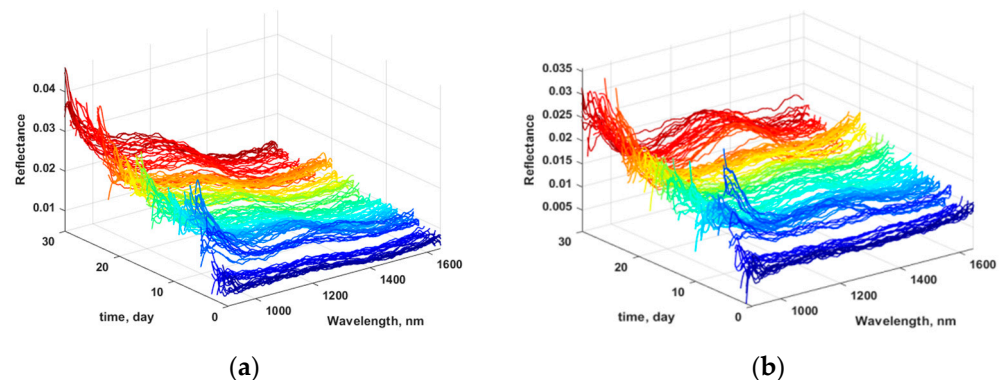


Figure 4. Development of the reflectance spectra of sample S6: (a) foil side excitation, (b) electrode side excitation. One color groups data measured during one day.

From the formal analysis of the obtained data, it was observed that the characteristic reflection spectrum from the active side (foil side) contained two peaks, one in the region of about 1100 nm, and the other in the region of about 1600 nm. Over time, the spectrum transformed slightly, and the relative intensity of the peak's changed. The objective parameter of these changes could not be described by the peak intensity alone, because the simplified measurement method used did not allow to determine the absolute value of the reflected light with high accuracy. However, the parameter of the relative strength of the peaks could be used as a ratio of the intensity of the reflected light in selected areas of the spectrum.

To objectively select these areas, the two-dimensional correlation spectroscopy (2D-COS) method [27] was applied. The 2D-COS approach examines the correlations that may exist between the time-varying reflectance spectra. The intensities of the peaks laying on the main diagonal of the 2D-COS synchronous spectrum (autocorrelation spectrum) are proportional to the relative extent of changes in the original spectra. The wavelengths

of the most and the least intense peaks observed on the main diagonal of the 2D-COS synchronous spectrum were chosen for the calculation of the reflectance ratio vs. time:

$$R_{\text{ratio}}(t) = R(t, \lambda_{\text{max}}) / R(t, \lambda_{\text{min}})$$

where:

t —time, λ_{max} , λ_{min} —wavelengths of the most and the least intense peaks on the main diagonal of the 2D-COS synchronous spectrum.

The raw reflectance data were used for 2D-COS synchronous spectrum calculation according to the equation [28]:

$$\Phi = \frac{1}{m-1} A(t, \lambda)^T A(t, \lambda) \quad (2)$$

where: $A(t, \lambda)$ is the $m \times n$ array of reflectance spectra data, m is the number of measurements, n is the number of points in the spectrum.

As a result of such analysis, it was possible to generate a series of 2D charts (the 2D-COS synchronous spectra) in which it was possible to determine the areas corresponding to the ranges on the reflection spectra, the intensity ratio of which was most sensitive to changes in the transition from spectrum to spectrum, in other words in the time domain. These 2D plots are shown in Figure 5 for the selected sample group (samples S2 and S6).

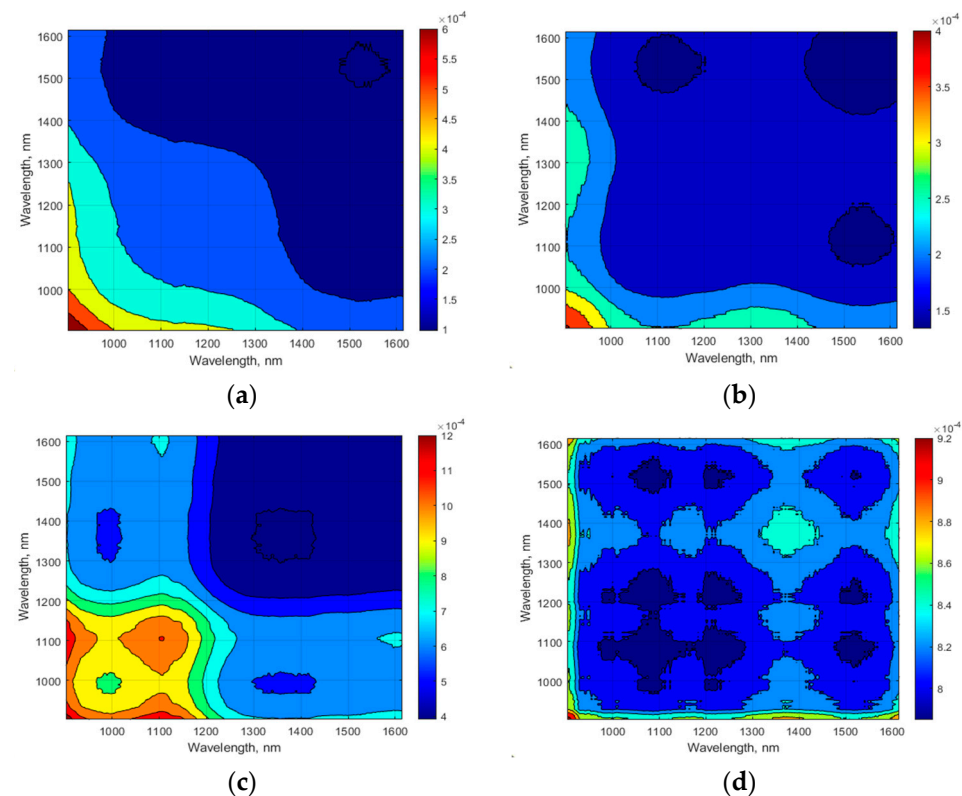


Figure 5. 2D-COS synchronous spectra of the samples S2 (c,d) and S6 (a,b). (a,c) Foil side excitation; (b,d) electrode side excitation.

The analysis of the 2D-COS synchronous spectra showed that the spectra most sensitive to changes in the intensity ratio were not the same for the individual analysed samples and also depended on the side of the sample from which the reflection spectrum was measured, from the foil side or the electrode side.

We observed that: first, samples without the sputtering electrode had a similar reflectance spectrum regardless of the side from which the reflection was measured; second, the most substantial peak of the reflected light intensity lay in the region of 900–1000 nm

(Figure 5c,d), while the exact location of the file was not stable from sample to sample and for the same sample over time. In diagram Figure 5b, there is a characteristic area of 1050–1150 m (the orange area in the chart). In the remaining areas, the 2D-COS synchronous spectra characteristics are similar to the characteristics presented in Figure 5c,d. The characteristic in Figure 5a obtained during the measurements from the Ag foil side was completely different from the others and did not undergo any noticeable changes in the time domain.

The analysis of the 2D-COS synchronous spectra allowed us to select the optimal spectral regions to determine the $R_{\text{ratio}}(t)$ parameter for a series of measurements for each of the measured samples. These results are shown in Figures 6a, 7a, 8a and 9a in the form of the autocorrelation spectra (main diagonal of the 2D-COS synchronous spectrum), and the dependence of the $R_{\text{ratio}}(t)$ parameter in the time domain over 720 h is shown in Figures 6b, 7b, 8b and 9b. In Figures 6b, 7b, 8b and 9b, the $R_{\text{ratio}}(t)$ parameter was normalised, to compare the results, to a value of 1.0 at the measurement start point (for $t = 0$).

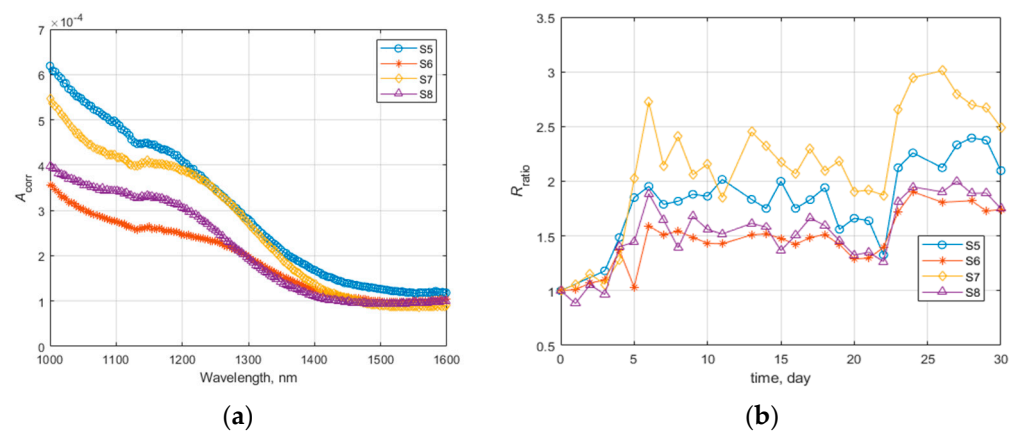


Figure 6. (a) Autocorrelation spectra (main diagonal of the 2D-COS synchronous spectrum) of samples without the Ag electrode (S5, S6, S7 and S8), excited from the foil side; the spectral region for the calculation of the parameter $R_{\text{ratio}}(t)$ was: $R_{\text{ratio}}(t) = R(t, 1000 \text{ nm})/R(t, 1550 \text{ nm})$. (b) The R_{ratio} vs. time.

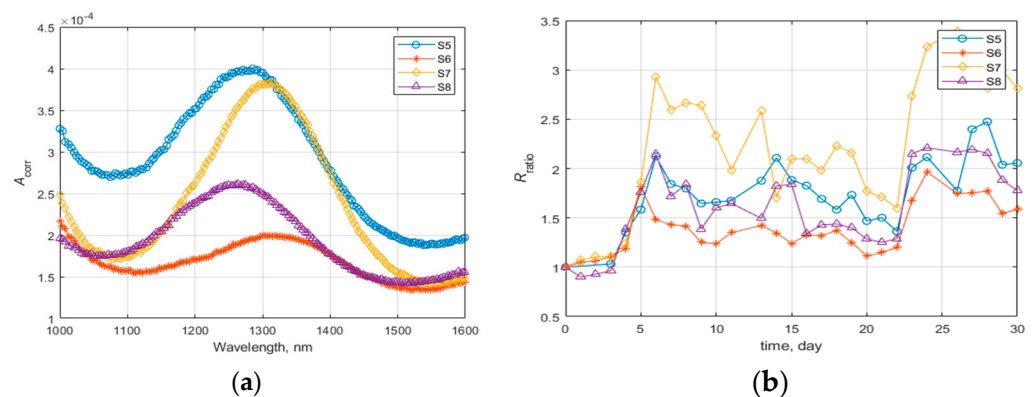


Figure 7. (a) Autocorrelation spectra (main diagonal of the 2D-COS synchronous spectrum) of samples without the Ag electrode (S5, S6, S7 and S8), excited from the electrode side. (b) The R_{ratio} vs. time.

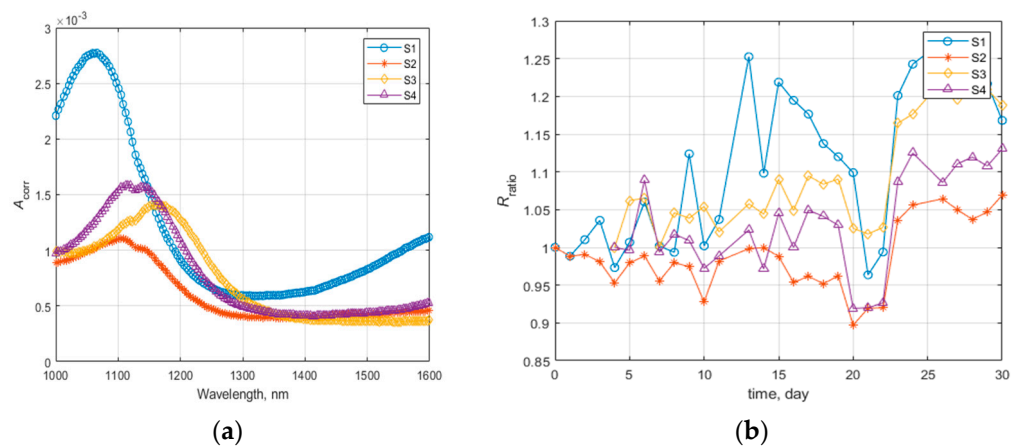


Figure 8. (a) Autocorrelation spectra (main diagonal of the 2D-COS synchronous spectrum) of samples with the Ag electrode (S1, S2, S3 and S4); excited from the foil side. (b) The R_{ratio} vs. time.

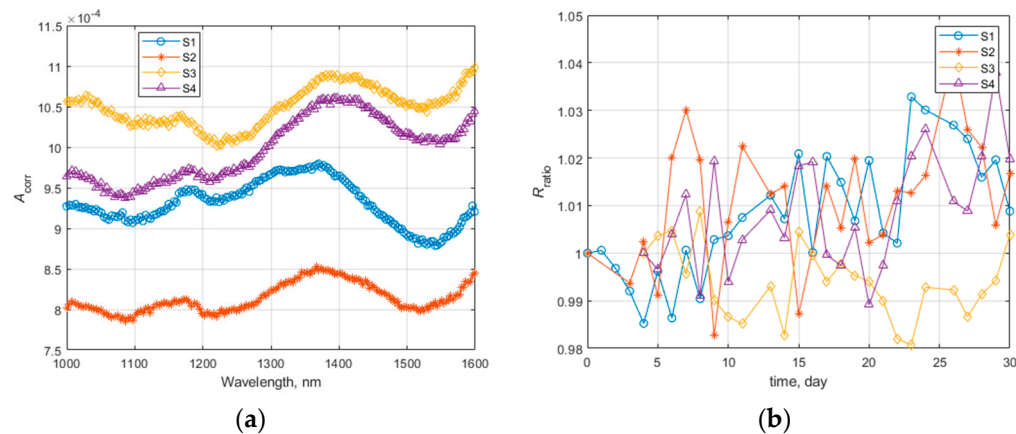


Figure 9. (a) Autocorrelation spectra (main diagonal of the 2D-COS synchronous spectrum) of samples with the Ag electrode (S1, S2, S3 and S4); excited from the electrode side; the spectral region for the calculation of the parameter $R_{\text{ratio}}(t)$ was: $R_{\text{ratio}}(t) = R(t, 1400 \text{ nm})/R(t, 1500 \text{ nm})$. (b) The R_{ratio} vs. time.

According to the autocorrelation spectra presented in Figure 7a, the chosen spectral regions for calculating the parameter $R_{\text{ratio}}(t)$ were recorded as follows:

- S1: $R_{\text{ratio}}(t) = R(t, 1278 \text{ nm})/R(t, 1583 \text{ nm})$
- S2: $R_{\text{ratio}}(t) = R(t, 1321 \text{ nm})/R(t, 1583 \text{ nm})$
- S3: $R_{\text{ratio}}(t) = R(t, 1314 \text{ nm})/R(t, 1583 \text{ nm})$
- S4: $R_{\text{ratio}}(t) = R(t, 1268 \text{ nm})/R(t, 1583 \text{ nm})$

As can be seen, the measurements of the $R_{\text{ratio}}(t)$ parameter varied over time, for this series of samples lacking a sputtered silver electrode, up to a maximum of 300%. The nature of the changes was very similar to that observed in the two series of measurements presented in Figures 5 and 6, regardless of the side from which the sizes of the reflection spectrum were determined. It can be concluded that the critical areas on the measurement time axis were approximately 4–6 days and 22–24 days. Under these measurement conditions, assuming that the parameters of the transparent film did not change, it can be concluded that the changes in the $R_{\text{ratio}}(t)$ parameter may be directly related to the changes in the optical properties of the perovskite layer and, in a sense, represent its so-called ageing.

According to the autocorrelation spectra presented in Figure 8a, the chosen spectral regions for the calculation the parameter $R_{\text{ratio}}(t)$ were the following:

- S1: $R_{\text{ratio}}(t) = R(t, 1059 \text{ nm})/R(t, 1332 \text{ nm})$

- S2: $R_{\text{ratio}}(t) = R(t, 1108 \text{ nm})/R(t, 1397 \text{ nm})$
- S3: $R_{\text{ratio}}(t) = R(t, 1176 \text{ nm})/R(t, 1397 \text{ nm})$
- S4: $R_{\text{ratio}}(t) = R(t, 1128 \text{ nm})/R(t, 1397 \text{ nm})$

As can be seen from Figure 9b, which presents the measurements from the Ag foil side, significant changes in the $R_{\text{ratio}}(t)$ parameter were not observed over time, i.e., the parameter fluctuations did not exceed 2%.

The results presented above indicate that in the reflectance spectra measured with the use of the express-measurement method using the DLP NIRSCAN NANO spectrometer, the parameter $R_{\text{ratio}}(t) = R(t, \lambda_1 \text{ nm})/R(t, \lambda_2 \text{ nm})$ can be determined, which can characterise changes in the optical characteristics of light reflection from the perovskite solar cell structure over time and be a specific ageing parameter of the cell. The obtained data show that this process is not monotonic. In the applied tracking area, the most characteristic changes were observed after 4–5 and 21–22 days from the start of the measurements (12–12 and 28–29 days from the production date). Obviously, introducing this type of measurement into the production cycle and starting the measurements immediately after the production of cell structures may provide a result that can be directly applied and considered in the technological process.

4. Conclusions

The spectra of optical reflectance in the NIR range for perovskite cell structures were analysed. Due to the possible changes in the absolute values of the spectra, the ratio of the reflectance for the wavelength for which the most significant changes were observed over time to the reflectance for the wavelength for which the most minor changes were observed was selected as an indicator for the evaluation of cell ageing. The 2D-COS method was used to determine the wavelengths. Two groups of samples (without the sputtered silver electrode and with the sputtered electrode) were characterised by the different shapes of the spectra and the different shapes of the reflectance ratio as a function of time. The reflectance ratio characteristics were similar for samples without a sputtered silver electrode, regardless of the surface (the side with the foil and the side with the active layer) on which the reflectance was measured. The greatest changes in reflectance were observed in the region between 1000 nm and 1350 nm, and the smallest changes in the region around 1600 nm. Characteristic differences in the reflectance ratio over time were observed after 4–5 days and 22–24 days. The most significant changes in the reflectance ratio after 30 days amounted to 300%. Much more minor changes in the reflectance ratio were observed for the samples with the sputtered silver electrode. For measurements from the foil side, the ratio changes amounted to a maximum of 25% after 30 days of measures and to a maximum of 3% for sizes from the silver foil side. Hence the conclusion is that the silver electrode protects the active layer against degradation to some extent. The presented method allows finding the moment at which changes in the physicochemical properties of the cell's active layer appear in a non-destructive and contactless way at any stage of the cell production.

In relation to the physical mechanism of the changes in the spectra, the most common degradation pathway is the generation of iodine vapour, I₂—which has low defect formation energies [29]. When under storage at ambient conditions, the iodine vapour could escape the perovskite lattice causing further degradation [30].

Metal-based counter electrodes could prevent this to a certain extent [31]. However, under illuminative or electrical stresses, the reaction of metal electrodes with iodine is a cause of defect formation due to the exhaustion of iodine from the perovskite lattice under the influence of an electric field [32]. We still have to carry out future experiments to quantify the chemical species observed by NIR reflection spectroscopy.

The applied method uses miniature, very mobile equipment. It allows us to conduct and record a six-fold measurement of the entire spectrum in a few seconds and is characterised by exceptional mobility and simplicity. Such approach, having an obvious limitation

as to the depth of the analysis of the processes involved, opens a new path for the practical study of the temporal stability of perovskite solar cells.

Author Contributions: Conceptualisation: K.W. and A.P.; data curation: M.G. and P.S.; formal analysis: P.S.; investigation: M.G., S.D., L.B. and T.A.; methodology: S.D., L.B., T.A., P.S., K.W. and A.P.; software: L.B.; supervision: K.W. and A.P.; validation: M.G., L.B., P.S. and A.P.; writing—original draft: M.G., S.D., L.B., T.A. and A.P.; writing—review & editing: S.D., P.S. and A.P. All authors have read and agreed to the published version of the manuscript.

Funding: The study was funded on the basis of internal work plans, there were no special grants.

Institutional Review Board Statement: Not applicable.

Informed Consent Statement: Not applicable.

Data Availability Statement: Not applicable.

Conflicts of Interest: The authors declare no conflict of interest.

References

1. Photovoltaic Report. Fraunhofer Institute for Solar Energy Systems Freiburg. 24 February 2022. Available online: <https://www.ise.fraunhofer.de/content/dam/ise/de/documents/publications/studies/Photovoltaics-Report.pdf> (accessed on 20 July 2022).
2. NREL Chart. Available online: <https://www.nrel.gov/pv/assets/pdfs/best-research-cell-efficiencies-rev220630.pdf> (accessed on 20 July 2022).
3. Kojima, A.; Teshima, K.; Shirai, Y.; Miyasaka, T. Organometal halide perovskites as visible-light sensitizers for photovoltaic cells. *J. Am. Chem. Soc.* **2009**, *131*, 6050–6051. [[CrossRef](#)] [[PubMed](#)]
4. Lee, M.M.; Teuscher, J.; Miyasaka, T.; Murakami, T.N.; Snaith, H.J. Efficient hybrid solar cells based on meso-superstructured organometal halide perovskites. *Science* **2012**, *338*, 643–647. [[CrossRef](#)] [[PubMed](#)]
5. Kim, H.-S.; Lee, C.-R.; Im, J.-H.; Lee, K.-B.; Moehl, T.; Marchioro, A.; Moon, S.-J.; Humphry-Baker, R.; Yum, J.-H.; Moser, J.E.; et al. Lead iodide perovskite sensitized all-solid-state submicron thin film mesoscopic solar cell with efficiency exceeding 9%. *Sci. Rep.* **2012**, *2*, 591. [[CrossRef](#)]
6. Green, M.A.; Dunlop, E.D.; Hohl-Ebinger, J.; Yoshita, M.; Kopidakis, N.; Hao, X. Solar Cell Efficiency Tables (Version 58). *Prog. Photovolt. Res. Appl.* **2021**, *29*, 657–667. [[CrossRef](#)]
7. Jeong, J.; Kim, M.; Seo, J.; Seo, J.; Lu, H.; Ahlawat, P.; Mishra, A.; Yang, Y.; Hope, M.A.; Eickemeyer, F.T.; et al. Pseudo-halide anion engineering for α -FAPbI₃ perovskite solar cells. *Nature* **2021**, *592*, 381–385. [[CrossRef](#)] [[PubMed](#)]
8. Al-Ashouri, A.; Köhnen, E.; Bor, L.; Magomedov, A.; Hempel, H.; Caprioglio, P.; Márquez, J.; Morales Vilches, A.B.; Kasparavicius, E.; Smith, J.A.; et al. Monolithic perovskite/silicon tandem solar cell with >29% efficiency by enhanced hole extraction. *Science* **2020**, *370*, 1300–1309. [[CrossRef](#)]
9. Leijtens, T.; Bush, K.; Cheacharoen, R.; Beal, R.; Bowring, A.; McGehee, M.D. Towards enabling stable lead halide perovskite solar cells; interplay between structural, environmental, and thermal stability. *J. Mater. Chem. A* **2017**, *5*, 11483–11500. [[CrossRef](#)]
10. Conings, B.; Drijkoningen, J.; Gauquelin, N.; Babayigit, A.; D’Haen, J.; D’Olieslaeger, L.; Ethirajan, A.; Verbeeck, J.; Manca, J.; Mosconi, E.; et al. Intrinsic thermal instability of methylammonium lead trihalide perovskite. *Adv. Energy Mater.* **2015**, *5*, 1500477. [[CrossRef](#)]
11. Yang, J.; Siempelkamp, B.D.; Liu, D.; Kelly, T.L. Investigation of CH₃NH₃PbI₃ degradation rates and mechanisms in controlled humidity environments using in situ techniques. *ACS Nano* **2015**, *9*, 1955–1963. [[CrossRef](#)]
12. Han, Y.; Meyer, S.; Dkhissi, Y.; Weber, K.; Pringle, J.M.; Bach, U.; Spiccia, L.; Cheng, Y.-B. Degradation observations of encapsulated planar CH₃NH₃PbI₃ perovskite solar cells at high temperatures and humidity. *J. Mater. Chem. A* **2015**, *3*, 8139–8147. [[CrossRef](#)]
13. Rolston, N.; Watson, B.L.; Bailie, C.D.; McGehee, M.D.; Bastos, J.P.; Gehlhaar, R.; Kim, J.-E.; Vak, D.; Mallajosyula, A.T.; Gupta, G.; et al. Mechanical integrity of solution-processed perovskite solar cells. *Extrem. Mech. Lett.* **2016**, *9*, 353–358. [[CrossRef](#)]
14. Cheacharoen, R.; Rolston, N.; Harwood, D.; Bush, K.A.; Dauskardt, R.H.; McGehee, M.D. Encapsulating perovskite solar cells to withstand damp heat and thermal cycling. *Sustain. Energy Fuels* **2018**, *2*, 2398–2406. [[CrossRef](#)]
15. Cheacharoen, R.; Rolston, N.; Harwood, D.; Bush, K.A.; Dauskardt, R.H.; McGehee, M.D. Design and understanding of encapsulated perovskite solar cells to withstand temperature cycling. *Energy Environ. Sci.* **2018**, *11*, 144–150. [[CrossRef](#)]
16. Ahmad, T.; Dasgupta, S.; Almosni, S.; Dudkowiak, A.; Wojciechowski, K. Encapsulation protocol for flexible perovskite solar cells enabling stability in accelerated aging tests. *Energy Environ. Sci.* **2022**, e12434. [[CrossRef](#)]
17. Braly, I.L.; Stoddard, R.J.; Rajagopal, A.; Jen, A.K.-Y.; Hillhouse, H.W. Photoluminescence and Photoconductivity to Assess Maximum Open-Circuit Voltage and Carrier Transport in Hybrid Perovskites and Other Photovoltaic Materials. *J. Phys. Chem. Lett.* **2018**, *9*, 3779–3792. [[CrossRef](#)]
18. Mei, A.; Sheng, Y.; Ming, Y.; Hu, Y.; Rong, Y.; Zhang, W.; Luo, S.; Na, G.; Tian, C.; Hou, X.; et al. Stabilizing Perovskite Solar Cells to IEC61215:2016 Standards with over 9000-h Operational Tracking. *Joule* **2020**, *4*, 2646–2660. [[CrossRef](#)]

19. Zhang, H.; Li, Y.; Tan, S.; Chen, Z.; Song, K.; Huang, S.; Shi, J.; Luo, Y.; Li, D.; Meng, Q. High-efficiency (>20%) planar carbon-based perovskite solar cells through device configuration engineering. *J. Colloid Interface Sci.* **2022**, *608*, 3151–3158. [[CrossRef](#)]
20. Kim, N.-K.; Min, Y.H.; Noh, S.; Cho, E.; Jeong, G.; Joo, M.; Ahn, S.-W.; Lee, J.S.; Kim, S.; Ihm, K.; et al. Investigation of Thermally Induced Degradation in CH₃NH₃PbI₃ Perovskite Solar Cells using In-situ Synchrotron Radiation Analysis. *Sci. Rep.* **2017**, *7*, 4645. [[CrossRef](#)]
21. Dou, B.; Wheeler, L.M.; Christians, J.A.; Moore, D.T.; Harvey, S.P.; Berry, J.J.; Barnes, F.S.; Shaheen, S.E.; van Hest, M.F. Degradation of Highly Alloyed Metal Halide Perovskite Precursor Inks: Mechanism and Storage Solutions. *ACS Energy Lett.* **2018**, *3*, 979–985. [[CrossRef](#)]
22. Gaşiorowski, M.; Patryn, A.; Bychto, L. *Possibilities and Area of Application of the Small Size DLP NIRSCAN NANO Spectrometer for Instant Spectral Measurements*; Research Notes of Faculty of Electronics and Computer Science; Koszalin University of Technology: Koszalin, Poland, 2020; pp. 57–70. (In Polish)
23. Gaşiorowski, M.; Szymak, P.; Bychto, L.; Patryn, A. Application of Artificial Neural Networks in Analysis of Time-Variable Optical Reflectance Spectra in Digital Light Projection. *Coatings* **2022**, *12*, 37. [[CrossRef](#)]
24. Singh, R.K.; Kumar, R.; Kumar, A.; Jain, N.; Singh, R.K.; Singh, J. Novel synthesis process of methyl ammonium bromide and effect of particle size on structural, optical and thermodynamic behavior of CH₃NH₃PbBr₃ organometallic perovskite light harvester. *J. Alloys Compd.* **2018**, *743*, 728–736. [[CrossRef](#)]
25. Ahmad, T.; Wilk, B.; Radicchi, E.; Pineda, R.F.; Spinelli, P.; Jan, H.; Castriotta, L.A.; Dasgupta, S.; Mosconi, E.; de Angelis, F.; et al. New Fullerene Derivative as an n-Type Material for Highly Efficient, Flexible Perovskite Solar Cells of a p-i-n Configuration. *Adv. Funct. Mater.* **2020**, *30*, 2004357. [[CrossRef](#)]
26. *DLP NIRScan Nano EVM User's Guide*; Texas Instruments: Dallas, TX, USA, 2017. Available online: <https://www.ti.com/lit/ug/dlpu030g/dlpu030g.pdf> (accessed on 20 July 2022).
27. Noda, I. Two-Dimensional Infrared (2D IR) Spectroscopy: Theory and Applications. *Appl. Spectrosc.* **1990**, *44*, 550–561. [[CrossRef](#)]
28. Park, Y.; Noda, I.; Jung, Y.M. Two-dimensional correlation spectroscopy in polymer study. *Front. Chem.* **2015**, *3*, 14. [[CrossRef](#)]
29. Zhang, T.; Meng, X.; Bai, Y.; Xiao, S.; Hu, C.; Yang, Y.; Chen, H.; Yang, S. Profiling the organic cation-dependent degradation of organolead halide perovskite solar cells. *J. Mater. Chem. A* **2017**, *5*, 1103–1111. [[CrossRef](#)]
30. Zhidkov, I.S.; Poteryaev, A.I.; Kukharenko, A.I.; Finkelstein, L.D.; Cholakh, S.O.; Akbulatov, A.F.; Troshin, P.A.; Chueh, C.-C.; Kurmaev, E.Z. XPS evidence of degradation mechanism in CH₃NH₃PbI₃ hybrid perovskite. *J. Phys. Condens. Matter* **2020**, *32*, 095501. [[CrossRef](#)]
31. Boyd, C.C.; Cheacharoen, R.; Bush, K.A.; Prasanna, R.; Leijtens, T.; McGehee, M.D. Barrier Design to Prevent Metal-Induced Degradation and Improve Thermal Stability in Perovskite Solar Cells. *ACS Energy Lett.* **2018**, *3*, 1772–1778. [[CrossRef](#)]
32. Besleaga, C.; Abramiuc, L.E.; Stancu, V.; Tomulescu, A.G.; Sima, M.; Trinca, L.; Plugaru, N.; Pintilie, L.; Nemnes, G.A.; Iliescu, M.; et al. Iodine Migration and Degradation of Perovskite Solar Cells Enhanced by Metallic Electrodes. *J. Phys. Chem. Lett.* **2016**, *7*, 5168–5175. [[CrossRef](#)]

Cite this: *J. Mater. Chem. A*, 2022, **10**, 11046

Solution-processable perylene diimide-based electron transport materials as non-fullerene alternatives for inverted perovskite solar cells†

German Soto Perez,^a Shyantana Dasgupta,^{be} Wiktor Żuraw,^{id}^{bf} Rosinda Fuentes Pineda,^c Konrad Wojciechowski,^{id}^{bc} Lethy Krishnan Jagadamma,^d Ifor Samuel^{id}^d and Neil Robertson^{id}^{*a}

Perylene diimide derivatives with different functional groups (OR) in the bay position were synthesised (PDI-1, OR = OC₆H₄OMe; PDI-2, OR = OC₆H₄CH₂CH₂NHBoc; PDI-3, OR = OC₆H₄CO₂Me) and their optoelectronic properties were characterised. The derivatives were applied as alternative electron transport materials (ETMs) to replace the commonly used PCBM in inverted perovskite solar cells (PSCs). Devices with the structure ITO/PTAA/Cs_{0.04}(MA_{0.17}FA_{0.83})_{0.96}Pb(I_{0.83}Br_{0.17})₃/ETM/Ag (ETM = PCBM or PDI-1, -2 or -3) were fabricated through solution processing techniques. A competitive power conversion efficiency (PCE) of 16.8% was obtained for the PDI-3-based device, which was comparable to the PCBM-based device with PCE of 17.3%. It was found that the electronic nature of the functional groups plays an important role in the charge extraction and band alignment of these small molecular semiconductors.

Received 17th February 2022

Accepted 21st April 2022

DOI: 10.1039/d2ta01321e

rsc.li/materials-a

Introduction

Over the last decade, perovskite solar cells (PSCs) have demonstrated their enormous potential in the photovoltaic field with simple and low-cost fabrication and a remarkable increase in power conversion efficiency from 3.8% in 2009 (ref. 1) to the current record of 25.5%.² Although the inherent properties of the organic-inorganic halide perovskites make them outstanding photoactive materials, a great contribution to the rapid development of PSCs is due to the research in device architecture, interface engineering and tailoring of charge transport materials.^{3–5} Unlike their dye-sensitised solar cell (DSSCs) predecessor, PSCs were found to perform better when the perovskite absorber is sandwiched between solid charge transport materials; commonly, TiO₂ as electron transport material (ETM) and 2,2',7,7'-tetrakis-(*N,N*-dip-methoxyphenylamine)-9,9'-spirobifluorene (spiro-OMeTAD) as hole transport

material (HTL) are used in an ITO/ETM/perovskite/HTM/Au configuration, also known as a regular or n-i-p architecture.⁶ In particular, TiO₂ prevailed as ETM due to its suitable conductivity ($0.11 \times 10^{-4} \text{ S cm}^{-1}$)⁷ and favourable conduction band level (-3.9 eV). However, its photocatalytic nature, its ease of surface defect formation and the high temperature processing, requiring $\sim 500 \text{ }^\circ\text{C}$, hinders large-scale manufacturing and limits the choice of substrates.

In order to overcome such drawbacks, perovskite-based absorbers have been studied in other device architectures, such as that akin to organic photovoltaics (OPVs), in which the organic semiconducting absorber layer was substituted by CH₃NH₃PbI₃ (MAPI) while leaving the PCBM ETM and PEDOT:PSS HTM unmodified, delivering an initial efficiency of 3.9%.⁸ A key point of this PSC was the inverted order of the ETM and HTM within the device compared to the regular architecture which gave birth to an inverted PSC (p-i-n) with an ITO/HTM/perovskite/ETM/Ag configuration. The organic nature of the transport materials enabled the use of flexible substrates due to their low temperature processing ($<150 \text{ }^\circ\text{C}$). The study of these inverted perovskite solar cells (i-PSCs) notably pushed the efficiency to 20.9% (ref. 9) within a few years. However, since most of the initial attention was drawn to device optimisation and interface engineering, the materials inherited from the initial OPV architecture remained, and most studies still rely on fullerene-based organic semiconductors due to their effective performance.

Although fullerenes possess good energy alignment and suitable electron mobility, the lack of other desirable features

^aSchool of Chemistry, University of Edinburgh, Kings Buildings, Edinburgh, EH9 3JJ, UK. E-mail: neil.robertson@ed.ac.uk

^bSaule Research Institute, Wroclaw PL 54-130, Poland

^cSaule Technologies, Wroclaw PL 54-427, Poland

^dOrganic Semiconductor Centre, School of Physics and Astronomy, SUPA, University of St Andrews, St Andrews, KY16 9SS, UK

^eFaculty of Materials Engineering and Technical Physics, Poznan University of Technology Piotrowo 3, 60-965 Poznan, Poland

^fDepartment of Semiconductor Materials Engineering, Wroclaw University of Science and Technology, Wybrzeże Wyspiańskiego 27, 50-370 Wroclaw, Poland

† Electronic supplementary information (ESI) available. See <https://doi.org/10.1039/d2ta01321e>



such as thermal and photochemical stability and cost-effective preparation and purification, remain drawbacks for these n-type organic semiconductors. Compared to fullerenes, non-fullerene organic semiconductors have shown better stability, simpler and more straightforward synthetic procedures and enhanced processability, in addition to low-cost production.¹⁰ For instance, polymers have been widely studied due to the tunability of their electronic properties, as well as the modulation of film morphology and tailored compatibility with the other layers in the device, which leads to improvement in efficiency and stability, however, their typical poor electron mobility requires the use of very thin layers (~ 5 nm) hindering their large-scale application.¹¹ Compared to their polymeric counterparts, small molecule semiconductors possess adjustable packing, monodispersity, high synthetic reproducibility and tunable conductivity. Naphthalene diimides are major representatives of this kind of molecule in inverted PSCs; their commercial availability, ease of synthesis and high solubility in several organic solvents, makes them excellent building blocks.¹² Other π -conjugated systems have so far been less explored, such as perylene diimide derivatives, which have recently attracted a lot of attention as n-type organic semiconductors with high electron mobility ($\sim 8 \times 10^{-2} \text{ cm}^2 \text{ V}^{-1} \text{ s}^{-1}$ for single crystals)¹³ and high thermal, chemical and photochemical stability.^{14–16} Perylene derivatives have the advantage of tunability of their optoelectronic properties through simple structural modifications, alongside easy and low-cost synthesis and purification with high yields and reproducibility, making them suitable substitutes for expensive and unstable fullerenes.^{17,18} Previous studies have shown the potential of PDIs as ETMs through the use of different functional groups attached to alkyl chains in the imide position,^{19–22} Click or tap here to enter text.as dimers or assemblies of higher dimensionality^{23–27} or as

buffer layer or additive either through solution^{28,29} or evaporation techniques.³⁰

In this study, three highly soluble perylene diimide electron acceptor molecules (Fig. 1a) were designed based on the core contortion approach,^{31,32} making them suitable for solution-processing technique while at the same time avoiding the use of long isolating alkyl chains. PDIs with four substituent groups in the bay position have received limited attention in PSCs^{33,34} despite the potential advantages in solubility while maintaining suitable pi-interactions. Their synthesis was carried out through the initial reaction of benzylamines in the imide position and further attachment of different functional groups at the bay positions of each molecule (Fig. 1a). Their optoelectronic properties were characterised and performance as ETMs studied in an inverted perovskite solar cell with the layout Glass/ITO/PTAA/Cs_{0.04}(MA_{0.17}FA_{0.83})_{0.96}Pb(I_{0.83}Br_{0.17})₃/PDI/BCP/Ag to assess them as potential alternatives to the commonly used PCBM.

Experimental section

Synthesis

Compound **1** was used as starting material for the three different PDI derivatives, it was synthesised following the procedure developed by R. K. Dubey *et al.*³⁵ Compounds **2** and **3** were synthesised from compound **1** by sequential reactions with the corresponding benzylamine following literature procedures.^{36,37}

PDI-1. Compound **2** (0.4 g, 0.54 mmol), 4-methoxyphenol (0.34 g, 2.7 mmol) and K₂CO₃ (0.19 g, 1.35 mmol) were mixed in *N*-methylpyrrolidone (NMP) (8 ml). The reaction was stirred at 120 °C for 68 h under N₂. After cooling to room temperature, the mixture was added dropwise to 40 ml of 1 M HCl solution and vigorously stirred for 1 hour at room temperature. The solid was separated by filtration and successively washed with water and methanol. The product was dried under vacuum and purified by chromatographic column with eluent DCM : MeOH [99 : 1] on neutral Al₂O₃. The final product was obtained as a purple powder (0.273 g, 46.3% yield). (ESI:MS): [M + H]⁺ calculated for C₆₆H₄₇O₁₄N₂: 1091.3021 and [M + Na]⁺ calculated for C₆₆H₄₆O₁₄N₂Na: 1113.2841; found, 1091.2973 and 1113.2862 respectively. Elemental analysis (CHN) calculated for C₆₆H₄₆N₂O₁₄: C: 72.65; H: 4.25; N: 2.57. Found: C: 72.61; H: 4.48; N: 2.50.

PDI-2. Compound **3** (0.22 g, 0.3 mmol), *N*-BOC-tyramine (0.43 g, 1.79 mmol) and K₂CO₃ (0.25 g, 1.79 mmol) were mixed in NMP (10 ml) and stirred at 110 °C for 20.5 h. After cooling to room temperature, the mixture was poured into a 0.5 M HCl solution and stirred for 5 minutes. Purification was performed through a chromatographic column with DCM : MeOH [95 : 5] eluent. The product was obtained as a dark-red powder (0.285 g, 61.68% yield). (ESI:MS): [M + Na]⁺ calculated for C₉₂H₉₄O₁₆N₆Na: 1561.66185; found, 1561.6595. Elemental analysis (CHN) calculated for C₉₂H₉₄N₆O₁₆: C: 71.76; H: 6.15; N: 5.46. Found: C: 71.89; H: 6.29; N: 5.35.

PDI-3. Compound **3** (0.2 g, 0.27 mmol), methyl-4-hydroxybenzoate (0.25 g, 1.63 mmol) and K₂CO₃ (0.23 mg, 1.63 mmol) were mixed in NMP (3.6 ml) and stirred for 15 h at

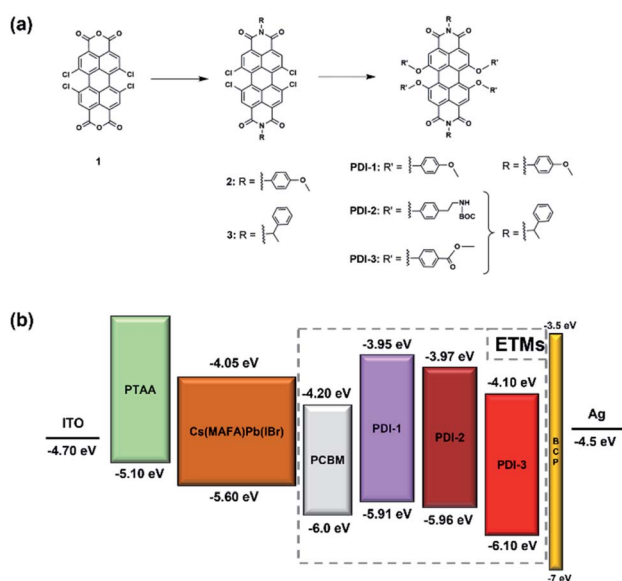


Fig. 1 (a) Molecular structure of the different PDI electron acceptors tested as ETMs, (b) energy band diagram of each material used in the perovskite solar cell.



110 °C under N₂. Once cooled to room temperature, the mixture was added dropwise to a 1 M HCl solution, the precipitate was filtered, dried and purified by chromatographic column with DCM : ethyl acetate [25 : 1] eluent. The pure product was obtained as a red powder (0.25 g, 77.4% yield). (ESI:MS): [M + Na]⁺ calculated for C₇₂H₅₀O₁₆N₂Na: 1221.30526; found, 1221.3056. Elemental analysis (CHN) calculated for C₇₂H₅₀N₂O₁₆: C: 72.11; H: 4.20; N: 2.34. Found: C: 72.00; H: 4.30; N: 2.27.

Corresponding NMR spectra and data are shown in Fig. S1.†

Device fabrication

Materials. Unless otherwise stated, all the materials were purchased from Sigma-Aldrich and used as received. Silver pellets were obtained from Kurt Lesker; glass/ITO substrates from Lumtec, and poly-triarylamine (PTAA) from Ossila (product code M0511A5).

Planar heterojunction PSCs were fabricated with the following architecture: ITO/PTAA/Cs_{0.04}(MA_{0.17}FA_{0.83})_{0.96}Pb(I_{0.83}Br_{0.17})₃/ETM/Ag (ETM = PCBM or PDI-1, -2 or -3). First, a PTAA solution (1.5 mg ml⁻¹ in toluene) was spin coated under ambient conditions at 5000 rpm for 30 s, followed by annealing at 100 °C for 10 min (≈ 20 nm thick). Subsequently, the samples were transferred into a nitrogen-filled glovebox for the perovskite layer deposition. For the perovskite precursor preparation, stock solutions of PbI₂ and PbBr₂ (1.5 M) in dimethylformamide (DMF)/dimethyl sulfoxide (DMSO) mixture [4 : 1 v/v] were prepared. Then, for FAPbI₃ and MAPbBr₃ solutions, FAI and MABr powders were weighed out into separate vials, followed by addition of PbI₂ (into FAI) and PbBr₂ (into MABr) solutions. Both lead solutions were added in excess, to obtain an over stoichiometric lead content (FAI/MABr : PbI₂/PbBr₂ equals 1.0 : 1.09). The final perovskite precursor solution was prepared by mixing the solutions of FAPbI₃ and MAPbBr₃ in a [5 : 1 v/v] ratio. Then, 40 μL of CsI solution (1.5 M solution in DMSO) was added to 1 ml of the mixture. Perovskite layer (≈ 580 nm thick) was deposited on top of PTAA with a two-step spin-coating procedure, 1500 rpm for 2 s and, 5000 rpm for 34 s. Anhydrous diethyl ether (500 μL) was dispensed on the sample in the last 2 seconds of the spinning sequence. The sample was annealed for 60 min at 100 °C. For the control device, a PCBM solution (20 mg ml⁻¹ in chlorobenzene) was spin-coated at 2000 rpm for 30 s and annealed at 60 °C for 10 min. For the devices with PDI-1, -2 and -3 ETM, PDI solutions (20 mg ml⁻¹ in chlorobenzene) were spin coated at 4000 rpm for 30 s, The solution-processed ETMs were annealed for 10 min at 60 °C. Finally, 5 nm of BCP buffer layer and 95 nm of Ag electrode were deposited on top of devices by thermal evaporation at ≈ 10⁻⁶ mbar, through a shadow mask.

Current-voltage measurements. *J-V* characterization and stabilized power output measurements were performed using a Keithley 2461 source measure unit (SMU) under simulated AM1.5G irradiation (100 mW cm⁻²) using an AAA-rated solar simulator (Abet Technologies, sun 2000) calibrated against an RR-208-KG5 silicon reference cell (Abet Technologies). The mismatch factor for the studied perovskite solar cells was calculated to be 0.968 using external quantum efficiencies (EQEs) of the reference and test cells, lamp's spectrum, and

AM1.5G, and this value was used to correct the intensity of the solar simulator lamp to provide one sun illumination.

Results and discussion

Structural and optoelectronic characterisation

Geometry optimisation of PDI-1 to -3 was carried out through DFT calculations using Gaussian 09 software with the hybrid B3LYP functional and the standard 6-31G(d) basis set for insight into the optoelectronic properties and the core contortion approach that influences the molecular geometry.

Fig. 2 shows that the perylene core in all the PDI derivatives was twisted in the range from 30° to 31° due to the steric effects of the bulky substituents (calculated from the torsion angles (Fig. S2†)); the loss of planarity of the molecules led to a higher solubility compared to unsubstituted perylene, which is prone to intermolecular stacking.³⁸

All the compounds (measured in solution) exhibited similar optical properties with absorption and emission maxima within the ranges of 560–590 nm and 590–625 nm, respectively (Fig. 3); the shifting between spectra is a result of the electronic interaction between the core and the functional groups attached to it. Compared to the literature values of unsubstituted perylene,³⁹ PDI-1 and -2 showed a more significant bathochromic shift of λ_{max(abs)} due to the electron-donating (ED) nature of the methoxyphenol and the BOC-tyramine groups respectively. In contrast, PDI-3 with the electron-withdrawing (EW) methylhydroxybenzoate substituent showed the shortest absorption and emission wavelengths among the three derivatives.⁴⁰

The linear relation between solutions with different concentrations and their corresponding absorption (Fig. S3†) was used to calculate the molar extinction coefficient of each derivative, the optical data are summarised in Table 1.

The electrochemical properties were measured through square wave voltammetry (SWV) and cyclic voltammetry (CV). The SWV in Fig. 4a shows two reversible reduction peaks, each of which represents a one-electron reduction to the stable radical anion and dianion species, respectively.

The chemical and electrochemical reversibility was confirmed by cyclic voltammetry (Fig. 4b), through the reduction and subsequent oxidation of the product to its original form. In addition, no shift of the current peaks with different

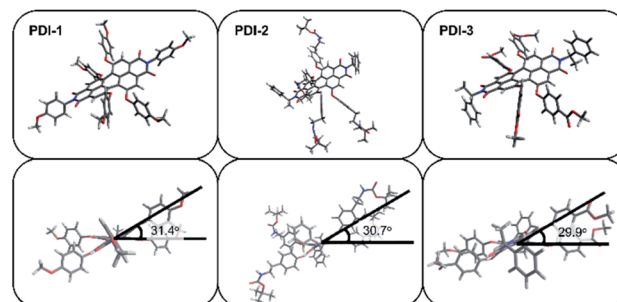


Fig. 2 Calculated geometry of PDI-1 to -3 and their corresponding contortion angle.



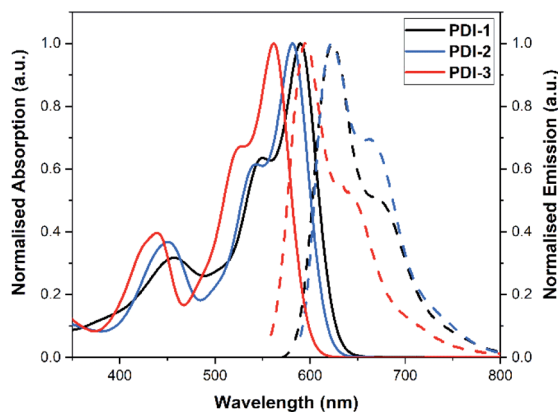


Fig. 3 Normalised absorption (solid line) and emission (dashed line) spectra of each PDI.

Table 1 Summary of the optical properties of PDI-1 to -3. Literature values of unsubstituted PDI are shown as a ref. 27

Sample	$\lambda_{\max}(\text{Abs})$ [nm]	ϵ [$\text{cm}^{-1} \text{M}^{-1}$]	$\lambda_{\max}(\text{Em})$ [nm]	$E_{\text{gap}}^{\text{opt}a}$ [eV]
PDI-1	590	47 200	623	2.04
PDI-2	582	65 200	622	2.05
PDI-3	562	59 300	594	2.14
PDI ²⁷	525	58 000	553	2.13

^a Optical band gap ($E_{\text{gap}}^{\text{opt}}$) was estimated from the intersection of normalised absorption and emission spectra.

scan rates was observed, and a linear relationship between the square root of the scan rate and the current peak was observed.

The electrochemical properties and the calculated levels of highest occupied molecular orbital (HOMO) and lowest unoccupied molecular orbital (LUMO) are summarised in Table 2.

From the data in Table 2, the reduction potentials of the different derivatives are shifted as a result of the electronic nature of the substituents used in each molecule. For instance, PDI-1 has the most negative potentials (due to the high ED nature of the methoxyphenols), followed by PDI-2; whereas PDI-3 has the potentials shifted to more positive values due to the EW nature of the ester group on the substituents. It was also observed that the first reduction potential of each derivative is broadly comparable to the literature value of PCBM ($E_{\text{red}}^{\text{1st}} = -1.16 \text{ V vs. Fc}$),⁴¹ which suggests that all derivatives could be suitable candidates as PCBM substituents. However, from the calculation of HOMO and LUMO levels using the CV experimental data and the equation:

$$E_{\text{HOMO/LUMO}} = -(E_{\text{ox/red}} + 5.1) \text{ (eV)}^{42} \quad (1)$$

PDI-3 shows a better band alignment to the conduction band (-4.05 eV (ref. 43)) of the triple cation perovskite used in this work. It is important to keep in mind however, that CV measurements carried out in solution do not account for any solid-state effects on the material within the final device.

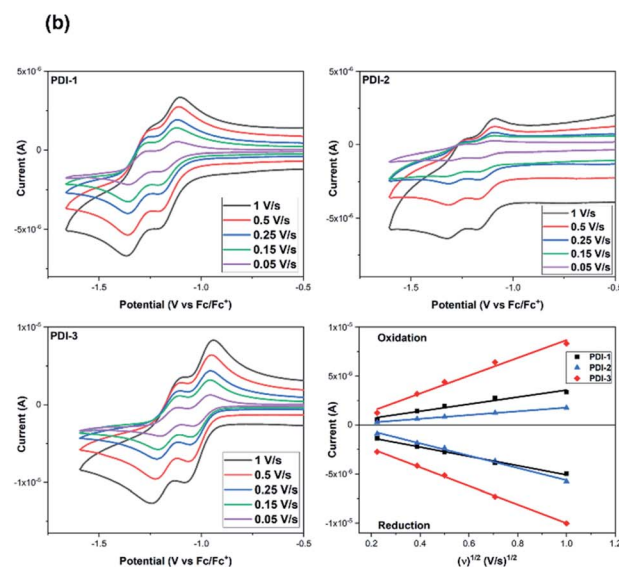
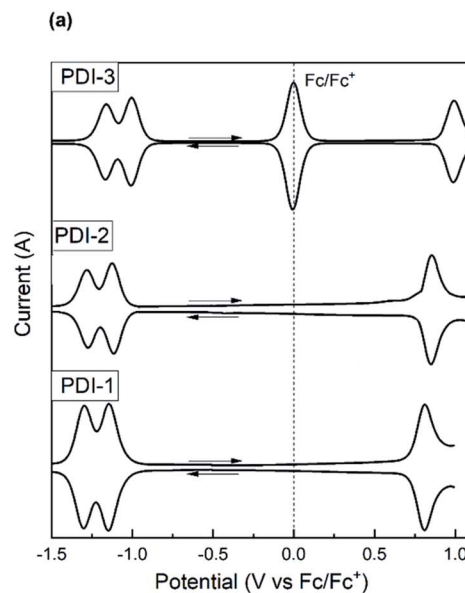


Fig. 4 (a) SWV of PDI-1 to -3, measured at a scan rate of 0.5 V s^{-1} ; the arrows indicate the scan direction. (b) CV of PDI-1 to -3 at different scan rates and the linear relation between the square root of the scan rate and the current peak. Both measurements were carried out in a 0.1 M solution of [TBA] [PF₆] in DCM at room temperature.

Table 2 Summary of the electrochemical properties of PDI-1, -2, and -3. Corresponding potentials (E) were determined from SWV peaks and are quoted against ferrocene/ferrocenium

Sample	E_{ox} [V]	$E_{\text{red}}^{\text{1st}}$ [V]	$E_{\text{red}}^{\text{2nd}}$ [V]	$E_{\text{gap}}^{\text{CV}}$ [eV]	E_{HOMO} [eV]	E_{LUMO} [eV]
PDI-1	+0.81	-1.15	-1.30	1.96	-5.91	-3.95
PDI-2	+0.86	-1.13	-1.28	1.99	-5.96	-3.97
PDI-3	+1.00	-1.00	-1.15	2.00	-6.10	-4.10



Photophysical characterisation

To investigate the suitability of the derivatives as ETMs, steady-state photoluminescence quenching (PLQ) and time-resolved photoluminescence (TRPL) were measured in glass/perovskite and glass/ $\text{Cs}_{0.04}(\text{MA}_{0.17}\text{FA}_{0.83})_{0.96}\text{Pb}(\text{I}_{0.83}\text{Br}_{0.17})_3/\text{ETM}$ (ETM = PCBM or PDI-1, -2 or -3) devices. The PL spectra in Fig. 5a show an intense emission peak at 760 nm from the perovskite-only device when excited at 405 nm; whereas the devices with the different ETMs (PDI-1 to -3 or PCBM) deposited on top of the perovskite show a significant quenching in emission (PCBM > PDI-3 > PDI-2 > PDI-1). Notably, the emission peak in these devices shows a blue shift of approximately 5 nm, which suggests passivation and reduction of trap density in the ETM/perovskite interface.⁴⁴

TRPL spectra in Fig. 5b shows a similar trend, in which PL lifetime of bare perovskite film (164 ns) decreases upon deposition of PCBM (20 ns), PDI-3 (70 ns), PDI-2 (76 ns) and PDI-1 (79 ns). Collectively, these spectroscopic and electrochemical results indicate the suitability of the PDIs to be tested as ETMs in n-i-p perovskite solar cells.

Additionally, charge mobility studies were carried out, using the space-charge limited current (SCLC) method (Fig. S4†) to assess the electron transport characteristics of the materials. Although it was not possible to observe the trap-free regime, a fit that estimated the trap-filling regime enabled mobilities of the order $10^{-5} \text{ cm}^2 \text{ V}^{-1} \text{ s}^{-1}$ for PDI-1 and PDI-3 and lower mobility around $10^{-6} \text{ cm}^2 \text{ V}^{-1} \text{ s}^{-1}$ for PDI-2, consistent with the bulkier substituents of the latter.

Device characterisation

To screen the performance of the ETMs, an initial set of perovskite solar cells with the configuration ITO/PTAA/ $\text{Cs}_{0.04}(\text{MA}_{0.17}\text{FA}_{0.83})_{0.96}\text{Pb}(\text{I}_{0.83}\text{Br}_{0.17})_3/\text{ETM}/\text{Ag}$ (ETM = PDI-1 to -3) with a 5 nm buffer layer of BCP in the ETM/Ag interface (Fig. S5†) were fabricated in ITO coated PET substrates and characterised. The PDI solutions were optimised to a concentration of 20 mg ml^{-1} and two different spin coating deposition speeds were tested (2000 (A) and 4000 (B) rpm). Fig. S5c† shows the box plots over eight repeats while Fig. S5b† shows the $J-V$ curves of champion devices with each PDI, and Table 3 summarises the corresponding PV parameters.

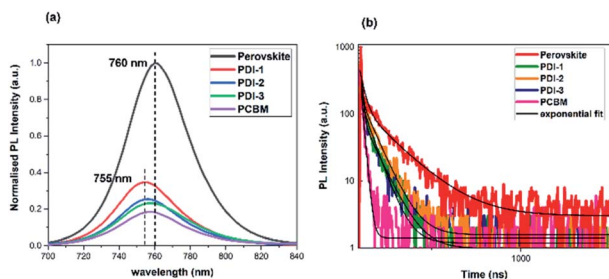


Fig. 5 (a) Steady-state photoluminescence quenching (PLQ). (b) Time-resolved photoluminescence (TRPL) of glass/perovskite and glass/perovskite/ETM devices.

Table 3 PV parameters of champion devices tested at different deposition speeds. A and B denotes 2000 and 4000 rpm deposition speed, respectively. Data in parenthesis are the average over 8 devices

Sample		J_{sc} [mA cm^{-2}]	V_{oc} [V]	FF [%]	PCE [%]
PDI-1	A	7.61 (2.99)	0.84 (0.14)	37.7 (30)	2.60 (0.84)
	B	9.80 (8.51)	0.85 (0.80)	60.2 (50)	5.01 (4.20)
PDI-2	A	0.21 (0.10)	0.69 (0.77)	18.9 (15)	0.03 (0.01)
	B	0.70 (0.15)	0.98 (0.38)	20.6 (18)	0.06 (0.01)
PDI-3	A	16.90 (16.5)	1.01 (0.98)	54.6 (45)	8.70 (8.50)
	B	16.90 (16.1)	1.02 (0.98)	58 (55)	9.80 (7.50)

It was found that PDI-3 was the only derivative suitable to be used as ETM in a full device, delivering the best performance when deposited at 4000 rpm. PDI-1 showed low performance at high-speed deposition whereas low-speed deposition showed an S-type curve, which could be related to a charge accumulation at the PDI-1/perovskite interface due to band offset and non-homogeneous interface.⁴⁵ The device with PDI-2 did not show any significant photocurrent output at all.

However, these results are in good agreement with the LUMO energy values calculated previously for the PDI derivatives. In particular, the LUMO level of PDI-3 ($E_{\text{LUMO}} = -4.1 \text{ eV}$) has a suitable energy alignment with the conduction band of the triple cation perovskite ($E_{\text{conduction}} = -4.05 \text{ eV}$)⁴³ used in the devices, which can also be linked to the PLQ in Fig. 5a, where PDI-3 showed the best quenching among the tested PDIs suggesting better charge extraction from the perovskite photoactive layers compared to the other two ETMs. In contrast, the LUMO values of PDI-1 and -2 (-3.95 and -3.97 eV , respectively) are not as energetically favourable for charge transfer. The apparently poorer (10 times lower) electron mobility of PDI-2 compared to PDI-1 and -3 may also play a role.

Based on the previous results, PDI-3 was used in another set of devices using ITO coated glass substrates and optimising deposition conditions to 5000 rpm ($\sim 40 \text{ nm}$ film thickness). The results were compared with the well-established solution-processable PCBM ETM ($\sim 30 \text{ nm}$ film thickness). The $J-V$ plots of champion cells are shown in Fig. 6a, and the PV parameters are summarised in Table 4.

Fig. 6b shows the stabilised power output over time under a bias voltage at maximum power point.⁴⁶ A stabilised PCE of 16.5% and 14.5% were observed within 35 s for PCBM and PDI-3 devices, respectively. Fig. 6c shows a high spectral response in the range of 400 to 750 nm for both devices and the integrated current density (derived from the IPCE) is 19.2 and 19.3 mA cm^{-2} for PCBM and PDI-3, respectively. The lower value of the J_{sc} from EQE compared to J_{sc} from $J-V$ plot may account for several reasons such as measuring time, sample degradation or measurement conditions,⁴⁷ however, the obtained values are consistent with the trend of J_{sc} values measured in the $J-V$ curves.

The relatively higher J_{sc} of PDI-3 device compared to the PCBM device could be related to a lower rate of recombination in the ETM/perovskite interface, which is in good agreement with the slightly higher value of IPCE for PDI-3 compared to



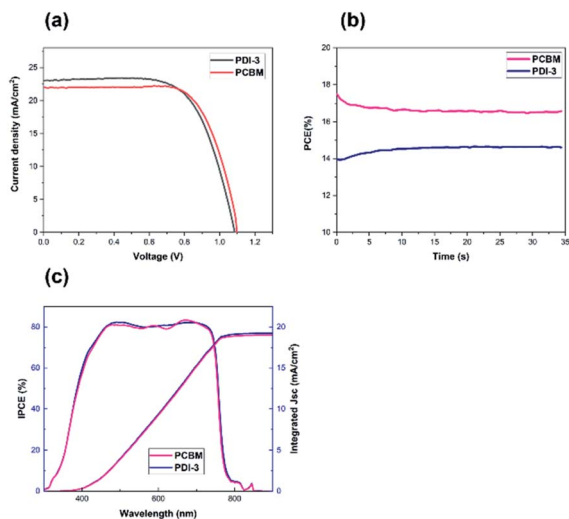


Fig. 6 (a) J - V curves of champion devices over four repeats. (b) Stabilised power output of PDI-3 and PCBM-based devices. (c) IPCE for PDI-3 and PCBM-based devices and the integrated short circuit current density.

Table 4 PV parameters (reverse scan) of PSCs using PDI-3 or PCBM ETMs. Data in parenthesis are the average over 4 devices

ETM	J_{sc} [mA cm^{-2}]	V_{oc} [V]	FF [%]	PCE [%]
PCBM	22.46 (21.70)	1.09 (1.08)	71.5 (70.7)	17.30 (17)
PDI-3	23.02 (22.80)	1.08 (1.08)	67.5 (64.5)	16.80 (16.10)

PCBM device, as shown in Fig. 6c.^{48–50} However, the PCBM device showed a better FF compared to the PDI-3 one, which could be related to a higher mobility of PCBM ($\mu_{\text{PCBM}} = 1.22 \times 10^{-3} \text{ cm}^2 \text{ V}^{-1} \text{ s}^{-1}$)⁵¹ compared to that of PDI-3 ($\mu_{\text{PDI-3}} = 1.6 \times 10^{-5} \text{ cm}^2 \text{ V}^{-1} \text{ s}^{-1}$).

Conclusions

In this work, we have designed, synthesised and assessed perylene diimide derivatives as solution-processable ETMs for PSCs. Also, their synthetic versatility and easy tailoring of optoelectronic properties was studied through the attachment of different functional groups (with different electronic nature) to the molecule. Substitution at the bay-positions of the PDI enabled excellent solubility of the molecules while maintaining sufficient charge mobility. Electrochemistry characterisation and LUMO calculations showed that PDI-3 had a better energy alignment with the triple cation perovskite compared to PDI-1 and -2, which indicates that the appropriate control of the electron donating/withdrawing character of functional groups benefits charge extraction through the modulation of electron affinity in the molecule. PLQ and TRPL experiments revealed a comparable charge extraction between commonly used PCBM and PDI-3, indicating that selection of the appropriate side-groups enables performance of PDI-derivatives which is similar to that of PCBM. Accordingly, the champion PDI-3-

based device delivered a PCE of 16.8%, which was comparable to the PCBM-based device with a 17.3% PCE. These results demonstrate that bay-substituted PDIs provide a successful strategy for replacement of PCBM by small-molecule ETM. Further design and tailoring of properties to optimise performance can be achieved through straightforward organic synthetic routes.

Conflicts of interest

There are no conflicts to declare.

Acknowledgements

Financial support from the National Council of Science and Technology (Conacyt) Mexico. Funding from the Foundation of Polish Science (First TEAM/2017-3/30).

Notes and references

- 1 A. Kojima, K. Teshima, Y. Shirai and T. Miyasaka, Organometal Halide Perovskites as Visible-Light Sensitizers for Photovoltaic Cells, *J. Am. Chem. Soc.*, 2009, **131**, 6050–6051.
- 2 NREL, *Best Research-Cell Efficiency*, <https://www.nrel.gov/pv/cell-efficiency.html>, accessed May 28, 2020.
- 3 M. A. Green, A. Ho-Baillie and H. J. Snaith, The emergence of perovskite solar cells, *Nat. Photonics*, 2014, **8**, 506–514.
- 4 M. Grätzel, The light and shade of perovskite solar cells, *Nature Publishing Group*, 2014, **13**, 838–842.
- 5 J. S. Shaikh, N. S. Shaikh, A. D. Sheikh, S. S. Mali, A. J. Kale, P. Kanjanaboos, C. K. Hong, J. H. Kim and P. S. Patil, Perovskite solar cells: In pursuit of efficiency and stability, *Mater. Des.*, 2017, **136**, 54–80.
- 6 H.-S. Kim, C.-R. Lee, J.-H. Im, K.-B. Lee, T. Moehl, A. Marchioro, S.-J. Moon, R. Humphry-Baker, J.-H. Yum, J. E. Moser, M. Grätzel and N.-G. Park, Lead Iodide Perovskite Sensitized All-Solid-State Submicron Thin Film Mesoscopic Solar Cell with Efficiency Exceeding 9%, *Sci. Rep.*, 2012, **2**, 591.
- 7 K. Wojciechowski, M. Saliba, T. Leijtens, A. Abate and H. J. Snaith, Sub-150 °C processed meso-superstructured perovskite solar cells with enhanced efficiency, *Energy Environ. Sci.*, 2014, **7**, 1142–1147.
- 8 J. Y. Jeng, Y. F. Chiang, M. H. Lee, S. R. Peng, T. F. Guo, P. Chen and T. C. Wen, $\text{CH}_3\text{NH}_3\text{PbI}_3$ perovskite/fullerene planar-heterojunction hybrid solar cells, *Adv. Mater.*, 2013, **25**, 3727–3732.
- 9 D. Luo, W. Yang, Z. Wang, A. Sadhanala, Q. Hu, R. Su, R. Shivanna, G. F. Trindade, J. F. Watts, Z. Xu, T. Liu, K. Chen, F. Ye, P. Wu, L. Zhao, J. Wu, Y. Tu, Y. Zhang, X. Yang, W. Zhang, R. H. Friend, Q. Gong, H. J. Snaith and R. Zhu, Enhanced photovoltage for inverted planar heterojunction perovskite solar cells, *Science*, 2018, **360**, 1442–1446.



- 10 M. Zhang and X. Zhan, Nonfullerene n-Type Organic Semiconductors for Perovskite Solar Cells, *Adv. Energy Mater.*, 2019, **1900860**, 1–12.
- 11 D. Li, C. Sun, H. Li, H. Shi, X. Shai, Q. Sun, J. Han, Y. Shen, H.-L. Yip, F. Huang and M. Wang, Amino-functionalized conjugated polymer electron transport layers enhance the UV-photostability of planar heterojunction perovskite solar cells, *Chem. Sci.*, 2017, **8**, 4587–4594.
- 12 Z. Zhang, J. Yuan, Q. Wei and Y. Zou, Small-Molecule Electron Acceptors for Efficient Non-fullerene Organic Solar Cells, *Front. Chem.*, 2018, **6**, 1–22.
- 13 L.-N. Nguyen, S. Kumar Pradhan, C.-N. Yen, M.-C. Lin, C.-H. Chen, C.-S. Wu, K.-S. Chang-Liao, M.-T. Lin and C.-D. Chen, High performance phototransistors based on single crystalline perylene-tetracarboxylic-dianhydride nanoparticle, *Appl. Phys. Lett.*, 2013, **103**, 183301.
- 14 H. Langhals, Control of the Interactions in Multichromophores: Novel Concepts. Perylene Bis-imides as Components for Larger Functional Units, *Helv. Chim. Acta*, 2005, **88**, 1309–1343.
- 15 K. Trofymchuk, A. Reisch, I. Shulov, Y. Mély and A. S. Klymchenko, Tuning the color and photostability of perylene diimides inside polymer nanoparticles: towards biodegradable substitutes of quantum dots, *Nanoscale*, 2014, **6**, 12934–12942.
- 16 F. Würthner, C. R. Saha-Möller, B. Fimmel, S. Ogi, P. Leowanawat and D. Schmidt, Perylene Bisimide Dye Assemblies as Archetype Functional Supramolecular Materials, *Chem. Rev.*, 2016, **116**, 962–1052.
- 17 L. Wang, G.-R. Li, Q. Zhao and X.-P. Gao, Non-precious transition metals as counter electrode of perovskite solar cells, *Energy Storage Mater.*, 2017, **7**, 40–47.
- 18 K. Jiang, F. Wu, H. Yu, Y. Yao, G. Zhang, L. Zhu and H. Yan, A perylene diimide-based electron transport layer enabling efficient inverted perovskite solar cells, *J. Mater. Chem. A*, 2018, **6**, 16868–16873.
- 19 J. L. Wu, W. K. Huang, Y. C. Chang, B. C. Tsai, Y. C. Hsiao, C. Y. Chang, C. T. Chen and C. T. Chen, Simple monohalogenated perylene diimides as non-fullerene electron transporting materials in inverted perovskite solar cells with ZnO nanoparticle cathode buffer layers, *J. Mater. Chem. A*, 2017, **5**, 12811–12821.
- 20 D. Zou, F. Yang, Q. Zhuang, M. Zhu, Y. Chen, G. You, Z. Lin, H. Zhen and Q. Ling, Perylene Diimide-Based Electron-Transporting Material for Perovskite Solar Cells with Undoped Poly(3-hexylthiophene) as Hole-Transporting Material, *ChemSusChem*, 2019, **12**, 1155–1161.
- 21 J. Huang, Z. Gu, L. Zuo, T. Ye and H. Chen, Morphology control of planar heterojunction perovskite solar cells with fluorinated PDI films as organic electron transport layer, *Sol. Energy*, 2016, **133**, 331–338.
- 22 H. Zhang, L. Xue, J. Han, Y. Q. Fu, Y. Shen, Z. Zhang, Y. Li and M. Wang, New generation perovskite solar cells with solution-processed amino-substituted perylene diimide derivative as electron-transport layer, *J. Mater. Chem. A*, 2016, **4**, 8724–8733.
- 23 E. Castro, T. J. Sisto, E. L. Romero, F. Liu, S. R. Peurifoy, J. Wang, X. Zhu, C. Nuckolls and L. Echegoyen, Cove-Edge Nanoribbon Materials for Efficient Inverted Halide Perovskite Solar Cells, *Angew. Chem., Int. Ed.*, 2017, **56**, 14648–14652.
- 24 S. R. Peurifoy, E. Castro, F. Liu, X. Y. Zhu, F. Ng, S. Jockusch, M. L. Steigerwald, L. Echegoyen, C. Nuckolls and T. J. Sisto, Three-Dimensional Graphene Nanostructures, *J. Am. Chem. Soc.*, 2018, **140**, 9341–9345.
- 25 R. Wang, K. Jiang, H. Yu, F. Wu, L. Zhu and H. Yan, Efficient inverted perovskite solar cells with truxene-bridged PDI trimers as electron transporting materials, *Mater. Chem. Front.*, 2019, **3**, 2137–2142.
- 26 F. Wu, Z. Luo, L. Zhu, C. Chen, H. Lu, Z. Chen, J. Tang and C. Yang, Sulfur-annulated perylenediimide as an interfacial material enabling inverted perovskite solar cells with over 20% efficiency and high fill factors exceeding 83%, *J. Mater. Chem. A*, 2019, **7**, 21176–21181.
- 27 Y. Fan, F. Wu, F. Liu, M. Han, K. Chang, L. Zhu, Q. Li and Z. Li, A perylene diimide dimer-based electron transporting material with an A–D–A structure for efficient inverted perovskite solar cells, *J. Mater. Chem. C*, 2022, **10**, 2544–2550.
- 28 J. Yang, C. Liu, C. Cai, X. Hu, Z. Huang, X. Duan, X. Meng, Z. Yuan, L. Tan and Y. Chen, High-Performance Perovskite Solar Cells with Excellent Humidity and Thermo-Stability via Fluorinated Perylenediimide, *Adv. Energy Mater.*, 2019, **9**, 1900198.
- 29 J. Min, Z. G. Zhang, Y. Hou, C. O. R. Quiroz, T. Przybilla, C. Bronnbauer, F. Guo, K. Forberich, H. Azimi, T. Ameri, E. Spiecker, Y. Li and C. J. Brabec, Interface engineering of perovskite hybrid solar cells with solution-processed perylene-diimide heterojunctions toward high performance, *Chem. Mater.*, 2015, **27**, 227–234.
- 30 M. Kaltenbrunner, G. Adam, E. D. Glowacki, M. Drack, R. Schwödiauer, L. Leonat, D. H. Apaydin, H. Groiss, M. C. Scharber, M. S. White, N. S. Sariciftci and S. Bauer, Flexible high power-per-weight perovskite solar cells with chromium oxide-metal contacts for improved stability in air, *Nat. Mater.*, 2015, **14**, 1032–1039.
- 31 Z. Xie, V. Stepanenko, B. Fimmel and F. Würthner, An organogelator design without solubilizing side chains by backbone contortion of a perylene bisimide pigment, *Mater. Horiz.*, 2014, **1**, 355–359.
- 32 F. Würthner, C. Thalacker, A. Sautter, W. Schartl, W. Ibach and O. Hollricher, Hierarchical Self-Organization of Perylene Bisimide–Melamine Assemblies to Fluorescent Mesoscopic Superstructures, *Chem.–Eur. J.*, 2000, **6**, 3871–3886.
- 33 W. Yan, Z. He, J. Jiang, D. Lu, Y. Gong, W. Yang, R. Xia, W. Huang and H. Xin, Highly thermal-stable perylene-bisimide small molecules as efficient electron-transport materials for perovskite solar cells, *J. Mater. Chem. C*, 2020, **8**, 14773–14781.
- 34 N. Zink-Lorre, E. Font-Sanchis, Á. Sastre-Santos and F. Fernández-Lázaro, Perylenediimides as more than just non-fullerene acceptors: versatile components in organic,



- hybrid and perovskite solar cells, *Chem. Commun.*, 2020, **56**, 3824–3838.
- 35 Z. Xie, V. Stepanenko, B. Fimmel and F. Würthner, An organogelator design without solubilizing side chains by backbone contortion of a perylene bisimide pigment, *Mater. Horiz.*, 2014, **1**, 355–359.
- 36 T. Kaiser, V. Stepanenko and F. Würthner, Fluorescent J-Aggregates of Core-Substituted Perylene Bisimides: Studies on Structure–Property Relationship, Nucleation–Elongation Mechanism, and Sergeants-and-Soldiers Principle, *J. Am. Chem. Soc.*, 2009, **131**, 6719–6732.
- 37 C. Yang, Donor/Spacer/Acceptor Block Copolymer Containing Poly(2,7-carbazole) and Perylenetetracarboxydiimide Subunits, *Macromol. Chem. Phys.*, 2010, **211**, 1446–1451.
- 38 S. Ogi, V. Stepanenko, K. Sugiyasu, M. Takeuchi and F. Würthner, Mechanism of self-assembly process and seeded supramolecular polymerization of perylene bisimide organogelator, *J. Am. Chem. Soc.*, 2015, **137**, 3300–3307.
- 39 S. H. Oh, B. G. Kim, S. J. Yun, M. Maheswara, K. Kim and J. Y. Do, The synthesis of symmetric and asymmetric perylene derivatives and their optical properties, *Dyes Pigm.*, 2010, **85**, 37–42.
- 40 C. C. Chao, M. K. Leung, Y. O. Su, K. Y. Chiu, T. H. Lin, S. J. Shieh and S. C. Lin, Photophysical and electrochemical properties of 1,7-diaryl-substituted perylene diimides, *J. Org. Chem.*, 2005, **70**, 4323–4331.
- 41 C. Yang, S. Cho, A. J. Heeger and F. Wudl, Heteroanalogues of PCBM: N-Bridged Imino-PCBMs for Organic Field-Effect Transistors, *Angew. Chem., Int. Ed.*, 2009, **48**, 1592–1595.
- 42 C. M. Cardona, W. Li, A. E. Kaifer, D. Stockdale and G. C. Bazan, Electrochemical considerations for determining absolute frontier orbital energy levels of conjugated polymers for solar cell applications, *Adv. Mater.*, 2011, **23**, 2367–2371.
- 43 I. Gelmetti, N. F. Montcada, A. Pérez-Rodríguez, E. Barrena, C. Ocal, I. García-Benito, A. Molina-Ontoria, N. Martín, A. Vidal-Ferran and E. Palomares, Energy alignment and recombination in perovskite solar cells: Weighted influence on the open circuit voltage, *Energy Environ. Sci.*, 2019, **12**, 1309–1316.
- 44 D. W. de Quilletes, S. M. Vorpahl, S. D. Stranks, H. Nagaoka, G. E. Eperon, M. E. Ziffer, H. J. Snaith and D. S. Ginger, Impact of microstructure on local carrier lifetime in perovskite solar cells, *Science*, 2015, **348**, 683–686.
- 45 F. Xu, J. Zhu, R. Cao, S. Ge, W. Wang, H. Xu, R. Xu, Y. Wu, M. Gao, Z. Ma, F. Hong and Z. Jiang, Elucidating the evolution of the current-voltage characteristics of planar organometal halide perovskite solar cells to an S-shape at low temperature, *Sol. Energy Mater. Sol. Cells*, 2016, **157**, 981–988.
- 46 F. Cai, L. Yang, Y. Yan, J. Zhang, F. Qin, D. Liu, Y.-B. Cheng, Y. Zhou and T. Wang, Eliminated hysteresis and stabilized power output over 20% in planar heterojunction perovskite solar cells by compositional and surface modifications to the low-temperature-processed TiO₂ layer, *J. Mater. Chem. A*, 2017, **5**, 9402–9411.
- 47 M. Saliba and L. Etgar, Current Density Mismatch in Perovskite Solar Cells, *ACS Energy Lett.*, 2020, **5**, 2886–2888.
- 48 W. Xu, X. Ma, J. H. Son, S. Y. Jeong, L. Niu, C. Xu, S. Zhang, Z. Zhou, J. Gao, H. Y. Woo, J. Zhang, J. Wang and F. Zhang, Smart Ternary Strategy in Promoting the Performance of Polymer Solar Cells Based on Bulk-Heterojunction or Layer-By-Layer Structure, *Small*, 2022, **18**, 2104215.
- 49 X. Ma, A. Zeng, J. Gao, Z. Hu, C. Xu, J. H. Son, S. Y. Jeong, C. Zhang, M. Li, K. Wang, H. Yan, Z. Ma, Y. Wang, H. Y. Woo and F. Zhang, Approaching 18% efficiency of ternary organic photovoltaics with wide bandgap polymer donor and well compatible Y6: Y6-1O as acceptor, *Natl. Sci. Rev.*, 2021, **8**, 8.
- 50 C. Xu, K. Jin, Z. Xiao, Z. Zhao, X. Ma, X. Wang, J. Li, W. Xu, S. Zhang, L. Ding and F. Zhang, Wide Bandgap Polymer with Narrow Photon Harvesting in Visible Light Range Enables Efficient Semitransparent Organic Photovoltaics, *Adv. Funct. Mater.*, 2021, **31**, 52.
- 51 H. Wang, F. Yang, Y. Xiang, S. Ye, X. Peng, J. Song, J. Qu and W.-Y. Wong, Achieving efficient inverted perovskite solar cells with excellent electron transport and stability by employing a ladder-conjugated perylene diimide dimer, *J. Mater. Chem. A*, 2019, **7**, 24191–24198.



Modification of a Buried Interface with Bulky Organic Cations for Highly Stable Flexible Perovskite Solar Cells

Shyantana Dasgupta, Wiktor Żuraw, Taimoor Ahmad, Luigi Angelo Castriotta, Eros Radicchi, Wojciech Mróz, Mateusz Ścigaj, Łukasz Pawlaczyk, Magdalena Tamulewicz-Szwajkowska, Marek Trzcinski, Jarosław Serafinczyk, Edoardo Mosconi, Aldo Di Carlo, Filippo De Angelis, Alina Dudkowiak, and Konrad Wojciechowski*



Cite This: *ACS Appl. Energy Mater.* 2022, 5, 15114–15124



Read Online

ACCESS |



Metrics & More



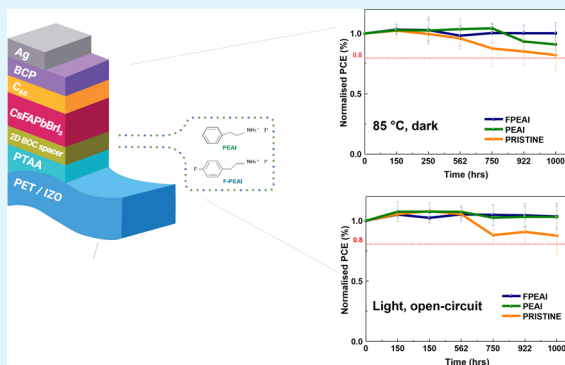
Article Recommendations



Supporting Information

ABSTRACT: Flexible perovskite solar cells triggered a vast interest within the scientific community, thanks to their broad commercialization prospects. However, the stability of these devices still poses one of the major concerns on the way to rapid industrial deployment. Here, we demonstrate an effective strategy to improve the technical aspects of this technology, improving the reliability and efficiency values of these devices. We apply large organic ammonium molecules for modifying a buried interface between a hole-transporting layer (HTL) and perovskite-absorbing material. With the 4-fluorophenethylammonium iodide (FPEAI), we achieve 18.66% efficiency for the large-area (1 cm²) flexible solar cell, a significant improvement over the pristine device without modification. The applied passivation strategy results in a better hole extraction and reduced nonradiative recombination loss at the buried interface. Moreover, we demonstrate the formation of low-dimensional perovskite phases in the vicinity of the hole-transporting material upon the incorporation of large ammonium cations. This results in a significantly enhanced thermal and light-soaking stability of fabricated devices. We obtained no loss in 1000 h of aging at 85 °C, no loss in 1000 h of light soaking at open circuit, and less than 10% drop in 1000 h of operation at maximum power point for the optimized passivation treatment with the FPEAI. We also demonstrate a method for monitoring the structural stability of perovskite thin films upon prolonged illumination, ensued by the amount of molecular iodine being released from the layer.

KEYWORDS: flexible photovoltaics, perovskite solar cell, interface modification, bulky organic cation, long-term stability



INTRODUCTION

Flexible perovskite solar cells (f-PSCs) garnered a lot of attention in the research community over the last couple of years, thanks to their broad and tangible commercial prospects.¹ Power conversion efficiency (PCE) reported for the lab-scale f-PSC devices recently exceeded 21%. Attainable high specific powers, thanks to the use of lightweight substrates and cost-effective manufacturing methods (roll-to-roll processing), constitute key benefits of this technology.² However, detailed performance loss mechanisms and long-term reliability of perovskite devices still require a better understanding and more technical advancements to fully utilize the commercial potential of this technology.

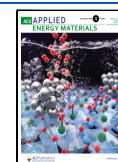
Perovskite thin films, due to their ionic and polycrystalline nature, are characterized by various defects, which derive from interruptions or imperfections in the semiconductor's crystal lattice.^{3–5} We can distinguish point defects (vacancies and interstitials) and extended defects (grain boundaries, twinning and stacking faults, etc.).^{6,7} These defects introduce electronic

states within the bandgap, which in turn are responsible for trapping photogenerated charge carriers, an increase of nonradiative recombination rates, and reduced solar cell performance. The majority of recombination losses in perovskite solar cells take place at the interfaces with charge-selective layers, primarily due to the higher density of defects within these areas.^{8,9} Additionally, these ionic defects can migrate within a perovskite layer in response to external stimuli, such as electric field or light. Iodide defects (vacancies and interstitials) were shown to have the lowest activation energy for charge distribution and are believed to dominate the migration mechanism.^{7,10} Such interstitial iodides upon

Received: August 29, 2022

Accepted: November 29, 2022

Published: December 11, 2022



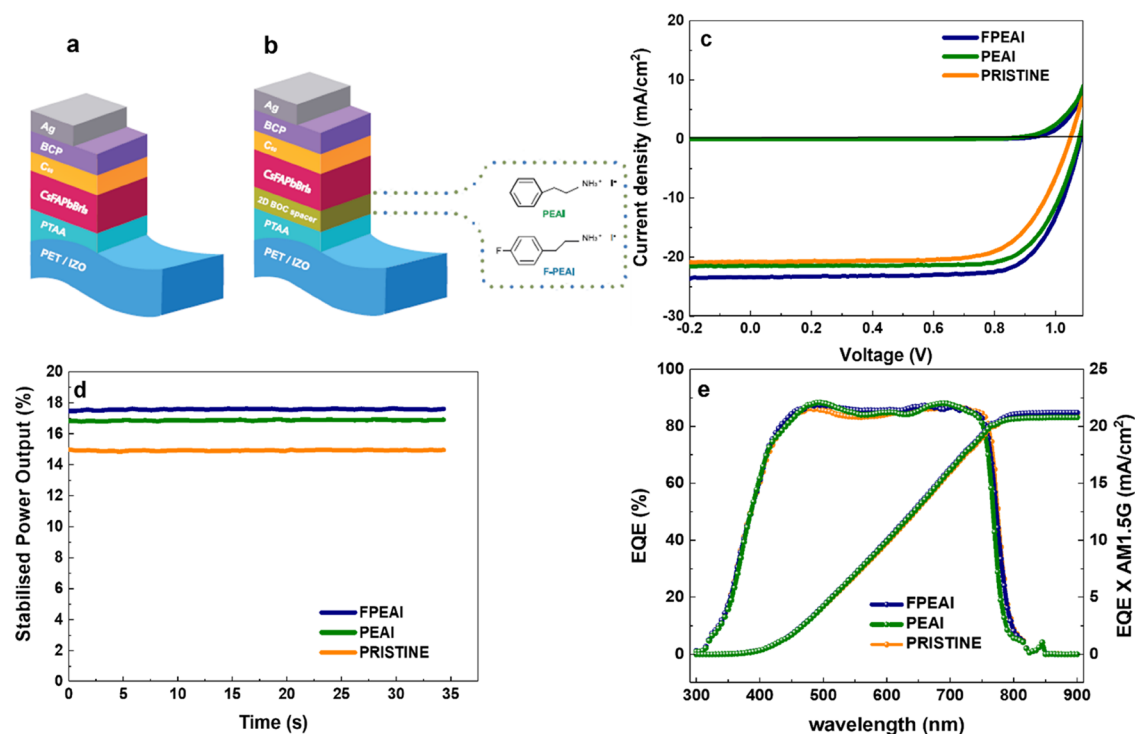


Figure 1. Schematic structures of perovskite solar cells (a) without modification and (b) with BOC-based interface modification, (c) J - V curves of the champion devices of each variation, (d) SPO curves for the same devices, and (e) EQE spectra with integrated current density values of representative devices of each variation.

illumination can undergo complex redox reactions, leading to the release of molecular iodine and the formation of deep trap states (primarily hole traps).^{11–13} Defect passivation, especially applied to the surface of perovskite thin films, was widely explored as an effective way to suppress recombination losses and also improve device stability.^{14,15} Popular passivation strategies include ionic or coordinating interactions with external materials containing electron-rich (stabilization of positively charged defects) or electron-deficient groups (negatively charged sites). Less attention was paid to the modification of a buried interface. Apart from influencing interfacial electronic effects, the change of surface energy onto which perovskite is grown can alter nucleation and crystallization dynamics, leading to differences in layer morphologies and bulk properties. Recently, Degani et al. and Cacovich et al. applied large organic ammonium halides to the surface of a hole-transporting material (HTM) onto which perovskite films were subsequently formed.^{16,17} They primarily observed improved layer uniformities with the elimination of nanovoids at the perovskite/HTM interface. No changes in the material's composition and dimensionality or clear passivation effects at the buried interface were observed.

Here, we modified a buried interface between the HTM and perovskite layer with bulky organic cations (BOCs) to improve this electronic contact and perovskite film quality. Additionally, we assessed the influence of fluorination of the organic cation on the effectiveness of this modification approach. By studying lift-off perovskite samples, we show the formation of two-dimensional (2D) perovskite phases at the buried interface, revealing the incorporation of large cations into the perovskite lattice. With multiple spectroscopic and electrical characterization techniques, we show improved hole extraction and reduced nonradiative recombination losses at the modified interfaces. Devices with the BOC-modified p-side contact show

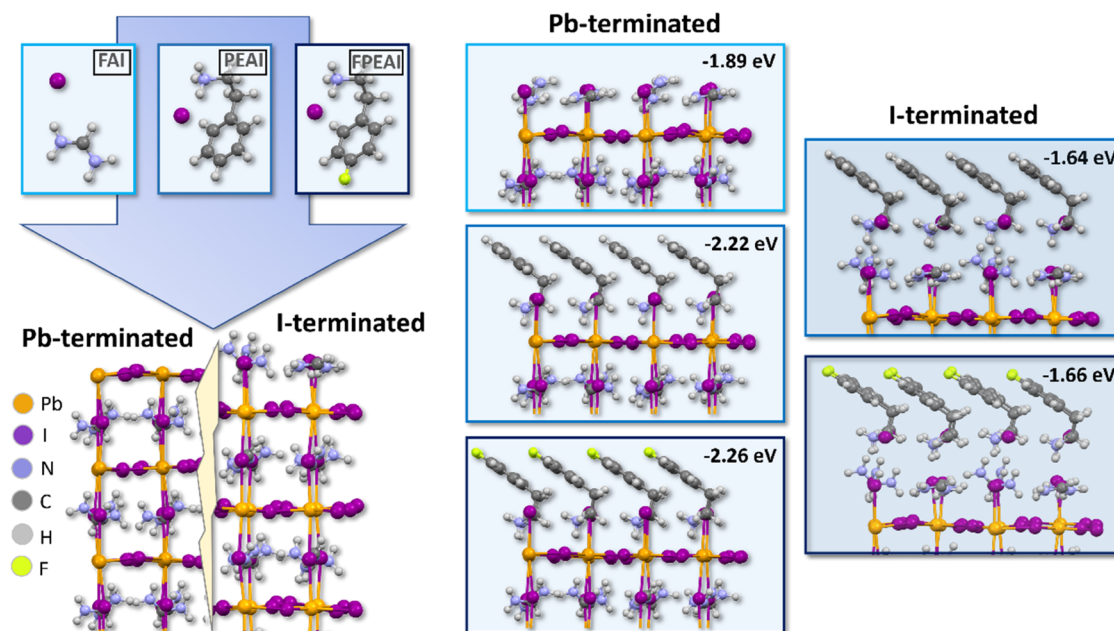
improved photovoltaic performance (approaching 19% for the champion large-area device on the flexible substrate) and display significantly enhanced long-term reliability in different stability tests (thermal test at 85 °C, operational test at maximum power point, light-soaking test at open circuit). Moreover, we corroborate these results by identifying the reinforced structural stability of perovskite films upon interface modification, which is evidenced by slower iodine release during continuous light soaking. This is also confirmed by computational modeling of the HTM/perovskite interfaces with and without modifications.

RESULTS AND DISCUSSION

Poly(triaryl)amine (PTAA) is one of the most commonly used hole-transporting material (HTM) for the p-i-n perovskite solar cells. Its interface with a perovskite thin film can be still a source of performance-limiting, nonradiative recombination losses.^{18,19} We applied PTAA surface modification based on large-cation organic halides to improve this electronic contact. We selected phenethylammonium iodide (PEAI) as a modifying compound, which is commonly used for perovskite surface passivation with the ability to form reduced dimensionality perovskite compositions.²⁰ We also tried a fluorinated variant, 4-fluoro-phenethylammonium iodide (FPEAI), in which cation exhibits a strong molecule dipole moment, thanks to the fluorine substitution.^{21,22} To evaluate the influence of PTAA modification on photovoltaic properties, we fabricated flexible perovskite solar cells of p-i-n configuration with the following structure: polyethylene terephthalate (PET)/indium zinc oxide (IZO)/(polybis(4-phenyl)(2,4,6-trimethylphenyl)amine (PTAA))/Cs_{0.17}FA_{0.83}Pb(I_{0.9}Br_{0.1})₃/fullerene C₆₀/bathocuproine (BCP)/Ag, which is shown in Figure 1a,b. Current density–voltage (J - V) and

Table 1. Photovoltaic Parameters Extracted from the J - V Characterization Measurements of Perovskite Solar Cells Processed with Different PTAA Surface Modifications

sample	PCE best (PCE _{average±SD}) [%]	FF best (FF _{average±SD}) [%]	V_{OC} best ($V_{OC,average±SD}$) [V]	J_{SC} best ($J_{SC,average±SD}$) [mA/cm ²]	SPO best [%]
pristine	16.03 (14.98 ± 0.85)	63.99 (58.66 ± 2.63)	1.05 (1.04 ± 0.01)	22.23 (21.21 ± 0.55)	14.96
FPEAI	18.66 (17.22 ± 0.78)	75.17 (71.62 ± 3.64)	1.09 (1.07 ± 0.01)	23.34 (22.59 ± 0.50)	17.81
PEAI	18.13 (16.72 ± 0.85)	74.32 (71.17 ± 2.76)	1.08 (1.06 ± 0.01)	23.32 (22.13 ± 0.69)	16.82

**Figure 2.** DFT simulation of the passivation of a Pb- and I-terminated perovskite surface. $E_{pass,mol}$ is reported in the inset for each case.

stabilized power output (SPO) characteristics of the devices with and without modifications are shown in Figure 1c,d. Performance parameters (champion cells and average values of 30 devices) are summarized in Table 1. For the pristine device without modification, we recorded an open-circuit voltage (V_{OC}) of 1.05 V, a short-circuit current density (J_{SC}) of 22.23 mA/cm², a fill factor (FF) of 63.99%, and a PCE of 16.03%. With the PEAI modification, the PCE improved to 18.13% with an FF of 74.32%, a V_{OC} of 1.08 V, and a J_{SC} of 23.32 mA/cm². The FPEAI modification yielded enhancements in all of the photovoltaic parameters, reaching the best PCE of 18.66% with a J_{SC} of 23.34 mA/cm², a V_{OC} of 1.09 V, and an FF of 75.17%. Statistics of all photovoltaic performance parameters, as extracted from the J - V characteristics, are shown in Figure S1. For the representative cells of each variant, we also measured external quantum efficiency (EQE) spectra (see Figure 1e) and derived integrated J_{SC} values. J - V curves of these cells are shown in Figure S2. All of the PV parameters for these devices are summarized in Table S1. The J_{SC} values derived from the EQE plots were slightly lower than the corresponding currents from the J - V curves. Ionic displacement screening an electric field in the perovskite film, which can be more severe during the EQE measurement (longer time at short-circuit conditions), was often suggested as a possible origin for these differences.²³ Nevertheless, the same trend of higher current density values and possibly improved charge extraction (especially in the higher-energy region) can be observed in the modified devices.

To study the possible interactions of the modifying compounds (PEAI and FPEAI) within the PTAA surface and subsequently forming perovskite materials, we performed

density functional theory (DFT) simulations. The computational details are presented in Supporting Note 1. Particularly, we evaluated the passivation power of different organic ammonium iodides (FAI—taken as a reference, PEAI, FPEAI) over Pb- and I-terminated FAPbI₃ surfaces, which are good approximations of the perovskite material employed in our study (Pb²⁺, FA⁺, and I⁻ are the main constituents). We depict this mechanism in Figure 2. The total passivation energy per spacer molecule, $E_{pass,mol}$, is evaluated by eq 1

$$E_{pass,mol} = [E_{slab,pass} - E_{slab,unpass} - 16 \times E_{molecule}]/16 \quad (1)$$

where $E_{slab,pass}$ and $E_{slab,unpass}$ are the energies of the passivated and nonpassivated slabs, respectively, and $E_{molecule}$ is the energy of the isolated FAI, PEAI, or FPEAI molecule.

The energy is normalized by dividing by the number of the passivating molecules (16), which corresponds to the number of the Pb atoms on the two surfaces. For the Pb-terminated surface, the $E_{slab,pass}$ energies equal -1.89 , -2.22 , and -2.26 eV for the FAI, PEAI, and FPEAI, respectively. This highlights how the employed large cations effectively stabilize the perovskite absorber surface through the coordination of the undercoordinated Pb atoms with slightly higher passivation energy found for the FPEAI.

In the case of the I-terminated perovskite surface, we only studied the passivation by PEAI and FPEAI, again obtaining highly spontaneous $E_{pass,mol}$ values of -1.64 and -1.66 eV, respectively, which however are lower than the values derived for the Pb-terminated surface. Similar observations were found in a previous manuscript.²⁴ The same conclusions were achieved following a slightly different approach, *i.e.*, evaluating

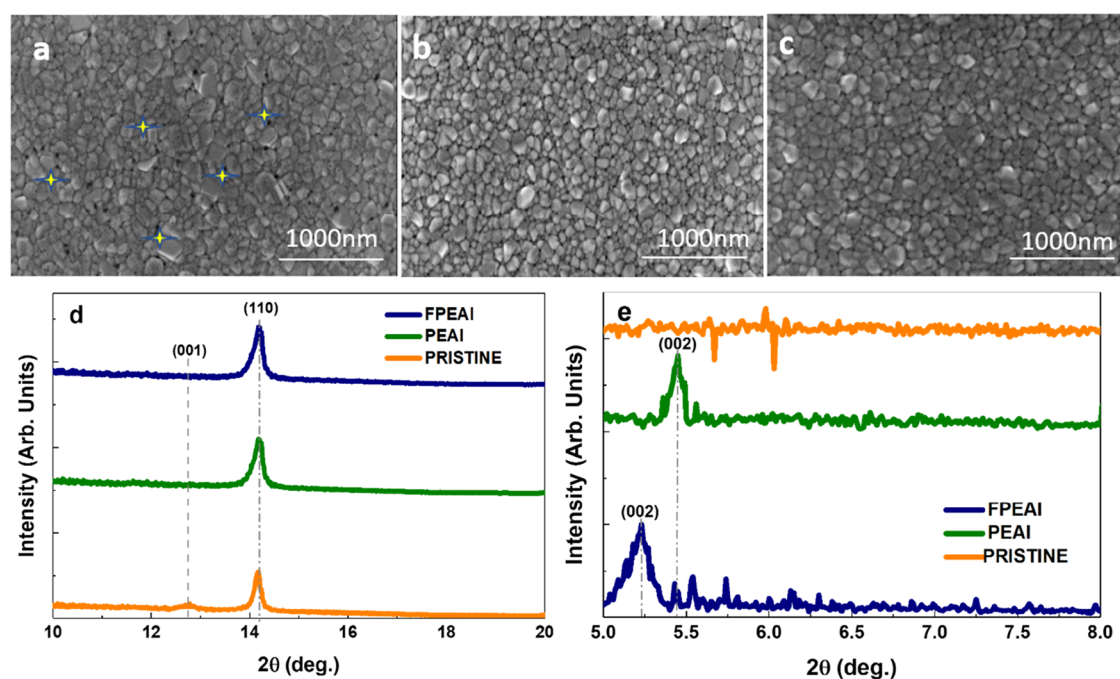


Figure 3. Top-view SEM images of perovskite films (a) without and (b) with PEAI- and (c) FPEAI-based PTAA modifications showing nanovoids are marked with yellow stars, (d) XRD of perovskite films of all three variations, and (e) XRD (zoomed at the low angle part) of the lift-off perovskite films.

the exchange reactions of FA^+/FAI with (F)PEA $^+/(F)$ PEAI up to three ions/molecules (eqs S1–S2 and Figure S3), showing slightly favored thermodynamics in the case of FPEAI vs PEAI (see Table S2). Overall, this showed that interface modification largely suppressed iodine- and lead-based point defects. Furthermore, the strong interaction of the FPEAI molecule with the perovskite lattice ((FPEA) $_n$ FAPbI $_3$ structures) could lock in the lead and iodine atoms in their positions, thus mitigating the point defect migration within the film. The analysis of the electronic properties, following the calculation of the density of states (see Figure S4), reveals a significant Fermi energy downshift (~ -0.5 eV) when moving from the PEAI- to the FPEAI-passivated systems. This leads to a different energy alignment between the perovskite valence band and the PTAA hole acceptor level, providing a higher hole injection driving force for the FPEAI system.²⁵ This could result in higher hole extraction efficacy.

To better understand the influence of a modified surface on the growth of the perovskite layer, we studied the morphology of perovskite films deposited on pristine and modified PTAA films. Figure 3a–c, shows top-view scanning electron microscopy (SEM) images of all of the samples. Cross-sectional SEM images are shown in Figure S5. All three variations show similar microstructures with domain sizes on the level of sub-100 nm. We note that perovskite films on a pristine PTAA show a higher density of nanovoids and pinholes, whereas modified PTAA results in more compact morphologies. This could increase the shunt resistance of the modified devices and contribute to higher FF values. In the cross-sectional images, we also observe very similar perovskite morphologies for all variations with slightly thicker perovskite films when grown on a FPEAI-modified surface. Additional morphological characterization was carried out with atomic force microscopy (AFM). The surface topography images are shown in Figure S6a–c. Table S3, displays root-mean-square

(RMS) roughness values for all of the studied samples. The layer grown on the FPEAI-modified sample displayed the smoothest surface, possibly due to improved wetting, and more homogeneous crystallization. Next, we performed X-ray diffraction (XRD) measurements for all three perovskite sample types. Diffractograms are shown in Figure 3d. For the PTAA-modified samples, we observed increased peak intensities at 14.1 and 28.3°, which correspond to the (110) and (220) planes of the perovskite structure, respectively. This could originate from enhanced crystallinity or a higher level of grain orientation in these films.²⁶ Additionally, modified samples, in contrast to the pristine PTAA, show no peak at 12.7°, which corresponds to the PbI $_2$ phase.²⁷ This implies complete perovskite transformation for these samples. We also applied the Williamson–Hall (WH) method to calculate the size of perovskite crystallites and derive microstrain values for the (110), (220), and (330) lattice planes.²⁸ Obtained results are shown in Table 2 and Figure S7. The samples grown on the

Table 2. Average Perovskite Crystallite Sizes and Microstrain Values Derived from XRD Measurements of Perovskite Thin Films Processed on the PTAA Surface with Different Modifications

sample	crystallite size [nm]	microstrain [%]
FPEAI	59	1.31
PEAI	53	1.57
pristine	49	1.63

FPEAI-modified surface exhibit a slightly larger average grain size and more importantly reduced microstrain, which can have a significant effect on the layer's optoelectronic quality (defect density and recombination profile) and ensuing long-term stability.²⁹ A detailed description of the WH method is provided in Supporting Note 2. To characterize perovskite crystallographic properties in the vicinity of the PTAA surface,

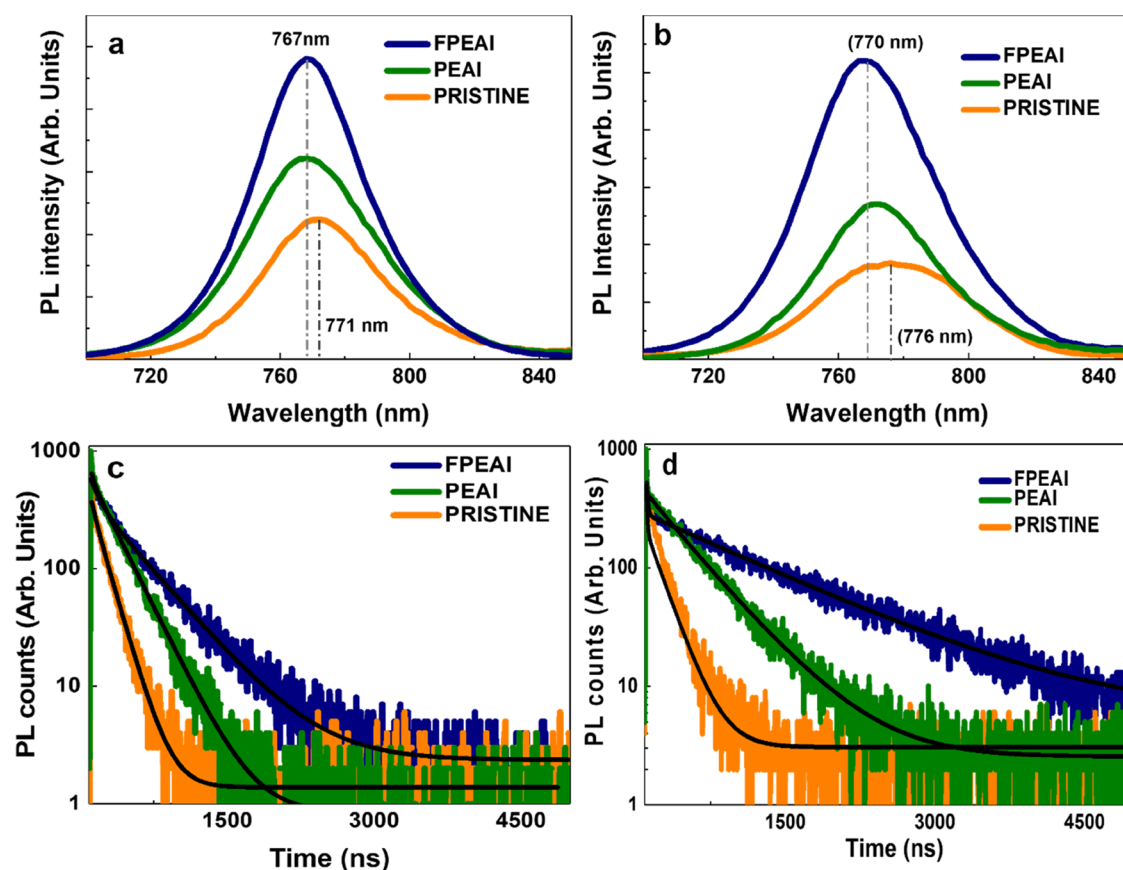


Figure 4. (a) Steady-state PL spectra of perovskite films processed on PET/ITO/PTAA substrates with and without modifications, (b) steady-state PL of the same perovskite variations taken for the lift-off samples, (c) time-resolved PL decays of the samples from panel (a), and (d) time-resolved PL decays of the samples from panel (b).

we applied a lift-off process to expose that side of the layer.³⁰ In short, we thermally evaporated copper layers on top of perovskite films and dipped them in a chlorobenzene solution to dissolve underlying PTAA and leave free-floating perovskite layers. A more detailed description of the experimental procedure is given in the Methods section. Diffractograms of all three perovskite types are shown in Figure 3e. For the layers grown on surfaces modified with the organic ammonium iodides, we recorded a distinct presence of additional peaks at a low angle range ($5\text{--}6^\circ$). We assign these reflections to the (002) lattice plane of the layered (2D) perovskite structure.³¹ A similar effect of the 2D/three-dimensional (3D) heterojunction formation at the buried interface upon application of an appropriate organic ammonium halide was previously reported in the literature.^{32,33}

Then, we studied the optoelectronic properties of perovskite films grown on modified and unmodified PTAA surfaces. The samples with an interfacial modification display significantly enhanced absorption in the high-energy part, below 550 nm (see Figure S8), which could originate from the contribution of layered phases.³² All of the films show the same optical bandgap as derived from the Tauc plot (Figure S9). Figure 4a shows the photoluminescence (PL) spectra of the samples with and without interface modifications. We note higher PL intensities recorded for the PTAA-modified films with the FPEAI type showing the highest signal. There was also a noticeable blueshift (~ 5 nm) in the PL peak position of the modified samples. The same trends were also observed for the excitation through the other side in the lift-off perovskite films

(see Figure 4b). Next, we performed time-resolved PL (TRPL) measurements for the same set of samples. The decay curves (excitation through the perovskite surface and through the lift-off buried interface) are presented in Figure 4c,d. Longer PL lifetimes for the modified samples imply a reduced non-radiative loss mechanism (trapping and recombination) in these films. Interestingly, we observed a 3-fold increase in lifetime for the interface-modified lift-off samples. This provides strong evidence that PTAA modification with the BOC molecules can effectively reduce nonradiative recombination losses at that interface.^{32,33} The PL decays were fitted with a nonlinear exponential function; all of the fitting parameters are displayed in Table S4.

To have a better insight into the charge recombination dynamics in the perovskite layer and at the interfaces, we performed electroluminescence (EL) measurements of complete solar cells. To this end, we applied a forward bias to our devices with and without PTAA modifications, making it operate in light-emitting diode (LED) mode to study the EL signal. Figure 5a presents the comparison of the EL spectra of the three devices with an applied forward bias of 2 V. The shapes of the EL spectra resemble closely the PL spectra; however, the intensity of emission for the FPEAI-modified devices is more than 2 times higher than the PEA1-modified and pristine devices. Figure 5b,c shows transient integrated EL intensity and the transient current flowing through the cells with an applied 2 V bias. After 20 s of stabilization time, the light emitted from the FPEAI- and PEA1-modified devices has comparable intensities, while emission from the pristine device

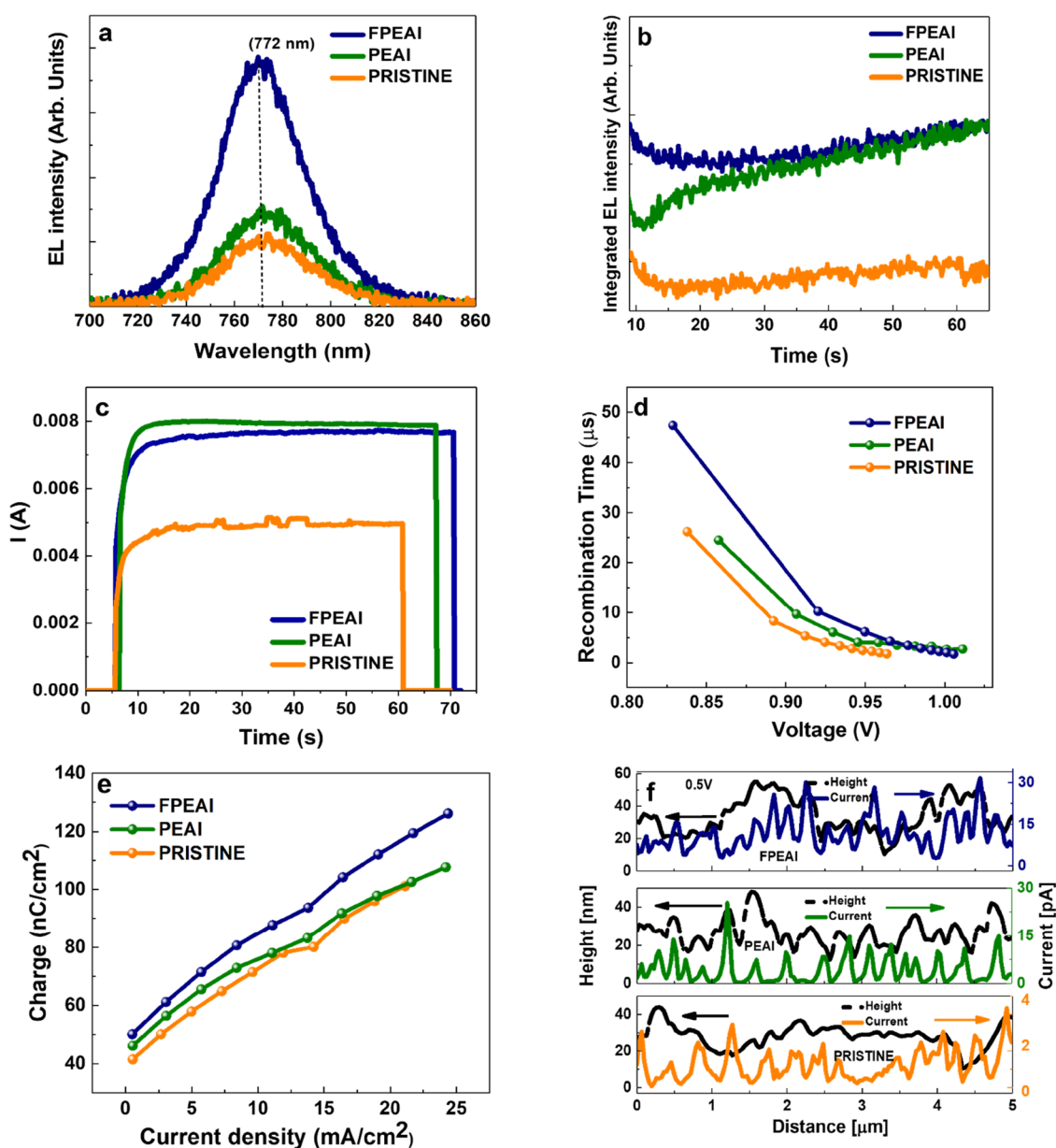


Figure 5. (a) EL spectra of the three PSC variations taken at the applied constant bias of 2 V, (b) integrated EL intensity of the same cells at 2 V bias, (c) current intensities corresponding to the transient EL from panel (b), (d) recombination lifetimes of the same cell variations derived from the fitting of photovoltage decays at varied background light intensities, (e) charge density extracted from the photocurrent decay measurements taken at varied perturbation light intensities, and (f) photocurrent values and morphological profile taken across the scanned distance, derived from the *c*-AFM measurements of perovskite films grown on different surface modifications.

Table 3. Photovoltaic Parameters Extracted from *J*–*V* measurements (V_{OC} , I_{SC}) and Series of Physical Parameters Derived from Electroluminescence Measurements^a

samples	V_{OC} (V)	I_{SC} (A)	$EQE_{EL}(@I_{SC})$	$V_{OC}^{rad\ limit}$ (V)	V_{OC} loss (V)	I_s (A)	n	m
pristine	1.047	0.013	1.06×10^{-4}	1.284	0.23	1.2×10^{-8}	3.8	1.3
PEAI	1.065	0.013	0.92×10^{-4}	1.305	0.24	2.0×10^{-9}	3.0	1.3
FPEAI	1.073	0.014	0.92×10^{-4}	1.314	0.24	7.9×10^{-12}	2.1	1.2

^aExternal quantum efficiency of EL, V_{OC} in radiative limit, V_{OC} loss, saturation current, ideality factors “ n ” and “ m ” are calculated from the current and photon flux, respectively.

is about 4 times lower. The evolution of current values shows similar trends with the FPEAI- and PEAI-modified cells, displaying around 2 times higher current than the pristine device. When we confronted recorded light intensities with the current intensities, we noticed that the brightness of the

pristine sample is about 3–4 times lower than the modified samples, but the current magnitude of the pristine cell is only less than or equal to a half of current values measured for the other samples. Therefore, in contrast to our previous work, where simple qualitative analysis was sufficient to give

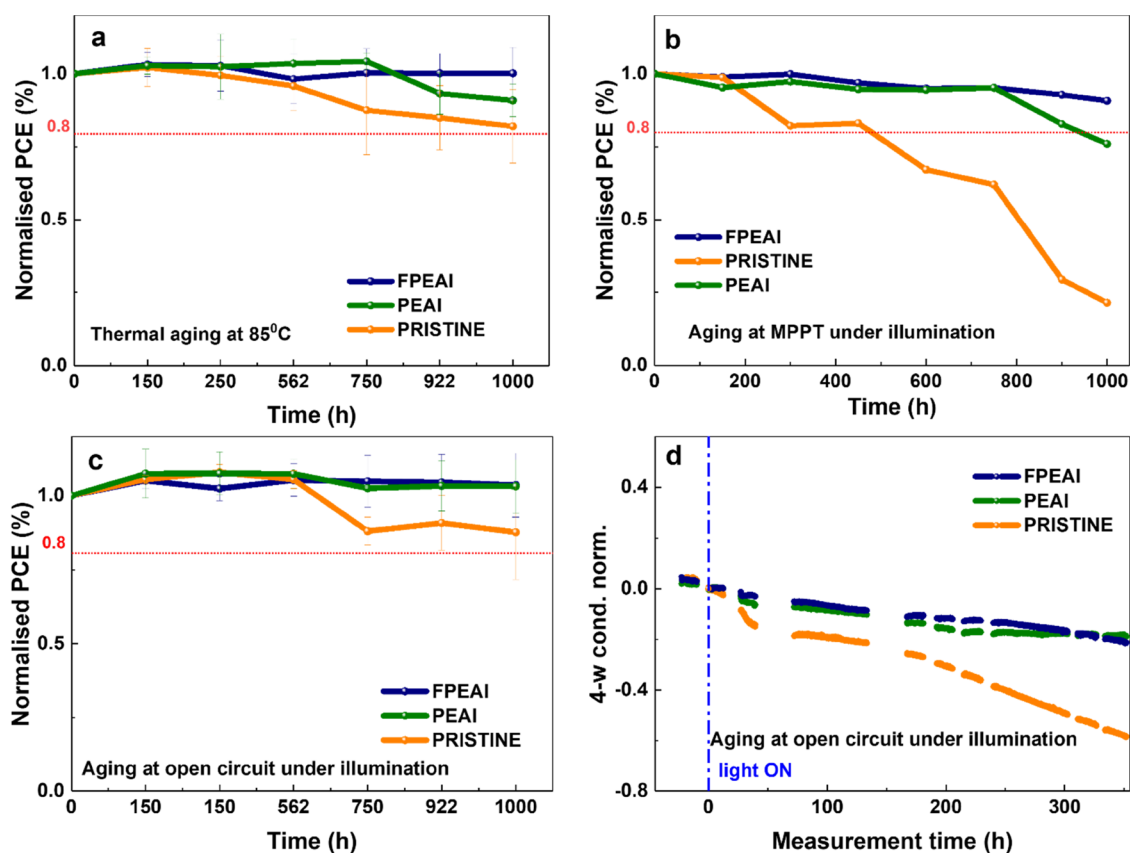


Figure 6. Time evolution of normalized PCE values of the three PSC variations, which were subjected to (a) thermal stress test at 85 °C (glovebox), (b) continuous operational test at maximum power point (glovebox), (c) continuous light-soaking test at open circuit (glovebox), and (d) time evolution of normalized conductance values of silver films laminated with different perovskite films measured upon continuous light soaking.

indications about devices' efficiencies, in this case, more detailed investigation was necessary.³⁴ We started with the determination of the devices' V_{OC} radiative limits following eq 2³⁵

$$V_{OC}^{\text{rad limit}} = V_{OC} - \frac{kT}{e} \ln(\text{EQE}_{EL}) \quad (2)$$

where V_{OC} is the open-circuit voltage measured for the cell, k denotes the Boltzmann constant, T is the temperature expressed in kelvin, e stands for the elementary charge, and EQE_{EL} is the external quantum efficiency of the electroluminescence of the device for the current intensity corresponding to the I_{SC} determined in the photovoltaic measurement. Table 3 shows all of the values obtained for the modified and unmodified samples. The calculated V_{OC} values in the radiative limit increase in the following order: pristine < PEAI < FPEAI, which is in agreement with the trend of the measured V_{OC} of these cells. The EQE_{EL} values are shown in Figure S10a–c. To have more insight into the device operation principles, we also applied the Shockley diode equation to the EL results and determined the ideality factors for these three device variations (see Supporting Note 3).

To further corroborate our findings on the influence of PTAA modification on the recombination characteristics at the perovskite interface, we carried out transient photovoltage (TPV) measurements of complete solar cells. The TPV method is performed in a small perturbation regime, where the LED light is illuminating a sample with specific light intensity, and a small overcurrent is sent to the cell, which creates a

voltage perturbation on the device in the range of 20 mV. The test is repeated for a range of light intensities. We applied intensities starting from 30.4 to 160.4 mW/cm². In Figure Sd, time constants extracted from a single exponential fit of voltage decays at different light intensities were plotted as a function of V_{OC} values, each measured at a given intensity. The FPEAI- and PEAI-modified devices displayed higher recombination lifetimes than the control sample. This is in good agreement with the reduced nonradiative recombination loss upon PTAA modification, which was implied by PL and EL analyses.

To investigate the possible influence of the PTAA modification on a hole extraction efficacy, we performed transient photocurrent (TPC) measurements of complete solar cells. TPC is performed in a high perturbation regime. The measuring sample is kept at short circuit and an LED light is illuminating the sample with different intensities. Then, the light is switched off and the current decay is measured and integrated. Figure 5e shows plotted extracted charge as a function of short-circuit current density, measured for a range of light intensities (same as in the TPV measurements). The PTAA-modified devices display improved carrier extraction over the control sample with the FPEAI type exhibiting the most effective charge collection (largest integrated charge values). To corroborate these findings, we applied the conductive AFM (c-AFM) technique to measure vertical charge transport properties of perovskite films, when grown on modified and unmodified PTAA layers (sample stack: glass/ITO/PTAA/BOC/perovskite) at different applied biases (−0.5, 0, and 0.5 V). Current maps obtained along the

scanned distance (at 0.5 V forward bias) are shown in Figure 5f. The FPEAI-modified sample showed the highest currents at all different biases. The PEAI-based sample also displayed higher signals than the pristine PTAA. Table S5 presents all of the results of *c*-AFM measurements (dark, light, different biases). This clearly indicates an improved hole transfer at the perovskite/PTAA interface modification, which is in good agreement with the TPC measurements.

In the next step, we investigated the influence of the PTAA modification strategy on the long-term stability of fabricated perovskite solar cells. For the aging tests, we continued with the double-cation perovskite recipe ($\text{Cs}_{0.17}\text{FA}_{0.83}\text{Pb}(\text{I}_{0.9}\text{Br}_{0.1})_3$), which is known to provide structurally more stable compositions than the commonly used formulas with the methylammonium cations.^{36–38} The reliability analysis was performed following ISOS (International Summit on Organic Photovoltaic Stability) protocols, which were recommended for the stability assessment of perovskite PV devices.³⁹ First, we subjected all of the device variations to a thermal stress in the dark (85 °C, inert atmosphere), compliant with the ISOS-D-2 test. The aging was periodically interrupted for electrical characterization measurements. The evolution of normalized PCE is shown in Figure 6a. We can observe that the FPEAI-modified devices outperformed the other two types (control and PEAI-modified cells), maintaining nearly 100% of the initial efficiency after 1000 h of aging. The PEAI-based samples preserved up to 90% of starting PCE, whereas control devices kept only 80% of the initial performance. Corresponding *J–V* curves of the most stable devices of each type (control, FPEAI- and PEAI-modified), which were collected along with the continued aging, are shown in Figure S12. To understand any structural changes in the perovskite layers upon exposure to elevated temperatures, we also measured XRD of perovskite films (PET/IZO/PTAA/BOC/perovskite), which were subjected to the same heating test (before the test and after 1000 h of heating). Diffractograms, shown in Figure S13, demonstrate improved structural stability of perovskite films, which were grown on the modified PTAA surface. The FPEAI treatment has the strongest stabilization effect, and no PbI_2 peak can be observed in this film. For the PEAI modification, a small PbI_2 reflection (12.7°) appears after 1000 h, whereas for the control sample, PbI_2 appears already after 500 h, and significant perovskite degradation is evident at the end of the test.

Next, we studied the effect of light stress on the stability of used perovskite devices (ISOS-L-1 protocol). Solar cells, with and without PTAA modifications, were subjected to continuous light soaking (LED source, intensity: ~60 mW/cm²) in a nitrogen-filled glovebox (inert atmosphere). Devices were aged in two different conditions, at maximum power point (MPP) and open circuit (OC). Electrical characterization measurements were periodically carried out to track the evolution of photovoltaic performance parameters (ca. every 150 h). Figure 6b,c shows normalized efficiency values as a function of aging time, extracted from *J–V* scans. The FPEAI-modified devices preserve over 90 and 100% of the initial PCE after 1000 h of aging at the MPPT, and OC aging conditions, respectively. The PEAI-modified cells were dropping faster in the MPPT test but showed full stability in the OC aging. The control samples were degrading significantly faster in both tests, yielding less than 30% and around 80% of the initial PCE at the MPPT and OC conditions, respectively. The *J–V* and SPO curves of the best devices, taken along the aging tests

(MPPT and OC conditions) for each device variation, are shown in Figure S14a–i. All of these results clearly show that the cells with the BOC-based PTAA modification exhibit significantly improved long-term reliability upon light exposure. It was previously reported that complex iodide chemistry is one of the major factors affecting the stability of perovskite compositions under illumination.^{40,41} Light drives the migration of ionic point defects, such as interstitial iodide ions (I_i) and iodide vacancies (V_i), and triggers photocatalytic chain reactions, leading to the oxidation and release of molecular iodine (I_2).^{11,42}

To compare the amount of I_2 being released from perovskite films (grown on modified and unmodified PTAA surfaces) upon prolonged light soaking, we devised a simple experimental setup based on electrical conductance measurement. A similar approach was reported by Kerner et al. to monitor I_2 mass transport through different HTMs.⁴³ They adopted an electrical Ca corrosion test by replacing Ca with Ag and took advantage of the susceptibility of Ag to corrosion by I_2 . We laminated the perovskite samples with glass slides equipped with cavities, where Ag layers were evaporated. Then, by measuring the change in Ag conductance, we were able to relate it to I_2 vapor being released from perovskite films upon light soaking. The schematic of the applied sample structure is shown in Figure S15. Figure 6d presents normalized conductance values as a function of light-soaking time for different perovskite films. The BOC-modified samples show significantly reduced conductance drop, implying slower iodine release, which could be a result of improved structural stability of perovskite films grown on the modified PTAA surfaces. The samples, which were subjected to the light soaking, were additionally characterized by X-ray photoelectron spectroscopy (XPS) to corroborate changes in the chemical composition of the perovskite surface. Table 4 shows extracted I/Pb ratios for

Table 4. Elemental Analysis of the Surface of Three Different Perovskite Variations Before and After 1000 h of Light Soaking Derived from XPS Measurements

samples	%I	%Pb	%O	%C	I/Pb
pristine_0 h	13.73	5.37	9.54	71.25	2.55
pristine_1000 h	11.27	6.86	12.80	69.12	1.64
PEAI_0 h	16.98	6.58	9.89	66.85	2.58
PEAI_1000 h	17.34	6.56	12.56	52.24	2.64
FPEAI_0 h	22.78	8.25	12.95	54.34	2.76
FPEAI_1000 h	23.02	6.93	17.59	56.55	2.85

different samples before and after the light soaking test. The spectra for I 3d and Pb 4f are shown in Figure S16. The pristine sample shows a decrease in the I/Pb ratio upon light aging, which could imply the release of iodine vapor.⁴⁴ Perovskite samples grown on the BOC-modified PTAA samples display nearly unchanged I/Pb ratios.

Overall, the modification of a buried interface with appropriate large organic cations, which can form low-dimensional perovskite phases, provides an effective avenue to reinforce the structural stability of these layers. The reduction of ionic migration effects leads to significantly improved long-term stability of these devices. This can be complementary to perovskite surface modification, where 2D perovskite formation is commonly explored as a strategy for improving stability of these cells.²⁰

CONCLUSIONS

In this work, we have demonstrated an effective strategy to enhance the performances and stability of flexible perovskite solar cells. By modifying a buried HTM/perovskite interface with bulky organic cations, we not only improve the characteristics of that electronic contact but also reinforce the structural stability of the perovskite material itself. With a range of spectroscopic and electrical characterization techniques, we evidence a reduction in nonradiative recombination loss and improved hole extraction upon PTAA surface modification. This results in over 18% PCE for the large-area flexible PSC obtained for the FPEAI-based passivation. Crystallographic analysis shows the formation of 2D phases at the buried interface. Notably, all of the passivated samples show significantly improved thermal and light-soaking stability. The FPEAI modification yields the most effective perovskite reinforcement with minimal iodine loss and compositional change upon prolonged light soaking. This work paves the way for improving state-of-the-art perovskite solar cell architectures and reaching commercial viability for this technology.

ASSOCIATED CONTENT

Supporting Information

The Supporting Information is available free of charge at <https://pubs.acs.org/doi/10.1021/acsaem.2c02780>.

Full description of experimental methods and additional (*J*–*V*, EQE, EL, TRPL, UV–vis, FIB-SEM, AFM, XRD, XPS) data and analyses on theoretical modeling and characterization measurements (PDF)

AUTHOR INFORMATION

Corresponding Author

Konrad Wojciechowski – Saule Research Institute, 54-427 Wrocław, Poland; Saule Technologies, 54-427 Wrocław, Poland; orcid.org/0000-0002-7664-801X; Email: konrad.wojciechowski@sauletech.com

Authors

Shyantam Dasgupta – Saule Research Institute, 54-427 Wrocław, Poland; Faculty of Materials Engineering and Technical Physics, Poznan University of Technology, 60-965 Poznan, Poland

Wiktor Żuraw – Saule Research Institute, 54-427 Wrocław, Poland; Department of Semiconductor Materials Engineering, Wrocław University of Science and Technology, 50-370 Wrocław, Poland

Taimoor Ahmad – Saule Technologies, 54-427 Wrocław, Poland; orcid.org/0000-0001-9922-9603

Luigi Angelo Castriotta – Centre for Hybrid and Organic Solar Energy (CHOSE), Department of Electronic Engineering, University of Rome Tor Vergata, Rome 00133, Italy; orcid.org/0000-0003-2525-8852

Eros Radicchi – Computational Laboratory for Hybrid/Organic Photovoltaics (CLHYO), Istituto CNR di Scienze e Tecnologie Chimiche “Giulio Natta” (CNR-SCITEC), Perugia (PG) I-06123, Italy; Nanomaterials Research Group, Department of Biotechnology, University of Verona, I-37134 Verona, Italy; orcid.org/0000-0003-0749-3824

Wojciech Mróz – Centre for Nano Science and Technology (CNST@PoliMi), Istituto Italiano di Tecnologia (IIT), 20133 Milano, Italy; Istituto di Scienze e Tecnologie Chimiche “Giulio Natta” (SCITEC), Consiglio Nazionale

delle Ricerche, 20133 Milan, Italy; orcid.org/0000-0002-4534-6238

Mateusz Ścigaj – Saule Technologies, 54-427 Wrocław, Poland

Lukasz Pawlaczyk – Department of Nanometrology, Wrocław University of Science and Technology, 50-372 Wrocław, Poland

Magdalena Tamulewicz-Szwajkowska – Department of Nanometrology, Wrocław University of Science and Technology, 50-372 Wrocław, Poland; orcid.org/0000-0002-7382-011X

Marek Trzciniński – Institute of Mathematics and Physics, Bydgoszcz University of Science and Technology, 85-796 Bydgoszcz, Poland

Jaroslav Serafińczuk – Department of Nanometrology, Wrocław University of Science and Technology, 50-372 Wrocław, Poland; Lukaszewicz Research Network—PORT Polish Centre for Technology Development, 54-066 Wrocław, Poland; orcid.org/0000-0001-9809-4233

Edoardo Mosconi – Computational Laboratory for Hybrid/Organic Photovoltaics (CLHYO), Istituto CNR di Scienze e Tecnologie Chimiche “Giulio Natta” (CNR-SCITEC), Perugia (PG) I-06123, Italy; orcid.org/0000-0001-5075-6664

Aldo Di Carlo – Centre for Hybrid and Organic Solar Energy (CHOSE), Department of Electronic Engineering, University of Rome Tor Vergata, Rome 00133, Italy; Istituto di Struttura della Materia (ISM-CNR), Rome 00133, Italy; orcid.org/0000-0001-6828-2380

Filippo De Angelis – Computational Laboratory for Hybrid/Organic Photovoltaics (CLHYO), Istituto CNR di Scienze e Tecnologie Chimiche “Giulio Natta” (CNR-SCITEC), Perugia (PG) I-06123, Italy; Dipartimento di Chimica, Biologia e Biotecnologie, Università degli Studi di Perugia & UdR INSTM di Perugia, 06123 Perugia, Italy; Department of Natural Sciences & Mathematics, College of Sciences & Human Studies, Prince Mohammad Bin Fahd University, Al Khobar 31952, Saudi Arabia; orcid.org/0000-0003-3833-1975

Alina Dudkowiak – Faculty of Materials Engineering and Technical Physics, Poznan University of Technology, 60-965 Poznan, Poland; orcid.org/0000-0001-5487-4051

Complete contact information is available at: <https://pubs.acs.org/doi/10.1021/acsaem.2c02780>

Author Contributions

The manuscript was written through the contributions of all authors. All authors have given approval to the final version of the manuscript.

Notes

The authors declare the following competing financial interest(s): T.A., M.S., and K.W. are employees of Saule Technologies, a company commercializing flexible perovskite photovoltaic technology.

ACKNOWLEDGMENTS

This work was partly funded by the Foundation of Polish Science (First TEAM/2017-3/30) and European Union’s Horizon 2020 research and innovation program under the Grant Agreement No. 764047 (Espresso project). The authors would like to acknowledge scientific and technical assistance by Saule Technologies Research and Development Team.

REFERENCES

- (1) Wojciechowski, K.; Forgács, D.; Rivera, T. Industrial Opportunities and Challenges for Perovskite Photovoltaic Technology. *Sol. RRL* **2019**, *3*, No. 1900144.
- (2) Gao, Y.; Huang, K.; Long, C.; Ding, Y.; Chang, J.; Zhang, D.; Etgar, L.; Liu, M.; Zhang, J.; Yang, J. Flexible Perovskite Solar Cells: From Materials and Device Architectures to Applications. *ACS Energy Lett.* **2022**, *7*, 1412–1445.
- (3) Siekmann, J.; Ravishankar, S.; Kirchartz, T. Apparent Defect Densities in Halide Perovskite Thin Films and Single Crystals. *ACS Energy Lett.* **2021**, *6*, 3244–3251.
- (4) Dunfield, S. P.; Bliss, L.; Zhang, F.; Luther, J. M.; Zhu, K.; van Hest, M. F. A. M.; Reese, M. O.; Berry, J. J. From Defects to Degradation: A Mechanistic Understanding of Degradation in Perovskite Solar Cell Devices and Modules. *Adv. Energy Mater.* **2020**, *10*, No. 1904054.
- (5) Gao, F.; Zhao, Y.; Zhang, X.; You, J. Recent Progresses on Defect Passivation toward Efficient Perovskite Solar Cells. *Adv. Energy Mater.* **2020**, *10*, No. 1902650.
- (6) Li, B.; Ferguson, V.; Silva, S. R. P.; Zhang, W. Defect Engineering toward Highly Efficient and Stable Perovskite Solar Cells. *Adv. Mater. Interfaces* **2018**, *5*, No. 1800326.
- (7) Walsh, A.; Stranks, S. D. Taking Control of Ion Transport in Halide Perovskite Solar Cells. *ACS Energy Lett.* **2018**, *3*, 1983–1990.
- (8) Zhang, S.; Shaw, P. E.; Zhang, G.; Jin, H.; Tai, M.; Lin, H.; Meredith, P.; Burn, P. L.; Neher, D.; Stolterfoht, M. Defect/Interface Recombination Limited Quasi-Fermi Level Splitting and Open-Circuit Voltage in Mono- and Triple-Cation Perovskite Solar Cells. *ACS Appl. Mater. Interfaces* **2020**, *12*, 37647–37656.
- (9) Xue, J.; Wang, R.; Yang, Y. The Surface of Halide Perovskites from Nano to Bulk. *Nat. Rev. Mater.* **2020**, *5*, 809–827.
- (10) Jiang, F.; Pothoof, J.; Muckel, F.; Giridharagopal, R.; Wang, J.; Ginger, D. S. Scanning Kelvin Probe Microscopy Reveals That Ion Motion Varies with Dimensionality in 2D Halide Perovskites. *ACS Energy Lett.* **2021**, *6*, 100–108.
- (11) Motti, S. G.; Meggiolaro, D.; Barker, A. J.; Mosconi, E.; Perini, C. A. R.; Ball, J. M.; Gandini, M.; Kim, M.; De Angelis, F.; Petrozza, A. Controlling Competing Photochemical Reactions Stabilizes Perovskite Solar Cells. *Nat. Photonics* **2019**, *13*, 532–539.
- (12) Yang, X.; Ni, Y.; Zhang, Y.; Wang, Y.; Luo, D.; Tu, Y.; Gong, Q.; Yu, H.; Zhu, R. Multiple-Defect Management for Efficient Perovskite Photovoltaics. *ACS Energy Lett.* **2021**, *6*, 2404–2412.
- (13) Ni, Z.; Jiao, H.; Fei, C.; Gu, H.; Xu, S.; Yu, Z.; Yang, G.; Deng, Y.; Jiang, Q.; Liu, Y.; Yan, Y.; Huang, J. Evolution of Defects during the Degradation of Metal Halide Perovskite Solar Cells under Reverse Bias and Illumination. *Nat. Energy* **2022**, *7*, 65–73.
- (14) Li, Y.; Wu, H.; Qi, W.; Zhou, X.; Li, J.; Cheng, J.; Zhao, Y.; Li, Y.; Zhang, X. Passivation of Defects in Perovskite Solar Cell: From a Chemistry Point of View. *Nano Energy* **2020**, *77*, No. 105237.
- (15) Chen, J.; Park, N. G. Materials and Methods for Interface Engineering toward Stable and Efficient Perovskite Solar Cells. *ACS Energy Lett.* **2020**, *5*, 2742–2786.
- (16) Degani, M.; An, Q.; Albaladejo-Siguan, M.; Hofstetter, Y. J.; Cho, C.; Paulus, F.; Grancini, G.; Vaynzof, Y. 23.7% Efficient Inverted Perovskite Solar Cells by Dual Interfacial Modification. *Sci. Adv.* **2021**, *7*, No. eabj7930.
- (17) Cacovich, S.; Vidon, G.; Degani, M.; Legrand, M.; Gouda, L.; Puel, J.-B.; Vaynzof, Y.; Guillemoles, J.-F.; Ory, D.; Grancini, G. Imaging and Quantifying Non-Radiative Losses at 23% Efficient Inverted Perovskite Solar Cells Interfaces. *Nat. Commun.* **2022**, *13*, No. 2868.
- (18) Wolff, C. M.; Caprioglio, P.; Stolterfoht, M.; Neher, D. Nonradiative Recombination in Perovskite Solar Cells: The Role of Interfaces. *Adv. Mater.* **2019**, *31*, No. 1902762.
- (19) Caprioglio, P.; Stolterfoht, M.; Wolff, C. M.; Unold, T.; Rech, B.; Albrecht, S.; Neher, D. On the Relation between the Open-Circuit Voltage and Quasi-Fermi Level Splitting in Efficient Perovskite Solar Cells. *Adv. Energy Mater.* **2019**, *9*, No. 1901631.
- (20) Wu, G.; Liang, R.; Ge, M.; Sun, G.; Zhang, Y.; Xing, G. Surface Passivation Using 2D Perovskites toward Efficient and Stable Perovskite Solar Cells. *Adv. Mater.* **2022**, *34*, No. 2105635.
- (21) Qiu, Y.; Liang, J.; Zhang, Z.; Deng, Z.; Xu, H.; He, M.; Wang, J.; Yang, Y.; Kong, L.; Chen, C. C. Tuning the Interfacial Dipole Moment of Spacer Cations for Charge Extraction in Efficient and Ultrastable Perovskite Solar Cells. *J. Phys. Chem. C* **2021**, *125*, 1256–1268.
- (22) Shi, J.; Gao, Y.; Gao, X.; Zhang, Y.; Zhang, J.; Jing, X.; Shao, M. Fluorinated Low-Dimensional Ruddlesden–Popper Perovskite Solar Cells with over 17% Power Conversion Efficiency and Improved Stability. *Adv. Mater.* **2019**, *31*, No. 1901673.
- (23) Saliba, M.; Etgar, L. Current Density Mismatch in Perovskite Solar Cells. *ACS Energy Lett.* **2020**, 2886–2888.
- (24) Yang, B.; Suo, J.; Mosconi, E.; Ricciarelli, D.; Tress, W.; De Angelis, F.; Kim, H. S.; Hagfeldt, A. Outstanding Passivation Effect by a Mixed-Salt Interlayer with Internal Interactions in Perovskite Solar Cells. *ACS Energy Lett.* **2020**, *5*, 3159–3167.
- (25) Thrithamarassery Gangadharan, D.; Valverde-Chávez, D.; Castro-Méndez, A. F.; Prakash, V.; Izquierdo, R.; Silva, C.; Ma, D.; Correa-Baena, J. P. Bulky Cations Improve Band Alignment and Efficiency in Sn-Pb Halide Perovskite Solar Cells. *ACS Appl. Energy Mater.* **2021**, *4*, 2616–2628.
- (26) Yang, J.; Chen, Y.; Tang, W.; Wang, S.; Ma, Q.; Wu, Y.; Yuan, N.; Ding, J.; Zhang, W. H. Crystallization Tailoring of Cesium/Formamidinium Double-Cation Perovskite for Efficient and Highly Stable Solar Cells. *J. Energy Chem.* **2020**, *48*, 217–225.
- (27) Hsiao, K. C.; Jao, M. H.; Li, B. T.; Lin, T. H.; Liao, S. H. C.; Wu, M. C.; Su, W. F. Enhancing Efficiency and Stability of Hot Casting P-i-n Perovskite Solar Cell via Dipolar Ion Passivation. *ACS Appl. Energy Mater.* **2019**, *2*, 4821–4832.
- (28) Zhao, Y.; Zhang, J. Microstrain and Grain-Size Analysis from Diffraction Peak Width and Graphical Derivation of High-Pressure Thermomechanics. *J. Appl. Crystallogr.* **2008**, *41*, 1095–1108.
- (29) Jones, T. W.; Osherov, A.; Alsari, M.; Sponseller, M.; Duck, B. C.; Jung, Y. K.; Settens, C.; Niroui, F.; Brenes, R.; Stan, C. V.; Li, Y.; Abdi-Jalebi, M.; Tamura, N.; MacDonald, J. E.; Burghammer, M.; Friend, R. H.; Bulović, V.; Walsh, A.; Wilson, G. J.; Lilliu, S.; Stranks, S. D. Lattice Strain Causes Non-Radiative Losses in Halide Perovskites. *Energy Environ. Sci.* **2019**, *12*, 596–606.
- (30) Yang, X.; Luo, D.; Xiang, Y.; Zhao, L.; Anaya, M.; Shen, Y.; Wu, J.; Yang, W.; Chiang, Y. H.; Tu, Y.; Su, R.; Hu, Q.; Yu, H.; Shao, G.; Huang, W.; Russell, T. P.; Gong, Q.; Stranks, S. D.; Zhang, W.; Zhu, R. Buried Interfaces in Halide Perovskite Photovoltaics. *Adv. Mater.* **2021**, *33*, No. 2006435.
- (31) Sutanto, A. A.; Drigo, N.; Queloz, V. I. E.; Garcia-Benito, I.; Kirmani, A. R.; Richter, L. J.; Schouwink, P. A.; Cho, K. T.; Paek, S.; Nazeeruddin, M. K.; Grancini, G. Dynamical Evolution of the 2D/3D Interface: A Hidden Driver behind Perovskite Solar Cell Instability. *J. Mater. Chem. A* **2020**, *8*, 2343–2348.
- (32) Li, J.; Zuo, L.; Wu, H.; Niu, B.; Shan, S.; Wu, G.; Chen, H. Universal Bottom Contact Modification with Diverse 2D Spacers for High-Performance Inverted Perovskite Solar Cells. *Adv. Funct. Mater.* **2021**, *31*, No. 2104036.
- (33) Liu, D.; Luo, D.; Iqbal, A. N.; Orr, K. W. P.; Doherty, T. A. S.; Lu, Z. H.; Stranks, S. D.; Zhang, W. Strain Analysis and Engineering in Halide Perovskite Photovoltaics. *Nat. Mater.* **2021**, *20*, 1337–1346.
- (34) Dasgupta, S.; Misztal, K.; Fuentes Pineda, R.; Mróz, W.; Pawlaczyk, Ł.; Serafińczuk, J.; Barker, A. J.; Ahmad, T.; Herman, A. P.; Sahayaraj, S.; Kudrawiec, R.; Petrozza, A.; Dudkowiak, A.; Wojciechowski, K. New Synthetic Route of Ultrapure Alkylammonium Iodides for Perovskite Thin Films of Superior Optoelectronic Properties. *Energy Technol.* **2020**, *8*, No. 2000478.
- (35) Rau, U. Reciprocity Relation between Photovoltaic Quantum Efficiency and Electroluminescent Emission of Solar Cells. *Phys. Rev. B* **2007**, *76*, No. 085303.
- (36) Schwenzer, J. A.; Hellmann, T.; Nejand, B. A.; Hu, H.; Abzieher, T.; Schackmar, F.; Hossain, I. M.; Fassl, P.; Mayer, T.; Jaegermann, W.; Lemmer, U.; Paetzold, U. W. Thermal Stability and

Cation Composition of Hybrid Organic-Inorganic Perovskites. *ACS Appl. Mater. Interfaces* **2021**, *13*, 15292–15304.

(37) Castriotta, L. A.; Matteocci, F.; Vesce, L.; Cina, L.; Agresti, A.; Pescetelli, S.; Ronconi, A.; Markus, L.; Stylianakis, M. M.; Giacomo, F. Di.; Mariani, P.; Stefanelli, M.; Speller, E. M.; Alfano, A.; Paci, B.; Generosi, A.; Fonzo, F. Di.; Petrozza, A.; Rellinghaus, B.; Kymakis, E.; Carlo, A. Di. Air-Processed Infrared-Annealed Printed Methylammonium-Free Perovskite Solar Cells and Modules Incorporating Potassium-Doped Graphene Oxide as an Interlayer. *ACS Appl. Mater. Interfaces* **2021**, 11741–11754.

(38) Ahmad, T.; Dasgupta, S.; Almosni, S.; Dudkowiak, A.; Wojciechowski, K. Encapsulation Protocol for Flexible Perovskite Solar Cells Enabling Stability in Accelerated Aging Tests. *Energy Environ. Mater.* **2022**, No. e12434.

(39) Khenkin, M. V.; Katz, E. A.; Abate, A.; Bardizza, G.; Berry, J. J.; Brabec, C.; Brunetti, F.; Bulović, V.; Burlingame, Q.; Di Carlo, A.; Cheacharoen, R.; Cheng, Y. B.; Colmann, A.; Cros, S.; Domanski, K.; Dusza, M.; Fell, C. J.; Forrest, S. R.; Galagan, Y.; Di Girolamo, D.; Grätzel, M.; Hagfeldt, A.; von Hauff, E.; Hoppe, H.; Kettle, J.; Köbler, H.; Leite, M. S.; Liu Frank, S.; Loo, Y. L.; Luther, J. M.; Ma, C. Q.; Madsen, M.; Manceau, M.; Matheron, M.; McGehee, M.; Meitzner, R.; Nazeeruddin, M. K.; Nogueira, A. F.; Odabaşı, Ç.; Osherov, A.; Park, N. G.; Reese, M. O.; De Rossi, F.; Saliba, M.; Schubert, U. S.; Snaith, H. J.; Stranks, S. D.; Tress, W.; Troshin, P. A.; Turkovic, V.; Veenstra, S.; Visoly-Fisher, I.; Walsh, A.; Watson, T.; Xie, H.; Yildirim, R.; Zakeeruddin, S. M.; Zhu, K.; Lira-Cantu, M. Consensus Statement for Stability Assessment and Reporting for Perovskite Photovoltaics Based on ISOS Procedures. *Nat. Energy* **2020**, *5*, 35–49.

(40) Motti, S. G.; Meggiolaro, D.; Martani, S.; Sorrentino, R.; Barker, A. J.; De Angelis, F.; Petrozza, A. Defect Activity in Lead Halide Perovskites. *Adv. Mater.* **2019**, *31*, No. 1901183.

(41) Meggiolaro, D.; Motti, S. G.; Mosconi, E.; Barker, A. J.; Ball, J.; Andrea Riccardo Perini, C.; Deschler, F.; Petrozza, A.; De Angelis, F. Iodine Chemistry Determines the Defect Tolerance of Lead-Halide Perovskites. *Energy Environ. Sci.* **2018**, *11*, 702–713.

(42) DeQuilettes, D. W.; Zhang, W.; Burlakov, V. M.; Graham, D. J.; Leijtens, T.; Osherov, A.; Bulović, V.; Snaith, H. J.; Ginger, D. S.; Stranks, S. D. Photo-Induced Halide Redistribution in Organic-Inorganic Perovskite Films. *Nat. Commun.* **2016**, *7*, No. 11683.

(43) Kerner, R. A.; Heo, S.; Roh, K.; MacMillan, K.; Larson, B. W.; Rand, B. P. Organic Hole Transport Material Ionization Potential Dictates Diffusion Kinetics of Iodine Species in Halide Perovskite Devices. *ACS Energy Lett.* **2021**, *6*, 501–508.

(44) Tan, S.; Yavuz, I.; Weber, M. H.; Huang, T.; Chen, C. H.; Wang, R.; Wang, H. C.; Ko, J. H.; Nuryyeva, S.; Xue, J.; Zhao, Y.; Wei, K. H.; Lee, J. W.; Yang, Y. Shallow Iodine Defects Accelerate the Degradation of α -Phase Formamidinium Perovskite. *Joule* **2020**, *4*, 2426–2442.

Encapsulation Protocol for Flexible Perovskite Solar Cells Enabling Stability in Accelerated Aging Tests

Taimoor Ahmad , Shyantant Dasgupta, Samy Almosni, Alina Dudkowiak, and Konrad Wojciechowski* 

Flexible perovskite solar cells (f-PSCs) offer attractive commercial prospects in the near future, enabled by new value propositions, such as mechanical flexibility, or high specific powers. The long-term reliability of these devices requires appropriate encapsulation to prevent degradation caused by environmental factors. Here, a lamination protocol is developed, incorporating adhesive materials, barrier foils, and edge sealants, which results in a robust device hermitization. By applying the developed procedure to three different perovskite solar cell configurations (p-i-n with carbon, p-i-n with silver, and n-i with carbon), fabricated with large active areas (1 cm²), the universality of this approach is demonstrated. The best devices preserved over 85% of the initial performance after a sequence of accelerated aging tests based on industry standards (compliant with the IEC 61215 and IEC 61646) comprised of 1400 h of damp heat, 50 thermal cycles, and 10 cycles of the humidity-freeze test.

1. Introduction

Organic–inorganic metal halide perovskite solar cell (PSC) technology emerged in the past decade as one of the biggest breakthroughs in photovoltaics, advancing toward commercialization at a prolific pace. This is largely owed to exceptional optoelectronic properties of the perovskite photoactive layers, resulting in high performance, which is also accompanied by the potential of very attractive cost factors (low material and processing costs) and new value propositions of PV products (high specific power, flexibility).^[1–4] PSCs recently reached a certified power conversion efficiency (PCE) value of 25.7%.^[5,6]

Historically, long-term stability has been a major concern in the roadmap for the successful commercial deployment of this technology.

Dr. T. Ahmad, Dr. S. Almosni, Dr. K. Wojciechowski
Saulé Technologies, Wrocław Technology Park, 11 Dunska Street, Sigma Building 54-130 Wrocław, Poland
Department of Electronics Engineering, University of Rome “Tor Vergata”, Via del Politecnico 1, 00133 Rome, Italy
E-mail: konrad.wojciechowski@sauletech.com

S. Dasgupta, Dr. K. Wojciechowski
Saulé Research Institute, Wrocław Technology Park, 11 Dunska Street, Sigma Building, 54-130 Wrocław, Poland
S. Dasgupta, Prof. A. Dudkowiak
Faculty of Materials Engineering and Technical Physics, Poznan University of Technology, Piotrowo 3, 60-965 Poznan, Poland

 The ORCID identification number(s) for the author(s) of this article can be found under <https://doi.org/10.1002/eam2.12434>.

DOI: 10.1002/eam2.12434

Great progress has been achieved in understanding the primary degradation mechanisms. Most important achievements include the development of robust perovskite structures (compositional variations), various routes for effective passivation of crystalline defects, understanding and mitigation of the negative repercussions of ionic motions in perovskite layers, or engineering charge selective contacts with improved chemical and electronic stability.^[7–13] All these points relate to the intrinsic stability of perovskite device structures. To exploit the full potential of perovskite PV technology, long-term operation in harsh weather conditions has to be ascertained. Due to ionic character and susceptibility to coordination by polar groups, metal halide perovskites most likely will always require some level of protection from external factors, especially humidity.^[14–16] The damp-

heat test (1000 h in 85 °C, 85% relative humidity, RH) is considered to be one the harshest reliability checks for any emerging PV technology. Few examples of perovskite devices successfully passing stress tests in such conditions were reported, typically applying different glass-based encapsulation protocols.^[17–22]

Flexible, polymeric foils used as a substrate and packaging materials deliver an attractive economic potential, originating from the prospects of large production throughputs, which are enabled by the roll-to-roll (R2R) processing.^[3,23,24] Flexible perovskite solar cells (f-PSCs) are expected to find an application as powering units in a wide range of sectors, including the Internet of things (IoT), smart integrated buildings, wearable and portable electronics, or self-powered bioelectronics.^[25] Glass is an excellent moisture barrier, exhibiting a water vapor transmission rate (WVTR) below $1 \times 10^{-6} \text{ g m}^{-2} \text{ day}^{-1}$. However, it is brittle, rigid, and heavy, hence not compatible with the R2R processing. Additionally, glass encapsulation will affect the device's integrability and attainable specific powers, making it unfit for many market segments. In order to provide long-term operational reliability of f-PSCs, an encapsulation concept that meets the criteria of high optical transmission, low gas permeation rates, good adhesion to the device stack, and appropriate edge sealing preventing lateral moisture ingress is needed. Flexible barrier materials were successfully explored for many organic electronic applications, including organic photovoltaics (OPV), where barriers of the WVTR at the range of 10^{-3} – $10^{-4} \text{ g m}^{-3} \text{ day}^{-1}$ provide effective protection.^[26,27] Although critical permeation rates for the f-PSCs have not been determined yet, barrier requirements similar to OPV devices can be expected.^[28,29]

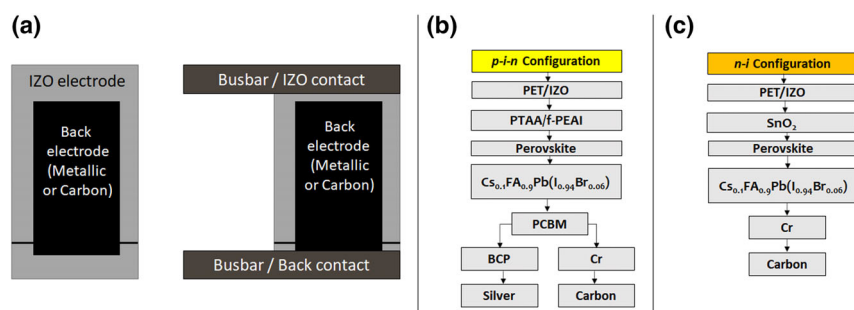


Figure 1. a) Schematic of the electrode design (front and back contacts) and electrical connections based on busbar attachment, which was applied for the perovskite solar cell fabrication; b) flow chart depicting the f-PSC architecture of p-i-n configuration, with metal or carbon back contacts; and c) n-i HTM-free configuration, with carbon electrode.

In this work, we developed an encapsulation protocol for large-area f-PSCs, employing polymer-based barrier foils and UV-curable adhesives, to provide robust hermetization against environmental factors. We also explored different edge sealants, and implemented hydrophobic buffer layers (HBL) based on polydimethylsiloxane (PDMS), to achieve good stability in the stressing environmental conditions. The reliability of these devices was assessed with three different aging tests, compliant with the IEC norms for established photovoltaic technologies (IEC 61215, IEC 61646), namely damp-heat (DH, 85 °C/85% relative humidity, RH), thermal cycling (TC, the temperature varied between −40 °C and 85 °C), and humidity-freeze (HF, between −40 °C with the long dwell time at 85 °C and 85% RH) test. Additionally, we have demonstrated the universality of the developed encapsulation protocol, by obtaining stable photovoltaic performance after aging for the three different f-PSC architectures (p-i-n with carbon and silver back contact electrodes, and n-i architecture with carbon electrode and no hole transporting layer). The best cell preserved over 85% of the initial PCE after a sequence of tests comprised of 1400 h of damp heat, 50 thermal cycles, and 10 cycles of the humidity-freeze test.

2. Results and Discussions

Perovskite solar cell typically is comprised of multiple layers arranged in a sandwich stack. The stability of such devices is affected by individual layers and their interactions.^[30] At first, we implemented PSC of a p-i-n configuration, applying the most commonly used device structure, with the poly(bis(4-phenyl)(2,4,6-trimethylphenyl)-amine) (PTAA) as a hole transporting material (HTM).^[31–33] PSCs incorporating PTAA often suffer from reduced charge-transport ability under heat and light stress, which limits the long-term reliability.^[34,35] In this work, we introduced an ultrathin interlayer between PTAA and perovskite film, which is based on a halide salt of bulky alkylammonium cation, fluoro-phenylethylammonium iodide (FPEAI). It was reported that such dipolar organic ammonium halides could passivate interfacial defects in the perovskite layer, such as uncoordinated lead ions, and negatively charged sites (interstitial, antisite defects).^[36] We applied FPEAI surface treatment to the PTAA layer for all the p-i-n cells in this study. For the photoactive layer, our first choice was a double-cation perovskite composition with the generic formula of $\text{Cs}_{0.1}\text{FA}_{0.9}\text{Pb}(\text{I}_{0.94}\text{Br}_{0.06})$, which was widely reported to exhibit improved structural stability, especially at elevated temperatures.^[22,37–39] We additionally

modified it by incorporating the 18-Crown-6 ether (18C6) into the perovskite precursor solution. This additive was shown to modulate perovskite growth (stabilization of α -phase of the FA-based perovskite), passivate undercoordinated Pb defects, and provide additional protection against moisture due to 18C6 hydrophobic character.^[40–42] In these devices, we also tested two different back contact electrode materials, thermally evaporated silver layer and solution-processed carbon paste, analogously to our previous report.^[43] Carbon-based back contact electrodes deliver interesting solutions for improving the industrial viability of perovskite solar cells, increasing chemical inertness, and offering facile processing with scalable printing techniques.^[44,45]

We also fabricated PSCs of reversed polarity, with a carbon electrode and without a hole transporting material. All the photovoltaic devices reported in this work were fabricated on flexible substrates (PET foil), with large active areas (1 cm²). We employed the commercial PET foil, coated with the indium doped zinc oxide (IZO) as a transparent conductive electrode, exhibiting sheet resistance of 15 Ohms/sq. The schematic of the optimized cell design is shown in **Figure 1a**. In **Figure 1b, c**, we present different solar cell architectures used in this study.

We compared the PV performance of different f-PSC device configurations by measuring current density–voltage (J-V) characteristics and stabilized power output (SPO). Extracted performance parameters for a batch of cells are shown in **Table 1**.

We obtained power conversion efficiencies (PCEs) close to 10% or more for all the device types, with the p-i-n cells employing metal electrode exceeding 14%. We present the J-V, and SPO curves of the most efficient devices of different configurations in **Figure S1a–e**. The external quantum efficiency (EQE) spectra and integrated current density values for each solar cell type are shown in **Figure 1f**.

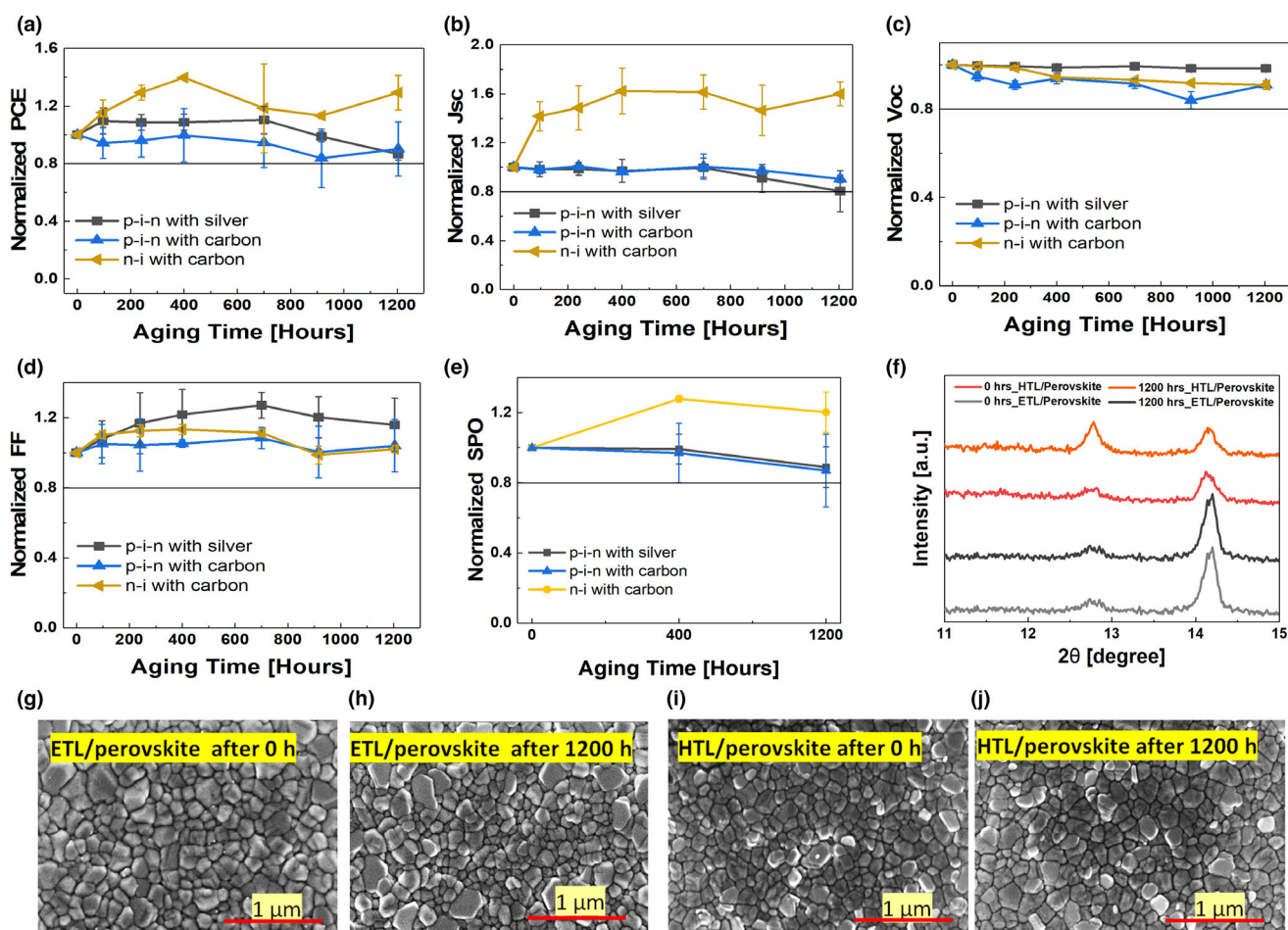
Then, we explored the intrinsic structural stability of applied perovskite material. Thermal stress can induce decomposition of perovskite active layer, typically leading to the release of volatile organic species, and appearance of PbI_2 phase.^[14] Humidity can further accelerate this process via complex formation and hydrogen bonding, weakening the attraction of organic cations to the inorganic octahedra.^[14,46] To confirm the hypothesis of enhanced thermal stability of perovskite composition without methylammonium cations, we compared the double-cation (2C) recipe described above— $\text{Cs}_{0.1}\text{FA}_{0.9}\text{Pb}(\text{I}_{0.94}\text{Br}_{0.06})$, with the triple-cation (3C) formulation— $\text{Cs}_{0.04}(\text{MA}_{0.17}\text{FA}_{0.83})_{0.96}\text{Pb}(\text{I}_{0.83}\text{Br}_{0.17})_3$. The p-i-n devices with Ag back contact electrode containing these two different perovskite thin films were subjected to 85 °C stress test, inside the nitrogen-filled glovebox. In **Figure S2a–d**, we show the evolution of normalized PCE values along the aging, together with X-ray diffractograms (XRD) of perovskite films, before and after the 1000-h-long test. The peak at 12.7°, which can be assigned to PbI_2 ((001) plane), is visible for all the samples, but its enhancement upon aging is much more pronounced for the 3C perovskite films. This is also combined with a significantly faster drop of performance values for this device type. For this reason, we used 2C perovskite composition for the remaining part of this study. In the next step, we further explored the intrinsic stability of perovskite solar cells by comparing different device configurations in the 85 °C stress test, inside the glovebox. The evolution of average performance parameters, extracted from

Table 1. Photovoltaic parameters extracted from the current–voltage characterization measurements of perovskite solar cells fabricated with different architecture.

Device type (with the different back electrode)	(PCE _{best}) PCE _{Avg} ± SD (%)	(FF _{best}) FF _{Avg} ± SD (%)	(V _{OC best}) V _{OC Avg} ± SD (V)	(J _{SC best}) J _{SC Avg} ± SD (mA cm ⁻²)	SPO _{best} (%)
p-i-n with silver	(14.24) 12.25 ± 1.3	(63.1) 55.23 ± 5.4	(1.06) 1.04 ± 0.02	(21.16) 21.25 ± 0.6	14.12
p-i-n with carbon	(10.51) 9.82 ± 1.5	(50.9) 45.4 ± 4.6	(0.97) 0.95 ± 0.02	(20.66) 22.67 ± 4.6	10.25
n-i, HTM free with carbon	(9.8) 8.78 ± 0.6	(45.1) 43.22 ± 2.6	(1.01) 0.99 ± 0.01	(21.2) 20.38 ± 1.1	9.64

periodic J-V and SPO characterization measurements taken for three individual cells per each device configuration (p-i-n with metal, p-i-n with carbon, and HTM-free n-i with carbon), is plotted in **Figure 2a–e**. Corresponding J-V curves are shown in Figure S3. For the HTM-free with carbon and p-i-n with silver cells, we observed an initial increase in PCE values, whereas p-i-n devices with carbon, in the beginning, showed a small performance decline, primarily caused by V_{OC} loss. After 1200 h of aging, all the cells displayed more than 80% of initial PCE, with the HTM-free carbon cells yielding about 20% higher PCE values than before the test. This increase, driven by J_{SC} enhancement,

we assign to improved hole extraction at the interface with carbon was also observed in our previous work.^[43] Likely, remnant solvents and organic binders present in the carbon paste have not been fully annealed during device processing. A prolonged elevated temperature could reduce contact resistance at the hole extraction interface. This could be also combined with some morphological changes of the carbon layer, making more conformal contact and easing the charge transfer process. In Figure S4, we show PL spectra of the “n-i with carbon” device, before and after 1000 h of 85 °C heating. Significant PL quenching was recorded upon aging. In combination with the distinct


Figure 2. a–e) Time evolution of normalized photovoltaic parameters of unencapsulated perovskite solar cells of different configurations (p-i-n with silver, p-i-n with carbon, and n-i with carbon), which were subjected to thermal stress at 85 °C on a hotplate, inside the glovebox; f) XRD of perovskite films (processed on HTL or ETL), before and after the thermal test; g–j) top-view SEM images of fresh and aged perovskite samples.

evolution of performance parameters (stable V_{OC} , increase of J_{SC} and FF), it evidences improved electronic contact and hole transfer at the carbon interface.

We also monitored the crystallographic and morphological evolution of perovskite layers upon thermal stress by carrying out XRD and top-view scanning electron microscopy (SEM) imaging. The XRD patterns of fresh and aged samples are shown in Figure 2f. Upon aging, the relative intensity of PbI_2 peaks become more pronounced for the p-i-n configuration (perovskite grown on the modified PTAA). In SEM images (Figure 2g–j), we can observe dense and well-preserved perovskite morphologies upon heat stress.

Having confirmed good intrinsic stability of selected perovskite solar cells in the thermal test, we moved on to develop effective flexible encapsulation to provide protection against external factors. The damp-heat test inside the climate chamber (85 °C/85% RH), with a periodically monitored photovoltaic performance of devices exposed to these conditions, was used as a primary guideline for this work. For all the encapsulation trials, we applied a commercial barrier foil, whose water vapor transmission rate (WVTR) and oxygen transmission rate (OTR) are $5.5 \times 10^{-3} \text{ g m}^{-2} \text{ day}^{-1}$ (50 °C, 100% R.H.) and $<0.0005 \text{ cm}^3 \text{ m}^{-2} \text{ day}^{-1}$ (23 °C, 0% R.H.), respectively.

We investigated different encapsulation protocols (varied laminate structures), using the same device configuration—carbon-based, HTM-free PSCs. First, we applied busbars to the device terminals (Figure 1b). We used commercially available Sn–Cu busbars with a conductive adhesive on one side. Next, a thermoplastic foil was laminated on the back of a device, and then, UV-curable material was applied on both sides of the device to provide good adhesion to the barrier foil. Thermoplastic foil was used to avoid permeation of the UV-curable ink inside the carbon pores, which could insulate that contact. Another advantage of this thermoplastic polymer film is that it provides improved adhesion between the busbar and the substrate. We noticed

that during the accelerated aging test, the busbar can delaminate from the ITO contact. Following the process of sandwiching the cell between the two sheets of barrier foil, UV-curing was applied to harden the adhesive. We monitored the curing level with the Fourier transform infrared spectroscopy (FTIR) measurements. In Figure S5, we show the spectra of cured and uncured adhesive films. The peaks in the region 1680–1620 cm^{-1} can be assigned to the C=C double bond, which gets reduced upon acrylate crosslinking. Also, the peaks in the 3000–2840 cm^{-1} range increase their intensity upon UV illumination, which indicates the formation of C–C bonds. The curing parameters (time, lamp power) were optimized to reach a complete level of crosslinking. After the encapsulation, we provided electrical contact to the device terminals via soldering iron to the busbar, through the barrier foil.

In the next step, as an alternative to the thermoplastic polymer, we used a hydrophobic PDMS (polydimethylsiloxane)-based formulation, which was deposited on top of the carbon layer, and subsequently laminated with a thin PET foil, before applying the UV-curable formulation and barrier foil. The PDMS coating provides adhesion to the PET, which in turn ascertains no permeation of the UV-curable ink inside the carbon pores. Additionally, its hydrophobicity can grant extra protection for the perovskite layer. It was also shown as an effective modifier of the perovskite–carbon interface.^[47] The schematic comparison of the two laminate stacks is shown in Figure 3a,b. J–V curves of the cells before and after applying thermoplastic foil or PDMS-based/PET laminate are shown in Figure S6. We recorded a small drop in performance for both lamination options, with the PDMS/PET showing a smaller FF reduction. The performance parameters extracted from J–V curves are shown in Table S2. Before stressing complete solar cells, we also investigated the effect of contact aging and possible busbar delamination. The dummy samples (IZO substrate connected with busbars and laminated with the two different routes) were prepared and subjected to the

damp-heat test. The results are shown in Figure S7d. We did not observe any sizable resistance increase, suggesting the quality of electrical contacts between busbars and device electrode is well preserved. However, after 335 h we observed signs of delamination taking place at the edges of the busbar, which is depicted in Figure S7a–c. The delamination is likely to be happening due to the soldering process, which involves local heating to temperatures above 300 °C. Such high temperature hardens the adhesive and can generate cracks and defects, where moisture ingress takes place. We tried to solve this problem by extending the busbar outside of the encapsulation stack, as shown in Figure S8. Encapsulated flexible PSCs were placed in the climate chamber (85 °C/85% R.H. conditions), and the test was periodically interrupted for the J–V characterization measurements. The time evolution of PV performance parameters, monitored for the cells finished with the two alternative lamination routes, is shown in Figure 3c,d. The cell with the thermoplastic foil dropped below 80% of initial performance within the first 120 h, whereas devices utilizing the hydrophobic buffer layer preserved 80% for over 700 h.

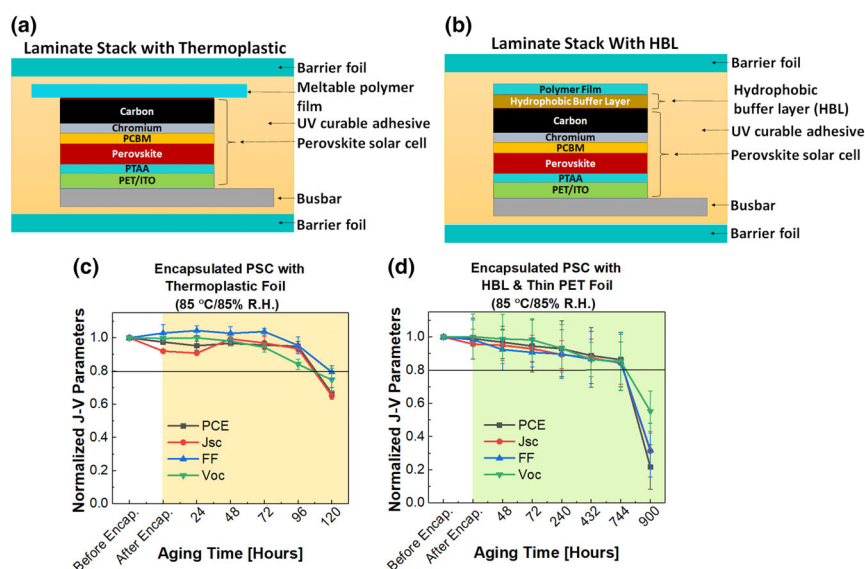


Figure 3. Schematic illustration of the perovskite solar cell encapsulation stack, incorporating a) meltable (thermoplastic) polymer or b) hydrophobic buffer layer (based on PDMS) and PET foil. Time evolution of normalized J–V parameters of f-PSCs encapsulated with the c) thermoplastic foil or d) hydrophobic buffer layer. Highlighted areas (beige and green colors) represent the duration of the damp-heat test (85 °C/85% R.H.).

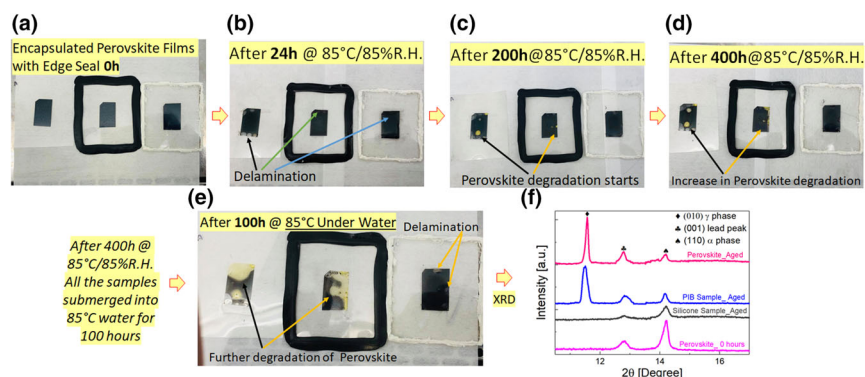


Figure 4. a–e) Photographic documentation of encapsulated perovskite thin films, with and without edge sealing (black rim—PIB seal; white rim—silicone), which were subjected to damp-heat aging conditions and hot water (85 °C) immersion. Samples were periodically removed from the climate chamber to take photographs; f) XRD of perovskite films after aging tests and peeling off encapsulation layers.

The second lamination strategy showed significantly improved stability results, but we still observed visual changes in the perovskite layers after a few hundred hours of aging. The discoloration was originating from the sides, which prompted us to find an effective technique to block this path of moisture ingress, as shown in Figure S9. We applied two different, commercially available edge sealants: polyisobutylene (PIB) and silicone paste. PIB, typically used in the form of a thick paste, was demonstrated as an effective edge sealant for the glass/glass PSC encapsulation.^[17,48] Here, we used PIB rubber ribbons, which are easier to apply on flexible substrates. To compare the rate of moisture ingress with different edge sealants,

we used encapsulated perovskite films (structure: barrier foil/UV-adhesive/PET-IZO/HTL/perovskite/adhesive/barrier foil), applied glue around the sample (PIB, silicone, or no sealant), and subjected such samples to the damp-heat test (85 °C/85% R.H. conditions). Photographic documentation of perovskite decomposition at different aging times is shown in Figure 4a–f.

After 24 h, we observed delamination taking place in all three cases, which was caused by poor adhesion of the UV-curable adhesive to the perovskite surface. There was no sign of debonding on the other side, where barrier foil adheres to the PET. The sample without any edge sealing material was the first to show perovskite yellowing (within the first 200 h), which indicates chemical decomposition caused by water. Slightly slower degradation was observed for the PIB type. The sample with the silicone seal had no visual change after 400 h of aging (see Figure 4a–d). To accelerate the moisture-induced perovskite decomposition, we immersed all the aged samples in the hot water (85 °C) and kept them there for another 100 h. After the test, we observed pronounced delamination areas; however, for the silicone-sealed sample, still, there was no visible perovskite yellowing effect (Figure 4e). We peeled off the barrier foil and measured the XRD of aged perovskite layers. The patterns are shown in Figure 4f. The samples without edge sealant and with the PIB show pronounced PbI_2 phase (diffraction peak at 12.7°) and non-perovskite $\delta\text{-FAPbI}_3$ (diffraction peak at 11.7°, (010) plane). The silicone-based sample also displays the presence of PbI_2 , but no

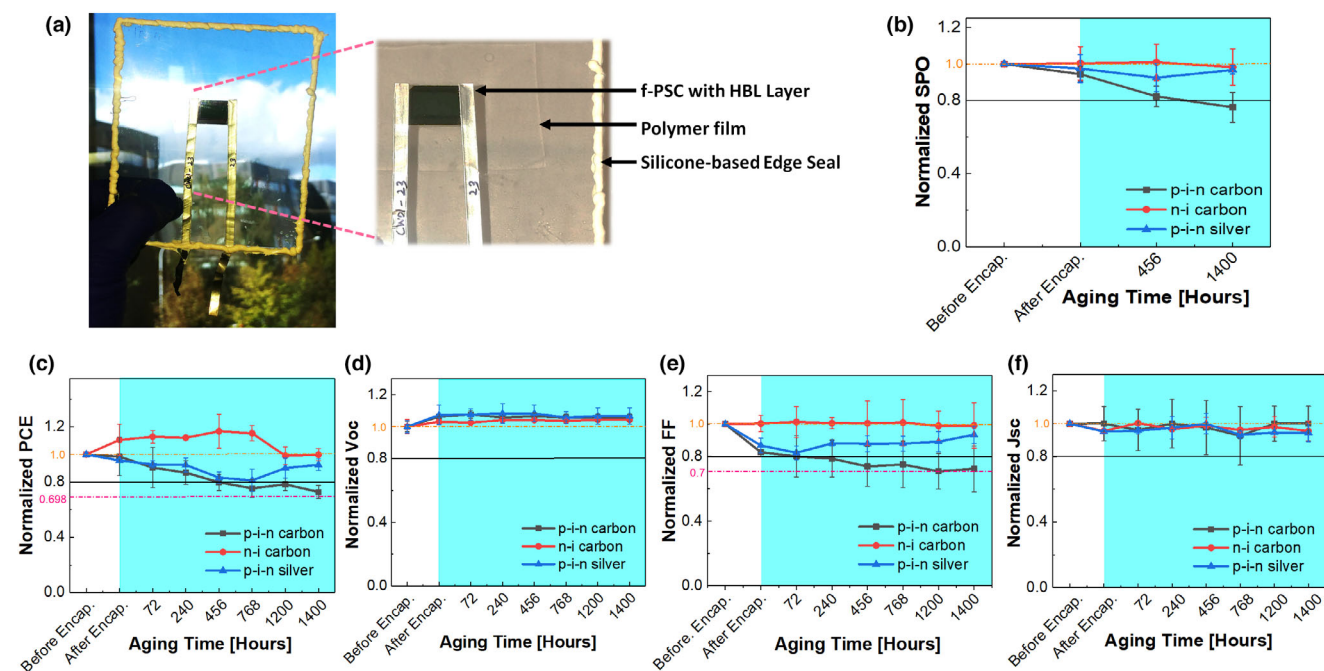


Figure 5. a) Pictures of an encapsulated f-PSC employing a silicone-based edge sealant; b–f) time evolution of normalized averaged photovoltaic parameters of f-PSCs of different configurations (three cells for each variation), which were subjected to damp-heat aging (85 °C/85% R.H.).

Table 2. Specification of aging tests compliant with the IEC61215:2016 standard.

Test	Conditions	Hours/cycles
Damp heat	85 °C/85% R.H.	1400 h
Thermal cycling	−40 °C to 85 °C with 10 min dwell time for each condition	50 cycles
Humidity freeze	50 rounds of thermal cycling as a prerequisite, followed by −40 °C to 85 °C (30 min of dwell time), and at 85% R.H. (20 h of dwell time) Ramp rate of 100 °C per hour for 0 °C ⇌ 85 °C Ramp rate of 200 °C per hour for 0 °C ⇌ −40 °C	10 cycles

hexagonal δ phase. This test highlights the importance of edge sealing for achieving robust device encapsulation.

In the next step, we applied the silicone edge sealant for the laminate stack with the hydrophobic buffer layer, which showed a superior aging profile. Such optimized encapsulation protocol was applied to the three different perovskite device architectures described above—HTM-free n-i with carbon, p-i-n with carbon, and p-i-n with silver. An example of the encapsulated solar cell with the silicone-based rim sealant is shown in **Figure 5a**. Subsequently, we placed the devices in the

climate chamber for the damp-heat test (85 °C/85% R.H. conditions). The cells were periodically removed from the aging setup to measure the PV performance. Time evolution of normalized $J-V$ parameters and SPO values (average from the three cells of each type) is shown in **Figure 5b–f**. $J-V$ and SPO curves, and a full list of PV parameters for the best devices of each type, which were subjected to the damp-heat test, before and after aging, are presented in **Figure S10** and **Table S3**.

The cells with carbon, embodying n-i architecture without HTM, displayed no drop of performance over 1400 h of stressing. Due to a small increase in FF, the final PCE was slightly higher than the initial efficiency. We attribute this effect to reduced contact resistance at the perovskite–carbon interface. In planar architectures, when carbon is processed on top of perovskite-based photoactive layers, due to the high porosity of carbon films the conformality of this interface is often problematic, as it increases the contact resistance and affects the solar cell fill factor.^[49,50] High temperatures imposed during aging can induce small morphological changes in the carbon layer, improving the quality of this electronic contact.^[43]

The cells employing the silver back contact electrode showed a 4% drop in performance after encapsulation, which was primarily caused by the FF reduction (**Figure 5c–f**). After 1400 h of damp-heat aging, the performance was largely preserved. This was rather unexpected, especially given notorious silver-iodide reactivity.^[51–53] On the contrary, the p-i-n cells with carbon electrode were the least stable of all the three PSC types, showing reductions in both J_{SC} and FF, over the aging time window. It yielded 73% of the initial PCE after 1400 h of aging. The fact that devices with silver back contact were more stable

was rather unexpected. Larger FF and J_{SC} drops in carbon-based p-i-n cells suggest that increasing contact resistance and reduced efficacy of carrier extraction could be a dominant degradation effect for this device type during the damp-heat test. Such contact resistance is likely to originate at the electron-selective contact. It could be induced by morphological changes of the carbon layer, possibly some delamination from the Cr interlayer, which could be induced by mechanical strain from the lamination materials. We measured PL spectra of these devices, before and after 500 h of damp-heat aging (**Figure S11**). We recorded higher PL intensities for the aged samples, which indeed points to the deterioration of carrier extraction, which is more pronounced for the carbon-based device. After the damp-heat test, the best cells of each type (the most stable ones) were subjected to further IEC-based aging. We carried out thermal cycling, followed by the humidity-freeze test. Both experiments were done according to the IEC61215:2016 specifications; the details are listed in **Table 2**. A single thermal cycle takes about 7 h, whereas 20 h is required to complete one humidity-freeze cycle. A detailed sequence of steps used for these tests is provided in **Table S1**.

When the temperature is varied in such a broad range (from −40 to +85 °C), it exerts large mechanical strain on the laminate stack. Delamination and cracking can provide fast

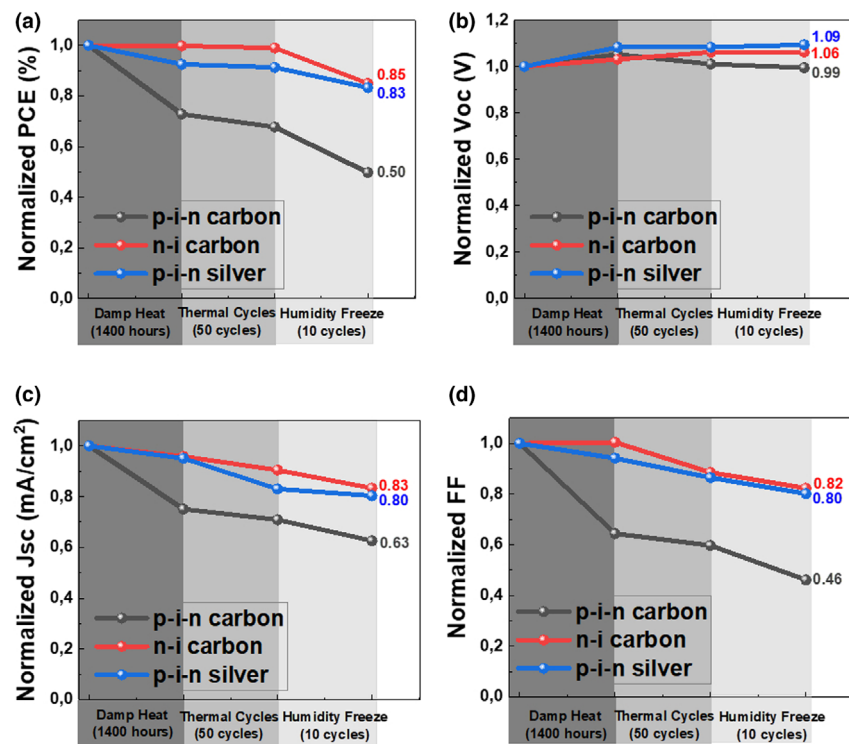


Figure 6. a–d) Time evolution of normalized photovoltaic parameter values (PCE, V_{OC} , J_{SC} , and FF), recorded for the encapsulated f-PSCs of different configurations (aging tests according to the IEC61215:2016 norm). The area highlighted in dark gray refers to the damp-heat test, the light gray area to the thermal cycling, and the lightest gray area to the humidity-freeze test.

penetration route for moisture to get inside the device, which in turn would degrade the photoactive layer. The performance evolution for the studied devices is shown in Figure 6. All the samples showed promising reliability, with the n-i-carbon and p-i-n-silver device types preserving over 80% of the initial performance after 1400 h of damp heat, 50 thermal cycles, and 10 humidity-freeze cycles. To the best of our knowledge, this is the first demonstration of a flexible perovskite solar cell of a large active area, which survives aging tests compliant with the IEC standards. The humidity-freeze test proved to be the most aggressive, even for the n-i-carbon architecture, which did not show any drop in the damp heat. After 10 HF cycles, ~14% of performance degradation was observed. This test provides the harshest stress factors due to the combined effects of a wide range of temperature variations and prolonged heating at high humidity levels. Engrossed water freezes inside the laminate can exert additional mechanical strain and originate some delamination. Reductions in FF and J_{SC} are the main factors driving the PCE drop (Figure 6). This could imply a propagating reduction in the efficacy of charge extraction, which in turn could be a consequence of strain-induced interfacial failures.^[18,54] Overall, these results suggest that further work on the thermo-mechanical stability of f-PSCs, especially related to the interfacial fracture resistance, is needed to fully prove the long-term reliability of these devices.

3. Conclusions

In summary, we have demonstrated large-area, flexible perovskite solar cells withstanding the IEC61215 standard damp-heat, thermal cycling, and humidity-freeze tests. We were able to achieve this by developing a holistic encapsulation protocol, where a barrier foil was combined with appropriately selected adhesive materials, an additional protective buffer layer, and effective edge sealants. The processing methodology (roll-to-roll lamination) is a commercially viable route, routinely applied in a thin-film PV manufacturing industry. Importantly, we showed the universality of the applied protocol, by obtaining promising stability results for different perovskite solar cell architectures, including p-i-n and n-i device configurations, with metallic and carbon back contact electrodes. We believe this is an important step, providing a convincing feasibility assessment for the long-term reliability of the flexible perovskite photovoltaics in real-life, outdoor conditions. Additionally, the supporting materials utilized in the encapsulation process (PDMS-based coating, thermoplastic foil, UV-curable adhesive, edge sealants) are cost-effective, having little impact on the final module production costs. Ultra-high barrier foils currently constitute a significant contribution to the overall price, typically exceeding \$15/m² for a single sheet, with WVTR below the 10⁻⁴ g m² day range.^[55,56] Nevertheless, with the increasing demand for flexible photovoltaics, and the development of new coating technologies, such as spatial-ALD, the price of these products is expected to be reduced in the near future.^[56,57]

Acknowledgements

T.A. and S.D. contributed equally to this work. This work was part-funded by the European Union's Horizon 2020 research and innovation program under the grant agreement no. 764047 (Espresso project), and the Foundation of Polish Science (First TEAM/2017-3/30). The authors would like to acknowledge scientific and technical assistance from Saule Technologies Research and Development Team.

Conflict of Interest

T.A., S.A., and K.W. are employees of Saule Technologies, a company commercializing flexible perovskite photovoltaic technology.

Supporting Information

Supporting Information is available from the Wiley Online Library or from the author.

Keywords

encapsulation, flexible photovoltaics, perovskite solar cell, stability

Received: January 17, 2022

Revised: April 19, 2022

Published online: April 27, 2022

- [1] G. Kieslich, S. Sun, A. K. Cheetham, *Chem. Sci.* **2014**, *5*, 4712.
- [2] N. L. Chang, A. W. Y. Ho-Baillie, D. Vak, M. Gao, M. A. Green, R. J. Egan, *Sol. Energy Mater. Sol. Cells* **2018**, *174*, 314.
- [3] K. Wojciechowski, D. Forgács, T. Rivera, *Sol. RRL* **2019**, *3*, 1900144.
- [4] M. O. Reese, S. Glynn, M. D. Kempe, D. L. McGott, M. S. Dabney, T. M. Barnes, S. Booth, D. Feldman, N. M. Haegel, *Nat. Energy* **2018**, *3*, 1002.
- [5] Best Research-Cell Efficiency Chart | Photovoltaic Research | NREL.
- [6] H. Min, D. Y. Lee, J. Kim, G. Kim, K. S. Lee, J. Kim, M. J. Paik, Y. K. Kim, K. S. Kim, M. G. Kim, T. J. Shin, S. Il Seok, *Nature* **2021**, *598*, 444.
- [7] Y. H. Khattak, F. Baig, A. Shuja, L. Atourki, K. Riaz, B. M. Soucase, *ACS Appl. Electron. Mater.* **2021**, *3*, 3509.
- [8] M. Zhang, Q. Chen, R. Xue, Y. Zhan, C. Wang, J. Lai, J. Yang, H. Lin, J. Yao, Y. Li, L. Chen, Y. Li, *Nat. Commun.* **2019**, *10*, 1.
- [9] S. Yang, J. Dai, Z. Yu, Y. Shao, Y. Zhou, X. Xiao, X. C. Zeng, J. Huang, *J. Am. Chem. Soc.* **2019**, *142*, 11937.
- [10] M. M. Byranvand, M. Saliba, *Sol. RRL* **2021**, *5*, 2100295.
- [11] A. Maiti, S. Chatterjee, L. Peedikakkandy, A. J. Pal, *Sol. RRL* **2020**, *4*, 2000505.
- [12] Z. Liu, K. Deng, J. Hu, L. Li, *Angew. Chemie* **2019**, *131*, 11621.
- [13] Y. Chen, J. Shi, X. Li, S. Li, X. Lv, X. Sun, Y.-Z. Zheng, X. Tao, *J. Mater. Chem. A* **2020**, *8*, 6349.
- [14] T. Leijtens, K. Bush, R. Cheacharoen, R. Beal, A. Bowring, M. D. McGehee, *J. Mater. Chem. A* **2017**, *5*, 11483.
- [15] Y. Han, S. Meyer, Y. Dkhissi, K. Weber, J. M. Pringle, U. Bach, L. Spiccia, Y. B. Cheng, *J. Mater. Chem. A* **2015**, *3*, 8139.
- [16] W. Chi, S. K. Banerjee, *Chem. Mater.* **2021**, *33*, 4269.
- [17] L. Shi, T. L. Young, J. Kim, Y. Sheng, L. Wang, Y. Chen, Z. Feng, M. J. Keever, X. Hao, P. J. Verlinden, M. A. Green, A. W. Y. Ho-Baillie, *ACS Appl. Mater. Interfaces* **2017**, *9*, 25073.
- [18] L. Shi, M. P. Bucknall, T. L. Young, M. Zhang, L. Hu, J. Bing, D. S. Lee, J. Kim, T. Wu, N. Takamura, D. R. McKenzie, S. Huang, M. A. Green, A. W. Y. Ho-Baillie, *Science* **2020**, *368*, eaba2412.
- [19] A. Mei, Y. Sheng, Y. Ming, Y. Hu, Y. Rong, W. Zhang, S. Luo, G. Na, C. Tian, X. Hou, Y. Xiong, Z. Zhang, S. Liu, S. Uchida, T. W. Kim, Y. Yuan, L. Zhang, Y. Zhou, H. Han, *Joule* **2020**, *4*, 2646.
- [20] M. Mohammadi, S. Gholipour, M. Malekshahi Byranvand, Y. Abdi, N. Taghavinia, M. Saliba, *ACS Appl. Mater. Interfaces* **2021**, *13*, 45455.
- [21] R. Cheacharoen, N. Rolston, D. Harwood, K. A. Bush, R. H. Dauskardt, M. D. McGehee, *Energy Environ. Sci.* **2018**, *11*, 144.
- [22] C. C. Boyd, R. Cheacharoen, T. Leijtens, M. D. McGehee, *Chem. Rev.* **2019**, *119*, 3418.
- [23] L. Chenglin, *E3S Web Conf.* **2021**, *242*, 01005.

- [24] B. Wilk, S. Öz, E. Radicchi, F. Ünlü, T. Ahmad, A. P. Herman, F. Nunzi, S. Mathur, R. Kudrawiec, K. Wojciechowski, *ACS Sustain. Chem. Eng.* **2021**, *9*, 3920.
- [25] G. Tang, F. Yan, *Nano Today* **2021**, *39*, 101155.
- [26] S. Cros, R. de Bettignies, S. Berson, S. Bailly, P. Maise, N. Lemaitre, S. Guillerez, *Sol. Energy Mater. Sol. Cells*, **2011**, *95*, S65.
- [27] I. A. Channa, A. Distler, M. Zaiser, C. J. Brabec, H. Egelhaaf, *Adv. Energy Mater.* **2019**, *9*, 1900598.
- [28] E. Planes, S. Juillard, M. Matheron, N. Charvin, S. Cros, D. Qian, F. Zhang, S. Berson, L. Flandin, *Adv. Mater. Interfaces* **2020**, *7*, 2000293.
- [29] I. A. Channa, A. Distler, C. J. Brabec, H.-J. Egelhaaf, *9 - Solution-Coated Barriers for Organic Electronics, Organic Flexible Electronics*, Woodhead Publishing Series in Electronic and Optical Materials, **2021**, pp. 249–303. ISBN 9780128188903.
- [30] N. Ali, N. Shehzad, S. Uddin, R. Ahmed, M. Jabeen, A. Kalam, A. G. Al-Sehemi, H. Alrobei, M. B. Kanoun, A. Khesro, S. Goumri-Said, *Int. J. Energy Res.* **2021**, *45*, 19729.
- [31] Z. Bagheri, F. Matteocci, E. Lamanna, D. Di Girolamo, A. G. Marrani, R. Zanoni, A. Di Carlo, A. Moshaii, *Sol. Energy Mater. Sol. Cells* **2020**, *215*, 110606.
- [32] N. Y. Nia, M. Méndez, B. Paci, A. Generosi, A. Di Carlo, E. Palomares, *ACS Appl. Energy Mater.* **2020**, *3*, 6853.
- [33] P. Ru, E. Bi, Y. Zhang, Y. Wang, W. Kong, Y. Sha, W. Tang, P. Zhang, Y. Wu, W. Chen, X. Yang, H. Chen, L. Han, *Adv. Energy Mater.* **2020**, *10*, 1903487.
- [34] M. Sendner, J. Trollmann, A. Pucci, *Org. Electron.* **2014**, *15*, 2959.
- [35] M. Petrović, T. Maksudov, A. Panagiotopoulos, E. Serpetzoglou, I. Konidakis, M. M. Stylianakis, E. Stratakis, E. Kymakis, *Nanoscale Adv.* **2019**, *1*, 3107.
- [36] K. C. Hsiao, M. H. Jao, B. T. Li, T. H. Lin, S. H. C. Liao, M. C. Wu, W. F. Su, *ACS Appl. Energy Mater.* **2019**, *2*, 4821.
- [37] H. S. Kim, J. Y. Seo, N. G. Park, *ChemSusChem* **2016**, *9*, 2528.
- [38] A. M. Ganose, C. N. Savory, D. O. Scanlon, *J. Phys. Chem. Lett.* **2015**, *6*, 4594.
- [39] M. I. Asghar, J. Zhang, H. Wang, P. D. Lund, *Renew. Sust. Energ. Rev.* **2017**, *77*, 131.
- [40] X. Kong, Y. Jiang, Z. Li, Y. Zhou, Z. Xu, C. Cong, X. Gao, X. Lu, G. Zhou, J. M. Liu, K. Kempa, J. Gao, *Sol. RRL* **2021**, *5*, 2000646.
- [41] T. Sen Su, F. T. Eickemeyer, M. A. Hope, F. Jahanbakhshi, M. Mladenović, J. Li, Z. Zhou, A. Mishra, J. H. Yum, D. Ren, A. Krishna, O. Ouellette, T. C. Wei, H. Zhou, H. H. Huang, M. D. Mensi, K. Sivula, S. M. Zakeeruddin, J. V. Milić, A. Hagfeldt, U. Rothlisberger, L. Emsley, H. Zhang, M. Grätzel, *J. Am. Chem. Soc.* **2020**, *142*, 19980.
- [42] R. Chen, Y. Wu, Y. Wang, R. Xu, R. He, Y. Fan, X. Huang, J. Yin, B. Wu, J. Li, N. Zheng, R. Chen, Y. Wu, Y. Wang, R. Xu, R. He, Y. Fan, X. Huang, J. Yin, B. Wu, J. Li, N. Zheng, *Adv. Funct. Mater.* **2021**, *31*, 2008760.
- [43] V. Babu, R. Fuentes Pineda, T. Ahmad, A. O. Alvarez, L. A. Castriotta, A. Di Carlo, F. Fabregat-Santiago, K. Wojciechowski, *ACS Appl. Energy Mater.* **2020**, *3*, 5126.
- [44] D. Bogachuk, S. Zouhair, K. Wojciechowski, B. Yang, V. Babu, L. Wagner, B. Xu, J. Lim, S. Mastroianni, H. Pettersson, A. Hagfeldt, A. Hinsch, *Energy Environ. Sci.* **2020**, *13*, 3880.
- [45] C. Zhou, S. Lin, *Sol. RRL* **2020**, *4*, 1900190.
- [46] R. K. Gunasekaran, D. Chinnadurai, A. R. Selvaraj, R. Rajendiran, K. Senthil, K. Prabakar, *ChemPhysChem* **2018**, *19*, 1507.
- [47] Z. Liu, B. Sun, T. Shi, Z. Tang, G. Liao, *J. Mater. Chem. A* **2016**, *4*, 10700.
- [48] R. Checharoen, C. C. Boyd, G. F. Burkhard, T. Leijtens, J. A. Raiford, K. A. Bush, S. F. Bent, M. D. McGehee, *Sustain. Energy Fuel* **2018**, *2*, 2398.
- [49] Y. Zhang, X. Zhuang, K. Zhou, C. Cai, Z. Hu, J. Zhang, Y. Zhu, *Org. Electron.* **2018**, *52*, 159.
- [50] L. Fagiolari, F. Bella, *Energy Environ. Sci.* **2019**, *12*, 3437.
- [51] J. Li, Q. Dong, N. Li, L. Wang, J. Li, Q. Dong, N. Li, L. Wang, *Adv. Energy Mater.* **2017**, *7*, 1602922.
- [52] S. Svanström, T. J. Jacobsson, G. Boschloo, E. M. J. Johansson, H. Rensmo, U. B. Cappel, *ACS Appl. Mater. Interfaces* **2020**, *12*, 7212.
- [53] Y. Kato, L. K. Ono, M. V. Lee, S. Wang, S. R. Raga, Y. Qi, *Adv. Mater. Interfaces* **2015**, *2*, 1500195.
- [54] R. Ichwani, R. Koech, O. K. Oyewole, A. Huda, D. O. Oyewole, J. Cromwell, J. L. Martin, R. L. Grimm, W. O. Soboyejo, *Extrem. Mech. Lett.* **2022**, *50*, 101515.
- [55] J. Xiao, *Technoeconomic Analysis of Perovskite Photovoltaic Manufacturing for Powering Telecommunications Towers*, S.B., Massachusetts Institute of Technology June 2018–2021–2029, <https://dspace.mit.edu/handle/1721.1/119698> (accessed: February 2022).
- [56] Barrier Layers for Flexible Electronics Market Report 2021–2029, <https://www.chemreportstore.com/report/barrier-layers-for-flexible-electronics-market-report-2021-2029> (accessed: February 2022).
- [57] P. O. Oviroh, R. Akbarzadeh, D. Pan, R. A. M. Coetzee, T. C. Jen, *Sci. Technol. Adv. Mater.* **2019**, *20*, 465.

I confirm that in the case of the following publications

S. Dasgupta, K. Misztal, R. Fuentes Pineda, W. Mróz, L. Pawlaczyk, J. Serafinczuk, A. J. Barker, T. Ahmad, A. P. Herman, S. Sahayaraj, R. Kudrawiec, A. Petrozza, A. Dudkowiak, K. Wojciechowski - **"New Synthetic Route of Ultrapure Alkylammonium Iodides for Perovskite Thin Films of Superior Optoelectronic Properties"** - *Energy Technology* 8(10), 2020, 2000478-1-2000478-12 - DOI: 10.1002/ente.202000478

My contribution was: Designing the experiment, preparing the perovskite ink, characterizing the perovskite solution, trying different perovskite engineering routes for the fabrication of films, characterization of the perovskite films, device fabrication and characterization and writing the manuscript.

M. Gąsiorowski, **S. Dasgupta**, L. Bychto, T. Ahmad, P. Szymak, K. Wojciechowski, A. Patryn - **"Analysis of Perovskite Solar Cell Degradation over Time using NIR Spectroscopy - a Novel Approach"** - *Energies* 15(15), 2022, 5397-1-5397-11- DOI: 10.3390/en15155397

My contribution was: Fabricating and characterizing the perovskite solar cell devices, aging the perovskite devices for stability tests, perovskite film characterization, and writing the device section for the manuscript. I also helped in the revision of the manuscript before the final submission.

G. Soto-Perez, **S. Dasgupta**, W. Żuraw, R. Fuentes Pineda, K. Wojciechowski, L. K. Jagadamma, I. Samuel, N. Robertson - **"Solution-processable perylene diimide-based electron transport materials as non-fullerene alternatives for inverted perovskite solar cells"** - *Journal of Materials Chemistry A*, 10, 2022, 11046-11053 - DOI: 10.1039/d2ta01321e

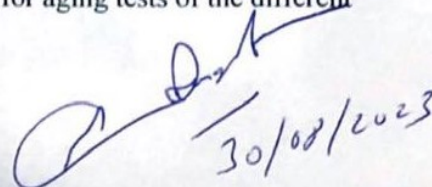
My contribution was: The fabrication of perovskite devices, guiding my master student, Wiktor Żuraw in the fabrication routes for this experiment who also contributed to the fabrication of devices. I also characterized the perovskite films and devices. I also wrote the device experimental section of the manuscript and helped with the revision of the manuscript before submission.

S. Dasgupta, W. Żuraw, T. Ahmad, L. A. Castriotta, E. Radicchi, W. Mróz, M. Ścigaj, L. Pawlaczyk, M. Tamulewicz-Szwajkowska, M. Trzciński, J. Serafinczuk, E. Mosconi, A. Di Carlo, F. De Angelis, A. Dudkowiak, K. Wojciechowski - **"Modification of a buried interface with bulky organic cations for highly stable flexible perovskite solar cells"** - *ACS Applied Energy Materials* 5(12), 2022, 15114-15124 - DOI: 10.1021/acsam.2c02780

My contribution was: Designing the experiment, Fabricating, and characterizing the perovskite solar cell films and devices, aging the perovskite devices for stability tests, perovskite film characterizations, and writing the manuscript.

T. Ahmad †, **S. Dasgupta** †, S. Almosni, A. Dudkowiak, K. Wojciechowski - **"Encapsulation protocol for flexible perovskite solar cells enabling stability in accelerated aging tests"** - *Energy and Environmental Materials* 6(5), 2023, 12434-1-12434-8 - DOI: 10.1002/eem2.12434
(† Authors contributed equally)

My contribution was: Co-designing the experiment and fabrication of solar cell devices and their characterization and testing different lamination routes and materials for aging tests of the different perovskite films. I was also involved in co-writing the manuscript.



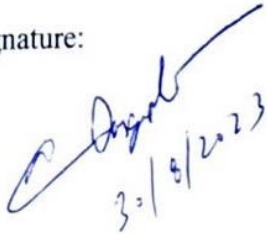
30/08/2023

I consent to the honest and truthful declaration of the above-mentioned work by me as part of the dissertation of doctoral studies in the form of a collection of published and thematically related scientific articles.

Name: Shyantana Dasgupta

Orcid ID: 0000-0003-0903-3709

Signature:



30/8/2023

I certify this publication

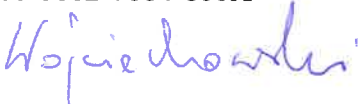
S. Dasgupta, T. Ahmad, Samy Almosni, Alina Dudkowiak, Konrad Wojciechowski
“Encapsulation protocol for flexible perovskite solar cells enabling stability in accelerated aging tests” DOI: 10.1002/eem2.12434

My contribution was: conceptualization, methodology, paper writing, paper revision, supervision, funding acquisition, project management

I consent to the submission of the above-mentioned work by Ph.D. student Shyantana Dasgupta as part of the dissertation of doctoral studies in the form of a collection of published and thematically related scientific articles.

Name: Konrad Wojciechowski

Orcid ID: 0000-0002-7664-801X

Signature: 

I certify this publication

German Soto-Perez, **S. Dasgupta**, Wiktor Zuraw, Rosinda Fuentes-Pineda, Konrad Wojciechowski, Lethy Krishnan Jagadamma, Ifor Samuel and Neil Robertson* "Solution-processable perylene diimide-based electron transport materials as non-fullerene alternatives for inverted perovskite solar cells. *Journal of Materials Chemistry A*, 2022, 10, 11046-11053 - DOI: 10.1039/D2TA01321E

My contribution was: methodology, conceptualization, resources, paper revision, supervision

I consent to the submission of the above-mentioned work by Ph.D. student Shyantana Dasgupta as part of the dissertation of doctoral studies in the form of a collection of published and thematically related scientific articles.

Name: Konrad Wojciechowski

Orcid ID: 0000-0002-7664-801X

Signature: 

I certify this publication

Marek Gąsiorowski , **S.Dasgupta**, Leszek Bychto , Taimoor Ahmad , Piotr Szymak , Aleksy Patryn, Konrad Wojciechowski- '*Analysis of Perovskite Solar Cell Degradation over Time Using NIR Spectroscopy—A Novel Approach*'. DOI: 10.3390/en15155397

My contribution was: methodology, conceptualization, paper revision, supervision

I consent to the submission of the above-mentioned work by Ph.D. student Shyantana Dasgupta as part of the dissertation of doctoral studies in the form of a collection of published and thematically related scientific articles.

Name: Konrad Wojciechowski

Orcid ID: 0000-0002-7664-801X

Signature: 

I certify this publication

Shyantana Dasgupta, Kasjan Misztal, Rosinda Fuentes Pineda, Wojciech Mróz, Łukasz Pawlaczyk, Jarosław Serafińczuk, Alex J. Barker, Taimoor Ahmad, Artur P. Herman, Sylvester Sahayaraj, Robert Kudrawiec, Annamaria Petrozza, Alina Dudkowiak, and Konrad Wojciechowski: *New Synthetic Route of Ultrapure Alkylammonium Iodides for Perovskite Thin Films of Superior Optoelectronic Properties*

DOI: 10.1002/ente.202000478

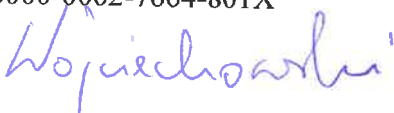
My contribution was: conceptualization, methodology, paper writing, paper revision, supervision, funding acquisition, project management

I consent to the submission of the above-mentioned work by Ph.D. student Shyantana Dasgupta as part of the dissertation of doctoral studies in the form of a collection of published and thematically related scientific articles.

Name: Konrad Wojciechowski

Orcid ID: 0000-0002-7664-801X

Signature:



I certify this publication

Dasgupta, S; Zuraw, Wiktor; Ahmad, Taimoor; Castriotta, Luigi Angelo; Radicchi, Eros; Mroz, Wojciech; Ścigaj, Mateusz; Pawlaczyk, Łukasz; Tamulewicz-Szwajkowska, Magdalena; Trzcíński, Marek; Serafińczuk, Jarosław; Mosconi, Edoardo; Di Carlo, Aldo; De Angelis, Filippo; Dudkowiak, Alina; Wojciechowski, Konrad- 'Modification of a buried interface with bulky organic cations for highly stable flexible perovskite solar cells'-DOI: 10.1021/acsaem.2c02780

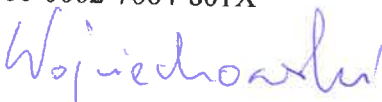
My contribution was: conceptualization, methodology, paper writing, paper revision, supervision, funding acquisition, project management

I consent to the submission of the above-mentioned work by Ph.D. student Shyantana Dasgupta as part of the dissertation of doctoral studies in the form of a collection of published and thematically related scientific articles.

Name: Konrad Wojciechowski

Orcid ID: 0000-0002-7664-801X

Signature:



I confirm that in case of the following publications:

1. **S. Dasgupta**, K. Misztal, R. Fuentes Pineda, W. Mróz, Ł. Pawlaczyk, J. Serafińczuk, A. J. Barker, T. Ahmad, A. P. Herman, S. Sahayaraj, R. Kudrawiec, A. Petrozza, A. Dudkowiak and K. Wojciechowski
'New Synthetic Route of Ultrapure Alkylammonium Iodides for Perovskite Thin Films of Superior Optoelectronic Properties'
Energy Technology 2020, 8(10), 2000478-1-2000478-12 (DOI:10.1002/ente.202000478)
2. **S. Dasgupta**, W. Żuraw, T. Ahmad, L. A. Castriotta, E. Radicchi, W. Mróz, M. Ścigaj, Ł. Pawlaczyk, M. Tamulewicz-Szwajkowska, M. Trzeciński, J. Serafińczuk, E. Mosconi, A. Di Carlo, F. De Angelis, A. Dudkowiak and K. Wojciechowski
'Modification of a Buried Interface with Bulky Organic Cations for Highly Stable Flexible Perovskite Solar Cells'
ACS Applied Energy Materials 2022, 5(12), 15114-15124
(DOI:10.1021/acsaem.2c02780)
3. T. Ahmad, **S. Dasgupta**, S. Almosni, A. Dudkowiak and K. Wojciechowski
'Encapsulation protocol for flexible perovskite solar cells enabling stability in accelerated aging tests'
Energy and Environmental Materials 2023, 6(5), 12434-1-12434-8
(DOI:10.1002/eem2.12434)

my contribution was co-supervision and co-revision of the manuscripts.

I consent to the submission of the above-mentioned works by Ph.D. student Shyantana Dasgupta as part of his doctoral dissertation prepared in the form of a collection of published and thematically related scientific articles.

Orcid ID: 0000-0001-5487-4051

Alina Dudkowiak



Poznan, August 28, 2023

Date: 30-Aug-2023

I confirm that in the case of the following publications

Shyantam Dasgupta, Kasjan Misztal, Rosinda Fuentes Pineda, Wojciech Mróz, Łukasz Pawlaczyk, Jarosław Serafińczuk, Alex J. Barker, Taimoor Ahmad, Artur P. Herman, Sylvester Sahayaraj, Robert Kudrawiec, Annamaria Petrozza, Alina Dudkowiak, and Konrad Wojciechowski: *New Synthetic Route of Ultrapure Alkylammonium Iodides for Perovskite Thin Films of Superior Optoelectronic Properties: Energy Technology* 8(10), 2020 - DOI: 10.1002/ente.202000478

My contribution was: Laser calibration and excitation for the Tyndall effect experiment and article revision.

Marek Gąsiorowski, **S. Dasgupta**, Leszek Bychto, Taimoor Ahmad, Piotr Szymak, Aleksy Patryn, Konrad Wojciechowski- *Analysis of Perovskite Solar Cell Degradation over Time Using NIR Spectroscopy—A Novel Approach*. DOI: 10.3390/en15155397

My contribution was: The preparation of aging setups and assisting in the fabrication of devices along with the measurement of devices and article revision.

Dasgupta, S; Zuraw, Wiktor; Ahmad, Taimoor; Castriotta, Luigi Angelo; Radicchi, Eros; Mroz, Wojciech; Ścigaj, Mateusz; Pawlaczyk, Łukasz; Tamulewicz-Szwajkowska, Magdalena; Trzeciński, Marek; Serafińczuk, Jarosław; Mosconi, Edoardo; Di Carlo, Aldo; De Angelis, Filippo; Dudkowiak, Alina; Wojciechowski, Konrad- *Modification of a buried interface with bulky organic cations for highly stable flexible perovskite solar cells*'-DOI: 10.1021/acsaem.2c02780

My contribution was: Setting the aging setup for device MPPT tracking and stability tests, preparation of solutions for transport layers in the perovskite solar cell stack and assisting in the characterization of different layers. Also helped advise the first author in the designing of the experiment and revising the article.

S. Dasgupta, T. Ahmad, Samy Almosni, Alina Dudkowiak, Konrad Wojciechowski *'Encapsulation protocol for flexible perovskite solar cells enabling stability in accelerated aging tests'* DOI: 10.1002/eem2.12434

My contribution was: Preparing solutions for different transport layers for device fabrication, partial device fabrication, setting up aging protocols for device aging tests, encapsulation of devices with different materials, calibration of the U.V chamber for adhesive crosslinking and co-writing the manuscript.

TA

I consent to the submission of the above-mentioned work by Ph.D. student Shyantana Dasgupta as part of the dissertation of doctoral studies in the form of a collection of published and thematically related scientific articles.

Name: *Taimoor Ahmad*

Orcid ID: *0000-0001-9922-9603*

Signature: *Taimoor*

I certify that in this publication:

Shyantana Dasgupta, Kasjan Misztal, Rosinda Fuentes Pineda, Wojciech Mróz, Łukasz Pawlaczyk, Jarosław Serafińczuk, Alex J. Barker, Taimoor Ahmad, Artur P. Herman, Sylvester Sahayaraj, Robert Kudrawiec, Annamaria Petrozza, Alina Dudkowiak, Konrad Wojciechowski

"New Synthetic Route of Ultrapure Alkylammonium Iodides for Perovskite Thin Films of Superior Optoelectronic Properties"

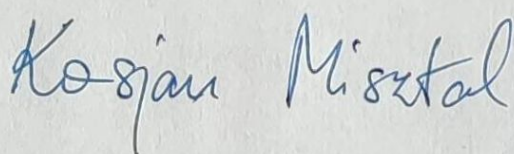
Energy Technol. 8 (2020) 202000478. DO: 10.1002/ente.202000478

My contribution was the development of new synthetic protocol towards synthesis of ultrapure alkylammonium iodides, including literature research, synthetic trials, development of purification method, analysis of obtained materials and interpretation of the results. I was also responsible for synthesis of different batches of material samples of alkylammonium iodides used in the study. I also wrote a paragraph regarding the synthesis of those materials and their characterization, and I participated in manuscript's revision.

I consent to the submission of the above-mentioned work by Ph.D. student Shyantana Dasgupta as part of the dissertation of doctoral studies in the form of a collection of published and thematically related scientific articles.

Kasjan Misztal

Orcid ID: 0000-0002-7240-4157



I certify this publication.

Shyantana Dasgupta, Kasjan Misztal, Rosinda Fuentes Pineda, Wojciech Mróz, Łukasz Pawlaczyk, Jarosław Serafińczuk, Alex J. Barker, Taimoor Ahmad, Artur P. Herman, Sylvester Sahayaraj, Robert Kudrawiec, Annamaria Petrozza, Alina Dudkowiak, and Konrad Wojciechowski: *New Synthetic Route of Ultrapure Alkylammonium Iodides for Perovskite Thin Films of Superior Optoelectronic Properties*

DOI: 10.1002/ente.202000478

My contribution was: First assessment and study of the materials, editing of draft manuscript. I consent to the submission of the above-mentioned work by Ph.D. student Shyantana Dasgupta as part of the dissertation of doctoral studies in the form of a collection of published and thematically related scientific articles.

Orcid ID:

Signature:

Rosinda Fuentes Pineda



I certify that in this publication:

Shyantana Dasgupta, Kasjan Misztal, Rosinda Fuentes Pineda, Wojciech Mróz, Łukasz Pawlaczyk, Jarosław Serafińczuk, Alex J. Barker, Taimoor Ahmad, Artur P. Herman, Sylvester Sahayaraj, Robert Kudrawiec, Annamaria Petrozza, Alina Dudkowiak, Konrad Wojciechowski

“New Synthetic Route of Ultrapure Alkylammonium Iodides for Perovskite Thin Films of Superior Optoelectronic Properties”

Energy Technol. 8 (2020) 2000478. DOI: 10.1002/ente.202000478

my contribution was a measurement of the perovskite solar cells' electroluminescence, interpretation of the results and writing a paragraph describing them. I participated also in the manuscript's revisions.

I consent to the submission of the above-mentioned work by Ph.D. student Shyantana Dasgupta as part of the dissertation of doctoral studies in the form of a collection of published and thematically related scientific articles.

Wojciech Mróz

Orcid ID: 0000-0002-4534-6238

Wojciech Mróz

I certify that in this publication:

Shyantana Dasgupta, Kasjan Misztal, Rosinda Fuentes Pineda, Wojciech Mroz, Łukasz Pawlaczyk, Jarostaw Serafinczuk, Alex J. Barker, Taimoor Ahmad, Artur P. Herman, Sylvester Sahayaraj, Robert Kudrawiec, Annamaria Petrozza, Alina Dudkowiak, Konrad Wojciechowski

"New Synthetic Route of Ultrapure Alkylammonium Iodides for Perovskite Thin Films of Superior Optoelectronic Properties"

Energy Technol. 8 (2020) 2000478. DOI: 10.1002/ente.202000478

My contribution was a measurement of microstrain values. These values were derived from the analysis of reflection peaks at X-ray diffractograms of perovskite polycrystalline layers. I also determine the size of crystallites in the structure. I was also responsible for interpretation of the results and writing a paragraph describing them.

I consent to the submission of the above-mentioned work by Ph.D. student Shyantana Dasgupta as part of the dissertation of doctoral studies in the form of a collection of published and thematically related scientific articles.

Łukasz Pawlaczyk

Orcid ID: 0000-0003-1592-855X

Łukasz
Pawlaczyk

I certify that in this publication:

Shyantana Dasgupta, Kasjan Misztal, Rosinda Fuentes Pineda, Wojciech Mroz, Łukasz Pawlaczyk, Jarostaw Serafińczuk, Alex J. Barker, Taimoor Ahmad, Artur P. Herman, Sylvester Sahayaraj, Robert Kudrawiec, Annamaria Petrozza, Alina Dudkowiak, Konrad Wojciechowski

“New Synthetic Route of Ultrapure Alkylammonium Iodides for Perovskite Thin Films of Superior Optoelectronic Properties”

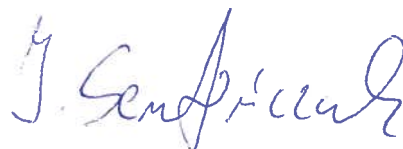
Energy Technol. 8 (2020) 2000478. DOI: 10.1002/ente.202000478

My contribution was XRD measurement and obtained results analysis. I was also responsible for interpretation of the results and writing a paragraph describing them.

I consent to the submission of the above-mentioned work by Ph.D. student Shyantana Dasgupta as part of the dissertation of doctoral studies in the form of a collection of published and thematically related scientific articles.

Jarostaw Serafińczuk, PhD. DSc., Prof. of WrUST

Orcid ID: 0000-0001-9809-4233

A handwritten signature in blue ink, appearing to read 'J. Serafińczuk', is positioned in the lower right area of the page.

I certify that in this publication:

Shyantana Dasgupta, Kasjan Misztal, Rosinda Fuentes Pineda, Wojciech Mróz, Łukasz Pawlaczyk, Jarosław Serafińczuk, Alex J Barker, Taimoor Ahmad, Artur P Herman, Sylvester Sahayaraj, Robert Kudrawiec, Annamaria Petrozza, Alina Dudkowiak, Konrad Wojciechowski : New Synthetic Route of Ultrapure Alkylammonium Iodides for Perovskite Thin Films of Superior Optoelectronic Properties, Energy Technology 8 (10), 2000478

<https://doi.org/10.1002/ente.202000478>

My contribution was: (4-5 lines)

I measured and analyzed photoluminescence quantum yield (PLQY).

I consent to the submission of the above-mentioned work by Ph.D. student Shyantana Dasgupta as part of the dissertation of doctoral studies in the form of a collection of published and thematically related scientific articles.

Alex J. Barker

Orcid ID:

0000-0002-5614-4113



Alex Barker

Milano 23-6-22

I certify this publication

Shyantana Dasgupta, Kasjan Misztal, Rosinda Fuentes Pineda, Wojciech Mróz, Łukasz Pawlaczyk, Jarosław Serafińczuk, Alex J. Barker, Taimoor Ahmad, Artur P. Herman, Sylvester Sahayaraj, Robert Kudrawiec, Annamaria Petrozza, Alina Dudkowiak, and Konrad Wojciechowski: *New Synthetic Route of Ultrapure Alkylammonium Iodides for Perovskite Thin Films of Superior Optoelectronic Properties*

DOI: 10.1002/ente.202000478

My contribution was: measurements and interpretation of time resolved-microwave photoconductivity transients

I consent to the submission of the above-mentioned work by Ph.D. student Shyantana Dasgupta as part of the dissertation of doctoral studies in the form of a collection of published and thematically related scientific articles.

Name: Artur Herman

Orcid ID: 0000-0002-1393-0317

Signature:



Date: 2023-09-14

I certify this publication

Shyantana Dasgupta, Kasjan Misztal, Rosinda Fuentes Pineda, Wojciech Mróz, Łukasz Pawlaczyk, Jarosław Serafińczuk, Alex J. Barker, Taimoor Ahmad, Artur P. Herman, Sylvester Sahayaraj, Robert Kudrawiec, Annamaria Petrozza, Alina Dudkowiak, and Konrad Wojciechowski: *New Synthetic Route of Ultrapure Alkylammonium Iodides for Perovskite Thin Films of Superior Optoelectronic Properties*

DOI: 10.1002/ente.202000478

My contribution was: measurement of the steady state and time resolved photoluminescence properties of the perovskite absorbers prepared with different MAI. I also helped initially with the preparation of the manuscript.

I consent to the submission of the above-mentioned work by Ph.D. student Shyantana Dasgupta as part of the dissertation of doctoral studies in the form of a collection of published and thematically related scientific articles.

Name: Sylvester Sahayaraj Masilamani Leo

Orcid ID:

Signature: *M. Sylvester*

I certify this publication

Shyantana Dasgupta, Kasjan Misztal, Rosinda Fuentes Pineda, Wojciech Mróz, Łukasz Pawlaczyk, Jarosław Serafińczuk, Alex J. Barker, Taimoor Ahmad, Artur P. Herman, Sylvester Sahayaraj, Robert Kudrawiec, Annamaria Petrozza, Alina Dudkowiak, and Konrad Wojciechowski: *New Synthetic Route of Ultrapure Alkylammonium Iodides for Perovskite Thin Films of Superior Optoelectronic Properties*

DOI: 10.1002/ente.202000478

My contribution was: measurements and analysis of time resolved microwave photoconductivity spectra.

I consent to the submission of the above-mentioned work by Ph.D. student Shyantana Dasgupta as part of the dissertation of doctoral studies in the form of a collection of published and thematically related scientific articles.

Name: Robert Kudrawiec

Orcid ID: 0000-0003-2593-9172

Signature:

R. Kudrawiec

I certify this publication

Shyantana Dasgupta, Kasjan Misztal, Rosinda Fuentes Pineda, Wojciech Mróz,
Łukasz Pawlaczyk, Jarosław Serafińczuk, Alex J. Barker, Taimoor Ahmad,
Artur P. Herman, Sylvester Sahayaraj, Robert Kudrawiec, Annamaria Petrozza,
Alina Dudkowiak, and Konrad Wojciechowski: *New Synthetic Route of Ultrapure
Alkylammonium Iodides for Perovskite Thin Films of Superior Optoelectronic Properties*

DOI: 10.1002/ente.202000478

My contribution was: SUPERVISION OF ELECTROCHROMISCEANCE STUDY

I consent to the submission of the above-mentioned work by Ph.D. student Shyantana Dasgupta as part of the dissertation of doctoral studies in the form of a collection of published and thematically related scientific articles.

Orcid ID:

Signature:



I certify this publication

Marek Gąsiorowski , **S.Dasgupta**, Leszek Bychto , Taimoor Ahmad , Piotr Szymak , Aleksy Patryn, Konrad Wojciechowski- '*Analysis of Perovskite Solar Cell Degradation over Time Using NIR Spectroscopy—A Novel Approach*'

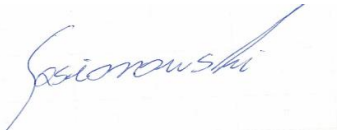
DOI: 10.3390/en15155397

My contribution was: Measurement, Method of Measurement, writing-orginal draft;

I consent to the submission of the above-mentioned work by Ph.D. student Shyantana Dasgupta as part of the dissertation of doctoral studies in the form of a collection of published and thematically related scientific articles.

Orcid ID: 0000-0001-8317-3692

Signature:

A handwritten signature in blue ink, appearing to read 'Gąsiorowski', is written over a light blue rectangular background.

I certify this publication

Marek Gąsiorowski , **S.Dasgupta**, Leszek Bychto , Taimoor Ahmad , Piotr Szymak , Aleksy Patryn, Konrad Wojciechowski- '*Analysis of Perovskite Solar Cell Degradation over Time Using NIR Spectroscopy—A Novel Approach*'.

DOI: 10.3390/en15155397

My contribution was: methodology and investigations of perovskite solar cells by NIR spectroscopy, validation of results and original draft writing.

I consent to the submission of the above-mentioned work by Ph.D. student Shyantana Dasgupta as part of the dissertation of doctoral studies in the form of a collection of published and thematically related scientific articles.

Orcid ID: 0000-0002-9516-3077

Signature:

Bychto Leszek

I certify this publication

Marek Gąsiorowski , **S.Dasgupta**, Leszek Bychto , Taimoor Ahmad , Piotr Szymak , Aleksy Patryn, Konrad Wojciechowski- '*Analysis of Perovskite Solar Cell Degradation over Time Using NIR Spectroscopy—A Novel Approach*'

DOI: 10.3390/en15155397

My contribution was:

data curation: co-author, formal analysis, methodology: co-author; validation: co-author;
writing—review & editing: co-author.

I consent to the submission of the above-mentioned work by Ph.D. student Shyantana Dasgupta as part of the dissertation of doctoral studies in the form of a collection of published and thematically related scientific articles.

Orcid ID: 0000-0002-4714-6192

Signature: 

I certify this publication

Marek Gašiorowski ,**S.Dasgupta**, Leszek Bychto , Taimoor Ahmad , Piotr Szymak , Aleksy Patryn, Konrad Wojciechowski- '*Analysis of Perovskite Solar Cell Degradation over Time Using NIR Spectroscopy—A Novel Approach*'.

DOI: 10.3390/en15155397

My contribution was: Conceptualisation, methodology: supervision, validation, writing—original draft, writing—review & editing.

I consent to the submission of the above-mentioned work by Ph.D. student Shyantana Dasgupta as part of the dissertation of doctoral studies in the form of a collection of published and thematically related scientific articles.

Orcid ID: 0000-0002-5507-6833

Signature:



Professor Aleksy Patryn DSc PhD
Dept. of Electronics and Computer Science
Koszalin University of Technology

2 Śniadeckich St., 75-453 Koszalin, Poland
phone: +48 94 347-87-25
fax: +48 94 343-34-79
mobile: +48 606 404 536
e-mail: aleksy.patryn@tu.koszalin.pl
aleksy.patryn@gmail.com

www.weii.tu.koszalin.pl

I certify that in this publication:

German Soto Perez, Shyantana Dasgupta, Wiktor Żuraw, Rosinda Fuentes Pineda, Konrad Wojciechowski, Lethy Krishnan Jagadamma, Ifor Samuel, Neil Robertson, Solution-processable perylene diimide-based electron transport materials as non-fullerene alternatives for inverted perovskite solar cells, *J. Mater. Chem. A*, 2022, **10**, 11046-11053; DOI: 10.1039/D2TA01321E

My contribution was: The synthesis and structural, chemical, and optoelectronic characterization of the perylene derivatives reported in this work, so as the writing of the manuscript and final version of the paper.

I consent to the submission of the above-mentioned work by Ph.D. student Shyantana Dasgupta as part of the dissertation of doctoral studies in the form of a collection of published and thematically related scientific articles.

Orcid ID: <https://orcid.org/0000-0001-6419-173X>



German Soto Perez

Wrocław, 25.08.2023

Name: Wiktor Żuraw
Orcid ID: 0000-0001-6656-0412

I certify this publication:

German Soto-Perez, **S. Dasgupta**, Wiktor Żuraw, Rosinda Fuentes-Pineda, Konrad Wojciechowski, Lethy Krishnan Jagadamma, Ifor Samuel and Neil Robertson, Solution-processable perylene diimide-based electron transport materials as non-fullerene alternatives for inverted perovskite solar cells, *Journal of Materials Chemistry A*, 2022, **10**, 11046-11053;
DOI: 10.1039/D2TA01321E

My contribution was:

- preparation of perovskite precursor solution
- fabrication of devices

I consent to the submission of the above-mentioned work by Ph.D. student Shyantana Dasgupta as part of the dissertation of doctoral studies in the form of a collection of published and thematically related scientific articles.



I, Dr Rosinda Fuentes-Pineda, hereby authorize Shyantana Dasgupta to include the publications listed below in his doctoral thesis.

German Soto Perez, Shyantana Dasgupta, Wiktor Żuraw, Rosinda Fuentes Pineda, Konrad Wojciechowski, Lethy Krishnan Jagadamma, Ifor Samuel, Neil Robertson, Solution-processable perylene diimide-based electron transport materials as non-fullerene alternatives for inverted perovskite solar cells, *J. Mater. Chem. A*, 2022, **10**, 11046-11053; DOI: 10.1039/D2TA01321E

My contribution was: joint conceptualization of the work for the solar cell's fabrication, aging test, supervision, and guidance of the 2nd author, editing and feedback on drafts of the manuscript.

I consent to the submission of the above-mentioned work by Ph.D. student Shyantana Dasgupta as part of the dissertation of doctoral studies in the form of a collection of published and thematically related scientific articles.

Orcid ID: <https://orcid.org/0000-0002-9230-6124>



Rosinda Fuentes Pineda

I certify that in this publication:

German Soto Perez, Shyantana Dasgupta, Wiktor Żuraw, Rosinda Fuentes Pineda, Konrad Wojciechowski, Lethy Krishnan Jagadamma, Ifor Samuel, Neil Robertson, Solution-processable perylene diimide-based electron transport materials as non-fullerene alternatives for inverted perovskite solar cells, *J. Mater. Chem. A*, 2022, 10, 11046-11053; DOI: 10.1039/D2TA01321E

My contribution was: the mobility measurement of the electron transport layers using the space charge limited current (SCLC) method. I fabricated the corresponding electron-only devices, measured the current-voltage characteristics, and analysed the experimental data to obtain electron mobility. I also contributed by giving feedback to the final draft of the manuscript.

I consent to the submission of the above-mentioned work by PhD student Shyantana Dasgupta as part of the dissertation of doctoral studies in the form of a collection of published and thematically related scientific articles.

ORCID: <https://orcid.org/0000-0002-4339-2484>



Email:lkj2@st-andrews.ac.uk

Dr Lethy Krishnan Jagadamma

I certify that in this publication

German Soto-Perez, **S. Dasgupta**, Wiktor Zuraw, Rosinda Fuentes-Pineda, Konrad Wojciechowski, Lethy Krishnan Jagadamma, Ifor Samuel and Neil Robertson* "Solution-processable perylene diimide-based electron transport materials as non-fullerene alternatives for inverted perovskite solar cells'. *Journal of Materials Chemistry A*, 2022, 10, 11046-11053 - DOI: 10.1039/D2TA01321E

My contribution was: to supervise the SCLC measurements of electron mobility, discuss the results with Dr Krishnan Jagadamma, and review the draft manuscript.

I consent to the submission of the above-mentioned work by Ph. D student Shyantana Dasgupta as part of the dissertation of doctoral studies in the form of a collection of published and thematically related scientific articles.

Orcid id: 0000-0001-7821-7208

Date: 27/10/2023



Prof. Dr. Ifor Samuel

I certify that in this publication:

German Soto Perez, Shyantana Dasgupta, Wiktor Żuraw, Rosinda Fuentes Pineda, Konrad Wojciechowski, Lethy Krishnan Jagadamma, Ifor Samuel, Neil Robertson, Solution-processable perylene diimide-based electron transport materials as non-fullerene alternatives for inverted perovskite solar cells, *J. Mater. Chem. A*, 2022, **10**, 11046-11053; DOI: 10.1039/D2TA01321E

My contribution was: joint conceptualisation of the work, supervision and guidance of the 1st author, editing and feedback on drafts of the manuscript, responsibility for final submitted version and oversight of revision.

I consent to the submission of the above-mentioned work by Ph.D. student Shyantana Dasgupta as part of the dissertation of doctoral studies in the form of a collection of published and thematically related scientific articles.

Orcid ID: <https://orcid.org/0000-0002-9230-6124>



Professor Neil Robertson

Wrocław, 21.12.2022

Name: Wiktor Żuraw

Orcid ID: 0000-0001-6656-0412

I certify this publication:

Shyantana Dasgupta, Wiktor Żuraw, Taimoor Ahmad, Luigi Angelo Castriotta, Eros Radicchi, Wojciech Mróz, Mateusz Scigaj, Łukasz Pawlaczyk, Magdalena Tamulewicz-Szwajkowski, Marek Trzcinski, Jarosław Serafińcu, Edoardo Mosconi, Aldo Di Carlo, Filippo De Angelis, Alina Dudkowiak, Konrad Wojciechowski, *Modification of a buried interface with bulky organic cations for highly stable flexible perovskite solar cells*, DOI: 10.1021/acsaem.2c02780

My contribution was:

- preparation of perovskite precursors solution
- fabrication of devices and layers for all measurements
- correction of the manuscript

I consent to the submission of the above-mentioned work by Ph.D. student Shyantana Dasgupta as part of the dissertation of doctoral studies in the form of a collection of published and thematically related scientific articles.



I certify this publication

Dasgupta, S; Zuraw, Wiktor; Ahmad, Taimoor; Castriotta, Luigi Angelo; Radicchi, Eros; Mroz, Wojciech; Ścigaj, Mateusz; Pawlaczyk, Łukasz; Tamulewicz-Szwajkowska, Magdalena; Trzcíński, Marek; Serafińczuk, Jarosław; Mosconi, Edoardo; Di Carlo, Aldo; De Angelis, Filippo; Dudkowiak, Alina; Wojciechowski, Konrad- 'Modification of a buried interface with bulky organic cations for highly stable flexible perovskite solar cells'-DOI:

10.1021/acsaem.2c02780

My contribution was:

I consent to the submission of the above-mentioned work by Ph.D. student Shyantana Dasgupta as part of the dissertation of doctoral studies in the form of a collection of published and thematically related scientific articles.

Name: Luigi Angelo Castriotta

Orcid ID: 0000-0003-2525-8852

Signature:



28/08/2023

I certify this publication:

Shyantana Dasgupta, Wiktor Żuraw, Taimoor Ahmad, Luigi Angelo Castriotta, Eros Radicchi, Wojciech Mróz, Mateusz Scigaj, Łukasz Pawlaczyk, Magdalena Tamulewicz-Szwajkowska, Marek Trzciniński, Jarosław Serafińczuk, Edoardo Mosconi, Aldo Di Carlo, Filippo De Angelis, Alina Dudkowiak, Konrad Wojciechowski: *Modification of a buried interface with bulky organic cations for highly stable flexible perovskite solar cells*: DOI: 10.1021/acsaem.2c02780

My contribution was: (4-5 lines)

I performed computational modeling of different terminated formamidinium lead iodide perovskite surfaces by means of Density Functional Theory simulations. I then evaluated both the thermodynamics of the adsorption process of organic cations on top of such systems and their density of states, to estimate the alignment between the (un)passivated perovskite surface and the hole transporting material employed in the experiments.

I consent to the submission of the above-mentioned work by Ph.D. student Shyantana Dasgupta as part of the dissertation of doctoral studies in the form of a collection of published and thematically related scientific articles.

Eros Radicchi, Orcid ID: 0000-0003-0749-3824



I certify this publication:

Shyantana Dasgupta, Wiktor Żuraw, Taimoor Ahmad, Luigi Angelo Castriotta, Eros Radicchi, Wojciech Mróz, Mateusz Scigaj, Łukasz Pawlaczyk, Magdalena Tamulewicz-Szwajkowski, Marek Trzcinski, Jarosław Serafińczuk, Edoardo Mosconi, Aldo Di Carlo, Filippo De Angelis, Alina Dudkowiak, Konrad Wojciechowski: *Modification of a buried interface with bulky organic cations for highly stable flexible perovskite solar cells*: DOI: 10.1021/acsaem.2c02780

My contribution was the measurement of electroluminescence (EL) spectra and electrical characterization of the solar cells. Based on the results, the EL external quantum efficiencies of the devices were calculated and from them the open circuit voltage radiative limit for each type of the cell was determined. Finally, the ideality factors were calculated using two methods for all the devices.

I consent to the submission of the above-mentioned work by Ph.D. student Shyantana Dasgupta as part of the dissertation of doctoral studies in the form of a collection of published and thematically related scientific articles.

Orcid ID: 0000-0002-4534-6238

20th December 2022

Wojciech Mróz



I certify this publication:

Shyantana Dasgupta, Wiktor Żuraw^c, Taimoor Ahmad, Luigi Angelo Castriotta, Eros Radicchi, Wojciech Mróz, Mateusz Ścigaj, Łukasz Pawlaczyk, Magdalena Tamulewicz-Szwajkowski^d, Marek Trzcinski, Jarosław Serafińcu¹, Edoardo Mosconi, Aldo Di Carlo, Filippo De Angelis, Alina Dudkowiak, Konrad Wojciechowski: *Modification of a buried interface with bulky organic cations for highly stable flexible perovskite solar cells*: DOI: 10.1021/acsaem.2c02780

My contribution was: (4-5 lines)

Performing the iodine test. General discussions.

I consent to the submission of the above-mentioned work by Ph.D. student Shyantana Dasgupta as part of the dissertation of doctoral studies in the form of a collection of published and thematically related scientific articles.

Orcid ID: 0000-0002-8703-948X

Name: Mateusz Ścigaj



28.08.2023

I certify this publication

Dasgupta, S; Zuraw, Wiktor; Ahmad, Taimoor; Castriotta, Luigi Angelo; Radicchi, Eros; Mroz, Wojciech; Ścigaj, Mateusz; Pawlaczyk, Łukasz; Tamulewicz-Szwajkowska, Magdalena; Trzciński, Marek; Serafińczuk, Jarosław; Mosconi, Edoardo; Di Carlo, Aldo; De Angelis, Filippo; Dudkowiak, Alina; Wojciechowski, Konrad- 'Modification of a buried interface with bulky organic cations for highly stable flexible perovskite solar cells'-DOI: 10.1021/acsaem.2c02780

My contribution was: making graphs, general discussion, XRD measurements

I consent to the submission of the above-mentioned work by Ph.D. student Shyantana Dasgupta as part of the dissertation of doctoral studies in the form of a collection of published and thematically related scientific articles.

Name: Łukasz Pawlaczyk

Orcid ID: 0000-0003-1592-855X

Signature:

*Łukasz
Pawlaczyk*

I certify this publication:

Shyantana Dasgupta, Wiktor Żuraw, Taimoor Ahmad, Luigi Angelo Castriotta, Eros Radicchi, Wojciech Mróz, Mateusz Ścigaj, Łukasz Pawlaczyk, Magdalena Tamulewicz-Szwajkowska, Marek Trzeciński, Jarosław Serafińczuk, Edoardo Mosconi, Aldo Di Carlo, Filippo De Angelis, Alina Dudkowiak, Konrad Wojciechowski: *Modification of a buried interface with bulky organic cations for highly stable flexible perovskite solar cells*: DOI: 10.1021/acsaem.2c02780

My contribution was the surface properties and roughness analysis of the samples, as well as electrical measurements using scanning probe microscopy in C-AFM mode. The scope of my work included processing and analyzing obtained results and preparing the description for publication.

I consent to the submission of the above-mentioned work by Ph.D. student Shyantana Dasgupta as part of the dissertation of doctoral studies in the form of a collection of published and thematically related scientific articles.

Orcid ID: 0000-0002-7382-011X

Magdalena Tamulewicz-Szwajkowska

27.12.2022



Tamulewicz-Szwajkowska
Magdalena

I certify this publication:

Shyantana Dasgupta, Wiktor Żuraw, Taimoor Ahmad, Luigi Angelo Castriotta, Eros Radicchi, **Wojciech Mróz**, Mateusz Ścigaj, Łukasz Pawlaczyk, Magdalena Tamulewicz-Szwajkowska, Marek Trzcinski, Jarosław Serafińczuk, Edoardo Mosconi, Aldo Di Carlo, Filippo De Angelis, Alina Dudkowiak, **Konrad Wojciechowski**: *Modification of a buried interface with bulky organic cations for highly stable flexible perovskite solar cells*: DOI: 10.1021/acsaem.2c02780

My contribution was: Performing XPS (X-ray Photoelectron Spectroscopy) measurements and quantitative analysis of obtained data by fitting the spectra to Gauss-Lorentz shapes. As a result, the surface atomic concentrations of the sample components were determined.

I consent to the submission of the above-mentioned work by Ph.D. student Shyantana Dasgupta as part of the dissertation of doctoral studies in the form of a collection of published and thematically related scientific articles.

Orcid ID: 0000-0001-7304-9655

Marek Trzcinski



Wroclaw 12.09.2023

I certify this publication

Dasgupta, S; Zuraw, Wiktor; Ahmad, Taimoor; Castriotta, Luigi Angelo; Radicchi, Eros; Mroz, Wojciech; Ścigaj, Mateusz; Pawlaczyk, Łukasz; Tamulewicz-Szwajkowska, Magdalena; Trzcíński, Marek; Serafińczuk, Jarosław; Mosconi, Edoardo; Di Carlo, Aldo; De Angelis, Filippo; Dudkowiak, Alina; Wojciechowski, Konrad- 'Modification of a buried interface with bulky organic cations for highly stable flexible perovskite solar cells'-DOI:
10.1021/acsaem.2c02780

My contribution was: XRD measurements, AFM measurements supervising, XRD and AFM results discussion.

I consent to the submission of the above-mentioned work by Ph.D. student Shyantana Dasgupta as part of the dissertation of doctoral studies in the form of a collection of published and thematically related scientific articles.

Name: Jarosław Serafińczuk

Orcid ID: 0000-0001-9809-4233

Signature:



28/08/2023

I certify this publication:

Shyantana Dasgupta, Wiktor Żuraw, Taimoor Ahmad, Luigi Angelo Castriotta, Eros Radicchi, Wojciech Mróz, Mateusz Scigaj, Łukasz Pawlaczyk, Magdalena Tamulewicz-Szwajkowska, Marek Trzciniński, Jarosław Serafińczuk, Edoardo Mosconi, Aldo Di Carlo, Filippo De Angelis, Alina Dudkowiak, Konrad Wojciechowski: *Modification of a buried interface with bulky organic cations for highly stable flexible perovskite solar cells*: DOI: 10.1021/acsaem.2c02780

My contribution was: (4-5 lines)

I performed computational modeling of different terminated formamidinium lead iodide perovskite surfaces by means of Density Functional Theory simulations. I then evaluated both the thermodynamics of the adsorption process of organic cations on top of such systems and their density of states, to estimate the alignment between the (un)passivated perovskite surface and the hole transporting material employed in the experiments.

I consent to the submission of the above-mentioned work by Ph.D. student Shyantana Dasgupta as part of the dissertation of doctoral studies in the form of a collection of published and thematically related scientific articles.

Edoardo Mosconi, Orcid ID: 0000-0001-5075-6664

A handwritten signature in blue ink that reads "Mosconi Edoardo". The signature is written in a cursive, flowing style.

I certify this publication

Dasgupta, S; Zuraw, Wiktor; Ahmad, Taimoor; Castriotta, Luigi Angelo; Radicchi, Eros; Mroz, Wojciech; Ścigaj, Mateusz; Pawlaczyk, Łukasz; Tamulewicz-Szwajkowska, Magdalena; Trzciniński, Marek; Serafińczuk, Jarosław; Mosconi, Edoardo; Di Carlo, Aldo; De Angelis, Filippo; Dudkowiak, Alina; Wojciechowski, Konrad- 'Modification of a buried interface with bulky organic cations for highly stable flexible perovskite solar cells'-DOI:
10.1021/acsaem.2c02780

My contribution was: Discussion of data and results, paper writing and revision

I consent to the submission of the above-mentioned work by Ph.D. student Shyantana Dasgupta as part of the dissertation of doctoral studies in the form of a collection of published and thematically related scientific articles.

Name: Aldo Di Carlo

Orcid ID: 0000-0001-6828-2380

Signature: 

28/08/2023

I certify this publication:

Shyantana Dasgupta, Wiktor Żuraw, Taimoor Ahmad, Luigi Angelo Castriotta, Eros Radicchi, Wojciech Mróz, Mateusz Scigaj, Łukasz Pawlaczyk, Magdalena Tamulewicz-Szwajkowska, Marek Trzciniński, Jarosław Serafińczuk, Edoardo Mosconi, Aldo Di Carlo, Filippo De Angelis, Alina Dudkowiak, Konrad Wojciechowski: *Modification of a buried interface with bulky organic cations for highly stable flexible perovskite solar cells*: DOI: 10.1021/acsaem.2c02780

My contribution was: (4-5 lines)

I performed computational modeling of different terminated formamidinium lead iodide perovskite surfaces by means of Density Functional Theory simulations. I then evaluated both the thermodynamics of the adsorption process of organic cations on top of such systems and their density of states, to estimate the alignment between the (un)passivated perovskite surface and the hole transporting material employed in the experiments.

I consent to the submission of the above-mentioned work by Ph.D. student Shyantana Dasgupta as part of the dissertation of doctoral studies in the form of a collection of published and thematically related scientific articles.

Filippo De Angelis, Orcid ID: 0000-0003-3833-1975



I certify that in this publication:

T. Ahmad, S. Dasgupta, S. Almosni, A. Dudkowiak, et K. Wojciechowski, « Encapsulation protocol for flexible perovskite solar cells enabling stability in accelerated aging tests », ENERGY & ENVIRONMENTAL MATERIALS, vol. n/a, n° n/a, p. e12434, doi: 10.1002/eem2.12434.

My contribution was that I participate to the design of the experiment by proposing to use a new type of hydrophobic buffer layer in the encapsulation process which led to record stability under damp-heat stress at 85C and 85% relative humidity. Moreover I participate by proposing some explanation about the effect the buffer layer. Final I participate by reviewing and correcting the paper before its ubmission.

I consent to the submission of the above-mentioned work by Ph.D. student Shyantana Dasgupta as part of the dissertation of doctoral studies in the form of a collection of published and thematically related scientific articles.

Orcid ID: 0000-0001-8249-120X

e-mail: samy.almosni@sauletech.com

23/06/2022

SAMY ALMOSNI